

Dissertation

Omics-Ansätze zur Analyse
der Shank1/3-assoziierten Autismus-Spektrum-Störungen
und des Lessel-Kreienkamp-Syndroms

vorgelegt von

Debora Rabea Uta Tibbe

Geboren in Bielefeld

An der Universität Hamburg

eingereichte Dissertation

Hamburg, Juli 2023

Zur Erlangung des Doktorgrades der Naturwissenschaften
Fakultät für Mathematik, Informatik und Naturwissenschaften

Fachbereich Chemie

Universität Hamburg

Dissertation

Omics Approaches for the Analysis of Shank1/3-associated Autism Spectrum Disorders and the Lessel-Kreienkamp Syndrome

submitted by

Debora Rabea Uta Tibbe

born in Bielefeld

Thesis submitted

to the University of Hamburg

Hamburg, July 2023

To achieve the doctoral degree of Natural Science
Faculty of Mathematics, Informatics and Natural Science

Department of Chemistry

University of Hamburg

Date of Disputation: 15.09.2023

Reviewer:

1. Prof. Dr. Andrew Torda - Advisor
2. Prof. Dr. Hans-Jürgen Kreienkamp - Supervisor

Committee members:

1. Prof. Dr. Andrew Torda
2. Prof. Dr. Hans-Jürgen Kreienkamp
3. Prof. Dr. Zoya Ignatova
4. Prof. Dr. Hartmut Schlüter
5. Prof. Dr. Daniel N. Wilson

The experimental work of this thesis was carried out between July 2020 and June 2023 in the Institute of Human Genetics as part of the center for Obstetrics, Paediatrics and Adolescent Medicine under the supervision of Prof. Dr. Hans-Jürgen Kreienkamp, as well as in the Institute of Neuroimmunology and Multiple Sclerosis at the Center for Molecular Neurobiology Hamburg supervised by Dr. Dr. Jan Broder Engler at the University Hospital Hamburg-Eppendorf.

Publications

1. Hassani Nia, F., Woike, D., Bento, I., Niebling, S., Tibbe, D., Schulz, K., Hirnet, D., Skiba, M., Hönck, H. H., Veith, K., Günther, C., Scholz, T., Bierhals, T., Driemeyer, J., Bend, R., Failla, A. V., Lohr, C., Alai, M. G., & Kreienkamp, H. J. (2022). Structural deficits in key domains of Shank2 lead to alterations in postsynaptic nanoclusters and to a neurodevelopmental disorder in humans. *Molecular psychiatry*, 10.1038/s41380-022-01882-3.
2. Tibbe, D., Ferle, P., Krisp, C., Nampoothiri, S., Mirzaa, G., Assaf, M., Parikh, S., Kutsche, K., & Kreienkamp, H. J. (2022). Regulation of Liprin- α phase separation by CASK is disrupted by a mutation in its CaM kinase domain. *Life science alliance*, 5(10), e202201512.
3. Woike, D., Wang, E., Tibbe, D., Hassani Nia, F., Failla, A. V., Kibæk, M., Overgård, T. M., Larsen, M. J., Fagerberg, C. R., Barsukov, I., & Kreienkamp, H. J. (2022). Mutations affecting the N-terminal domains of SHANK3 point to different pathomechanisms in neurodevelopmental disorders. *Scientific reports*, 12(1), 902.
4. Tibbe, D., Pan, Y. E., Reißner, C., Harms, F. L., & Kreienkamp, H. J. (2021). Functional analysis of CASK transcript variants expressed in human brain. *PloS one*, 16(6), e0253223.
5. Pan, Y. E., Tibbe, D., Harms, F. L., Reißner, C., Becker, K., Dingmann, B., Mirzaa, G., Kattentidt-Mouravieva, A. A., Shoukier, M., Aggarwal, S., Missler, M., Kutsche, K., & Kreienkamp, H. J. (2021). Missense mutations in CASK, coding for the calcium-/calmodulin-dependent serine protein kinase, interfere with neurexin binding and neurexin-induced oligomerization. *Journal of neurochemistry*, 157(4), 1331–1350.

1. Table of Contents

Publications	i
Abbreviations.....	vi
Zusammenfassung.....	1
Abstract	3
1. Introduction.....	3
1.1. Neurodevelopmental Disorders.....	4
1.2. Autism Spectrum Disorders	4
1.2.1. Shank Proteins Function as Scaffolds of the Postsynaptic Density	5
1.2.2. Modelling of ASDs in <i>Shank</i> Knockout Mice.....	7
1.3. Association of RNA-Binding Protein with NDDs	8
1.3.1. RNA interference	8
1.3.2. MicroRNAs	9
1.3.3. Argonaute Proteins	9
1.3.4. The RNA-induced Silencing Complex	10
1.4. Omics approaches.....	12
2. Aim of the Project.....	13
3. Materials and Methods.....	14
3.1. Materials.....	14
3.1.1. Laboratory Mice.....	14
3.1.2. Bacterial Strains and Cell Lines	14
3.1.3. Antibodies.....	14
3.1.4. Oligonucleotides	15
3.1.5. Plasmids	16
3.1.6. Commercial Kits	16
3.1.7. Buffers, Solutions and Supplements	17
3.2. Methods.....	20
3.2.1. Molecular Biology Methods.....	20
3.2.1.1. Transformation of <i>E.coli</i> Top10F' by Heat Shock	20
3.2.1.2. Purification of Plasmid DNA from <i>E. coli</i> - small scale (Miniprep)	20
3.2.1.3. Purification of Plasmid DNA from <i>E. coli</i> - large scale (Midiprep)	21
3.2.1.4. Restriction Digest.....	21
3.2.1.5. Gel Electrophoresis.....	21
3.2.1.6. Gel Extraction.....	21
3.2.1.7. Ligation	21

3.2.1.8. Mutagenesis.....	21
3.2.1.9. Sanger Sequencing of Plasmid DNA	22
3.2.2. Cell Culture Methods	23
3.2.2.1. Cell Culture with HEK293T Cells	23
3.2.2.2. Transient Transfection of HEK293T Cells	23
3.2.2.3. Primary Cell Culture of Mouse Cortical Neurons	23
3.2.2.4. Transduction of Cortical Neurons with Adeno-associated Viruses	23
3.2.3. Biochemical Methods	24
3.2.3.1. Cell Lysis of HEK293T Cells	24
3.2.3.2. Coimmunoprecipitation (RFP-trap).....	24
3.2.3.3. SDS-PAGE and Western Blot	24
3.2.3.4. Immunocytochemistry and Confocal Microscopy.....	24
3.2.3.5. MicroRNA Affinity Purification	25
3.2.3.5.1. Quantitative Polymerase Chain Reaction for detection of miRNAs.....	25
3.2.4. Animal Testing	28
3.2.4.1. Housing of Laboratory Mice.....	28
3.2.4.2. Breeding of Laboratory Mice	28
3.2.4.3. Generation and Breeding of Lypd1-bacTRAPx <i>Shank1</i> -KO and Lypd1-bacTRAPx <i>Shank3αβ</i> -KO mice	28
3.2.4.4. Genotyping.....	28
3.2.4.5. Open Field Test	30
3.2.4.6. Preparation of Postsynaptic Densities.....	30
3.2.4.7. Translating Ribosome Affinity Purification	31
3.2.4.7.1. Quantitative Polymerase Chain Reaction for mRNA	32
3.2.5. Analytical Methods and Bioinformatics	33
3.2.5.1. RNA Sequencing.....	33
3.2.5.2. Mass spectrometry	33
4. Results	35
4.1. The Neuronal Translatome and the Postsynaptic Proteome are Affected by Knockout of <i>Shank1</i> or <i>Shank3αβ</i> in ASD Mouse Models.....	35
4.1.1. Validation of an ASD-typical Phenotype in <i>Shank1</i> and <i>Shank3αβ</i> Knockout Mouse Models	35
4.1.2. The Neuronal Translatome of Lypd1-bacTRAP- <i>Shank3αβ</i> -KO Mice.....	39
4.1.2.1. Validation of the ASD-typical Phenotype in Lypd1-bacTRAP- <i>Shank1</i> -KO and Lypd1-bacTRAP- <i>Shank3αβ</i> -KO Mice	40
4.1.2.2. Evaluation of Cell Specificity of GFP-tagged Rpl10 Expression	41

4.1.2.3. A Translatomics Approach to Decipher the Consequence of <i>Shank3αβ</i> Knockout on Regulation of Translation	42
4.1.3. The Proteome of the Postsynaptic Density in <i>Shank1</i> -KO and <i>Shank3αβ</i> -KO Mice	46
4.1.3.1. Validation of Efficiency and Specificity of the Postsynaptic Density Purification	46
4.1.3.2. Evaluation of the Effect of <i>Shank1</i> and <i>Shankαβ</i> Knockout on Shank and CaMKII Protein Abundance	48
4.1.3.3. Knockout of <i>Shank1</i> and <i>Shank3αβ</i> Alters the Postsynaptic Proteome	49
4.1.3.4. Knockout of <i>Shank1</i> and <i>Shank3αβ</i> Results in Increased Levels of CaMKIIα in the Postsynaptic Density	53
4.2. The Ago2 Patient Variant L192P Affects the miRNome and the miRNAs Bound to the RISC.....	56
4.2.1. Validation of GFP-Ago2 Expression in AAV-transduced Primary Cortical Neurons	56
4.2.2. The Ago2 Variant L192P Induces an Increased Occurrence of Dendritic P-Bodies	57
4.2.3. Evaluation of miRNA Concentration and Relative Enrichment of Neuron-specific miRNA-124 for Quality Assurance of the miRAP Assay	58
4.2.4. The Ago2-L192P Variant Induces Changes in the miRNome and RISC-associated miRNAs..	60
4.2.5. Ago2 Variants Affect the Expression of Alternative miRNA Strands and Mediate miRNA Arm Switching Events in the RISC	62
4.2.6. The Ago2 Patient Variant L192P Induces Enhanced Incorporation of isomiRs into the RISC.....	66
4.2.7. Target Predictions for Deregulated miRNAs	67
5. Discussion	74
5.1. Loss of <i>Shank1</i> or <i>Shank3αβ</i> Affect Neuronal Protein Synthesis and the Postsynaptic Protein Network	74
5.1.1. Original and Novel <i>Shank1</i> and <i>Shank3αβ</i> Knockout Mice Models Displayed an ASD-typical Phenotype.....	74
5.1.2. Absence of the N-terminal Domains of <i>Shank3</i> Lead to Subtle Alterations in the Translatome of Hippocampal Neurons	76
5.1.3. Loss of <i>Shank1</i> and <i>Shank3αβ</i> Causes Differences in the Postsynaptic Proteomes	79
5.1.4. Absence of <i>Shank1</i> and <i>Shank3αβ</i> Affect the Activation Status of the CaMKIIα at the Postsynapse	83
5.1.5. Comparison of the Translatome and Proteome in the Hippocampus of <i>Shank3αβ</i> Knockout mice	84
5.2. L192P-RISC Induces Deregulation of the RNA Interference Pathway	87
5.2.1. The Expression of Ago2-L192P Altered Dynamics of P-Bodies.....	88
5.2.2. The miRAP Method Targeted RISC-bound miRNAs Specifically in Neurons.....	88
5.2.3. Ago2-L192P Affected the miRNome and the Formation of RISC	89
5.2.4. The Ago2 Mutant L192P Exhibited Altered Strand Selectivity	91
5.2.5. Increased Incorporation of isomiRs into the L192P-RISC.....	94

5.2.6. Ago2-L192P Induces Deregulation of miRNAs of the miR379-409 Cluster	95
5.2.7. Gene Ontology Analyses with Predicted Targets of miRNAs Differentially Bound to the L192P-RISC.....	96
5.3. Do Pathomechanisms of NDDs Converge in Common Pathways?.....	98
6. References	100
7. Appendix.....	134
7.1. Hazardous Substances	134
7.2. Tables.....	135
7.3. List of Figures	140
7.4. List of Tables	145
7.5. Plasmid maps	149
8. <i>Curriculum Vitae</i>	153
9. Acknowledgements	156
10. Eidesstattliche Versicherung.....	157

Abbreviations

μ

μg · microgram
μL · microlitres
μM · micromolar

3

3'UTR · 3'-untranslated region

A

aa · amino acids
AAVs · adeno-associated viruses
ADHD · attention deficit hyperactivity disorder
Ago · Argonaute
Ago2 · Argonaute-2
AMPA · α-amino-3-hydroxy-5-methyl-4-isoxazolepropionic acid receptor
ANK · ankyrin repeats
ASD · autism spectrum disorders

B

bac · bacterial artificial chromosome
BP · biological pathways
BSA · bovine serum albumin

C

c · concentration
cDNA · complementary DNA
CHX · cycloheximide
cm · centimetre
CNS · central nervous system
CoIP · coimmunoprecipitation

D

ddH₂O · ultra pure water
DEGs · differential expressed genes
DHPC · 1,2-diheptanoyl-sn-glycero-3-phosphocholine
DIV · days in vitro
DMEM · Dulbecco's Modified Eagle Medium

DNA · desoxyribonucleic acid
dNTP · deoxynucleoside triphosphate
DTT · dithiothreitol

E

eAgo · eukaryotic Argonaute proteins
EGFP · enhanced green fluorescent protein
Eif2a · Eukaryotic translation initiation factor 2A

F

F · female
FA · formic acid
FCS · foetal calf serum
FDR · false discovery rate
FE · fold enrichment
FTH · Forschungstierhaltung
fwd · forward
FXS · fragile X syndrome

G

g · standard gravity
GFP · green fluorescent protein
Gnb5 · Guanine nucleotide-binding protein subunit beta 5
GO · Gene ontology
GTEx · Genotype-Tissue Expression

H

h · hour
HBSS · Hanks' Balanced Salt Solution
HEPES · 4-(2-hydroxyethyl)-1-piperazineethanesulfonic acid
HiDi · highly deionized formamide
HRP · horseradish peroxidase
HS · horse serum
hSyn1 · human synapsin 1
HZ · heterozygous

I

IC · input control, whole cell lysates
ICC · Immunocytochemistry
ID · Intellectual disability
IgG · Immunoglobulin G
IN · input sample
IP · immunoprecipitate
ISC · RNA-induced silencing complex
isomiR · miRNA isoform

K

kb · kilobases
KO · knockout

L

L10a · 60S ribosomal protein L10a
LB · Lysogeny broth
LESKRES · Lessel-Kreienkamp syndrome
LLPS · liquid-liquid phase separation
Lypd1 · Ly6/PLAUR domain-containing protein 1

M

M · molar, male
Mef2 · factor myocyte enhancing factor 2
mg · milligram
MGI · Mouse Genome Informatics
MID · middle domain
min · minutes
miRAP · microRNA affinity purification
mL · millilitres
mM · millimolar
mmu · *mus musculus*
MOI · multiplicity of infection
MP · milk powder
mTOR · mammalian target of rapamycin

N

Naaa · N-acyl ethanolamine-hydrolyzing acid amidase
NaAc · sodium acetate
NDDs · Neurodevelopmental disorders
NGS · Next Generation Sequencing

NMDAR · N-methyl-D-aspartic acid-type glutamate receptor
NP-40 · nonyl phenoxypolyethoxyethanol
nt · nucleotides
nuc.ex · nucleotide exchange

P

pAgos · prokaryotic Argonaute proteins
PBS · phosphate-buffered saline
PCA · principal component analysis
PCR · polymerase chain reaction
PEG · Polyethylenglycol
pen/strep · penicillin/streptavidin
PFA · paraformaldehyde
PIWI · Pelement-induced wimpy testis
PLL · poly-L-lysine
PMSF · phenylmethylsulfonyl fluoride
PND · postnatal day
pre-miRNA · precursor miRNA
pri-miRNA · primary miRNA
PSD · postsynaptic density
PTGR · posttranscriptional gene regulation

R

Rabep1 · Rab GTPase-binding effector-protein 1
rev · reverse
RFP · red fluorescent protein
Rgs7bp · Regulator of G-protein signaling 7-binding protein
RISC · RNA-induced silencing complex
Rn · normalized reporter value
RNA · Ribonucleic acid
RNAi · RNA interference
RNA-seq · RNA sequencing
ROX · Carboxyrhodamine
rpm · rounds per minute
RT · room temperature

S

s · second
SAM · sterile alpha motif
SDC · sodium deoxycholate
SDS · sodium dodecyl sulphate

SDS-PAGE · sodium dodecyl sulphate
polyacrylamide gel electrophoresis
SH3 · SRC homology 3
Shank · SH3 and multiple ankyrin repeat
domains
ProSAP · proline-rich synapse-associated
protein
SPN · Shank/ProSAP N-terminal domain
sRNA · small RNA

T

T · thymine
TAE · Tris-acetate-EDTA
TBS-T · Tris-buffered saline with Tween
TE · Tris-EDTA
TEAB · triethylammonium bicarbonate
TRAP · translating ribosome affinity
purification

U

U · uracil

UV · ultraviolet

V

V · volt
v/v · volume concentration

W

w/v · mass concentration
WB · western blot
WT · wildtype

Z

ZMNH · Centre for Molecular Neurobiology
Hamburg
Zn²⁺ · zinc ion

α

αCaMKII · α subunit of the calcium/calmodulin
dependent kinase II

Zusammenfassung

Neurologische Entwicklungsstörungen entstehen durch Störungen der Gehirnentwicklung, die oft genetisch bedingt sind. Die krankheitsassoziierten Gene kodieren für drei funktionelle Klassen von Proteinen: Transkriptionsregulatoren, synaptische Proteine und RNA-bindende Proteine. Es wurde vermutet, dass den Pathomechanismen die gleichen molekularen Signalwege zugrunde liegen. In diesem Projekt wurden Pathomechanismen analysiert und verglichen, die durch Fehlfunktion von Genen aus zwei dieser funktionellen Klassen bedingt sind. Mutationen in den *SHANK1*- und *SHANK3*-Genen sind mit Autismus-Spektrum-Störungen assoziiert, und die *SHANK*-Gene kodieren für synaptische Gerüstproteine. Das Gen *AGO2* kodiert für das RNA-bindende Protein Argonaute-2. Varianten in *AGO2* wurden als Auslöser des Lessel-Kreienkamp-Syndroms identifiziert.

Shank-Proteine sind Gerüstproteine von exzitatorischen, glutamatergen Synapsen. Shank-Proteine verbinden postsynaptische Glutamaterezeptoren indirekt mit F-Aktin über ein Proteinnetzwerk. Der N-Terminus von Shank3 interagiert mit G-Proteinen der Ras-Familie, wodurch Shank Proteine mit dem MAPK-Signalweg in Verbindung stehen. Dieser ist wiederum an der Regulation der Translation beteiligt. Es wird vermutet, dass eine veränderte Translation bei diversen Autismus-Spektrum-Störungen zu dem Pathomechanismus beiträgt. Die Hypothese dieses Projekts war, dass der Verlust von Shank die Translation verändern könnte. Diese Hypothese wurde mit *Omics*-Ansätzen überprüft. Das Translatom und Proteom von Mausmodellen für Shank-assoziierte Autismus-Spektrum-Störungen wurden untersucht. Aktiv translatierte mRNAs wurden aus hippocampalen Neuronen von *Shank3 $\alpha\beta$* -Knockout-Mäusen mittels microRNA-Affinitätsreinigung präpariert und durch RNA-Sequenzierung analysiert. Der Verlust von Shank3 $\alpha\beta$ führte zu einer geringfügig veränderten Translation von einer Untergruppe neuronaler Transkripte. Proteomics-Studien wurden an biochemisch aufgereinigten postsynaptischen Dichtefraktionen aus Hippocampi von *Shank1*- und *Shank3 $\alpha\beta$* -Knockout-Mäusen durchgeführt. Durch Verlust von Shank1 und Shank3 $\alpha\beta$ wurde das postsynaptische Proteom stark verändert. Die Menge der aktiven, phosphorylierten CaMKII α war in Postsynapsen von *Shank*-Knockout-Mäusen erhöht, was zu einer fehlregulierten neuronalen Signalübertragung beitragen kann.

Argonaute-2 spielt eine Rolle in der RNA-Interferenz. Um eine Hemmung der Translation durchzuführen, assoziiert Argonaute-2 mit microRNA und bildet den RNA-induzierten *Silencing*-Komplex. Es wurde die Hypothese aufgestellt, dass von Patienten stammende Argonaute-2-Mutanten andere microRNAs binden als Wildtyp-Argonaute-2 und dadurch die RNA-Interferenz beeinflusst werden könnte. Um diese Hypothese zu testen, wurden primäre kortikale Neuronen mit Adeno-assoziierten Viren infiziert und damit die Expression der Argonaute-2-Mutante L192P induziert. Die Expression der L192P-Variante führte zu einem vermehrten Auftreten von dendritischen Prozessierungsclustern, was durch Immunzytochemie und konfokale Mikroskopie nachgewiesen wurde. Es wurde eine microRNA-Affinitätsaufreinigung durchgeführt und microRNAs sequenziert. Die exprimierten und die an Argonaute-2-gebundenen microRNAs wurden identifiziert. Vier verschiedene Aspekte der microRNA-abhängigen RNA-Interferenz waren in Neuronen, die die Argonaute-2-Mutante exprimierten, verändert. Einige microRNAs wurde unterschiedlich stark exprimiert, was auf ein verändertes miRNom hinweist. Mehrere microRNAs wiesen eine veränderte Assoziation mit dem RNA-induzierten *Silencing*-Komplex auf. Die Argonaute-2-Mutante besaß eine veränderte Strangselektivität, die „*arm switching*“ Ereignisse zwischen Leit- und Passagiersträngen von microRNAs induzierte. Die Patientenvariante führte zu einem verstärkten Einbau von Isomeren von microRNAs, den so genannten isomiRs. Einige der isomiRs waren ausschließlich an Argonaute-2 L192P gebunden, während keine der isomiRs ausschließlich mit dem Wildtyp-Protein assoziiert war. Die Argonaute-2-Variante führte zu einer Deregulierung des genomischen Clusters miR379-409. Die Deregulierung dieses Clusters beeinflusst wahrscheinlich die Neurogenese, die neuronale Migration und die synaptische Funktion.

Analysen des Translatoms, des Proteoms, des miRNoms und der an Argonaute-2 gebundenen microRNAs zeigten unterschiedliche Aspekte einer Deregulation, die zu den molekularen Defekten in Modellsystemen für neuronale Entwicklungsstörungen beitragen. Dies deutet darauf hin, dass die Pathomechanismen der Shank-assoziierten Formen von Autismus-Spektrum-Störungen und des Lessel-Kreienkamp-Syndroms nicht in gemeinsamen Pfaden konvergieren, sondern vielmehr zu weitreichenden und Gen-spezifischen Veränderungen von zellulären Funktionen führen.

Abstract

Neurodevelopmental disorders arise due to malfunctions in brain development and often are genetically caused. The disease-associated genes encode three major classes of proteins: transcriptional regulators, synaptic proteins, and RNA-binding proteins. It was proposed that the pathomechanisms may converge in shared molecular pathways. I functionally analyzed and compared the pathomechanisms of insufficiency for *SHANK1* and *SHANK3*, two genes associated with autism spectrum disorders, with a variant of the *AGO2* gene, encoding the RNA-binding protein Argonaute-2 and causing Lessel-Kreienkamp syndrome.

The *SHANK* genes encode Shank proteins, scaffolds of excitatory, glutamatergic synapses that indirectly connect postsynaptic glutamate receptors to F-actin via a protein network. The N-terminus of Shank3 interacts with Ras family G-proteins, connecting Shank to the MAPK pathway, which is involved in translational regulation. Altered translation has been implicated in the pathology of autism spectrum disorders. The hypothesis of this project was that loss of Shank may alter the regulation of translation. Omics were applied to test this hypothesis. The transcriptome and proteome of mouse models for Shank-associated autism spectrum disorders were investigated. Actively translated mRNAs were purified from hippocampal neurons of *Shank3 $\alpha\beta$* knockout mice via microRNA affinity purification and analyzed by RNA sequencing. Absence of Shank3 $\alpha\beta$ resulted in subtly altered translation of a subset of neuronal transcripts. Proteomics were performed with biochemically purified postsynaptic density fractions from hippocampi of *Shank1* and *Shank3 $\alpha\beta$* knockout mice. The loss of Shank1 and Shank3 $\alpha\beta$ severely altered the postsynaptic proteome. The abundance of active, phosphorylated CaMKII α was increased in *Shank* knockout mice, which may contribute to misregulated neuronal signaling.

Argonaute-2 functions in RNA interference. To execute translational silencing, Argonaute-2 associates with microRNA and forms the RNA induced silencing complex. It was hypothesized that patient derived Argonaute-2 mutants may bind different microRNAs, altering RNA interference. To test this hypothesis, primary cortical neurons were infected with adeno-associated viruses to induce expression of the Argonaute-2 mutant L192P. Expression of the L192P variant induced increased occurrence of dendritic processing bodies, shown by immunocytochemistry and confocal microscopy. MicroRNA affinity purification was applied, and microRNAs were sequenced. The expressed and Argonaute-2-bound microRNAs were identified. Four different aspects of microRNA-dependent RNA interference were altered in neurons that expressed the Argonaute-2 mutant. A subset of microRNAs was differentially expressed, indicating an affected miRNome. Several microRNAs exhibited altered association to the RNA induced silencing complex. The Argonaute-2 mutant showed altered strand selectivity, which resulted in arm switching events between guide and passenger strands of microRNAs. The patient variant induced enhanced incorporation of isomers of microRNAs, termed isomiRs. A subset of isomiRs was exclusively bound to Argonaute-2 L192P, whereas none of the isomiRs associated exclusively with the wildtype protein. The Argonaute-2 variant resulted in deregulation of the miR379-409 genomic cluster. Deregulation of this cluster likely affects neurogenesis, neuronal migration, and synaptic function.

Analyses of transcriptome, proteome, miRNome, and Argonaute-2-bound microRNAs demonstrated variable deregulations contributing to the molecular defects in model systems for neurodevelopmental disorders. This suggests that the pathomechanisms of Shank-associated forms of autism spectrum disorders and Lessel-Kreienkamp syndrome do not converge in common pathways, but rather result in broad and gene-specific alterations of cellular functions.

1. Introduction

1.1. Neurodevelopmental Disorders

Neurodevelopmental disorders (NDDs) are diseases that arise due to malfunctions during brain development. The clinical presentation of NDDs is characterized by deficits in cognition, communication, and motor skills. Patients are often unable to achieve developmental milestones and NDDs are regularly diagnosed in childhood (Parenti *et al.* 2020). Intellectual disability (ID), autism spectrum disorders and attention deficit hyperactivity disorder (ADHD) are examples of well-known NDDs (Niemi *et al.* 2018, Tarlunganu and Novarino 2018). Frequently, a combination of ID, ASD and epilepsy is the patient's phenotype (van Bokhoven 2011, Du *et al.* 2018). NDDs often have a genetic cause (Parenti *et al.* 2020). NDD-causing mutations include chromosomal rearrangements, insertions and deletions of varying sizes, and single nucleotide variants (SNVs) in which only a single DNA base is exchanged (Kong *et al.* 2012, Bourgeron 2015, Parenti *et al.* 2020). Frequently, these variants are not inherited from the parents but occur *de novo*.

Brain development requires extensive spatial and temporal regulation of migration, function, and plasticity of neurons (Prashad and Gopal 2021). Neurons, the key players of the central nervous system (CNS), are highly polarized and complex. In addition to the cell body, which is called the soma, neurons have long and branched extensions: the axons and dendrites (Chklovskii 2004). Synapses are asymmetric intercellular connections between axons and dendrites of different neurons through which they transmit information (Sheng and Hoogenraad 2007, Sudhof 2018). Synaptic transmission between presynaptic sites on an axon and postsynaptic sites formed on a dendrite is enabled by the release and reception of neurotransmitters. For this, the pre- and postsynapse must be precisely aligned. Mutations in genes encoding synaptic scaffold or adhesion proteins disrupt synaptogenesis, which is increasingly recognized as a major cause of NDDs (Zoghbi 2003, Grabrucker *et al.* 2011, Bourgeron 2015).

More than 900 NDD risk genes have been identified (Wright *et al.* 2015, Clark *et al.* 2018, Srivastava *et al.* 2019). Interestingly, the proteins encoded by these genes appear to belong to different subgroups depending on their cellular function. The major classes of proteins are chromatin remodellers and other transcriptional regulators, synaptic proteins, and RNA-binding proteins (Wright *et al.* 2015, Clark *et al.* 2018, Srivastava *et al.* 2019). In this thesis, I functionally analyzed and compared the pathomechanisms of two classes of NDD risk genes using omics approaches. First, I analyzed *SHANK1* and *SHANK3*, ASD-associated genes which encode postsynaptic scaffold proteins (Sheng and Kim 2000, Grabrucker *et al.* 2011, Sato *et al.* 2012). Second, I analyzed a NDD-causing variant of the *AGO2* gene encoding the RNA-binding protein Argonaute-2, which plays a key role in the RNA interference signaling pathway (Hammond *et al.* 2000, Lessel *et al.* 2020).

1.2. Autism Spectrum Disorders

Autism spectrum disorders (ASD) are a clinically heterogeneous subgroup of NDDs characterized by impairment of social interaction and communication, restricted interests, stereotypic or repetitive behaviors, restlessness, and sensory impairments (Asperger 1944, Kanner 1968, Lord *et al.* 2000, Foxe *et al.* 2015). The phenotype exhibits wide variability among autistic individuals. ASD is rarely diagnosed alone but rather as a comorbidity with other NDD-typical symptoms such as ID, ADHD, epilepsy, and anxiety (Skuse *et al.* 2009, Gillberg 2010, Constantino 2011, Moreno-De-Luca *et al.* 2013). While the extent to which environmental and epigenetic factors contribute to ASD remains unclear, a strong genetic contribution has been demonstrated in several studies, and the estimated heritability of ASD ranges from 38%-90% (Hallmayer *et al.* 2011, Ronald and Hoekstra 2011, Sandin *et al.* 2014). 10%-25% of ASD cases are monogenic forms in which a single mutation in one gene causes the core symptoms. Mutations in all three *SHANK* genes, encoding the Shank/ProSAP proteins, have been reported in

individuals diagnosed with ASD (Bonaglia *et al.* 2001, Durand *et al.* 2007, Moessner *et al.* 2007, Berkel *et al.* 2010, Sato *et al.* 2012). Although high homology exists between *SHANK1*, *SHANK2*, and *SHANK3*, patients with *SHANK* mutations display a variable phenotype of ASD in combination with ID, schizophrenia, and other comorbidities (Grabrucker *et al.* 2011, Berkel *et al.* 2012, Sato *et al.* 2012). *SHANK3* was first described as a disease-causing gene. Haploinsufficiency of *SHANK3* was identified as the cause of Phelan-McDermid syndrome, also known as deletion 22q13.3 syndrome, characterized by ASD-like features, ID, delayed development or absence of speech, and hypotonia (Bonaglia *et al.* 2001, Wilson *et al.* 2003, Manning *et al.* 2004, Phelan 2008). Various *SHANK3* variants have been identified in autistic patients, including deletions and duplications of genomic sections of varying sizes, translocations and point mutations (Bonaglia *et al.* 2005, Bonaglia *et al.* 2011, Boccutto *et al.* 2013). The point mutations include frame shift, splice site, and missense variants (Durand *et al.* 2007, Moessner *et al.* 2007, Gauthier *et al.* 2009). Collectively, mutations in *SHANK3* account for 1% of genetically caused ASDs (Moessner *et al.* 2007, Boccutto *et al.* 2013). ASD-associated mutations in *SHANK1* contribute to 0.04% of all ASD cases and are rarer compared to *SHANK3* (Leblond *et al.* 2014). *De novo* deletions spanning *SHANK1* and adjacent genes, as well as missense and splice site variants have been reported in males diagnosed with mild ASD with ID and in females with depression or anxiety (Sato *et al.* 2012, Qin *et al.* 2022).

1.2.1. Shank Proteins Function as Scaffolds of the Postsynaptic Density

The Shank/ProSAP proteins are postsynaptic scaffold proteins of excitatory, glutamatergic synapses (Sheng and Kim 2000, Gundelfinger *et al.* 2006, Kreienkamp 2008, Grabrucker *et al.* 2011). These synapses localize to the tip of dendritic spines, protrusions originating from dendrites. Spines form a biochemical microcompartment for calcium ion (Ca^{2+}) signaling by separating the spine head from the dendritic shaft through a narrow spine neck (Noguchi *et al.* 2005, Higley and Sabatini 2012, Raghuram *et al.* 2012). Thus, a single neuron can be equipped with up to 10,000 of these microcompartments, allowing for complex signal processing (Sorra and Harris 2000, Carlisle and Kennedy 2005). Spines change dynamically in size and protein composition to adapt to the signals they receive, which is the molecular basis of synaptic plasticity (Grunditz *et al.* 2008, Colgan and Yasuda 2014). The morphological and molecular adaptations of spines are enabled by activity-dependent rearrangement of filamentous actin (F-actin), a cytoskeletal protein enriched in spine heads (Fischer *et al.* 1998, Hotulainen and Hoogenraad 2010, Dent *et al.* 2011). The Shank proteins, i.e. Shank1, ProSAP1/Shank2, and ProSAP2/Shank3, indirectly connect F-actin to neurotransmitter receiving receptors at the postsynaptic membrane (Du *et al.* 1998, Boeckers *et al.* 1999, Lim *et al.* 1999). Through several protein-protein interaction domains, Shank proteins interact with various postsynaptic proteins and scaffold a dense protein network beneath the postsynaptic membrane (Sheng and Kim 2000, Sheng and Hoogenraad 2007, Kreienkamp 2008). This sub-membranous network is the so-called postsynaptic density fraction or PSD (Chen *et al.* 2005, Sugiyama *et al.* 2005, Sheng and Hoogenraad 2007, Sheng and Kim 2011). All three Shank proteins exhibit a broad expression pattern throughout brain regions, cell populations and developmental time points. Notably, higher expression of Shank was observed in the hippocampus and cortex, brain areas implicated in learning processes and cognition (Zitzer *et al.* 1999, Bockers *et al.* 2001, Bockers *et al.* 2004, Roussignol *et al.* 2005). The domain structure is highly conserved among the three members of the Shank protein family. From the N- to the C-terminus, full-length Shank consists of the Shank/ProSAP N-terminal (SPN), the ankyrin repeats (ANK), the SRC homology 3 (SH3) and PSD-95/Discs large/ZO-1 (PDZ) domains, followed by a proline-rich region and a sterile alpha motif (SAM) (Figure 1) (Naisbitt *et al.* 1999, Tu *et al.* 1999, Sheng and Kim 2000, Bockers *et al.* 2001, Gundelfinger *et al.* 2006, Kreienkamp 2008, Jiang and Ehlers 2013).

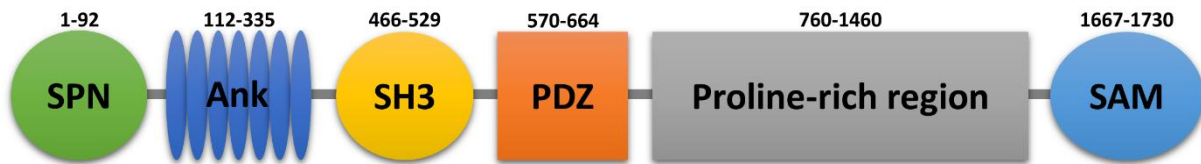


Figure 1: Domains of the Shank proteins. The domains are highly conserved among all Shank proteins, though individual domains may be missing in some transcript variants. The numbers indicate the length and position of the amino acid sequence of the respective domain of Shank3 in full length. From the N- to the C-terminus: Shank/ProSAP N-terminal (SPN) domain, the ankyrin repeats (ANK), the SRC homology 3 (SH3) domain, the PSD-95/Discs large/ZO-1 (PDZ) domain, the proline-rich region (PRR) and the sterile alpha motif (SAM). Adapted from Lilja *et al.* 2017 and the PhD thesis of D. Woike 2022.

The SPN domains of Shank1 and Shank3 associate with active Ras and Rap small G-proteins, linking this domain to G-protein-mediated signaling (Lilja *et al.* 2017). The inactive α -subunit of the calcium/calmodulin dependent kinase II (CaMKII α) binds to the SPN domain and the linker region between the SPN and ANK domain (Cai *et al.* 2021). The ankyrin repeats facilitate regulation of F-actin via binding to α -fodrin (Bockers *et al.* 2001). Additional binding sites for the actin-regulatory proteins Abi1, IRSp53 and cortactin are located in the proline-rich region (Du *et al.* 1998, Soltau *et al.* 2002, Proepper *et al.* 2007). The PDZ domain and the Homer binding site inside the PRR connect Shank either directly or indirectly with ionotropic and metabotropic glutamate receptors (Naisbitt *et al.* 1999, Tu *et al.* 1999, Uchino *et al.* 2006). Ionotropic α -amino-3-hydroxy-5-methyl-4-isoxazolepropionic acid receptors (AMPA receptors) either interact with the PDZ domain of Shank or indirectly associate with Shank via the Shank-GKAP-PSD-95-Stargazin-AMPA receptor complex (Garner *et al.* 2000, Uchino *et al.* 2006). GKAP and PSD-95 connect Shank to N-methyl-D-aspartic acid-type glutamate receptors (NMDARs) (Boeckers *et al.* 1999, Naisbitt *et al.* 1999, Tu *et al.* 1999). Self-association of the C-terminal SAM domain allows Shank proteins to multimerize into helical fibers that, when stacked side by side, form sheet structures (Boeckers *et al.* 2005, Baron *et al.* 2006, Kreienkamp 2008, Hayashi *et al.* 2009). This clustering requires incorporation of zinc ions (Zn^{2+}) into the polymers of SAM domains and the SAM domains of Shank2 and Shank3 bind Zn^{2+} efficiently (Baron *et al.* 2006, Grabrucker *et al.* 2011), (Boeckers *et al.* 2005, Gundelfinger *et al.* 2006). Through the multiple interactions described, Shank proteins are involved in various signaling cascades at the PSD and are believed to be essential for synapse formation (Figure 2).

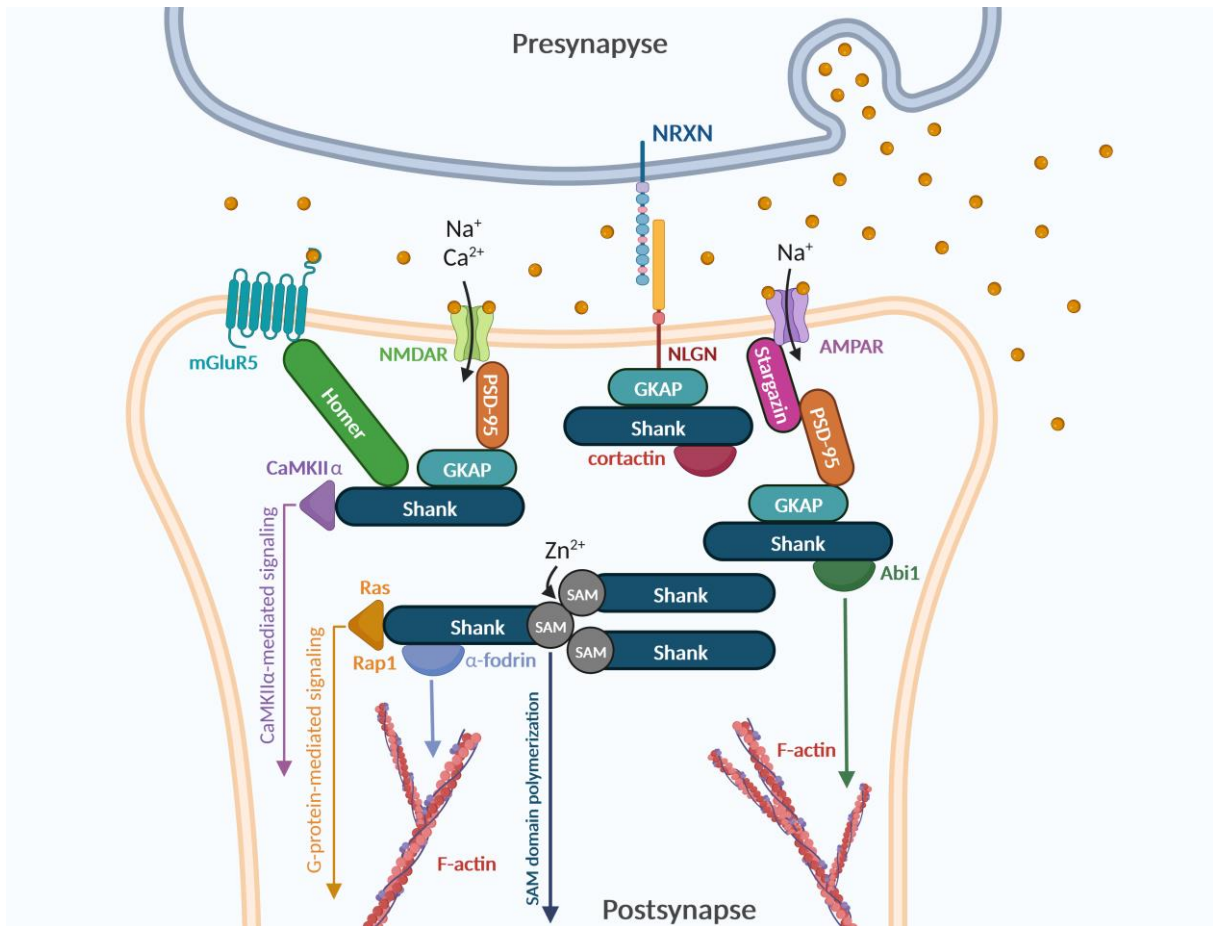


Figure 2: Shank proteins function as scaffold of the postsynapse. Shanks localize at excitatory, glutamatergic synapses on dendritic spines. Shanks links F-actin to glutamate receiving receptors at the postsynaptic membrane. Shank is either directly or indirectly connected with ionotropic and metabotropic glutamate receptors. AMPARs either interact with the PDZ domain of Shank or indirectly associate with Shank via the Shank-GKAP-PSD-95-Stargazin-AMPAR complex. GKAP and PSD-95 connect Shank to NMDARs. Shank proteins are connected to the cell adhesion molecule Neurologin (NLGN) via GKAP. Neurologin interacts with presynaptic neurexin (NRXN) in the synaptic cleft. Shank binds mGluR5 indirectly via Homer. Zn^{2+} -dependent self-association of the C-terminal SAM domain allows Shank proteins to multimerize. Shank facilitates regulation of F-actin via binding to actin-regulatory proteins such as α -fodrin, Abi1 and cortactin. The N-terminal domains link Shank to CaMKII α and Ras/Rap1-mediated signaling pathways. Created with BioRender.com.

1.2.2. Modelling of ASDs in *Shank* Knockout Mice

Monogenic forms of ASD provide the possibility to introduce the respective genomic alterations into mouse models and to investigate neurobiological mechanisms *in vivo* (Jiang and Ehlers 2013). *SHANK1* and *SHANK3* mutations are promising candidates for the rodent model system since the genetic contribution in *SHANK*-associated ASDs is strong (Schmeisser 2015). Mouse models allow one to test for an autistic phenotype and to study the rescue effects of drug candidates in behavioral tests, paving a road to treatment (Murphy and Sporen 2012, Ecker *et al.* 2013, Sungur *et al.* 2014). *Shank3* can be transcribed from six alternative promoters, making this gene complex to manipulate (Lim *et al.* 1999, Naisbitt *et al.* 1999). Hence, several mouse models were generated that differ by deletion of different genomic segments, resulting in isoform-specific or complete loss of the encoded Shank3 protein. (Bozdagi *et al.* 2010, Peca *et al.* 2011, Wang *et al.* 2011, Schmeisser *et al.* 2012, Kouser *et al.* 2013, Lee *et al.* 2015, Wang *et al.* 2016, Jaramillo *et al.* 2017). In this study, I used the Δ x11 mouse model, hereafter referred to as the *Shank3* $\alpha\beta$ -knock out mouse model. In this mouse model, deletion of the 11th exon disrupts transcripts arising from the first three promoters in *Shank3*, resulting in the loss of the three longer isoforms of Shank3 containing the SPN, ANK and SH3 domains (Schmeisser *et al.* 2012). Behavioral assays concluded that these mice exhibit extensive self-grooming, resembling the

ASD core phenotype of repetitive behavior. Biochemical investigations of these mice demonstrated that the protein composition of the postsynaptic density is altered (Schmeisser *et al.* 2012).

Shank1 includes two different promoters and can be transcribed into two *Shank1* isoforms (Lim *et al.* 1999, Bockers *et al.* 2004). *Shank1* knockout mice were created by deletion of exon 14 and 15, resulting in a complete knockout of the *Shank1* protein (Hung *et al.* 2008). The *Shank1* knockout mice showed moderate autistic behaviors, as their frequency of self-grooming was slightly increased as adults. They also exhibited impairments in social interaction, communication and contextual fear memory (Hung *et al.* 2008, Silverman *et al.* 2011, Wöhr *et al.* 2011, Sungur *et al.* 2014). Remarkably, *Shank1* knockout mice displayed enhanced spatial learning and memory, resembling the phenotype of the rare Savant syndrome, in which autistic individuals possess extraordinary abilities in isolated skills mostly related to memory tasks (O'Connor and Hermelin 1989, Heaton and Wallace 2004, Hung *et al.* 2008). On the molecular level, postsynaptic protein composition was altered and the size of postsynaptic sites was reduced in the *Shank1* knockout mouse model (Hung *et al.* 2008).

1.3. Association of RNA-Binding Protein with NDDs

Mutations in several genes coding for RNA-binding proteins (RBPs) have been identified as causes of NDDs and form the second subset of NDD risk genes studied here. These include translation initiation and elongation factors, ribosomal proteins, and Argonaute proteins (Kapur and Ackerman 2018, Lennox *et al.* 2018, McLachlan *et al.* 2019, Lessel *et al.* 2020, Schalk *et al.* 2022). The *AGO2* gene encodes the Argonaute-2 (Ago2) protein that belongs to the Argonaute protein family (Hammond *et al.* 2001). *AGO2* was identified as a disease gene, as heterozygous variants underlie a NDD termed Lessel-Kreienkamp syndrome (LESKRES) (Lessel *et al.* 2020). Across 21 patients, 11 different missense variants were described, of which 10 occurred *de novo* and five were recurrent. One inherited missense variant, one in-frame deletion, and one deletion spanning the first three exons were described among this cohort. Missense variants lead to the exchange of a single amino acid in the protein primary structure. All LESKRES patients exhibited ID and mild to severe global neurodevelopmental delay with motor and speech impairments. 56% also showed ASD-typical symptoms including stereotypic and repetitive behavior (Lessel *et al.* 2020). Knockout of *Ago2* is lethal in mice during early embryonic development, indicating that *Ago2* plays a crucial role in development (Liu *et al.* 2004). In contrast, *Ago1* knockout mice are viable although heterozygous mutations in *AGO1* are associated with a severe NDD in humans (Van Stry *et al.* 2012, Schalk *et al.* 2022). The clinical representation of *AGO1* variants showed high similarity to LESKRES (Lessel *et al.* 2020, Schalk *et al.* 2022). Interestingly, several missense variants alter homologous amino acid residues between *Ago1* and *Ago2*. For example, the leucine 192 substitution in a LESKRES patient (L192P) corresponds to a leucine 190 to proline substitution in a patient with an *AGO1*-associated NDD (L190P) (Lessel *et al.* 2020, Schalk *et al.* 2022).

1.3.1. RNA interference

RNA interference (RNAi) is a mechanism for posttranscriptional gene regulation (PTGR) that acts on mRNA (Gerstberger *et al.* 2014). Axons, dendrites, and individual synapses display distinct transcriptomes (all mRNA transcripts) and translomes (actively translated mRNAs) (Prashad and Gopal 2021). RNAi allows for precise adjustment of these transcript levels and dynamic fine-tuning of RNA-dependent processes (Holt and Schuman 2013). Repression of translation is a central aspect of RNAi (Eulalio *et al.* 2007). To convey translational repression, RNA-binding proteins assemble with different classes of non-coding RNAs (ncRNAs) to ribonucleoprotein complexes (Gerstberger *et al.* 2014, Hirose *et al.* 2014). A large proportion of these ncRNAs are small RNAs, typically 20 to 30 nucleotides (nt) long (Carninci *et al.* 2005). The family of small RNAs (sRNA) is divided into three classes: small interfering RNA (siRNA), P-element-induced wimpy testis (PIWI)-interacting RNA (piRNAs), and microRNA (miRNA), which differ in their biogenesis and mechanism of function (Lee *et al.* 1993, Wightman *et al.* 1993, Vagin *et al.* 2006, Ghildiyal and Zamore 2009, Ketting 2011).

1.3.2. MicroRNAs

MicroRNAs are transcribed from the genome as primary miRNA (pri-miRNA) by RNA polymerase II and thereby share their transcription machinery with mRNA (Figure 4) (Lee *et al.* 2004). The pri-miRNA typically spans more than one kilobase (kb) and features a partially base-paired stem-loop structure with 5'-cap and 3'-poly(A) tail (Lee *et al.* 2002, Cai *et al.* 2004). In the nucleus, the microprocessor complex, which includes the type-III RNase Drosha and its binding partner DGCR8, mediates a maturation process. In this process, the pri-miRNA is cleaved to produce the precursor miRNA (pre-miRNA), a hairpin-shaped RNA approximately 65 nt in length (Lee *et al.* 2003, Denli *et al.* 2004, Gregory *et al.* 2004, Han *et al.* 2004). From the nucleus, the pre-miRNA is exported to the cytoplasm by Exportin-5 via a RanGTP-dependent pathway (Yi *et al.* 2003, Bohnsack *et al.* 2004, Lund *et al.* 2004). Further cleavage steps are carried out in the cytosol by a second type-III RNase, called Dicer (Bernstein *et al.* 2001, Grishok *et al.* 2001, Knight and Bass 2001, Caudy *et al.* 2002). The product is a duplex miRNA with an average length of 22 nt, which is subsequently loaded on an Argonaute (Ago) protein (Figure 4) (Hammond *et al.* 2000, Hutvagner *et al.* 2001, Ketting *et al.* 2001). Alternative processing by Drosha and Dicer, for example the use of alternative cleavage sites in pri- and pre-miRNA, can result in isoforms of miRNA derived from the same precursor transcript, called isomiRs (Wu *et al.* 2009, Yang and Lai 2011). Non-templated isomiRs are created by the addition of nucleotides that do not match the pre-miRNA sequence (Wyman *et al.* 2011, Ameres and Zamore 2013). Polymorphic isomiRs are created by enzymatic exchange or editing of nucleotides to yield isomiRs that differ from the corresponding canonical miRNA not in length but in sequence (Nielsen *et al.* 2012, Ameres and Zamore 2013). IsomiRs add another layer of complexity to the miRNA-mediated pathway of RNAi (Kim *et al.* 2020). MicroRNAs participate in diverse regulatory pathways, influencing organism development, adaptation to the environment, and neuronal function. 50% of identified miRNAs are highly or exclusively expressed in the brain (Lee *et al.* 1993, Cao *et al.* 2006, Phillips *et al.* 2007). RNAi via miRNAs has properties distinguishing it from other regulatory mechanisms (Hobert 2008). In comparison with transcription factors that function exclusively in the nucleus to regulate gene expression, miRNAs influence translation of mRNAs locally in different intracellular localizations (Hobert 2008). This is of particular importance in neurons because local translation is fundamental for synaptic plasticity and miRNAs have been implicated in this phenomenon (Schratt 2009). To execute RNAi, miRNAs associate with Ago proteins (Bartel 2004, Czech and Hannon 2011).

1.3.3. Argonaute Proteins

Argonaute proteins occur in all domains of life and have been identified in prokaryotes (pAgos) and eukaryotes (eAgos). Although there is little sequence homology between pAgos and eAgos, the architecture and especially the function are evolutionarily conserved (Tolia and Joshua-Tor 2007, Swarts *et al.* 2014, Olina *et al.* 2018, Wu *et al.* 2020). P- and eAgos share a common catalytic cycle: binding of small RNA, recognition, binding, and eventually release or cleavage of the target mRNA (Lisitskaya *et al.* 2018, Wu *et al.* 2020). In humans, eight different Ago proteins are expressed with a typical molecular weight of around 100 kDa (Sasaki *et al.* 2003, Kobayashi and Tomari 2016). The protein family is divided into two subfamilies. The Ago subfamily consists of Ago1, Ago2, Ago3, and Ago4, all of which bind to miRNAs and siRNAs (Sasaki *et al.* 2003, Kuhn and Joshua-Tor 2013, Azlan *et al.* 2016). The PIWI proteins form the second subfamily and bind to piRNAs (Sasaki *et al.* 2003, Kuhn and Joshua-Tor 2013, Azlan *et al.* 2016, Kobayashi and Tomari 2016, Doxzen and Doudna 2017). The protein domains of Ago fold into a two-lobed configuration. The first lobe consists of the N-terminal domain (N), Linker region 1 (L1) and the PIWI/Argonaute/Zwille (PAZ) domain. The α -helix-7-containing Linker 2 (L2) links the first lobe to the second lobe, which consists of the Middle (MID) domain and the PIWI domain (Figure 3). L1 and L2 allow structural rearrangements during RNA binding (Wu *et al.* 2020). The N-terminal domain is necessary for RNA duplex unwinding. L1 connects the N-terminal domain to the PAZ domain. The PAZ domain anchors the 3'-hydroxyl end of sRNA in a specialized binding pocket

(Hock and Meister 2008, Simon *et al.* 2011, Tian *et al.* 2011, Kwak and Tomari 2012). The MID domain, located C-terminal to the PAZ domain, provides a pocket for the 5'-terminal phosphorylated end of a sRNA (Wang *et al.* 2008, Boland *et al.* 2011). The PAZ and MID domains, connected by L2, functionally coordinate anchoring of the sRNA into Ago (Wang *et al.* 2008, Wu *et al.* 2020). The α -helix-7 in L2 is a structural element indispensable for dynamic, rapid RNA recognition and ejection (Klum *et al.* 2018). The C-terminal PIWI domain forms an interface with the MID domain (Figure 3) (Jinek and Doudna 2009). The PIWI domain can contain an active site with endonuclease activity for cleavage of RNA species (Leuschner *et al.* 2006, Wang *et al.* 2009). In mammals, exclusively Ago2 holds this activity and was therefore named "slicer" (Liu *et al.* 2004, Matranga *et al.* 2005, Rand *et al.* 2005). All Argonautes associate with sRNAs to assemble the RNA-induced silencing complex (RISC), the effector ribonucleoprotein complex of translational silencing (Bartel 2004).

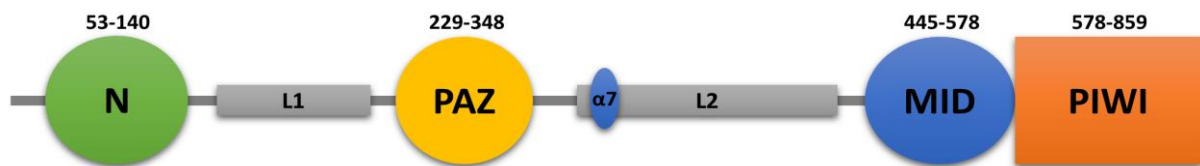


Figure 3: Domains of the Argonaute proteins. The numbers indicate the length and position of the amino acid sequence of the respective domain of human Argonaute-2. Folded in a two-lobed configuration, an Argonaute protein comprises the following domains from N- to C-terminus: the N-terminal domain (N) linked by linker 1 (L1) to the PIWI/Argonaute/Zwille (PAZ) domain, connected by linker 2 (L2), which includes the α -helix-7 (α 7), the middle (MID) and the P-element-induced whimpy testes (PIWI) domains. Adapted from Lessel *et al.* 2020

1.3.4. The RNA-induced Silencing Complex

When a miRNA associates with Ago, they form the core component of RISC (Figure 4) (Rivas *et al.* 2005, Faehnle and Joshua-Tor 2007). During the assembly, Ago interacts with additional key factors. The Hsc70/Hsp90 multichaperone machinery assists miRNA duplex loading by facilitating conformational changes in an ATP-dependent process to induce an active state of Ago (Iwasaki *et al.* 2009, Tsuboyama *et al.* 2018). GW182 proteins act as a flexible scaffold that provides multiple sites for miRNA-loaded Ago, which brings RISCs into spatial proximity to downstream RNAi effectors (Pfaff *et al.* 2013, Elkayam *et al.* 2017, Zhang *et al.* 2018). The miRNA duplex consists of two complementary strands bound by Watson-Crick base pairing, one of which originated from the 5'-, and one from the 3'-side of the pre-miRNA. These are referred to as the 5p and 3p strand, respectively (Ghildiyal and Zamore 2009, Okamura *et al.* 2009, Medley *et al.* 2021). Only one of these two strands remains anchored in Ago (Schwarz *et al.* 2003). Although either of the 5' and 3' strands could be retained, one strand frequently dominates for a given miRNA (Schwarz *et al.* 2003, Medley *et al.* 2021). The preferentially selected strand is named guide, also called miR, whereas the ejected strand is named passenger or miR* strand (Khvorova *et al.* 2003, Schwarz *et al.* 2003, Kim *et al.* 2020). Several features determine strand selection, such as the identity of the 5'-terminal nucleotides of 3p and 5p strand (Khvorova *et al.* 2003, Schwarz *et al.* 2003, Krol *et al.* 2004, Frank *et al.* 2010, Medley *et al.* 2021). Uracil is favored at the 5'-terminal position of the guide due to the shape of a binding pocket located in the MID domain (Mi *et al.* 2008, Ghildiyal and Zamore 2009, Frank *et al.* 2010, Warf *et al.* 2011). The chosen guide is divided into distinct functional segments upon association with Ago. The anchoring point of the 5'-terminal nt is located in the MID domain, followed by the "seed sequence" spanning from 2nd to 8th nt. Nucleotides nine to 12 comprise the central section and the 13th to 16th nt a supplementary segment. The remaining 3'-terminal nt form the tail region, embedded in the PAZ domain (Ma *et al.* 2004, Song *et al.* 2018). The passenger/miR* strand is ejected from the RISC and degraded (Schwarz *et al.* 2003, Matranga *et al.* 2005, Rand *et al.* 2005, Wang *et al.* 2009). The seed sequence of the retained miR strand determines the binding specificity of the RISC. Through sequence complementarity of the guide miRNA sequence to a segment in the 3'-untranslated region (3'UTR) of the target mRNA, the RISC binds to the mRNA

via partial base pairing (Figure 4) (Lai 2002, Bartel 2004). Most miRNAs in humans display partial sequence complementarity to the target, and a single miRNA regulates numerous mRNAs, frequently more than a hundred (Bartel 2004, Baek *et al.* 2008, Selbach *et al.* 2008). The association of the RISC to the target induces either decay or translational silencing. RISC thus acts as a posttranscriptional regulator of gene expression (Hammond *et al.* 2000, Bartel 2004, Filipowicz 2005). Several proteins and RNA involved in RNAi and the mRNA degradation machinery localize in cytosolic clusters, named processing bodies (p-bodies) (van Dijk *et al.* 2002, Parker and Sheth 2007, Pillai *et al.* 2007). These include miRNA, translationally silenced mRNA, as well as Dicer, Ago and GW182 proteins (Eystathiou *et al.* 2002, Cougot *et al.* 2004, Liu *et al.* 2005). Due to the detection of factors implicated in mRNA decay such as the decapping factor Dcp1a, p-bodies were determined to be sites of mRNA decay. In neurons, p-bodies are distributed in the cell body and along dendrites (van Dijk *et al.* 2002, Lugli *et al.* 2005, Barbee *et al.* 2006).

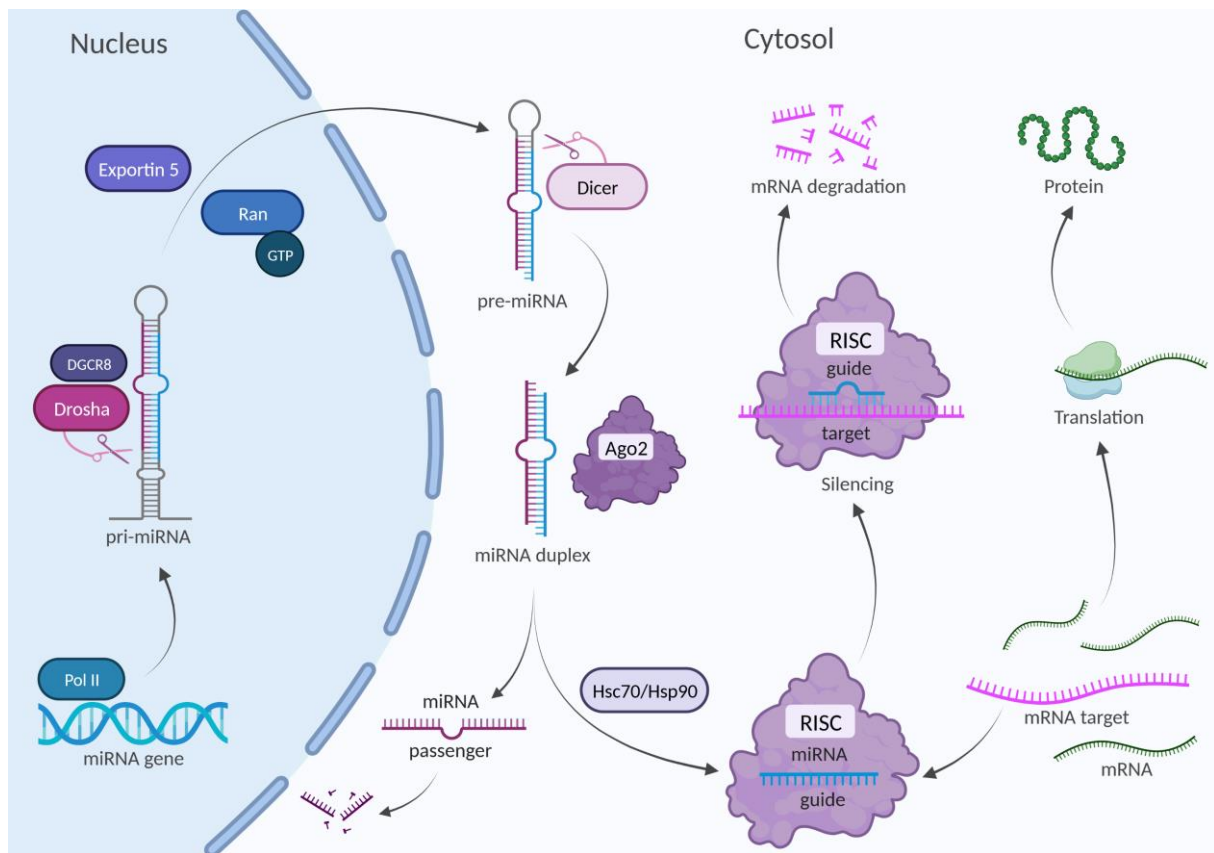


Figure 4: Biogenesis of miRNA and RISC-mediated RNAi. RNA polymerase II (Pol II) transcribes pri-miRNA from the genome. The microprocessor complex, including DGCR8 and Drosha, generates the pre-miRNA. Nuclear export of the pre-miRNA into the cytosol is facilitated by Exportin 5 via a RanGTP-dependent pathway. Dicer processes the pre-miRNA and generates a miRNA duplex. The RISC is formed by incorporation of the guide strand into Ago2, assisted by the Hsc70/Hsp90 multichaperone machinery. The passenger strand is degraded. RISC silences translation of specific mRNA targets by binding of partially complementary sequences in the 3' UTR of the mRNA. After prolonged silencing, the mRNA is degraded. Unsilenced mRNAs can be translated into proteins by the translation machinery. Created with BioRender.com.

1.4. Omics approaches

Omics studies aim to characterize and quantify the entirety of a type of biomolecule (Subramanian *et al.* 2020). Genomics analyze the whole genetic code through DNA sequencing (Hasin *et al.* 2017). In transcriptomics and translomics, RNA sequencing (RNA-seq) decodes all transcribed RNAs (transcriptome) or translated mRNAs (translatome). Protein abundances are studied using proteomics (Subramanian *et al.* 2020). Table 1 provides an overview of selected omics approaches. Omics generate large data sets to elucidate biological pathways at the DNA, RNA, and protein level and unravel the molecular signature of an individual cell type, developmental stage, or disease state (Hasin *et al.* 2017). In NDD research, omics approaches are used to identify deregulated signaling pathways and investigate pathomechanisms in neurodevelopment (Prashad and Gopal 2021).

Table 1: Overview of Omics Approaches.

Biomolecules Studied	Entirety of Biomolecules	Omics Approach	Analytical Method
DNA	Genome	Genomics	Next Generation Sequencing
Total RNA	Transcriptome	Transcriptomics	RNA sequencing
miRNA	miRNome	Transcriptomics	Small RNA sequencing
Translated mRNA	Translatome	Translomics	RNA sequencing
Protein	Proteome	Proteomics	Mass spectrometry

ge was developed on the basis of Sanger sequencing but yields a much higher throughput (Margulies *et al.* 2005). In contrast to the Sanger method, which sequences one template at a time, NGS sequences billions of DNA strands in parallel coupled with simultaneous data acquisition (Sanger *et al.* 1977, McCombie *et al.* 2019). NGS advanced the field of genomics by its massive application in research and clinical diagnostics. Various NDD risk genes and NDD-causing variants were characterized using NGS-based genomic approaches (Wright *et al.* 2015, Clark *et al.* 2018, Srivastava *et al.* 2019). Thus, NGS enormously contributed to the field of genetically caused NDDs (Carneiro *et al.* 2018). RNA-seq uses NGS technologies to determine sequences of RNA transcripts in high-throughput scale. In transcriptomics and translomics, expression of coding and non-coding RNAs is analyzed. Many novel RNA species were characterized by RNA-seq, advancing the research field of small RNAs (Djebali *et al.* 2012, Morris and Mattick 2014). Bioinformatics analysis of differential gene expression (DGE) has been successfully applied using RNA-seq data to study RNA biogenesis and metabolisms as well as RNAi (Djebali *et al.* 2012, Morris and Mattick 2014). Using the DGE approach to transcriptomics and translomics, RNA signatures have been compared between different tissues, cell populations, or developmental stages, and RNA deregulations have been linked to disease (Moreno *et al.* 2012, Wang *et al.* 2016, Leibovitch and Topisirovic 2018).

Proteins are the major effectors in cells and the field of proteomics studies protein abundances using mass spectrometry (Tuli and Resson 2009, Selevsek *et al.* 2015). Protein identification and subtractive proteomics (label-free proteomics) revolutionized the field by enabling the determination and comparison of relative protein abundances (Oh *et al.* 2004, Rotello and Veenstra 2021). Because synapses are complex structures with a dense protein network, proteomics provided a valuable tool to study them. Application of proteomics on biochemically purified synaptosomes and PSD fractions revealed that more than 2000 proteins locate to forebrain synapses (Walikonis *et al.* 2000, Satoh *et al.* 2002, Yoshimura *et al.* 2004, Collins *et al.* 2006). Furthermore, a change of synaptic protein composition has been described in various diseases, including NDDs (Pennington *et al.* 2008, Klemmer *et al.* 2011, Wesseling *et al.* 2014).

2. Aim of the Project

Neurodevelopmental disorders result from defects in processes essential for neuronal development. NDD-causing genomic variants have been discovered in many genes encoding synaptic proteins, but mutations in genes encoding RNA-binding proteins have also recently been linked to NDDs. Although these proteins differ greatly in function, perturbations lead to similar symptoms and manifestation of NDDs, raising the question of whether the underlying pathomechanisms converge in shared signaling pathways. *SHANK1* and *SHANK3* are known ASD risk genes and encode synaptic scaffold proteins. Therefore, *SHANK* alterations will be analyzed here as an example of synaptic protein dysfunction responsible for NDD pathogenesis. Variants in *AGO2*, which encodes a core component of the RNA interference pathway, have been identified as the cause of Lessel-Kreienkamp syndrome, an example of a NDD caused by altered function of an RNA-binding protein. The aim of this PhD project is to apply omics approaches to decipher the pathomechanisms underlying the *SHANK1*- and *SHANK3*-associated forms of autism spectrum disorders and the Lessel-Kreienkamp syndrome.

The N-termini of Shank3 has been characterized as binding domain for Ras proteins, which are part of the MAPK signaling pathway controlling gene expression. Misregulated translation has been linked to the pathogenicity of ASD. In Fragile-X-syndrome, the function of the translational repressor FMR1, encoded by *FRMP*, is impaired. Furthermore, deregulation of the mTOR pathway, which is also involved in translational regulation, has been implicated in ASD pathologies. Together, this leads to the hypothesis that loss of Shank proteins may alter the regulation of translation, and that deregulation of this function might contribute to ASD pathogenesis. To test this hypothesis, *Shank3 $\alpha\beta$* knockout mice were used and translomics were applied to decipher the hippocampal translome. By using the *Shank3 $\alpha\beta$* knockout mouse line which only expresses *Shank3* variants lacking their N-terminal domains, an emphasis was placed on the function of the N-terminus of Shank3 in translational regulation. *Shank* knockout mice were crossed with a mouse line expressing GFP-tagged ribosomal protein (L10a) which enabled the pull-down of GFP-tagged ribosomes and the sequencing of actively translated mRNAs. Proteomics with mass spectrometry was performed with biochemically purified postsynaptic density fractions from hippocampal tissue of *Shank1* and *Shank3 $\alpha\beta$* knockout mice to decipher the postsynaptic proteome and the impact of an altered translome at the protein level.

Argonaute-2 and miRNA together form the RNA-induced silencing complex, which represses translation of target mRNA. It was hypothesized that LESKRES-causing missense variants could result in different miRNAs being loaded onto mutant forms of the Ago2 protein, altering the properties of RISC-mediated translational silencing. To test this hypothesis, miRNA affinity purification was applied to cortical neurons expressing a patient derived Ago2 mutant, and Ago2-bound miRNA were sequenced by sequencing of small RNAs.

Collectively, the results of this dissertation may shed light on the deregulation of distinct or shared signaling pathways between *SHANK*-associated ADSs and LESKRES and contribute to the research field of genetic NDDs.

3. Materials and Methods

3.1. Materials

Unless otherwise stated, all chemicals used were purchased from Sigma-Aldrich (Taufkirchen, Germany), Merck (Darmstadt, Germany) or Carl Roth (Karlsruhe, Germany).

3.1.1. Laboratory Mice

All mice used in experiments were bred in the laboratory animal facility (FTH, *Forschungstierhaltung*) of the UKE Hamburg. Two mouse lines were obtained from collaboration partners prior to this project and one line was obtained during this study. In addition, two new mouse lines were generated.

Table 2: Laboratory mice.

Line	Origin	MGI ID
C57BL/6J	FTH, UKE Hamburg	3028467
Shank1 ^{tm1Shng}	(Hung <i>et al.</i> 2008)	3762757
Shank3 ^{tm1.1Geno}	(Schmeisser <i>et al.</i> 2012)	5435700
Tg(Lypd1-EGFP/Rpl10a)OI82Htz	INIMS, ZMNH	6359832
Lypd1-bacTRAP x Shank1 ^{tm1Shng}	Breeding, see 3.2.4.3	Novel line
Lypd1-bacTRAP x Shank3 ^{tm1.1Geno}	Breeding, see 3.2.4.3	Novel line

The Tg(Lypd1-EGFP/Rpl10a)OI82Htz mouse line will be named Lypd1-bacTRAP from here on.

3.1.2. Bacterial Strains and Cell Lines

Table 3: Suppliers of bacterial strains and cell lines.

Cells	Supplier
<i>E. coli</i> Top10F'	Thermo Fisher Scientific (Waltham, USA)
NEB Stable Competent <i>E. coli</i> (High Efficiency)	New England Biolabs (Ipswich, USA)
HEK293T	ATCC (Manassas, USA)

3.1.3. Antibodies

For western blot (WB), all antibodies were diluted in 5% milk powder (MP) in TBS-T (Table 4). For immunocytochemistry (ICC), the antibodies were used in 2% horse serum (HS) in PBS (Table 5).

Table 4: Primary antibodies used in western blot analyses.

Target	Species	Dilution	Manufacturer	Details
RFP	Rat	1:1000	ChromoTek (Planegg-Martinsried, Deutschland)	Clone 5F8
Shank3	Guinea pig	1:1000	Synaptic Systems (Göttingen, Deutschland)	162 304
Shank PDZ domain	Rabbit	1:5000	Custom made serum	SSTRIP – PDZ. 90 th day
T7-tag	Mouse	1:10,000	Novagen (Temecula, USA)	69522-3
CaMKII α	Rabbit	1:1000	Abcam (Cambridge, UK)	EP1829Y ab52476
CAMKII α phospho T286	Rabbit	1:1000	Abcam (Cambridge, UK)	ab32678
PSD-95	Mouse	1:2000	Thermo Fisher Scientific (Waltham, USA)	MA1-046
α -tubulin	Mouse	1:5000	Abcam (Cambridge, UK)	DM1A ab7291
GFP	Mouse	1:5000	BioLegend (San Diego, USA)	Clone B34 MMS-118P
Ago2	Rat	1:1000	Merck (Darmstadt, Germany)	Clone 11A9 MABE253

Table 5: Primary antibodies used for immunocytochemistry.

Target	Species	Dilution	Manufacturer	Details
Dcp1a	Rabbit	1:250	Abcam (Cambridge, UK)	ab183709
MAP2	Chicken	1:500	Antibodies online (Aachen, Germany)	AB_2338133

Secondary antibodies coupled to horseradish peroxidase (HRP) were diluted in TBS-T for application in western blot analyses (Table 6).

Table 6: HRP-coupled secondary antibodies used in western blot analyses.

Target Species	Origin Species	Dilution	Manufacturer	Details
Rat	Goat	1:2500	Jackson ImmunoResearch (Ely, UK)	112-035-062
Guinea pig	Goat	1:2500	Jackson ImmunoResearch (Ely, UK)	GtxGp-003-DHRPX
Rabbit	Goat	1:2500	Jackson ImmunoResearch (Ely, UK)	GtxRb-003-EHRPX
Mouse	Goat	1:2500	Jackson ImmunoResearch (Ely, UK)	GtxMu-003-E2HRPX

For ICC, secondary antibodies labelled with fluorescent dyes were diluted in PBS (Table 7).

Table 7: Secondary antibodies used in ICC experiments.

Fluorophore	Target Species	Origin Species	Dilution	Manufacturer	Details
Alexa 405	Chicken	Goat	1:1000	Thermo Fisher Scientific (Waltham, USA)	ab175674
Alexa 633	Rabbit	Goat	1:1000	Thermo Fisher Scientific (Waltham, USA)	A-21072

3.1.4. Oligonucleotides

All oligonucleotides were purchased from the manufacturer Sigma-Aldrich (Taufkirchen, Germany). The primers were adjusted to a concentration of 100 μ M with ddH₂O. 10 μ M stock solutions were prepared in ddH₂O, which were used for genotyping (Table 8), sequencing (Table 9), cloning (Table 10) or mutagenesis (Table 11).

Table 8: Primers used for genotyping.

Primer	Sequence
Short arm fwd	5'-CTGTAGTGTGTAGTGTTCCGACCTCC-3'
Deletion rev	5'-CCATCCACCCATCCATTCAGC-3'
NEO 250 rev	5'-GCTACTTCCATTGTGACGTC-3'
S12 WT	5'-CAAGTTCATCGCTGTGAAGG-3'
S10 KO	5'-CCTCTAGGCCTGCTAGCTGT-3'
AS3	5'-AAGAAGCCCCAGAAGTGACA-3'
EGFP 3'	5'-CGGCGAGCTGCACGCTGCCGTCTC-3'
EGFP 5'	5'-CCTACGGCGTGCACTGCTTCAGC-3'
Actin fwd	5'-AGAGGGAAATCGTGCGTGAC-3'
Actin rev	5'-CAATAGTGATGACCTGGCCGT-3'

Table 9: Oligonucleotides for sequencing of plasmids coding for GFP-tagged Ago2.

Primer	Sequence
GFP1 fwd	5'- GTTCATGACCGCCGCCGGGA-3'
GFP-n-fwd	5'-AATGTCGTAACAAC-3'
GFP rev	5'-AGCTCGACCAGGATGGGCACC-3'
hSyn1 Mid for	5'-CAAACCTCCCCTCCCGCCAC-3'
V117F for	5'-GGACAAGGTGGAGCTGGAGTTCACGCTGCCAGGAGAAGGC-3'
N359H for	5'-GTATTAATAAATAACGGACCATCAGACCTCAACCATGATC-3'

Primer	Sequence
I365V rev	5'-CGACCTAGCAGTCGCTCTGACCATGGTTGAGGTCTGATTG-3'
E531Q for	5'-GACGCCGTGTACGCCAGGTCAAGCGCTGGGAGAC-3'
D619N fwd	5'-CGTGGTGGGCAGCAGAACGCCCCCAATCGCTA-3'
R714W for	5'-CAGAAGAGGCACACACCTGGCTCTTCTGCACTGACAAG-3'
Ago733F	5'-TGGAAACATTCCAGCACGCACGACTGTGGAC-3'

Table 10: Oligonucleotides used for cloning.

Primer	Sequence
For hSyn + BstAPI	5'-TTTGAGATGCTGCAGTGAAGTGGGTTTTAGACCAGG-3'
Rev hSyn + HindIII	5'-TTTAAGCTTCTTCTGACTGCGCTCTCAGGC-3'

Table 11: Primers for mutagenesis.

Primer	Sequence
Ago192F	5'-GCTCTAACCTCCTGGCGGGGCCG-3'
Ago192R	5'-CGCCCCCGCCAGGAGGGTTAGAGC-3'

3.1.5. Plasmids

Plasmids from the stock of the Kreienkamp research group (Institute of Human Genetics, UKE Hamburg) were provided (Table 12). Plasmids for the production of adeno-associated viruses that induce the expression of GFP-tagged Ago2 variants were generated using the neuron-specific human synapsin 1 (hSyn1) promoter (Hilfiker *et al.* 1999) from a commercially available plasmid (Table 13). The plasmid maps are attached in the appendix (see 7.5).

Table 12: Plasmids from the stock of the Kreienkamp research group.

Plasmid	Resistance	Origin
pmRFP-C1	Kanamycin	Kreienkamp research group
pmRFP-Shank1 aa1-483	Kanamycin	Kreienkamp research group
pmRFP-Shank2 n-term	Kanamycin	Kreienkamp research group
pmRFP-Shank3 aa76-414	Kanamycin	Kreienkamp research group
pcDNA3-T7-CaMKII α	Ampicillin	Kreienkamp research group

Table 13: Purchased or generated plasmids.

Plasmid	Resistance	Origin
hSyn1-eYFP	Ampicillin	Addgene (Watertown, USA) #117382
pAAV-hSyn1-EGFP-CW3SL	Ampicillin	Generated by Hans-Hinrich Hönck and Debora Tibbe
pAAV-hSyn1-EGFP-Ago2-WT-CW3SL	Ampicillin	Generated by Hans-Hinrich Hönck and Debora Tibbe
pAAV-hSyn1-EGFP-Ago2-L192P-CW3SL	Ampicillin	Generated by Hans-Hinrich Hönck and Debora Tibbe

3.1.6. Commercial Kits

Table 14: Commercial kits used.

Application	Commercial Kit	Manufacturer
Purification of DNA fragments from agarose gels	GeneJET Gel Extraction Kit	Thermo Fisher Scientific (Waltham, USA)
Targeted mutagenesis to create new protein variants	QuickChange II Site-directed Mutagenesis Kit	Agilent Technologies (Santa Clara, USA)
Isolation and purification of plasmid DNA	NucleoBond Xtra Midi	Macherey-Nagel (Düren, Deutschland)

Application	Commercial Kit	Manufacturer
Determination of protein concentration	Bradford Protein Assay Kit	BioRad (Munich, Deutschland)
Reverse transcription of total RNA and mRNA into cDNA	RevertAid H Minus First Strand cDNA Synthesis Kit	Thermo Fisher Scientific (Waltham, USA)
Reverse transcription of miRNA into cDNA	TaqMan Advanced miRNA cDNA Synthesis Kit	Thermo Fisher Scientific (Waltham, USA)
Digestion of DNA	RNase-free DNase Set	Qiagen (Hilden, Germany)
RNA purification after bacTRAP	RNeasy Micro Kit	Qiagen (Hilden, Germany)
miRNA purification after miRAP	miRNeasy Micro Kit	Qiagen (Hilden, Germany)
Determination of the concentration of total RNA and mRNA	Qubit RNA HS Assay Kit	Thermo Fisher Scientific (Waltham, USA)
Determination of the concentration of miRNA	Qubit microRNA Assay Kit	Thermo Fisher Scientific (Waltham, USA)

3.1.7. Buffers, Solutions and Supplements

The supplements dithiothreitol (DTT; Sigma-Aldrich, Taufkirchen, Germany), cycloheximide (CHX; Sigma-Aldrich, Taufkirchen, Germany), Rnasin (Promega, Madison, USA), Superasin (Thermo Fisher Scientific, Waltham, USA), and protease inhibitors were added to buffers and solutions (Table 15) immediately before use.

Table 15: Buffers, solutions, and supplements.

Buffer	Composition
BacTRAP dissection buffer	Hanks' Balanced Salt Solution (HBSS) 2.5 mM 4-(2-hydroxyethyl)-1-piperazineethanesulfonic acid (HEPES)-KOH pH 7.4 35 mM glucose 4 mM NaHCO ₃ 100 µg/ml CHX
Lysis buffer	20 mM HEPES 150 mM KCl 5 mM MgCl ₂ 0.5 mM DTT 100 µg/ml CHX 40 U/ml Rnasin 10 U/ml Superasin 1:100 Complete Protease Inhibitors (Roche, Basel, Schweiz)
Fixation buffer	Phosphate-buffered saline (PBS) 4% (w/v) paraformaldehyde (PFA) 4% (w/v) sucrose
IP buffer	50 mM Tris-HCl 120 mM NaCl 0.5% (v/v) nonyl phenoxy polyethoxy ethanol (NP-40) 1 mM ethylenediaminetetraacetic acid (EDTA)
Ketamine and xylazine solution	PBS 12 mg/ml ketamine (Ketanest; Pfizer, Berlin, Germany) 1.6 mg/ml xylazine (Rompun; Bayer, Leverkusen, Germany)
0.15 M KCl IP wash buffer	150 mM KCl 20 mM HEPES 5 mM MgCl ₂ 1% (v/v) NP-40 0.5 mM DTT 100 µg/ml CHX

Buffer	Composition
0.35 M KCl wash buffer	350 mM KCl 150 mM KCl 20 mM HEPES 5 mM MgCl ₂ 1% (v/v) NP-40 0.5 mM DTT 100 µg/ml CHX
5x KCM	500 mM KCl 150 mM CaCl ₂ 250 mM MgCl ₂
5x Lämmli	300 mM Tris-HCl pH 6.8 50% (w/v) glycerol 7.5% (w/v) sodium dodecyl sulphate (SDS) 0.5 M DTT 0.01% (w/v) bromophenol blue
PBS	140 mM NaCl 2.7 mM KCl 8 mM Na ₂ HPO ₄ 2 mM KH ₂ PO ₄ pH 7.7
PLL	PBS 1 mg/ml poly-L-lysine (PLL)
PSD buffer A	4 mM HEPES pH 7.4 320 mM sucrose 1 mM MgCl ₂ 0.5 mM CaCl ₂ 44 µg/ml phenylmethylsulfonyl fluoride (PMSF) 10 µg/ml leupeptin 2 µg/ml pepstatin A
PSD buffer B	4 mM HEPES 320 mM sucrose 44 µg/ml PMSF 10 µg/ml leupeptin 2 µg/ml pepstatin A
PSD Triton X-100 buffer	12 mM Tris-HCl pH 8.1 320 mM sucrose 1% (v/v) Triton X-100 44 µg/ml PMSF 10 µg/ml leupeptin 2 µg/ml pepstatin A
Running buffer	1x Tris-glycine 0.1% (v/v) SDS
Separation gel	2.6 ml 1.5 M Tris-HCl pH 8.8 3.3 ml 30% (v/v) acrylamide 3.9 ml ddH ₂ O 100 µL 10% (v/v) SDS 100 µL 10% (v/v) ammonium peroxodisulfate (APS) 7 µL tetramethylethylenediamine (TEMED)
10% stacking gel	500 µL 1.0 M Tris-HCl pH 6.8 700 µL 30% acrylamide 2.8 ml ddH ₂ O 40 µL 10% (v/v) SDS 40 µL 10% (v/v) APS 3 µL TEMED
TAE	40 mM Tris-acetate pH 8.0 4 mM EDTA
TE	10 mM Tris-HCl pH 8.0 1 mM EDTA
TBS-T	10 mM Tris-HCl pH 8.0 150 mM NaCl 0.05% (v/v) Tween 20

Buffer	Composition
Transfer buffer	1x Tris-glycine 0.02% (v/v) SDS 20% (v/v) methanol
Versene	PBS 0.5 mM EDTA

Table 16: Culture media for bacteria, HEK293T cells and primary neurons.

Media	Composition
Lysogeny broth (LB) medium	10 mg/ml tryptone 5 mg/ml yeast extract 5 mg/ml NaCl pH 7.5
LB agar	10 mg/ml tryptone 5 mg/ml yeast extract 5 mg/ml NaCl 15 mg/ml agar pH 7.5
HEK293T culture medium	Dulbecco's Modified Eagle Medium (DMEM) 10% (v/v) foetal calf serum (FCS) 100 µg/ml penicillin/streptavidin (pen/strep)
Neuron preparation medium	HBSS 100 µg/ml pen/strep
Neuron plating medium	DMEM 0.6% (v/v) glucose 1% (v/v) GlutaMAX 10% (v/v) HS 100 µg/ml pen/strep
Neuron culture medium	Neurobasal 2% (v/v) B-27 supplement 1% (v/v) GlutaMAX 100 µg/ml pen/strep

Table 17: Antibiotics used for bacteria and cell culture.

Antibiotics	Concentration
Ampicillin	50 µg/ml
Kanamycin	10 µg/ml
Penicillin	100 µg/ml
Streptavidin	100 µg/ml

Table 18: Software and tools.

Application	Software and Tools	Supplier
Quantification of band intensities for the determination of protein amounts in western blot analyses	ImageLab	BioRad, Munich, Germany
Assembly of sequenced DNA sections with reference sequences	SeqMan Pro	DNASTAR, Madison, USA
Statistical analyses and plotting	GraphPad Prism	GraphPad Software Inc. Dotmatics, Boston, USA
Display vector maps	SnapGene Viewer	GSL Biotech LLC, Chicago, USA
Assessment of distance travelled and time spent in center during open field test	EthoVision	Noldus, Wageningen, the Netherlands

Application	Software and Tools	Supplier
Evaluation of self-grooming and rearing behavior after open field test	The Observer	Noldus, Wageningen, the Netherlands
Alignment of RNA sequencing reads to a reference genome	STAR	(Dobin <i>et al.</i> 2013)
Assessment of overlap of uniquely aligned reads with annotated gene loci	FeatureCounts	(Liao <i>et al.</i> 2014)
Detection of contaminations in RNA sequencing data	FastQ Screen	(Wingett and Andrews 2018)
Processing of miRNA sequencing data	OASIS	(Capece <i>et al.</i> 2015)
Quality control of RNA sequencing data, calculation of dispersion estimates and fold change shrinkages	DESeq2	(Love <i>et al.</i> 2014)
Detection of isomiRs in RNA sequencing data	miRMaster	(Fehlmann <i>et al.</i> 2017)
Algorithm for miRNA target prediction	miTarget	(Liu and Wang 2019)
Target predictions and functional annotations for miRNAs	miRDB	(Chen and Wang 2020)
Gene ontology overrepresentation test for biological processes of miRNA targets	PANTHER	(Mi and Thomas 2009, Mi <i>et al.</i> 2019, Thomas <i>et al.</i> 2022)
Gene ontology overrepresentation test for biological processes of PSD proteins	EnrichR	(Chen <i>et al.</i> 2013, Kuleshov <i>et al.</i> 2016, Xie <i>et al.</i> 2021)
Hierarchical clustered gene ontology	Cytoscape Bingo	(Shannon <i>et al.</i> 2003, Maere <i>et al.</i> 2005)

3.2. Methods

3.2.1. Molecular Biology Methods

3.2.1.1. Transformation of *E. coli* Top10F' by heat shock

Top10F' *E. coli* bacteria were thawed on ice from -80 °C storage. A solution of 79 µl of ddH₂O, 20 µl of 5x KCM and 1 µg of plasmid DNA was added to 100 µl of bacteria suspension. The mixture was incubated on ice for 20 min and then subjected to a heat shock at 37 °C for 5 min. 1 ml of preheated, antibiotics-free LB medium was added to the transformation mixture which was then incubated at 37 °C for 1 h with shaking at 300 rpm. The *E. coli* were pelleted at 13,000 rpm for 1 min and resuspended in 100 µl of LB medium. The bacterial suspension was spread onto LB agar plates containing a selection antibiotic and incubated at 37 °C overnight.

3.2.1.2. Purification of Plasmid DNA from *E. coli* - small scale (Miniprep)

Colonies of transformed *E. coli* of the Top10F' strain were picked from LB agar plates and added to 3 ml of medium with a selection antibiotic. After incubation overnight at 37 °C and 200 rpm shaking, 1.5 ml of the bacteria culture was pelleted by centrifugation for 1 min at 13,300 rpm and room temperature (RT). Buffers from the NucleoBond Midiprepkit by Macherey-Nagel (Düren, Germany) were used in the following steps. The bacteria pellet was resuspended in 100 µl of resuspension buffer with RNase. 100 µl of lysis buffer was added and the reaction tube was inverted five times, followed by an incubation for 2 min at RT. Subsequently, 100 µl of neutralization buffer was added and mixed thoroughly. The lysate was centrifuged at 13,000 rpm and RT for 20 min and the supernatant collected. The DNA was precipitated by adding 210 µl of isopropanol, followed by a 20 min centrifugation at 13,000 rpm and RT. The obtained supernatant was discarded and the pellet was washed twice with 500 µl of ethanol

(EtOH) (70%, v/v) at 13,000 rpm and RT for 5 min. Afterwards, the supernatant was discarded again and the DNA pellet was dried at RT for 10 min before being dissolved in 100 μ l of ddH₂O.

3.2.1.3. Purification of Plasmid DNA from *E. coli* - large scale (Midiprep)

1.5 ml of bacteria culture (see 3.2.1.2) were added to 100 ml of LB medium containing an appropriate antibiotic. The culture grew overnight at 37 °C with 200 rpm shaking motion and was pelleted the next day by centrifugation at 6000 g and 4 °C for 10 min. To perform cell lysis and DNA isolation, the NucleoBond Midiprepkit (Macherey-Nagel, Düren, Germany) was used according to the manufacturer's protocol. The DNA was precipitated by adding 3.5 ml of isopropanol and mixing, followed by a centrifugation step at 4500 g and 4 °C for 30 min. The resulting DNA pellet was washed twice with 70% EtOH and the supernatant discarded. The DNA was dried for 15 min at RT and then dissolved in 200 μ l of TE buffer. The concentration of purified DNA was determined using a spectrophotometer and adjusted to 1 μ g/ μ l with TE buffer.

3.2.1.4. Restriction Digest

Double-stranded DNA was digested to control cloning and mutagenesis products. Specific enzymes generated DNA fragments of distinct sizes, depending on the chosen enzymes and restriction sites in the respective plasmid. The mixture contained 2 μ l of Green FastDigest (FD) buffer and 0.5 μ l of restriction enzymes (Thermo Fisher Scientific, Waltham, USA), as well as 7 μ l of ddH₂O and 10 μ l of plasmid DNA. The reaction was incubated at 37 °C with shaking at 200 rpm for 1 h.

3.2.1.5. Gel Electrophoresis

To analyze cloning reactions and polymerase chain reaction (PCR) products, a gel electrophoresis was applied. A 1% or 1.3% agarose gel, based on the size of fragments analyzed, with ethidium bromide was cast and the running chamber filled with TAE buffer. 20 μ l of the DNA samples and 10 μ l of a 1 kb DNA ladder (Thermo Fisher Scientific, Waltham, USA) were pipetted into the gel wells. 100 V was applied for 25 min to separate the DNA fragments based on their size. Once sufficient separation was achieved, the bands of DNA were detected using a UV transilluminator.

3.2.1.6. Gel Extraction

To extract DNA fragments from an agarose gel, the DNA bands of interest were cut out of the gel with a scalpel under UV light illumination. The fragments were then purified using the GeneJET gel extraction kit (Thermo Fisher Scientific, Waltham, USA) according to the manufacturer's protocol.

3.2.1.7. Ligation

To ligate DNA fragments with plasmids (see 3.2.1.4), a mixture of DNA fragment and plasmid in a 3:1 ratio was prepared. Ligation buffer with ATP as well as 1 μ l of T4-DNA ligase (Thermo Fisher Scientific, Waltham, USA) were added and the volume adjusted to a total of 20 μ l with ddH₂O. The reaction was incubated overnight at 16 °C.

3.2.1.8. Mutagenesis

Site-directed mutagenesis was used to generate mutant constructs. For this, a PCR reaction was prepared according to Table 19.

Table 19: PCR reaction for site directed mutagenesis.

Component	Volume [μ l]
10x reaction buffer	5
10 μ M forward primer	1
10 μ M reverse primer	1
10 mM dNTP mix	1
Quick Solution	3

Component	Volume [μ l]
10 μ M DNA template	0.1
ddH ₂ O	38
Polymerase Pfu Ultra	1

The thermal cycler was programmed according to Table 20.

Table 20: Thermal cycler program for site-directed mutagenesis.

Process	Temperature [$^{\circ}$ C]	Duration	Cycles
Initialisation	95	1 min	-
Denaturation	95	50 s	17
Annealing	60	50 s	
Elongation	68	1 min/kb DNA	
Final elongation	68	7	-
Hold	4	∞	-

Subsequently, a restriction digest was carried out by adding 1 μ l of DpnI to the reaction and incubating for 1 h at 37 $^{\circ}$ C. Reaction products were transformed into the bacterial strain Top10F' according to 3.2.1.1.

3.2.1.9. Sanger Sequencing of Plasmid DNA

For sequencing of DNA with the Sanger method, a reaction was prepared as described in Table 21.

Table 21: Reaction mixture of a sequencing PCR.

Component	Volume [μ l]
ddH ₂ O	5
5x sequencing buffer	2
Component	Volume [μ l]
Big Dye	1
10 μ M primer	1
1 μ g/ μ l DNA template	1

The sequencing reaction was performed using the thermal cycler program shown in Table 22.

Table 22: Thermal cycler program for sequencing.

Process	Temperature [$^{\circ}$ C]	Duration	Cycles
Initialisation	96	1 min	-
Denaturation	96	10 s	30
Annealing	50	5 s	
Elongation	60	4 min	
Hold	4	∞	-

2 μ l of 3 M sodium acetate (NaAc), 10 μ l of ddH₂O and 50 μ l of absolute EtOH (\geq 99.8%) were added to the PCR product. The reaction was mixed, incubated for 15 min at RT and centrifuged at 3000 g and 20 $^{\circ}$ C for 15 min. The supernatant was discarded and the pellet was washed with 100 μ l of EtOH (70%, v/v). After a centrifugation at 3000 g and 20 $^{\circ}$ C for 10 min, the supernatant was removed and the pellet was incubated for 15 min at RT. The DNA was resuspended in highly deionized formamide (HiDi). The reaction products were analyzed in the diagnostic department of the Institute of Human Genetics (UKE Hamburg) using capillary electrophoresis.

3.2.2. Cell Culture Methods

3.2.2.1. Cell Culture with HEK293T Cells

Human embryonic kidney 293 cells expressing the SV40 large T antigen (HEK293T cells) taken from the stock of Kreienkamp research group (Institute of Human Genetics, UKE Hamburg) were used for cell culture. The HEK293T cells were cultured in 10 cm plates in DMEM medium supplemented with fetal bovine serum (FBS) and penicillin/streptavidin (pen/strep) antibiotics at 37 °C, in 5% CO₂ and humidified air. The cells were transferred to new plates when a confluence of 70% was reached. For passaging, the HEK293T cells were washed with Versene and treated with trypsin to detach them from the culture dish. After resuspension in medium, an appropriate amount of cells for the required confluence was seeded into fresh culture dishes and cultivated further.

3.2.2.2. Transient Transfection of HEK293T Cells

HEK293T cells at 40% confluence were transiently transfected with required plasmids using the TurboFect transfection reagent (Thermo Fisher Scientific, Waltham, USA). A transfection mixture consisting of 950 µl of serum-free DMEM medium, 18 µl of TurboFect and 4-12 µg DNA was prepared and mixed thoroughly. After incubation at RT for 20 min, the transfection mixture was added dropwise onto the cells which were then incubated for 24 h at 37 °C, in 5% CO₂ and humidified air.

3.2.2.3. Primary Cell Culture of Mouse Cortical Neurons

To isolate embryonal, cortical neurons from mice, a pregnant mouse was anaesthetised with CO₂ and sacrificed by cervical dislocation. The abdominal wall was opened and the uterus removed. The embryos (E18) were isolated from the amniotic sacs and decapitated. The brains were excised and transferred to HBSS containing pen/strep. Using a binocular dissection microscope, the hemispheres were separated and the meninges detached. The cortices were prepared by removing all other brain regions and then transferred to a 15 ml tube. The volume was reduced to 4.5 ml. 500 µl of 10x neuron isolation enzyme with papain (Thermo Fisher Scientific, Waltham, USA) was added and the cortices incubated for 30 min in a 37 °C water bath. The tissue was washed five times with neuron plating medium and the volume reduced to 2 ml. For trituration, glass pipettes were prepared with a gas burner flame to generate tips with progressively smaller openings. The tissue was triturated through the pipettes and the volume was adjusted to 10 ml using neuron plating medium. Subsequently, the cells were counted using a Neubauer counting chamber and seeded on PLL-coated 6-well dishes at a density of 1 million cells per well. After 24 h of incubation at 37 °C, in 5% CO₂ and humidified air, the neuron plating medium was replaced by neuron culture medium and the neurons were cultured for 12-14 days.

3.2.2.4. Transduction of Cortical Neurons with Adeno-associated Viruses

For viral transduction of primary cultured cortical neurons, pAAV-hSyn1-EGFP-CW3SL, pAAV-hSyn1-EGFP-Ago2-WT-CW3SL, and pAAV-hSyn1-EGFP-Ago2-L192P-CW3SL plasmids were generated to induce expression of GFP empty vector control, GFP-tagged Ago2-wildtype (WT), and GFP-tagged Ago2-L192P. Adeno-associated viruses (AAVs) of the serotype PHP-eB were produced by the Vector Facility of the UKE Hamburg using the appropriate packaging plasmid (plasmid no. 103005; Addgene, Watertown, USA) (Chan *et al.* 2017). The AAVs were thawed on ice and appropriate amounts were resuspended in the neuron culture medium to achieve a multiplicity of infection (MOI) of 25,000. For one sample, 24 million neurons were transduced. 24 h after plating the murine cortical neurons (see 3.2.2.3), the neuronal plating medium was replaced with AAV-containing neuron culture medium. AAV-infected neurons were cultivated for another 11 days in vitro (DIV).

3.2.3. Biochemical Methods

3.2.3.1. Cell Lysis of HEK293T Cells

HEK293T cells were lysed 24 h after transfection (see 3.2.2.2). Transfection efficiency was checked under a fluorescence microscope. When the transfection efficiency was 40% or more, cells were washed three times with 4 °C cold PBS and lysed in 1 ml of IP buffer, supplemented with protease inhibitors (1:500 0.125 M PMSF, 5 mg/ml leupeptin, 1 mg/ml pepstatin A). After 15 min on ice, the cells were transferred to 1.5 ml reaction tubes for centrifugation at 20,000 g and 4 °C for 15 min. The supernatant constituted the cell lysate which was transferred to clean reaction tubes.

3.2.3.2. Coimmunoprecipitation (RFP-trap)

For coimmunoprecipitation (CoIP), 25 µl of RFP magnetic trap beads (ChromoTek, Planegg-Martinsried, Germany) were washed twice with 500 µl of ice-cold IP buffer. 60 µl of cell lysate (see 3.2.3.1) was taken as input sample (IN) and 12.5 µl of 5x Lämmli buffer was added. All remaining cell lysate was added to the beads and rotated for 2 h at 4 °C. Afterwards, the samples were washed five times with IP buffer and the supernatant was discarded. The beads were resuspended in 60 µl of Lämmli buffer to generate the immunoprecipitation (IP) sample. Subsequently, input and IP samples were denatured for 5 min at 95 °C and 300 rpm.

3.2.3.3. SDS-PAGE and Western Blot

Cell lysates or samples from coimmunoprecipitation assays were analyzed by sodium dodecyl sulfate polyacrylamide gel electrophoresis (SDS-PAGE) with subsequent western blotting. Separation gels of 10% were poured with stacking gels of 1 cm width. The gels were put into a running chamber (BioRad, Munich, Germany) and covered with SDS running buffer. 20 µl of samples or 2 µl to 8 µl of PageRuler Prestained Protein Ladder (Thermo Fisher Scientific, Waltham, USA) were added to the gel wells. 80 V was applied to allow the samples to run from the pockets into the stacking gel. Then, the voltage was increased to 160 V, which separated the proteins based on their size. Proteins were transferred to a nitrocellulose membrane using the wet blot method. The wet blot transfer chamber was filled with transfer buffer and a voltage of 100 V was applied for 2 h. For blocking, the nitrocellulose membranes were incubated in 10 ml of 5% MP in TBS-T for 30 min at RT. This was followed by incubation with the primary antibody in 5% MP in TBS-T at 4 °C with rotation overnight. Membranes were washed three times with TBS-T for 10 min at RT and incubated with horseradish peroxidase coupled secondary antibody in TBS-T for 1 h at RT. Again, the membranes were washed three times with TBS-T and then incubated in chemiluminescent substrate (WesternBright from Biozym, Hamburg, Germany) before detection of the protein bands with an imaging system (BioRad, Munich, Germany). The relative protein amounts were quantified using ImageLab (BioRad, Munich, Germany).

3.2.3.4. Immunocytochemistry and Confocal Microscopy

Immunocytochemistry (ICC) and confocal microscopy were used for protein localization studies and to control for protein expression in HEK293T cells and cortical neurons. HEK293T cells were seeded on PLL-coated 12 well plates and transfected 24 h before fixation (see 3.2.2.2). Neurons were transduced at 1 DIV and fixed at 12 DIV. Fixation was performed with PFA fixation buffer (see Table 15). Cells were washed three times in PBS and permeabilised with 500 µl of 0.1% (v/v) Triton X-100 in PBS for 3 min at RT. After washing three times with PBS, cells were incubated for 1 h with 10% HS in PBS to reduce non-specific antibody binding. Dilutions of respective primary antibodies were prepared in 2% HS in PBS. For antibody staining, a sealed box was prepared by lining it with a layer of moistened filter paper beneath a sheet of parafilm. 100 µl drops of primary antibody solution were pipetted onto the parafilm sheet. The coverslips were placed face-down onto the antibody drops and the sealed boxes were placed in a fridge for overnight incubation at 4 °C. The coverslips were placed back into the 12 well plate and washed three times with PBS for 10 min at RT. Then, the samples were incubated with the

secondary antibodies in PBS for 1 h at RT in the sealed box with a fresh layer of parafilm. Following three washes with PBS, the coverslips were washed once with ddH₂O and mounted on slides using ProLong Diamond Antifade mounting medium with or without DAPI (Thermo Fisher Scientific, Waltham, USA). Samples were stored at RT overnight to dry. ICC samples were analyzed using a SP8 confocal microscope with a 63x oil immersion objective (Leica, Wetzlar, Germany), provided by the UKE Microscopy Imaging Facility (UMIF, Hamburg).

3.2.3.5. *MicroRNA Affinity Purification*

Preparation of beads: A microRNA affinity purification (miRAP), adapted from He 2012, was applied to analyze Ago2-associated miRNAs. 300 μ l of Streptavidin MyOne T1 Dynabeads (Thermo Fisher Scientific, Waltham, USA) were resuspended in 900 μ l of PBS. 120 μ l of Biotinylated Pierce Recombinant Protein L (Thermo Fisher Scientific, Waltham, USA) was added and the mixture was rotated for 35 min at RT. After coating, beads were washed five times with 3% IgG + Protease-free bovine serum albumin (BSA; Jackson ImmunoResearch, Ely, UK) in PBS. Next, beads were resuspended in 930 μ l of 0.15 M KCl IP wash buffer. Monoclonal antibodies Htz-GFP 19C8 and Htz-GFP 19F7 (Heintz Lab, Rockefeller University, Cat# Htz-GFP-19F7, RRID:AB_2716736) were thawed on ice and centrifuged at 13,000 g and 4 °C for 10 min. 50 μ g of each anti-GFP antibody was added to the beads and rotated slowly at RT for 1 h. Beads were washed three times in 900 μ l of 0.15 M KCl IP wash buffer and then resuspended in 200 μ l of 0.15 M KCl IP wash buffer.

Preparation of neurons: Cortical neurons from mice were infected with AAVs at 1 DIV to induce the expression of GFP-tagged Ago2 variants (see 3.2.2.3 and 3.2.2.4). The neurons were washed three times in PBS and scraped from the culture dishes in 500 μ l of RNase-free PBS per well. After centrifugation at 2000 g and 4 °C for 5 min, the obtained cell pellet was resuspended in 1 ml of lysis buffer and incubated for 15 min on ice. Cell lysates of 22 million neurons were combined to generate one sample, divided into IC and IP. Neuron lysates were centrifuged at 2000 g and 4 °C for 10 min and the supernatant transferred to prechilled reaction tubes on ice. 100 μ l of 10% (v/v) NP-40 in ddH₂O was added and mixed by inversion. Then, 100 μ l of 300 mM 1,2-diheptanoyl-sn-glycero-3-phosphocholine (DHPC; Sigma-Aldrich, Taufkirchen, Germany) was added and again mixed by inversion. Samples were incubated on ice for 5 min and centrifuged for 10 min at 4 °C and 20,000 g. The supernatant was again transferred to a new tube on ice. At that point, 100 μ l was taken as IC and directly frozen at -80 °C. For immunoprecipitation, 200 μ l of prepared beads was added to the sample and incubated overnight at 4 °C with gentle rotation. The beads were washed four times with 0.35 M KCl wash buffer and resuspended in 700 μ l of QIAzol (Qiagen, Hilden, Germany). Simultaneously, 700 μ l of QIAzol was added to the IC samples and from then on IC and IP samples were processed in parallel. After incubation at RT for 5 min, 140 μ l of chloroform was added and the samples were shaken vigorously for 15 s. An incubation at RT for 3 min as well as a centrifugation step at 12,000 g for 15 min at 4 °C followed, which led to phase separation of a colorless aqueous RNA phase, a white interphase containing DNA, and an organic phase below that contained proteins and lipids. The upper phase was extracted to which 525 μ l \geq 99.8% of EtOH was added and mixed. For subsequent RNA purification, the miRNeasy Micro Kit (Qiagen, Hilden, Germany) was used according to the manufacturer's protocol. The miRNA concentration was determined with the Qubit microRNA Assay-Kit (Thermo Fisher Scientific, Waltham, USA) following manufacturer's instructions.

3.2.3.5.1. *Quantitative Polymerase Chain Reaction for Detection of miRNAs*

As quality control for input and IP samples generated with miRAP (see 3.2.3.5), a quantitative PCR (qPCR) on miRNAs was applied using the TaqMan Advanced miRNA Assay (Thermo Fisher Scientific, Waltham, USA). First, a 3'-poly(A) tailing reaction was performed according to Table 23.

Table 23: Reaction mixture for 3'-poly(A) tailing of miRNA.

Component	Volume [μ l]
10x poly(A) buffer	0.5
10 mM ATP	0.5
Poly(A) enzyme	0.3
RNase-free H ₂ O	1.7
RNA sample	2

The reaction was incubated in a thermal cycler with settings shown in Table 24.

Table 24: Thermal cycler program for 3'-poly(A) tailing.

Process	Temperature [$^{\circ}$ C]	Duration [min]
Polyadenylation	37	45
Stop reaction	65	10
Hold	4	∞

As a second step, a 5'-ligation to adapters at 16 $^{\circ}$ C for 1 h was carried out with the constituents listed in Table 25. The 5'-adapter sequences were used to extend the miRNA sequence on the 5'-side and allowed the differentiation of bases along the entire miRNA sequence, including the terminal 5'-bases, which are normally difficult to determine.

Table 25: Components of a 5'-ligation reaction following 3'-poly(A) tailing.

Component	Volume [μ l]
5x DNA ligase buffer	3
50% PEG 8000	4.5
25x ligation adapter	0.6
RNA ligase	1.5
RNase-free water	0.4
Poly(A) reaction	5

In a third step, cDNA synthesis by reverse transcription was performed in a reaction mixture shown in Table 26.

Table 26: Reverse transcription reaction of polyadenylated miRNA ligation products.

Component	Volume [μ l]
5x RT buffer	6
25 mM dNTP mix	1.2
20x universal RT primer	1.5
10x RT enzyme mix	3
RNase-free water	3.3
Ligation product	15

The following thermal cycler program was used (Table 27).

Table 27: Thermal cycler program for reverse transcription of polyadenylated miRNA.

Process	Temperature [$^{\circ}$ C]	Duration [min]
Reverse transcription	42	15
Stop reaction	85	5
Hold	4	∞

To ensure detection of low expressing miRNAs, amplification of the generated cDNA was performed in a reaction mixture according to Table 28. Universal primers that recognized the 5'-adapters and 3'-poly(A) tails were used to amplify the cDNA of all miRNAs evenly.

Table 28: Components for miRNA-originated cDNA amplification.

Component	Volume [μ l]
2x miR-Amp Master Mix	25
20x miR-Amp Primer Mix	2.5
RNase-free water	17.5
cDNA template	5

Table 29 lists the thermal cycler settings for amplification of miRNA-originated cDNA.

Table 29: Thermal cycler program for amplification of miRNA-originated cDNA.

Process	Temperature	Duration	Cycles
Enzyme activation	95	5 min	-
Denaturation	95	3 s	14
Annealing and extension	60	30 s	
Stop reaction	99	10 min	-
Hold	4	∞	-

The following qPCR was performed in technical triplicates. TE buffer and cDNA templates were diluted 1:10. PCR reactions were prepared according to Table 30 and two specific miRNAs (Malmevik *et al.* 2015) were detected using specific TaqMan probes (Table 31).

Table 30: The qPCR reaction for miRAP quality control.

Component	Volume [μ l]
2x Fast Advanced Master Mix	5
20x Advanced miRNA Assay	0.5
RNase-free water	2
1:10 cDNA template	2.5

Table 31: Chosen Advanced miRNA Assays for marker miRNAs in miRAP quality control.

Marker miRNA	Advanced miRNA Assay	Cell population
mmu-miR-124-3p	mmu480901_mir	Neurons
mmu-miR-21-5p	mmu482709_mir	Glia cells

The qPCR was done in a thermal cycler using the following settings (Table 32).

Table 32: Thermal cycler settings for qPCR for miRAP quality control.

Process	Temperature [$^{\circ}$ C]	Duration [s]	Cycles
Enzyme activation	95	20	-
Denaturation	95	3	40
Annealing and extension	60	30	

Carboxyrhodamine (ROX) was used as a passive reference dye because the fluorescence signal of the inert dye remains stable throughout the PCR reaction, independent of the amount of amplification products. The signal from ROX is affected by technical variations, e.g. evaporation, condensation or bubbles, and normalization to ROX reduces the variability between technical replicates. The fluorescent signal from the specific TaqMan probes was normalized to the ROX signal to calculate the

normalized reporter value R_n . Amplification was plotted as the difference in normalised reporter values, ΔR_n , against cycle. The cycle threshold or C_t value was determined in the exponential phase of amplification, where the curve was linear. The relative enrichment (ΔC_t) of miRNAs was calculated as C_t of the IP samples normalised to the C_t value measured in IC with $\Delta C_t = [C_t(IP) - C_t(IN)]$.

3.2.4. Animal Testing

3.2.4.1. Housing of Laboratory Mice

The laboratory animals were bred specifically for animal experiments and obtained directly from the UKE Hamburg laboratory animal facility. Housing conditions complied with §11 of the Animal Welfare Act and the hygiene status was controlled quarterly using sentinel animals. A maximum of five animals were kept per cage of the blue line type II L series. Access to water and food was given *ad libitum* and all mice were kept under 12-12 h light to dark cycles with monitored temperature and humidity in the vivarium.

3.2.4.2. Breeding of Laboratory Mice

All mice were kept in the C57BL/6J background. The *Shank1*-knockout (KO) and *Shank3 $\alpha\beta$* -KO mice were bred in heterozygous breeding pairs for conservational breeding or to generate cohorts for behavioral analyses. For the latter, 10 male (M) and female (F) KO mice of both Shank lines with wildtype littermates were bred. To reduce litter effects, only two mice per genotype from the same litter were used for the open field test cohort (see 3.2.4.5). Transgenic mouse lines for the translating ribosome affinity purification (TRAP) have been generated using bacterial artificial chromosomes (bac) and are therefore referred to as bacTRAP lines. In the *Lypd1*-bacTRAP line, which expresses an EGFP-tagged L10a ribosomal protein (L10a) under control of the *Lypd1* promoter, the transgene was always kept in a heterozygous state, by breeding heterozygous mice with a C57BL/6J WT mice.

3.2.4.3. Generation and Breeding of *Lypd1*-bacTRAPx*Shank1*-KO and *Lypd1*-bacTRAPx*Shank3 $\alpha\beta$* -KO Mice

To analyze the effects of *Shank1* or *Shank3 $\alpha\beta$* knockout on neuronal translation, two new mouse lines were generated. Heterozygous (HZ) mice of the *Lypd1*-bacTRAP line were crossed with homozygous knockout mice of the *Shank1*- or *Shank3 $\alpha\beta$* lines. This resulted in the generation of *Lypd1*-bacTRAPx*Shank1* and *Lypd1*-bacTRAPx*Shank3 $\alpha\beta$* mice, all of which were heterozygous for the *Shank* alleles. Half of the offspring carried the *Lypd1*-bacTRAP allele coding for EGFP-tagged L10a ribosomal protein in the heterozygous state, while the other half were wildtype in respect to the *Lypd1* allele. These two groups were crossed to produce a second generation with homozygous *Shank1* and *Shank3* knockout alleles and *Lypd1*-EGFP-positive heterozygous mice. The cohorts to be used in bacTRAP experiments were bred in wildtype or homozygous knockout breeding pairs regarding the *Shank1* or *Shank3* allele, while the transgene of the *Lypd1* allele was kept in a heterozygous state. To reduce effects of maternal imprinting on behavior, a wildtype female was always housed with a knockout female from litter to weaning. Mice carrying the *Lypd1* transgene were selected for experimental cohorts and housed in mixed cages with respect to the *Shank* allele genotype until 12 weeks of age.

3.2.4.4. Genotyping

Genotyping of laboratory mice was performed using tail tip biopsies. Genomic DNA was obtained through incubation of a tail tip in 60 μ l of DirectPCR Tail (Viagen BIOTECH, Los Angeles, USA) with 2 μ l of proteinase K (10 mg/ml) at 55 °C and 600 rpm shaking motion overnight. The proteinase K was then inactivated by incubation for 1 h at 85 °C and 600 rpm. The wildtype and the knockout allele of *Shank1* or *Shank3* were determined in PCRs with specific primer pairs (Table 33 and Table 34).

Table 33: PCR reaction for genotyping of *Shank1*-KO mice.

Component	Volume [μ l]
ddH ₂ O	18.2

Component	Volume [μ l]
10x CoralLoad PCR buffer	3.2
10 mM dNTPs	1.3
25 mM MgCl ₂	1.9
10 μ M Primer 1: Short arm fwd	2.2
10 μ M Primer 2: Deletion rev	2.2
10 μ M Primer 3: NEO 250 rev	2.2
Taq polymerase S1	1
Genomic DNA	2

Table 34: PCR reaction for genotyping of *Shank3 α 6*-KO mice.

Component	Volume [μ l]
ddH ₂ O	15.2
10x CoralLoad PCR buffer	3.2
Q-Solution	4.3
10 mM dNTPs	1.3
25 mM MgCl ₂	0.6
10 μ M Primer 1: S12 WT	2.2
10 μ M Primer 2: S10 KO	2.2
10 μ M Primer 3: AS3	2.2
Taq polymerase S1	1
Genomic DNA	2

The following temperature program was used to amplify specific DNA loci for genotyping (Table 35).

Table 35: Thermal cycler temperature program for *Shank1* or *Shank3* genotyping via PCR.

Process	Temperature [$^{\circ}$ C]	Duration	Cycles
Initialisation	94	1 min	-
Denaturation	94	30 s	30
Annealing	64	5 s	
Elongation	72	30 s	
Final elongation	72	5 min	-
Hold	4	∞	-

Additionally, the presence or absence of the *Lypd1*-bacTRAP transgene was verified in separate reactions (Table 36).

Table 36: Components of the PCR reaction for verification of the *Lypd1*-bacTRAP transgene.

Component	Volume [μ l]
ddH ₂ O	14.28
10x CoralLoad PCR buffer	2.5
10 mM dNTPs	1.3
25 mM MgCl ₂	0.64
10 μ M Primer 1: Actin fwd	1
10 μ M Primer 2: Actin rev	1
10 μ M Primer 3: EGFP 5'	0.9
10 μ M Primer 4: EGFP 3'	0.9
Taq polymerase S1	1
Genomic DNA	2

The PCR was carried out under the following conditions (Table 37).

Table 37: PCR program for genotyping of Lypd1-bacTRAP transgene.

Process	Temperature [°C]	Duration	Cycles
Initialisation	94	2 min	-
Denaturation	94	30 s	38
Annealing	64	30 s	
Elongation	72	30 s	
Final elongation	72	5 min	-
Hold	4	∞	-

The PCR products were loaded onto an agarose gel. Expected PCR product sizes for tested alleles are listed in Table 38. The band pattern was evaluated to determine the genotype of the mice.

Table 38: Expected PCR product band sizes in genotyping.

Allele	Band size [bp]
<i>Shank1</i> -WT	240
<i>Shank1</i> -KO	430
<i>Shank3αβ</i> -WT	360
<i>Shank3αβ</i> -KO	190
Lypd1-EGFP	350
Actin	150

3.2.4.5. Open Field Test

All mice used in the experiments were tested in an open field test to ensure that the mice exhibited an ASD phenotype at the time of sampling. These behavioral analyses were done in cooperation with Dr. Fabio Morellini from the Behavioral Biology Research Group at the Center for Molecular Neurobiology Hamburg. Two weeks prior to the open field tests, 10-weeks-old mice were transferred to Dr. Morellini's facility and accustomed to a reversed 12-12 h dark to light cycle. Mice were handled daily and their weight was monitored. The open field test was conducted by placing a mouse in a 50 cm x 50 cm x 40 cm open field arena illuminated with 25 lux white light. The mouse freely explored this area over a period of 20 min. The distance travelled and the time spent in the central zone were evaluated using EthoVision software. Between experiments, the open field arena was cleaned thoroughly with water and soap and then ethanol to ensure no distracting scents for the next mouse to be tested. Self-grooming and rearing behavior were evaluated retrospectively by analysing the video footage with the Observer software.

3.2.4.6. Preparation of Postsynaptic Densities

For brain region specific preparation of postsynaptic densities (PSD), 12-weeks-old mice were anaesthetised with CO₂ and sacrificed by cervical dislocation. The skull was opened and the brain removed. Using a binocular dissection microscope, hemispheres were separated and the olfactory bulb and cerebellum were removed. The forebrain or cortex and hippocampus were dissected. A forebrain was processed as one sample, whereas cortices or hippocampi from five mice of same genotype and sex were combined per sample. Brain tissue was homogenised in 3 ml of PSD buffer A using a glass homogeniser. The homogenate was centrifuged at 1400 g and 4 °C for 10 min, the supernatant was transferred, and the pellet resuspended in 3 ml of PSD buffer A and homogenised again in a glass homogeniser. After centrifugation at 1400 g and 4 °C for 10 min the supernatants were combined. From the pooled supernatant, the postnuclear fraction was obtained by further centrifugation at 710 g and 4 °C for 10 min, while the cell nuclei were pelleted. 100 µl of supernatant was taken as P1 sample (postnuclear fraction) and 25 µl of 5x Lämmli buffer was added. The remaining sample was centrifuged at 13,800 g and 4 °C for 15 min and the supernatant discarded. The pellet was resuspended in 3 ml of

PSD buffer B to obtain the membrane fraction from which 200 μ l was mixed with 37.8 μ l of 5x Lämmli buffer to produce the P2 sample. A sucrose gradient of three molarities, 1.2 M, 1.0 M and 0.85 M, was cast into Ultra-Clear Centrifuge Tubes (Beckman Coulter, Brea, USA). The sample was loaded on the gradient and centrifuged at 82,500 g, 4 °C, and under vacuum conditions for 2 h. The components of the sample were distributed across the gradient dependent on their density, which led to accumulation of the synaptosomal fraction between the 1.2 M and the 1.0 M sucrose layers. This fraction was isolated from that location by carefully piercing through the gradient with a Pasteur pipette. After transferring to a new tube, the volume was adjusted to a total of 5 ml with PSD buffer B. 5 ml of PSD Triton X-100 buffer was added and the sample rotated at 4 °C for 30 min. A centrifugation at 20,000 g and 4 °C for 45 min followed to pellet the PSD, which was then resuspended in 300 μ l of PSD buffer B. 60 μ l of resuspended PSD was taken as P3 sample and 15 μ l of 5x Lämmli added. The efficiency of PSD purification was validated by western blot analyses (see 3.2.3.3) of the P1-P3 samples.

3.2.4.7. Translating Ribosome Affinity Purification

For translating ribosome affinity purification (TRAP or bacTRAP), the monoclonal antibodies HtZ-GFP 19C8 and HtZ-GFP 19F7 were thawed on ice and centrifuged for 10 min at 20,000 g and 4 °C. 300 μ l of Streptavidin MyOne T1 Dynabeads was resuspended in 1 ml of RNase-free PBS and 120 μ l of Biotinylated Protein L was added. After gentle rotation for 35 min at RT, the coated beads were washed five times in RNase-free PBS buffer containing 3% IgG- and protease-free BSA. 50 μ g of both monoclonal anti-GFP antibodies, 19C8 and 19F7, were added, followed by an incubation under slow rotation at RT for 1 h. Beads were washed three times in 1 ml of 0.15 M KCl IP wash buffer, then resuspended in 200 μ l of 0.15 M KCl IP wash buffer and stored on ice during brain lysate preparation. *Lypd1*-bacTRAPx*Shank*-KO mice and wildtype littermates were anaesthetised by intraperitoneal injection of 15 μ l/g bodyweight of a ketamine and xylazine solution. The solution contained 12 mg/ml ketamine and 1.6 mg/ml xylazine and a maximum of 450 μ l was injected. Surgical tolerance was verified by the absence of toe reflexes. The thorax was opened and a syringe was inserted into the left ventricle. The mouse was perfused with 4 °C cold bacTRAP dissection buffer using a constant pump rate of 30 ml/min for 1 min. The brain was dissected and the hippocampi of three animals were combined in 1 ml of lysis buffer. The tissue was homogenised in a glass homogeniser and the homogenate was transferred to a prechilled tube on ice. By centrifugation of the homogenate for 10 min at 2000 g and 4 °C, cell nuclei were pelleted and subsequently flash frozen with liquid nitrogen. The supernatant was transferred to a tube on ice and 100 μ l of 10% (v/v) NP-40 in ddH₂O was added to a final concentration of 1%. The tube was inverted five times and then 100 μ l of 300 mM DHPC was added. Again, the sample was mixed by inversion and subsequently incubated on ice for 5 min. A centrifugation at 20,000 g and 4 °C for 10 min followed to collect the postmitochondrial fraction as the supernatant, of which 100 μ l was kept as input control. For immunoprecipitation, prepared beads were resuspended, 200 μ l was added to each sample and incubated overnight at 4 °C with gentle rotation. The next day, the IP sample was washed five times in 1 ml of 0.35 M KCl wash buffer and then further processed in parallel with the corresponding IC sample for RNA purification. 800 μ l of Trizol was added to the IC and IP samples and mixed by pipetting. Following incubation at RT for 5 min, 200 μ l of chloroform was added, the samples were shaken vigorously for 15 s and then incubated for 3 min at RT. Phase separation was achieved by centrifugation at 12,000 g and 4 °C for 15 min. The colorless upper phase was extracted and 1/10 of the volume of this RNA phase of 3 M sodium acetate solution was added. 550 μ l of isopropanol was added and inverted for five times. After adding 5 μ l of Glycoblu (AM9515; Thermo Fisher Scientific, Waltham, USA), the samples were stored overnight at -80 °C. The next day, samples were centrifuged at 13,000 g and 4 °C for 15 min. The blue stained RNA pellet was washed twice with 70% EtOH by centrifugation for 5 min at 13,000 g and 4 °C. To dry the RNA pellet, the open tube was incubated at RT for 15 min under the closed fume hood. The pellet was then

resuspended in 100 µl of RNase-free water and the RNeasy micro kit (Qiagen, Hilden, Germany) was applied for RNA purification according to the manufacturer's protocol.

3.2.4.7.1. Quantitative Polymerase Chain Reaction for mRNA

A reverse transcriptase qPCR was performed on RNA samples generated with the bacTRAP method from *Shank1*-KO mice (see 3.2.4.7). The RNA of input control (IC) and immunoprecipitate (IP) were reverse transcribed into cDNA using the RevertAid H Minus First Strand cDNA Synthesis Kit (Thermo Fisher Scientific, Waltham, USA). Table 39 shows the components for the reverse transcription.

Table 39: Components for a reverse transcription reaction.

Component	Volume [µl]
5x reaction buffer	4
Ribolock RNase inhibitor	1
10 mM dNTP mix	2
RevertAid H Minus M-MuLV reverse transcriptase	1
RNA sample	1

The reverse transcription proceeded in a thermal cycler according to the temperature program in Table 40.

Table 40: Temperature program for cDNA synthesis.

Temperature [°C]	Duration [min]
25	5
42	60
70	5

Six TaqMan Gene Expression Assays (Thermo Fisher Scientific, Waltham, USA) were selected, as listed in Table 41, to investigate the expression of marker genes which are typically highly expressed in a specific cell population.

Table 41: Chosen marker genes for TaqMan Gene Expression Assays.

Marker Gene	Abbreviation	TaqMan Assay	Cell Population
TATA-box binding protein	Tbp	Mm01277042_m1	Internal control, ubiquitously expressed
2',3'-Cyclic-nucleotide 3'-phosphodiesterase	Cnp	Mm01306641_m1	Oligodendrocytes
Glial fibrillary acidic protein	Gfap	Mm01253033_m1	Astrocytes
Desmoplakin	Dsp	Mm01351876_m1	Mature granule cells
Ly6/PLAUR domain-containing protein 1	Lypd1	Mm00513929_m1	Promotor controlling EGFP-L10a expression
Enhanced green fluorescent protein	EGFP	Mr03989638_mr	Tag of L10a ribosomal protein

The composition of the qPCR mixture is shown in Table 42.

Table 42: The qPCR reaction with TaqMan Gene Expression Assays.

Component	Volume [µl]
20x TaqMan Gene Expression Assay	0.5
2x TaqMan Gene Expression Master Mix	5
RNase-free water	2.5
cDNA template	2

The samples were measured as technical triplicates on a 96 well plate in an ABI Prism 7900HT Fast Real-Time PCR System (Thermo Fisher Scientific, Waltham, USA) following the temperature program listed in Table 43.

Table 43: Thermal cycler program used for qPCR.

Process	Temperature [°C]	Duration	Cycles
Enzyme activation	95	10 min	-
Denaturation	95	15 s	40
Annealing and extension	60	1 min	

ROX was used as a passive reference dye and amplification was measured as ΔRn . ΔCt was calculated as the expression of the marker genes (Cnp, Gfap, Dsp, Lyppd1 and EGFP) normalized to the expression of the ubiquitously expressed TATA-box binding protein (Tbp), with $\Delta Ct = [Ct(\text{marker}) - Ct(\text{Tbp})]$. The relative gene expression was calculated as $2^{-\Delta Ct}$ with ΔCt values of the IP normalized to the corresponding ΔCt of the IC (Livak and Schmittgen 2001).

3.2.5. Analytical Methods and Bioinformatics

3.2.5.1. RNA Sequencing

The bacTRAP samples (see 3.2.4.7) and miRAP samples (see 3.2.3.5) were analyzed using Next Generation Sequencing. The samples were sent to the NGS Integrative Genomics Core Unit at the Institute of Human Genetics at the University Medical Center Göttingen. For preparation of RNA libraries and NGS, the SMART-Seq v4 Ultra Low Input RNA Kit for Sequencing (TAKARA, Kusatsu, Japan) and the NovaSeq6000 S1 100 cycles Flow cell (Illumina, San Diego, USA) were used. Whereas miRNA libraries were prepared using the QIAseq miRNA Library Kit (Qiagen, Hilden, Germany). The bioinformatics analyses were carried out by Dr. Dr. Jan Broder Engler from the Institute for Neuroimmunology and Multiple Sclerosis at the Center for Molecular Neurobiology Hamburg (ZMNH). The RNA-seq reads were aligned to an Ensembl mouse reference genome using STAR (Dobin *et al.* 2013) v2.5 with default settings. FeatureCounts (Liao *et al.* 2014) was applied to assess the overlap of uniquely aligned reads with annotated gene loci. Contaminations originating from non-mouse genomes or other typical sources of contamination were detected using the FastQ Screen tool (Wingett and Andrews 2018). Processing of miRNA sequencing data was facilitated with the OASIS tool (Capece *et al.* 2015). Further analyses were conducted in the R environment v4.2.1 with publicly available packages. The DEseq2 tool (Love *et al.* 2014) v1.36.0 performed quality control through identifying and excluding outlier samples by calculated Cook's distances. Dispersion estimates, as well as fold change shrinkages were calculated. Normalized and shrunken \log_2 fold changes were used for subsequent assessment of sample similarity and differential gene expression. Differentially expressed genes (DEGs), determined with the bacTRAP method, were identified by a \log_2 fold change of > 0.5 and a false discovery rate (FDR) of < 0.1 . Differentially expressed miRNAs were selected by having an absolute \log_2 fold change of > 1 and a FDR of < 0.05 . DEGs were visualised in volcano plots and in heatmaps using the pheatmap v1.0.12 tool. Gene set enrichment analysis of translome data was carried out with GSEA.

3.2.5.2. Mass spectrometry

To prepare a PSD sample for mass spectrometric measurements, the PSD was pelleted by centrifugation at 20,000 g and 4 °C for 30 min. The pellet was resuspended in 300 μ l of 0.1 M triethylammonium bicarbonate (TEAB) buffer. After washing two times with TEAB buffer (20,000 g, 4 °C, 30 min), the PSD was resuspended in 0.1 M TEAB buffer with 1% sodium deoxycholate (SDC). Further sample processing and mass spectrometric measurements were performed in collaboration with Hannah Voß at the Core Facility for Mass Spectrometric Proteomics at UKE Hamburg. Protein extraction was performed for 10 min at 99 °C. Tryptic digestion was performed using the Single-pot,

solid-phase-enhanced sample preparation (SP3) protocol (Hughes *et al.* 2019). 1 µg of peptides were subjected to Liquid-chromatography coupled Tandem Mass Spectrometry (LC-MS/MS) analysis in 0.1% formic acid (FA). LC analyses were performed on a nano-UPLC (Dionex Ultimate 3000 UPLC system, Thermo Fisher Scientific, Waltham, USA). Tryptic peptides were injected to the LC system via an autosampler and purified and desalted by using a reverse phase trapping column (Acclaim PepMap 100 C18 trap; 100 µm × 2 cm, 100 Å pore size, 5 µm particle size; Thermo Fisher Scientific), followed by separation with a reverse phase column (Acclaim PepMap 100 C18; 75 µm × 25 cm, 100 Å pore size, 2 µm particle size, Thermo Fisher Scientific). Separation was performed by a linear gradient from 2%-30% solvent B (0.1% FA in acetonitrile; solvent A: 0.1 % FA in H₂O) in 65 min at a flow rate of 0.3 µl/min. Eluting peptides were ionized by using a nano-electrospray ionization source (nano-ESI) with a spray voltage of 1800 V, transferred to a quadrupole-ion-trap-orbitrap MS (QExactive, Thermo Fisher Scientific), and analyzed using data dependent acquisition (DDA) in the positive ionization mode. Peptides with a mass to charge ratio between 400 and 1200 were considered. LC-MS/MS raw spectra were searched with a combined workflow, including the CHIMERYS and SEQUEST algorithm integrated in the Proteome Discoverer software (v3.0, Thermo Fisher Scientific) against a reviewed murine Swissprot database (December 2022) containing 17144 entries. A strict cutoff (FDR < 0.01) was set for peptide and protein identification. Protein quantification was carried out using the Minora Algorithm implemented in Proteome Discoverer. Retrieved abundancies were normalized at the peptide level using all peptides. Protein abundances were log₂ transformed. Principal component analyses (PCA) and hierarchical clustering (HC) were generated in Perseus (Version 2.0.3, Max Plank Institute of Biochemistry, Munich, Germany). For ANOVA and Student's t-tests a p-value cutoff of < 0.05 was applied. For the identification of significantly changed proteins, a fold change cutoff of > 1.5 was applied. Volcano plots were generated, using an in-house script in the R-Software environment (Version 4.1.3.)

4. Results

4.1. The Neuronal Translatome and the Postsynaptic Proteome are Affected by Knockout of *Shank1* or *Shank3αβ* in ASD Mouse Models

Mutations in the *SHANK1* and *SHANK3* genes are associated with ASD (Grabrucker *et al.* 2011, Berkel *et al.* 2012, Sato *et al.* 2012). The encoded Shank proteins are postsynaptic scaffold proteins localized at the postsynapse of excitatory, glutamatergic synapses, where they indirectly connect glutamate receptors to the actin cytoskeleton (Du *et al.* 1998, Boeckers *et al.* 1999, Sheng and Kim 2000, Kreienkamp 2008). Previous research of the Kreienkamp group identified the N-terminus of Shank3, comprising the SPN and ANK domains, as Ras association domains, linking Shank proteins to the MAPK signaling pathway, which is involved in regulation of translation. The *Shank3αβ* knockout mouse line used in this study lacks the isoforms of Shank3 that contain the SPN-ANK-SH3 domains, whereas all Shank1 isoforms are absent in the *Shank1*-KO mouse model. Importantly, many ASD-related mutations, for example in the genes *FMR1*, *PTEN* or *TSC1/2*, lead to altered translation (Wiznitzer 2004, Butler *et al.* 2005, Lai *et al.* 2014, Richter *et al.* 2015). The molecular effects caused by *SHANK* variants and consequences for postsynaptic functions were analyzed here as an example of the subgroup of ASD risk genes which encode for synaptic proteins. I wanted to test the hypothesis that autism-associated mutations of the *SHANK1* and *SHANK3* genes lead to dysregulation of translation and an altered postsynaptic proteome, which might result in altered synaptic development and plasticity. Two novel bacTRAP-*Shank* knockout mouse models were generated and behavioral studies performed. The neuronal translatome of Lypd1-bacTRAPx*Shank3αβ* mice was analyzed. Furthermore, the composition of the protein network of the postsynaptic density fraction from *Shank1* and *Shankαβ* knockout mice was determined. In this proteomics approach, quantitative mass spectrometry was used to investigate the postsynaptic proteome in *Shank* knockout mice.

4.1.1. Validation of an ASD-typical Phenotype in *Shank1* and *Shank3αβ* Knockout Mouse Models

Initially, behavioral experiments were performed to determine an autistic phenotype at the time point of analyzing the translatome and proteome. The *Shank1* and *Shank3αβ* knockout mouse lines were tested at 12 weeks of age. Locomotor activity and the ASD core symptom of repetitive behavior were assessed by the open field test in collaboration with Dr. Fabio Morellini. All mice were tested for their behavior in one cohort at the same time and compared with the respective control group of WT littermates. For two weeks before the behavior experiment, mice were handled daily and their weight measured (Figure 5). Female (F) and male (M) *Shank1*-KO mice showed significantly reduced body weight (Figure 5A). In contrast, the *Shank3αβ* knockout had no effect on body weight (Figure 5B). Furthermore, in preliminary screening experiments to train the mice for a Morris water maze experiment, it was observed that the *Shank1* knockout mice demonstrated severe impairments in locomotor skills, as they could not swim. Here again, the *Shank3αβ*-KO mice did not show the same phenotype and were not impaired in their swimming ability.

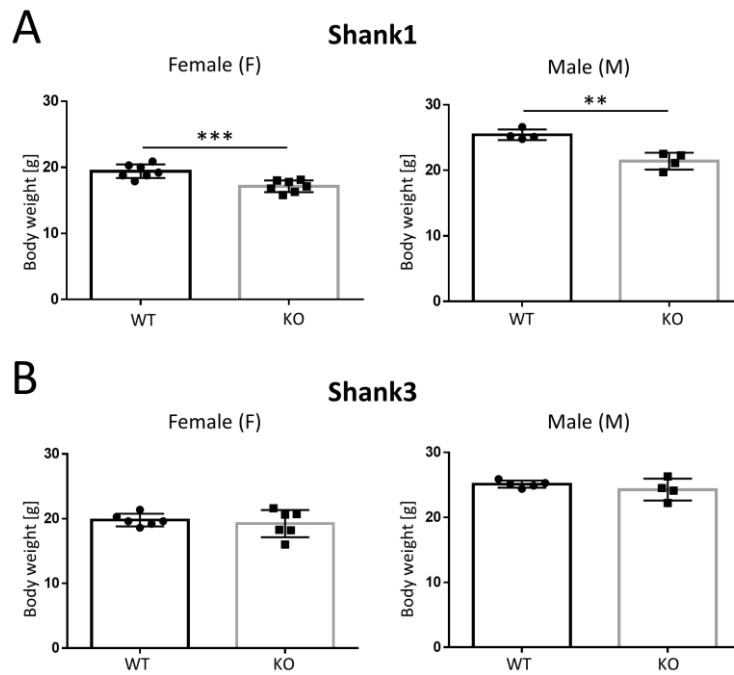


Figure 5: Knockout of *Shank1* resulted in reduced body weight in mice. The body weight of *Shank1* and *Shank3αβ* knockout mice and their WT littermates was measured. **(A)** The body weight of male and female *Shank1*-KO mice was reduced. **(B)** *Shank3αβ*-KO mice had no change in body weight compared to the controls. The body weight of each sampled mouse at 12 weeks of age is shown as mean with standard deviation of each group. Statistical significance was determined by two-tailed Student's t-test ($p \leq 0.01 = **$, $p \leq 0.001 = ***$).

In the following open field test, all changes in the location of the mouse were detected over a fixed time period. The complete distance moved, the distance to the wall of the testing area and the time in the center of the open field were determined and compared between knockout and WT mice (Figure 6 and Figure 7). *Shank1*-KO mice moved less distance during the time course of 20 minutes (min) with the most pronounced differences at the 20 min time point for female mice and at 15 min for males (Figure 6A). Female *Shank1*-KO mice (KO-F) showed a smaller distance to the field wall at 20 min compared to WT littermates (Figure 6B, middle panel). Furthermore, the KO-F mice spent significantly less time in the center of the open field after 20 min (Figure 6C, middle panel). In contrast, KO-M mice showed not altered distance to the wall, or time in the center compared to controls (Figure 6B-C, right panels).

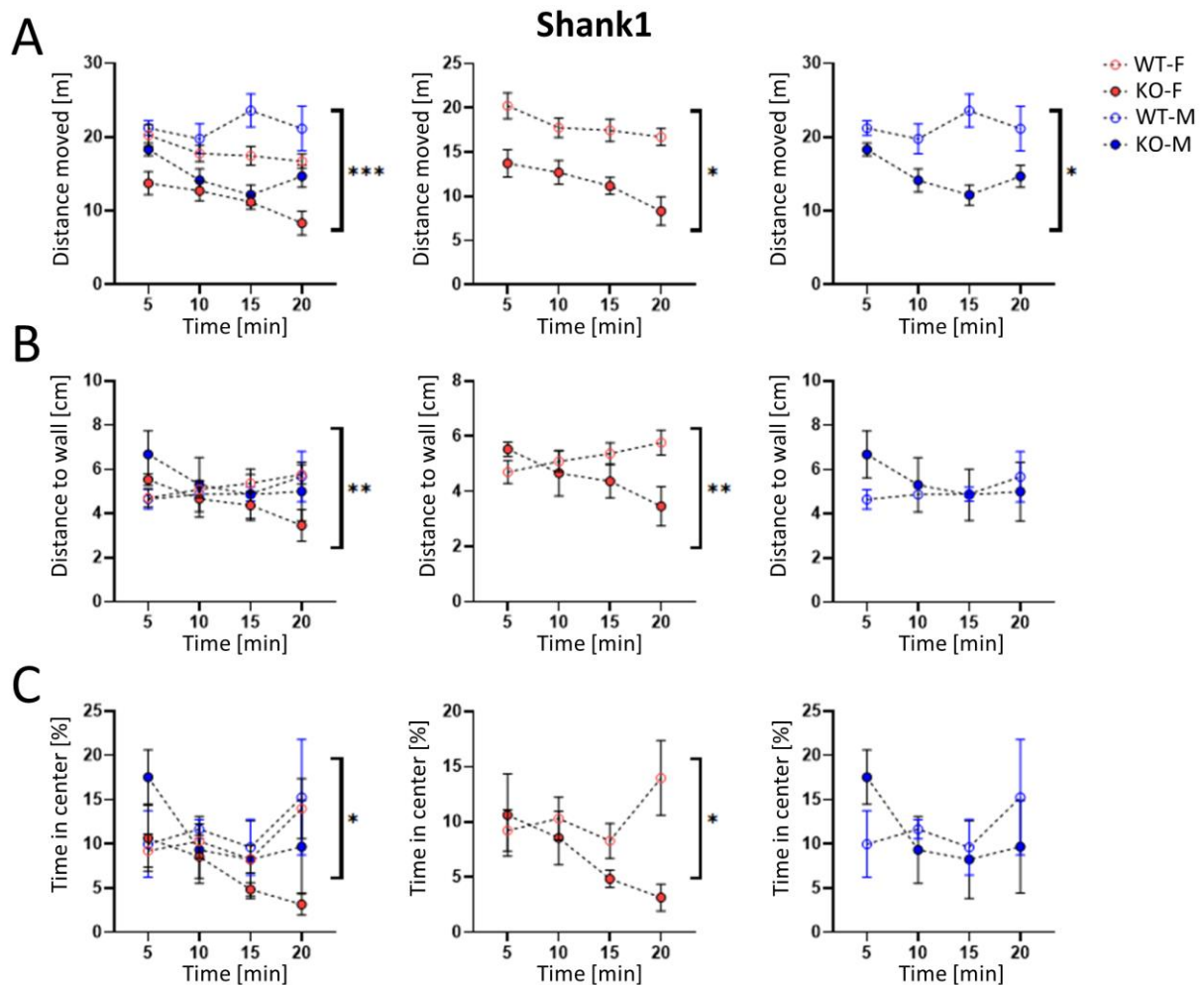


Figure 6: *Shank1* knockout induced altered locomotion behavior in the open field test. Locomotion of *Shank1*-KO mice and the WT littermates was measured in an established open field experimental set up to assess distance travelled (A), the distance to the wall of the field (B) and the time spent in the center of the testing area (C). The mean with standard deviation of each group at each time point is shown (left panels). Female (middle panels) and male cohorts (right panels) differed in their behavior. **(A)** *Shank1*-KO mice moved less distance compared to WT. **(B)** Female *Shank1*-KO mice (KO-F) showed a smaller distance to the field wall at 20 min. **(C)** KO-F mice spent significantly less time in the center. Statistical significance was calculated with two-way ANOVA, with genotype and sex as the two factors tested, followed by Sidak's multiple comparisons tests ($p \leq 0.05 = *$, $p \leq 0.01 = **$, $p \leq 0.001 = ***$).

With the *Shank3 $\alpha\beta$* -KO mice, a decrease in the travelled distance was also measured in the open field test. Compared to sex-matched littermate controls, male *Shank3 $\alpha\beta$* -KO mice travelled progressively less over time, whereas female *Shank3 $\alpha\beta$* -KO mice travelled consistently and significantly less at all four time points (Figure 7A). The other two parameters, distance to the wall and time in the center, were not altered by knockout of *Shank3 $\alpha\beta$* (Figure 7B-C). There was a tendency of female *Shank3 $\alpha\beta$* knockout mice to spend less time in the center of the field after 20 min although this difference did not reach statistical significance for the KO-F cohort (Figure 7C, middle panel)

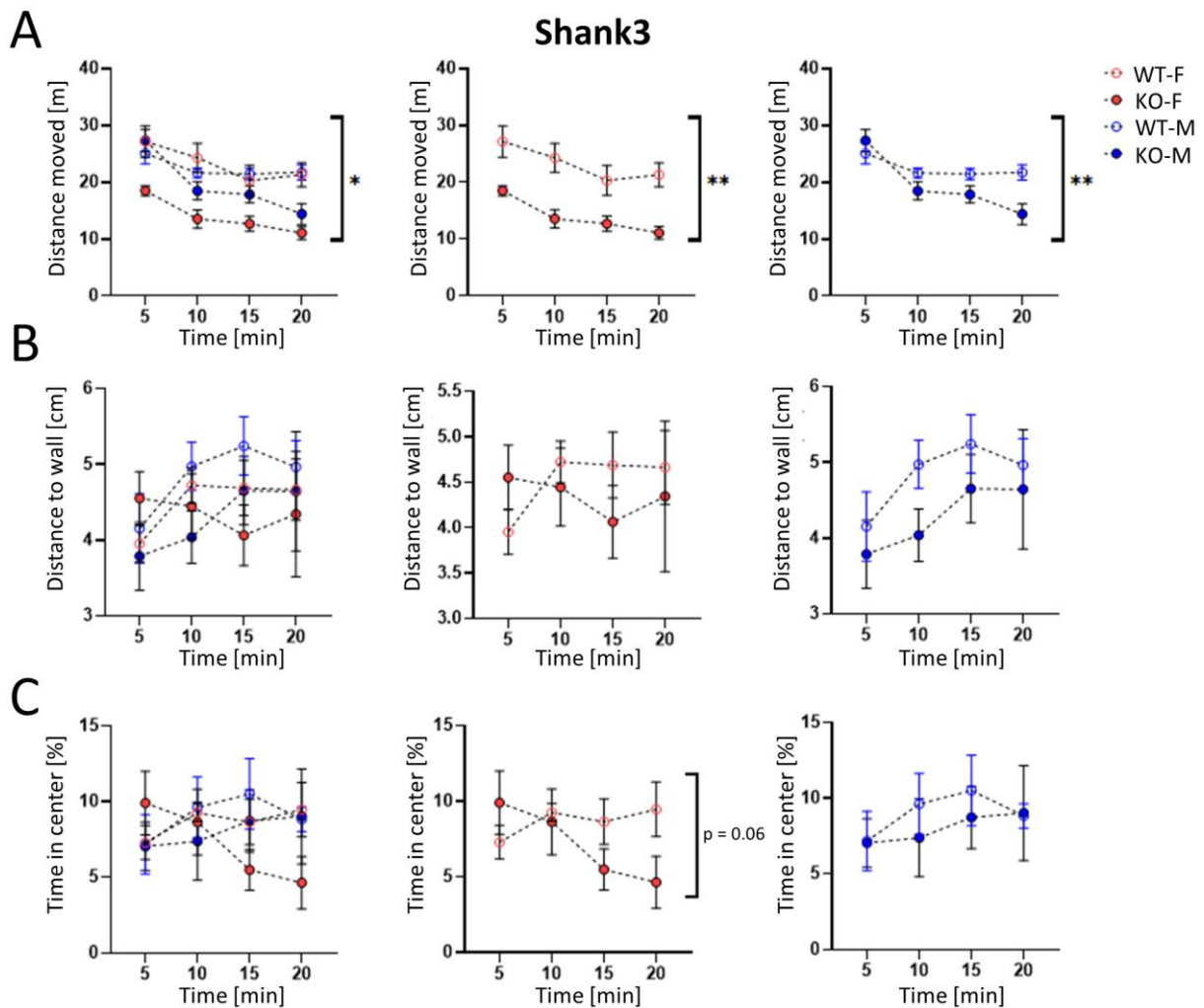


Figure 7: *Shank3αβ* knockout mice moved less during the open field test. Locomotor parameters of *Shank3αβ*-KO mice and littermate controls were quantified using an open field test. The distance travelled (A), the distance to the wall (B) and the time spent in the center (C) were determined. The mean and standard deviation of each group at each time point is shown (left panels). Female (middle panels) and male cohorts (right panels) are shown separately for each parameter. (A) *Shank3αβ*-KO mice moved less distance compared to WT. For males, the difference occurred after 20 min whereas females moved less distance at each time point measured. (B) No alterations in distance to the wall were observed. (C) The time spent in the center did not significantly change with *Shank3αβ* knockout. The KO-F mice displayed a tendency to spend less time in the center at 20 min. Statistical significance was calculated with two-way ANOVA followed by Sidak's tests ($p \leq 0.05 = *$, $p \leq 0.01 = **$).

Repetitive behavior is a core phenotype of ASD and increased grooming has been described for several *Shank* knockout mouse lines (Lord *et al.* 2000, Schmeisser *et al.* 2012, Sungur *et al.* 2014). Thus, self-grooming was assessed for both mouse models. Additionally, rearing was quantified to determine the exploration behavior of the mice. Evaluation of self-grooming, measured in seconds (s) spent grooming, demonstrated that knockout of *Shank1* and *Shank3αβ* increased self-grooming at 20 min. This repetitive behavior was more prominent in the female mice of the *Shank1*-KO line, whereas within the *Shank3αβ*-KO mouse model, males were affected more severely (Figure 8A). Due to high variability among each cohort analyzed, the measured alterations in behavior did not reach statistical significance. This result partially recapitulated observations published before, where the mouse lines used here were initially characterized and shown to exhibit increased duration of self-grooming, although no sex-dependent differences were described in these studies (Schmeisser *et al.* 2012, Sungur *et al.* 2014, Vicidomini *et al.* 2017). The rearing frequency of both *Shank*-KO lines was strikingly reduced, showing a decrease in explorative behavior (Figure 8B). Reduced rearing was described in the *Shank1* knockout mice before, but the effect of the specific knockout of *Shank3αβ* has not been measured so far (Sungur *et al.* 2014). Interestingly, enhanced rearing was observed in another *Shank3*

knockout mouse line lacking exon 9, indicating an isoform-specific effect of Shank proteins on exploration behavior (Lee *et al.* 2015).

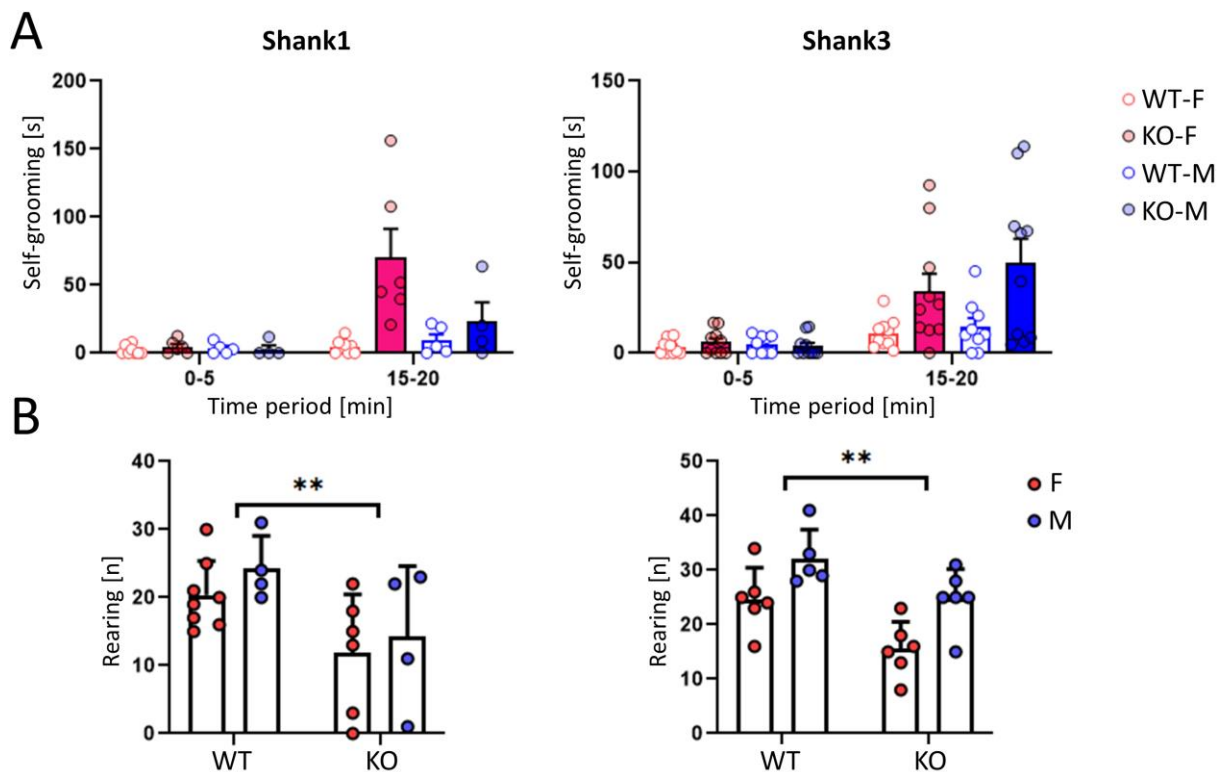


Figure 8: *Shank*-KO mouse models displayed altered self-grooming and rearing behavior. Video footage of the open field experiment with *Shank1*-KO (left panels) and *Shank3 $\alpha\beta$* -KO (right panels) mice was analyzed to evaluate self-grooming (A) and rearing (B). (A) Self-grooming was quantified as time spent for self-grooming during the first 5 min (0-5) and the last 5 min (15-20) of the open field test. Both mouse models showed a tendency towards increased duration of self-grooming during the second measuring period. (B) *Shank*-KO mice exhibited decreased rearing behavior, measured as frequency of rearing events. Male and female mice of both lines were affected to the same degree. Mean with standard deviation of each group is shown with statistical significance determined between WT and KO of male and female mice by two-way ANOVAs followed by Sidak's tests ($p \leq 0.01 = **$).

Importantly, *Shank1*-KO and *Shank3 $\alpha\beta$* -KO mice demonstrated features of an autistic phenotype at 12 weeks of age, as measured by locomotor activity, self-grooming, and rearing behavior. Therefore, all further analyses were performed with 12-week-old mice, and each mouse used for transcriptome and proteome analyses was previously analyzed in the open field assay. The cohorts of *Shank1*-KO and *Shank3 $\alpha\beta$* -KO mouse lines, whose results of the open field assay were presented here, were subsequently used for purification of postsynaptic density fractions and mass spectrometric analyses of the postsynaptic protein composition using a proteomics approach.

4.1.2. The Neuronal Transcriptome of *Lypd1*-bacTRAP-*Shank3 $\alpha\beta$* -KO Mice

The *Shank* knockout mouse lines were crossed with *Lypd1*-bacTRAP mice, which express a fusion protein of the 60S ribosomal protein L10a with EGFP under control of a neuron-specific promoter (*Lypd1*). The novel *Lypd1*-bacTRAPx*Shank1*-KO and *Lypd1*-bacTRAPx*Shank3 $\alpha\beta$* -KO mice enabled targeted immunoprecipitation of ribosomes from *Lypd1*-positive hippocampal neurons together with the actively translated mRNA (bacTRAP, see 3.2.4.7) (Heiman *et al.* 2014). Actively translated mRNA from the *Lypd1*-bacTRAPx*Shank3 $\alpha\beta$* -KO mice was sequenced and the transcriptome analyzed.

4.1.2.1. Validation of the ASD-typical Phenotype in *Lypd1-bacTRAP-Shank1-KO* and *Lypd1-bacTRAP-Shank3 $\alpha\beta$ -KO* Mice

The autistic phenotype of *Lypd1-bacTRAP-Shank1-KO* and *Lypd1-bacTRAP-Shank3 $\alpha\beta$ -KO* mice was examined at 12 weeks of age using the open field assay. In the translational approach, five biological replicates were analyzed with three mice of the *Lypd1-bacTRAP-Shank3 $\alpha\beta$* line per replicate. These mice were tested sequentially in small groups for their behavior due to the technical complexity of the following bacTRAP experiment. Several male *bacTRAP-Shank1-KO* mice had to be excluded from the open field test because they were kept in isolation, as aggressive behavior was observed between them and their littermates. Mice housed alone show altered behavior in the open field test, which would have biased the results. To compensate for the difficulties in the breeding strategy, female and male mice of the *Lypd1-bacTRAP-Shank3 $\alpha\beta$* line were combined in one cohort to measure the translational. Accordingly, the results of the open field test, which was performed before the bacTRAP assay, were also quantified in mixed cohorts. Both mouse models displayed decreased distance moved (Figure 9A). Unlike in the screening experiments, the *bacTRAP-Shank3 $\alpha\beta$ -KO* mice showed differences in the distance to wall and time in center parameters compared to their wildtype littermates. They exhibited less distance to the wall and spent less time in the center of the area, with increasing differences over the 20-minute period (Figure 9B-C). The duration of self-grooming was unaltered in *bacTRAP-Shank1-KO* mice, quantified as the sum of time spent self-grooming during the whole experiment (Figure 9D, left panel). Self-grooming behavior was increased in *bacTRAP-Shank3 $\alpha\beta$ -KO* mice, although this trend was not statistically significant when results of all separately measured groups were combined (Figure 9D, right panel). The same applied to the evaluation of rearing behavior, where both mouse models showed a tendency towards decreased exploration behavior (Figure 9E).

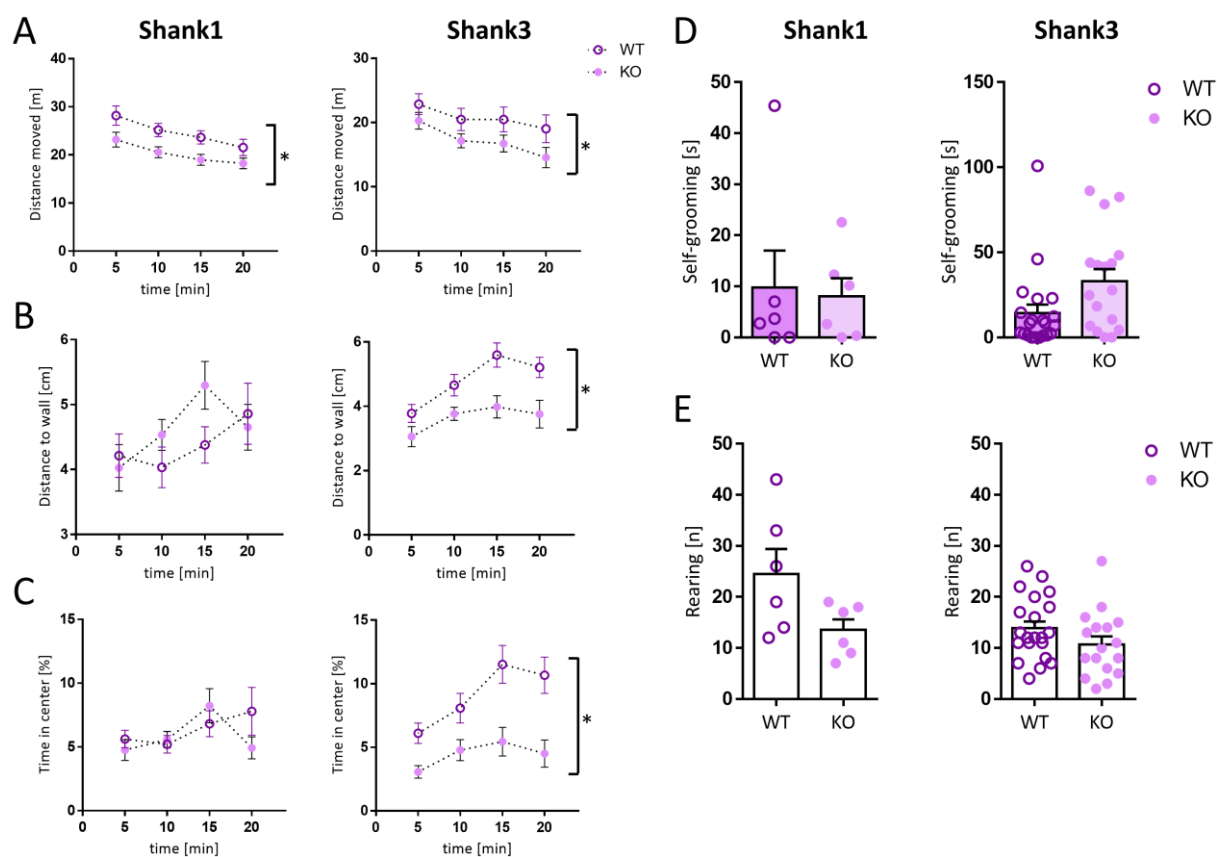


Figure 9: Validation of an autistic phenotype in the novel *Lypd1*-bacTRAP-*Shank1*-KO and *Lypd1*-bacTRAP-*Shank3 $\alpha\beta$* -KO mouse lines. Separate groups of mice were tested at 12 weeks of age in an open field test. Distance moved (A), distance to the wall (B), time in center (C), self-grooming (D) and rearing behavior (E) were analyzed. Shown is the mean with standard deviation. Two-tailed Student's t-tests revealed significant differences in several parameters tested. (A) In both mouse models, knockout mice moved less distance. (B) *Shank3 $\alpha\beta$* knockout resulted in reduced distance to the field wall. (C) *Shank3 $\alpha\beta$* -KO mice spent less time in the center of the area. (D) Assessment of self-grooming behavior demonstrated a trend toward increased self-grooming in the *Shank3 $\alpha\beta$* -KO mice. (E) Knockout mice of both lines exhibited a tendency to reduced rearing behavior ($p \leq 0.05 = *$).

4.1.2.2. Evaluation of Cell Specificity of GFP-tagged *Rpl10* Expression

Quantitative PCR was performed to ensure that the *Lypd1* promoter mediated a neuron-specific expression of GFP-tagged L10a, a protein of the large ribosomal subunit, and to check for the enrichment of GFP-L10a in bacTRAP immunoprecipitates. The hippocampi of three *Lypd1*-bacTRAP-*Shank1*-KO mice were combined to obtain sufficient RNA. Total RNA (input control, IC) and actively translated mRNA (IP) were purified and the relative amount of GFP and cell population-specific transcripts were measured in both fraction (Figure 10A) (see 3.2.4.7.1 and Table 41). The abundance of each transcript in the IP fraction (Figure 10A, green bars) relative to the IC fraction (Figure 10A, black bars) was calculated (Figure 10B). The transcript of the ubiquitously expressed TATA-box binding protein (*Tbp*) was used as a baseline of enrichment. Contrary to what was expected, transcripts comprising the promoter region of *Lypd1*, which controlled the expression of the GFP-L10a transgene, showed no enrichment in the IP fraction. Importantly, GFP-encoding transcripts were highly enriched in IP compared to total cell lysate and showed the highest amount of all detected transcripts when IP signals were normalized to IC signals. *Dsp*, a marker transcript of mature granule cells, which are highly abundant neurons in the hippocampus, exhibited slight enrichment in IP compared to IC, indicating that the neuronal cell population was targeted. The marker transcripts for oligodendrocytes (*Cnp*) and astrocytes (*Gfap*) showed a depletion, which confirmed that the non-neuronal cell populations were

not targeted. In conclusion, the *Lypd1*-bacTRAP mice and the bacTRAP method allowed for the purification of actively translated mRNAs specifically from neurons.

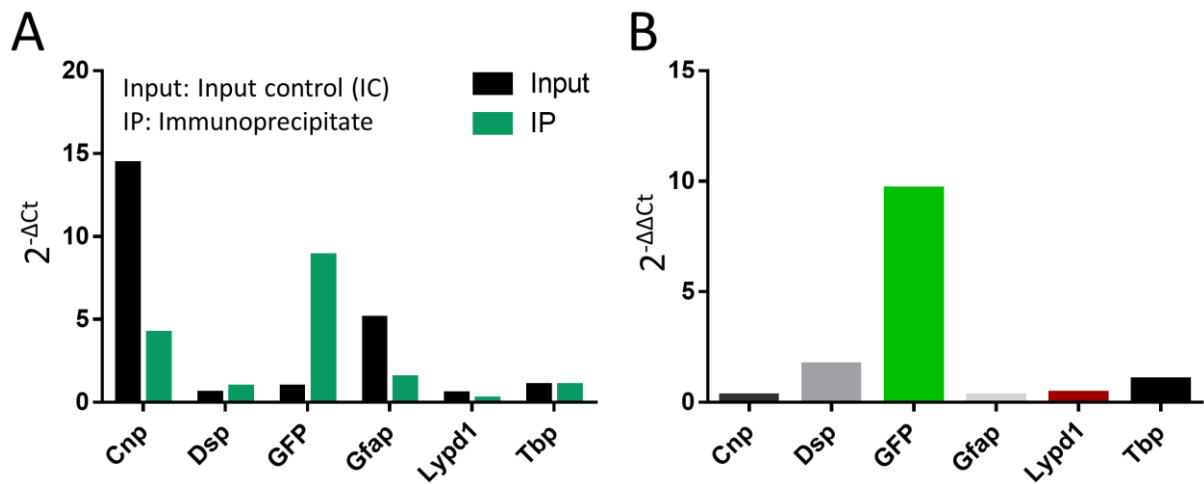


Figure 10: The qPCR detected enrichment of GFP and neuron-specific transcripts in bacTRAP IP samples. (A) IC and IP bacTRAP samples were analyzed for the relative abundance of cell type-specific transcripts. *Cnp*, *Dsp* and *Gfap* were analyzed as markers for oligodendrocytes, astrocytes, and neurons respectively. GFP-encoding transcripts were analyzed to verify the expression and precipitation of the GFP-tagged ribosomal protein L10a. A region of the *Lypd1* promoter was detected. *Tbp* was used as a ubiquitously expressed control. **(B)** The relative enrichment was calculated as transcript abundance in IP normalized to IC. GFP and *Dsp* showed higher relative enrichment compared to the *Tbp* control, while the abundance of the remaining transcripts was reduced. Tissue from three mice was combined and reverse transcriptase qPCR performed in technical triplicates. Shown is the mean of technical replicates. As no biological replicates were measured, no standard deviation was calculated.

4.1.2.3. A Translatomics Approach to Decipher the Consequence of *Shank3aβ* Knockout on Regulation of Translation

To decipher the neuronal translatoome of *Lypd1*-bacTRAPx*Shank3aβ* knockout mice, the transcribed (IC) and translated (IP) mRNAs were analyzed using Next Generation Sequencing. Bioinformatics analyses were conducted by Dr. Dr. Jan Broder Engler (see 3.2.5.1). Similarities between IC and IP samples of five biological replicates were assessed by principal component analysis (PCA). The samples exhibited rather high variability, shown as widely scattered data points in the PCA (Figure 11). IC samples from WT and KO mice formed a subpopulation that was separated from the more widely dispersed IP samples. The sample types (IC and IP) were grouped together but the KO and WT condition had less influence. Thus, the total expressed RNA measured in IC, was vastly different from the actively translated mRNA coprecipitated with GFP-L10a-containing ribosomes during the bacTRAP method. This indicated that the transcribed mRNAs (IC) were more similar between samples compared to translated mRNAs (IP), which showed greater variability. Notably, three KO-IP samples clustered together closely, visualizing high resemblances between these biological replicates (Figure 11).

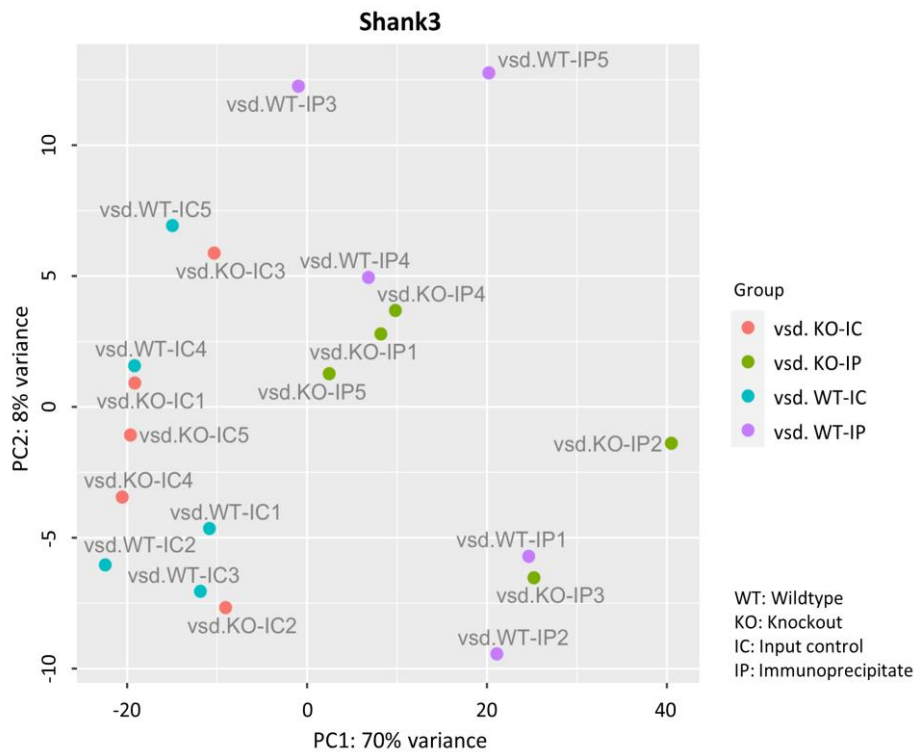


Figure 11: Analysis of similarity based on RNA sequencing. BacTRAP samples were prepared from *Lypd1*-bacTRAPx *Shank3αβ*KO mice and WT littermates. RNA purified from ICs and IPs was sequenced. The PCA illustrates the similarities between five biological replicates (n = 5). IC and IP samples formed separate subpopulation.

Differentially translated mRNAs, purified from bacTRAP IP samples, were identified using differential gene expression analysis. The actively translated mRNAs from KO-IP were compared to those originated from the WT-IP. P-values and fold changes of all detected mRNAs were $-\log_{10}$ and \log_2 transformed and visualized in a volcano plot (Figure 12). Statistical significance of altered translation was determined by having an adjusted p-value, also termed false discovery rate, of ≤ 0.1 and a fold change of > 0.5 of the given transcript. Significantly less (blue) or more (red) translated mRNAs in the KO conditions were highlighted by their gene symbols. Analysis of the hippocampal neurons of *Shank3αβ*-KO mice detected 26 differentially translated mRNAs, of which nine were less translated and 17 were more translated (Figure 12). Table 49 in the appendix lists all differentially translated mRNAs (see 7.2).

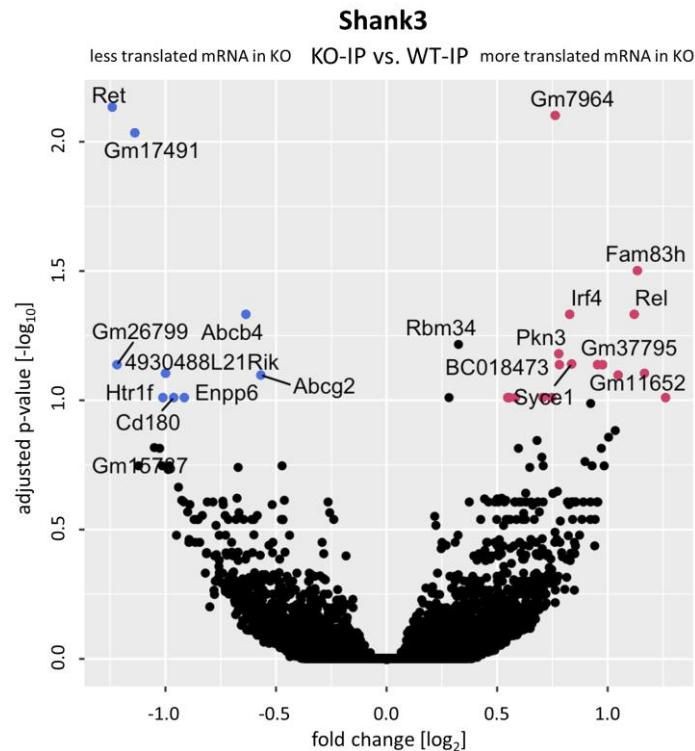


Figure 12: Differentially translated mRNAs in hippocampal neurons of *Shank3αβ*-KO mice. Differential gene expression analysis was performed using DESeq2. Significance was defined by an adjusted p-value ≤ 0.1 and a fold change of > 0.5 , plotted as $-\log_{10}$ and \log_2 transformed values. Significantly less translated mRNAs are shown in blue and more translated mRNAs are shown in red. The mRNAs of both categories are highlighted by their gene symbols. 26 mRNAs were differentially translated under loss of *Shank3αβ* of which nine were less and 17 were more translated compared to the WT control. A detailed list of all deregulated mRNAs is shown in Table 49.

To further analyze the differentially translated neuronal mRNAs in hippocampi of *Lypd1*-bacTRAPx*Shank3αβ*-KO mice, 12 deregulated transcripts were selected and their expression values visualized in detail. Expression values of KO and WT condition were shown to compare overall expression of a given mRNA, which was measured in the IC, to the translational state of the mRNA that was sampled in the IP (Figure 13). The *Shank3*-encoding mRNA showed highest expression and translation among the differentially expressed transcripts across all conditions (Figure 13). The residual expression and translation of 40% in KO compared to WT was in keeping with the notion of the specific knockout of *Shank3αβ* isoforms. The *Abcb4* mRNA stood out as second highest expressed and translated transcript. Several unannotated mRNAs, indicated by Gm accession numbers, were detected in ICs as well as IPs. Although the observed association of these transcripts to ribosomes suggests they are protein-coding, it is unknown if these RNAs indeed encode functional proteins. The three mRNAs *Irf4*, *Pkn3* and *Syce1* were evenly expressed between KO and WT condition, shown by comparable expression values in KO-IC and WT-IC. Interestingly, these transcripts were absent in the WT-IP, thus not translated, but were detected in the KO-IP, showing exclusive translation as result of *Shank3αβ* loss. The transcript whose translation was most decreased by *Shank3αβ* knockout was the mRNA encoding the receptor tyrosine kinase *Ret*. One of the transcripts that showed enhanced translation following *Shank3αβ* knockout was the transcript coding for *Rel*, a component of NF-κB signaling pathways (Figure 12B and Figure 13).

Shank3

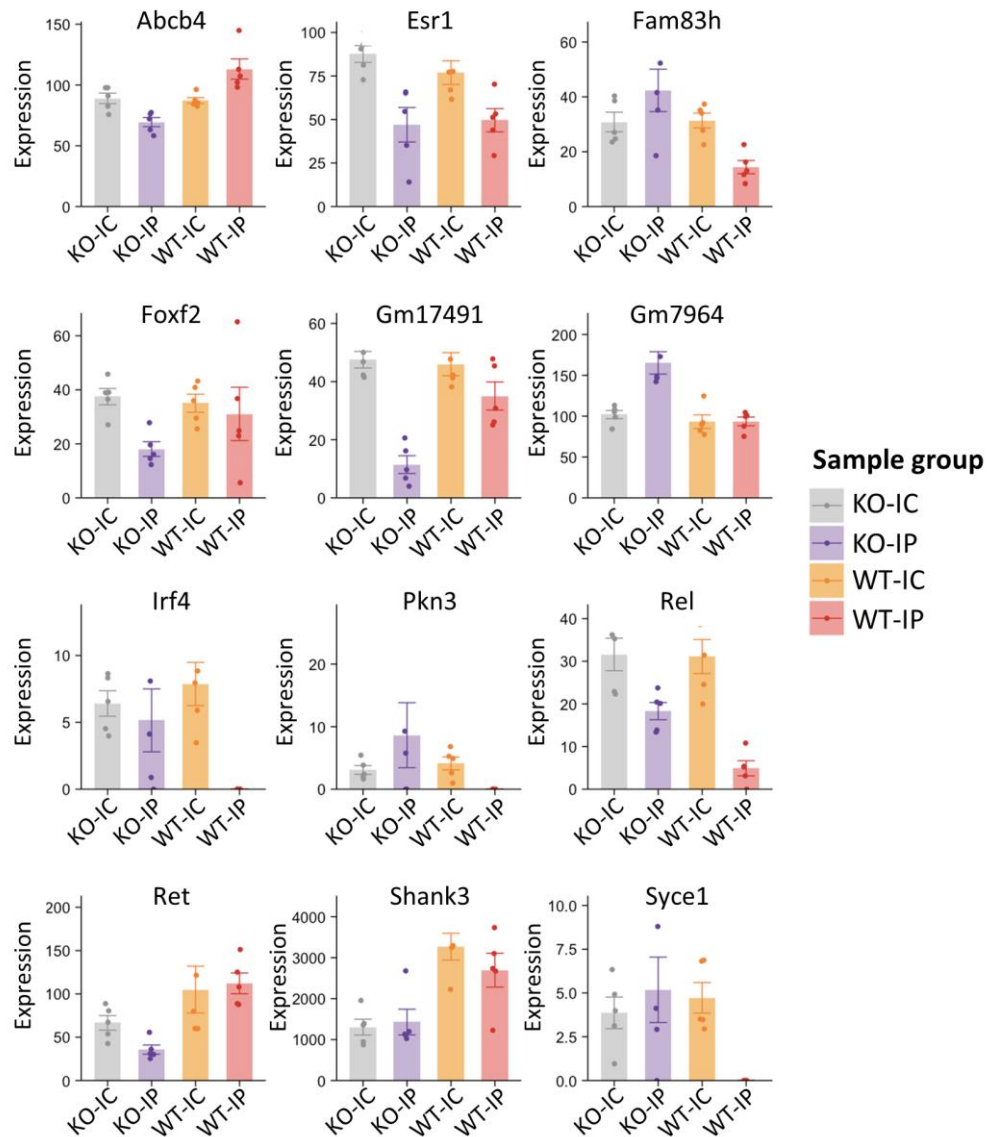


Figure 13: Expression and translation of selected mRNAs from hippocampal neurons of *Shank3 $\alpha\beta$* -KO mice. Expression values, determined with RNA-seq, of a subset of mRNAs in IC and IP samples generated with the bacTRAP method. Expression (IC) and active translation (IP) of transcripts were compared between *Shank3 $\alpha\beta$* -KO mice and WT littermates. The mean with standard deviation of five biological replicates is shown (n = 5). Gm accession numbers annotate transcripts, for which it is unknown whether they encode functional proteins.

In conclusion, I showed by applying translomics that absence of the N-terminal domains of Shank3 resulted in mild alterations in translation of a distinct subset of neuronal mRNAs, which might hint towards an involvement of Shank3 in translational regulation.

Gene ontology analyses were performed for all differentially translated mRNAs from the comparison of KO-IP with WT-IP to determine biological processes to which the deregulated transcripts are known to contribute. The 20 most affected biological processes were visualized. The highest enriched biological process was “nucleosome organization”. Among the 20 most enriched terms, five biological processes were directly connected to mRNA splicing. Furthermore, several biological processes of RNA processing of different types of RNA were enriched, among these rRNA processing, ncRNA processing, mRNA processing and RNA modification. The most severely decreased term was “sphingolipid metabolic process”. Especially interesting in the context of neurodevelopmental disorders was the

result that the terms “axon ensheathment”, “ensheathment of neurons”, “myelination” and “axon guidance” were decreased. This hints towards a connectivity of the Shank3-associated pathomechanism underlying ASD to malfunction in neuron ensheathment and projection during brain development. The decreased biological processes “associative learning” and “learning” stood out as learning deficits are a core symptom in ASD patients.

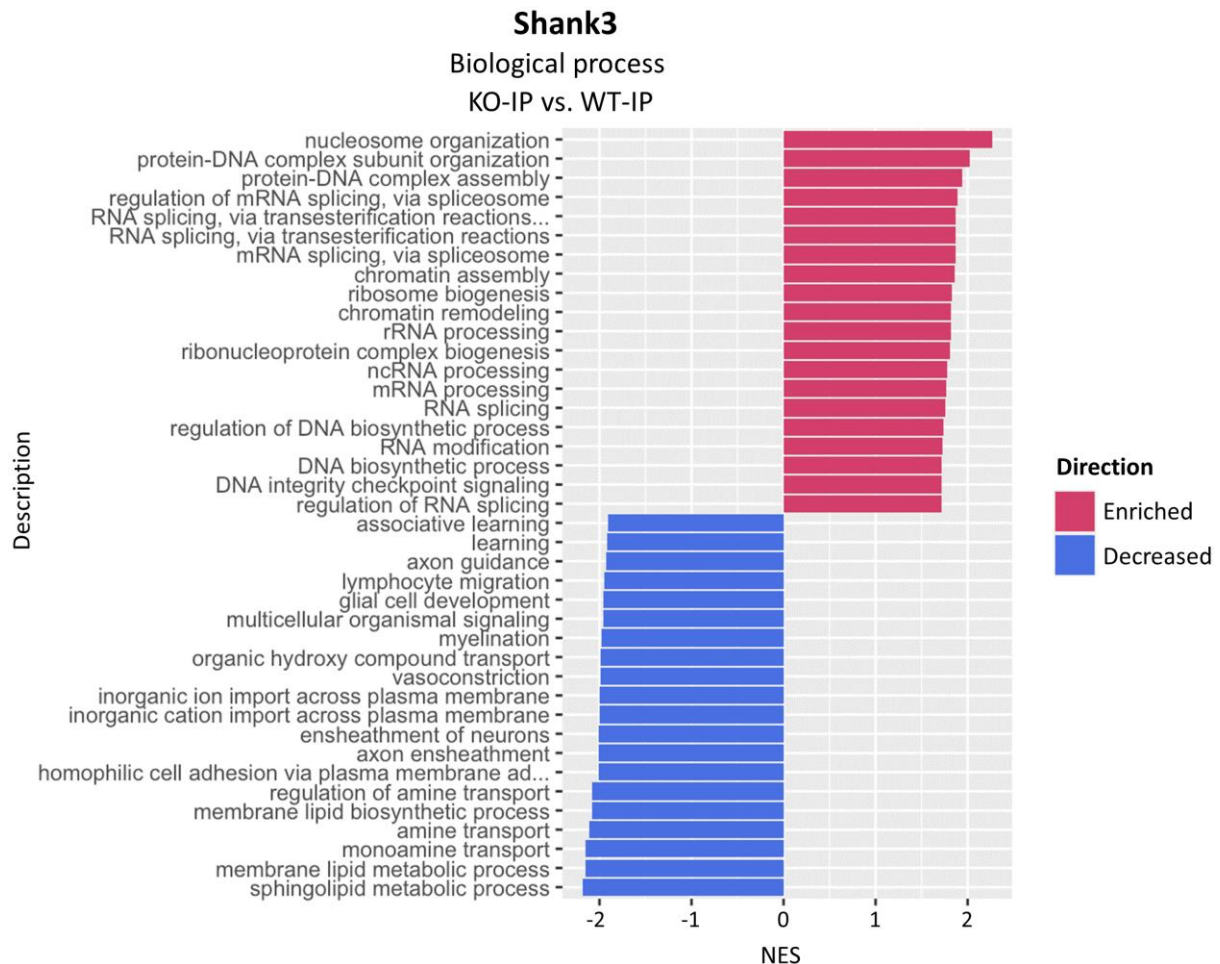


Figure 14: GO analysis of biological processes altered by differentially translated mRNAs in hippocampal neurons of *Shank3αβ*-KO mice. Statistical significance of altered translation was appointed by a p-value ≤ 0.1 and a fold change of > 0.5 . All differentially translated mRNAs found in the KO-IP to WT-IP comparison were submitted to a GO analysis for biological processes. The normalized enrichment scores (NES) of the 20 most enriched (red) and decreased (blue) terms are shown.

4.1.3. The Proteome of the Postsynaptic Density in *Shank1*-KO and *Shank3αβ*-KO Mice
Shank proteins act as scaffolds of the postsynapse by interacting with various proteins to form a network that connects glutamate receptors to the F-actin cytoskeleton (Boeckers *et al.* 1999, Sheng and Kim 2000, Kreienkamp 2008). The effect of *Shank1* or *Shank3αβ* knockout on the composition of proteins in the postsynaptic density was analyzed with a proteomics approach. The aim was to determine the consequences of loss of Shank1 or the long isoforms of Shank3 on postsynaptic signaling pathways and to compare those to the effects that *Shank3αβ* knockout has on translation. Furthermore, I wanted to answer the question of whether the pathomechanisms underlying *SHANK1* and *SHANK3* mutations in ASD patients differ on a molecular level or if they converge in common signaling pathways.

4.1.3.1. Validation of Efficiency and Specificity of the Postsynaptic Density Purification

Postsynaptic density fractions were prepared from hippocampal tissue of *Shank1* and *Shank3αβ* knockout mouse lines (see 3.2.4.6). To validate the efficiency and specificity of PSD purification,

samples were taken at different fractionation steps and analyzed in comparison to the PSD fractions in western blot analyses (see 3.2.3.3). PSD-95 was detected as a postsynaptic marker and tubulin as reference control. Shank proteins were detected via an antibody directed at Shank PDZ domains, which are very similar across the Shank proteins. By quantifying band intensities in the immunoblots, relative protein abundances were determined and compared between the postnuclear fraction (P1), the membrane fraction (P2) and the postsynaptic density fraction (P3) across WT and KO conditions (Figure 15). A progressive enrichment of PSD-95 and Shank proteins from P1 to P3 was observed in all conditions (Figure 15C, G and K), most strongly in *Shank3αβ*-KO samples (Figure 15I and K). The number of detected bands of Shank proteins was decreased in both KO conditions compared to WT. The pattern of bands detected with the Shank antibody varied in the intensity of bands of different sizes. In WT P3, larger Shank3 isoforms were detected with higher intensity (Figure 15A, 250 kDa), whereas the *Shank3αβ* knockout resulted in depletion of these band sizes. Here, the band of highest intensity corresponded to shorter isoforms of Shank3 (Figure 15I, 130 kDa). In conclusion, the specific enrichment of postsynaptic proteins by PSD purification was verified and the knockout of *Shank1* and *Shank3αβ* was indicated.

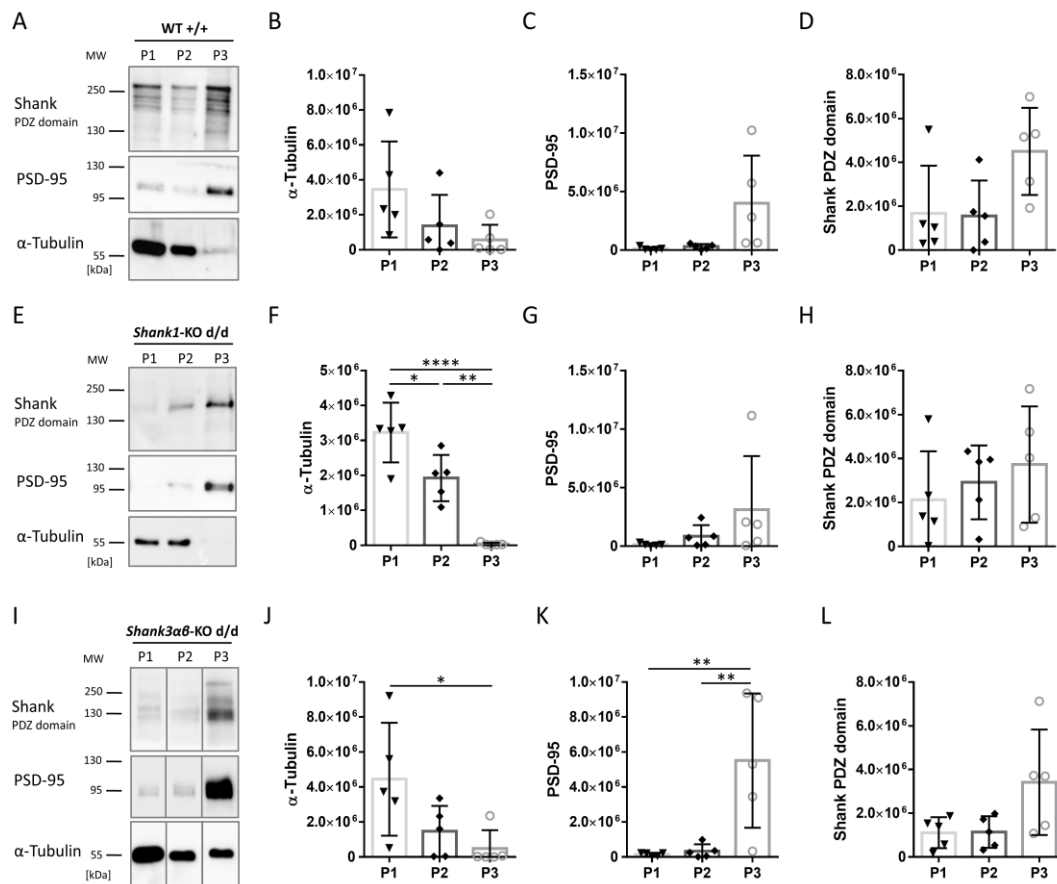


Figure 15: Validation of PSD purification from hippocampal tissue of two ASD mouse models. PSD fractions were prepared from hippocampi of *Shank1*-KO (E), *Shank3αβ*-KO (I) mice, and WT littermates. (A) Samples of the postnuclear fraction (P1), the membrane fraction (P2) and the PSD fraction (P3) were prepared. Shank, PSD-95 and tubulin were detected via immunoblot (A, E and I). Band intensities were quantified (B-D, F-H, J-L). The postsynaptic marker PSD-95 and Shank proteins were enriched from P1 to P3 fractions (C-D, G-H, K-L), whereas tubulin decreased during PSD purification (B, F, J). A reduction of band intensities was detected by the Shank PDZ domain antibody, indicating specific reduction of Shank proteins. The mean with standard deviation was calculated and statistical significance determined by one-way ANOVA followed by Tukey's test ($p \leq 0.05 = *$, $p \leq 0.01 = **$, $p \leq 0.0001 = ****$). Tissues of five mice were pooled for one biological replicate ($n = 5$).

4.1.3.2. Evaluation of the Effect of Shank1 and Shank $\alpha\beta$ Knockout on Shank and CaMKII Protein Abundance

The Shank protein levels were determined to validate the *Shank1* and *Shank $\alpha\beta$* knockout in ASD mouse models, which were previously tested for their autistic behavior in the open field assay (see 4.1.1). LC-MS/MS mass spectrometric measurement of the PSD proteome was performed by Hannah Voß. Protein quantification was based solely on unique peptides, as previous results had shown high homology for deregulated candidate proteins in the PSD. A total of 5176 proteins were quantified. Proteins found at least twice in at least two of the compared conditions were included in further statistical analysis. To validate the *Shank* knockout, the relative protein abundances of Shank1 and Shank3 were compared to the abundance of all other detected proteins. In addition, the abundance of the CaMKII was determined due to its interaction with the N-terminus of Shank3 and because of its involvement in several synaptic signaling cascades (Lisman *et al.* 2012, Hell 2014, Cai *et al.* 2021). Heterozygous littermates were included in this analysis to determine the dose dependency of the *Shank* knockouts on Shank protein levels. In both analysis, one KO sample was excluded due to low protein concentration. A complete loss of Shank1 protein (Figure 16A, blue) was detected in all KO samples, whereas the abundance of Shank3 (Figure 16A, green) and CaMKII (Figure 16A, orange) were unchanged. Surprisingly, no difference in relative Shank1 abundance was determined for the HZ mice compared to WT littermates (Figure 16A). The reduction in relative protein abundance of Shank3 was not as severe, consistent with the notion of an isoform-specific knockout of only the Shank3 isoforms comprising the N-terminal domains. Again, relative abundance Shank1 and CaMKII were not affected (Figure 16B).

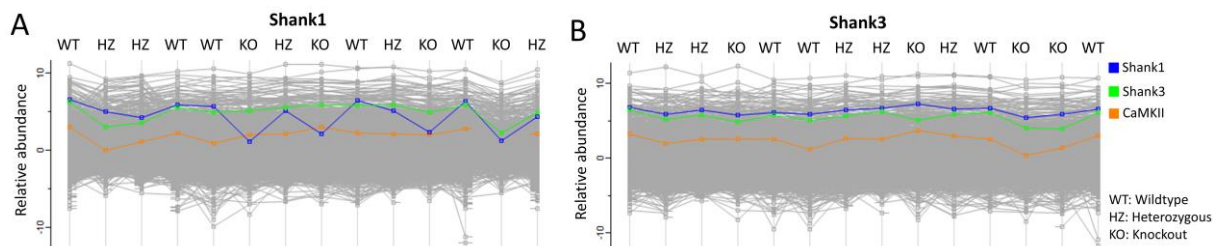


Figure 16: Relative protein abundances of Shank1, Shank3 and CaMKII in postsynaptic density fractions of two ASD mouse models. Postsynaptic density purification was performed using hippocampal tissue from *Shank1*-KO and *Shank3 $\alpha\beta$* -KO mice. WT and HZ littermates were used as controls. Two KO samples had to be excluded from the analyses due to low protein concentration, resulting in four biological repeats for both KO conditions. The relative abundance of Shank1 (blue), Shank3 (green) and CaMKII (orange) was compared to all quantified proteins (grey lines) in PSDs of the two mouse models. **(A)** *Shank1*-KO resulted in a complete loss of Shank1 protein in the PSD of KO mice without affecting the relative abundances Shank3 and CaMKII. HZ and WT mice showed no significant reduction of Shank1 protein. **(B)** *Shank3 $\alpha\beta$* -KO induced a modest reduction of Shank3 protein only in the KO mice, but not in WT and HZ mice. Shank1 and CaMKII protein levels were unchanged across conditions.

Following the detection of a moderately reduced Shank3 protein abundance in *Shank3 $\alpha\beta$* -KO PSD fractions, the specific loss of Shank3 isoforms α and β was quantified. Forebrain PSD fractions of three mice of the *Shank3* knockout line were purified and analyzed in comparison to the five WT littermates. Deletion of exon 11 in the *Shank3* gene was predicted to knockout the expression of Shank3 isoforms containing the SPN, ANK and SH3 domains (Schmeisser *et al.* 2012). To test this, four peptides scattered over the different domains of the Shank3 protein were chosen (Figure 17A) and their relative abundance compared between KO and WT (Figure 17B). The first two peptides from the SPN domain (aa 26-36; green) and from the SH3 domain (aa 433-460; yellow) were absent in KO mice (Figure 17B). In contrast, two peptides quantified which originated from the proline-rich region were only reduced in KO mice to a residual abundance of 10-20% compared to WT (aa 1165-1174 and aa 1535-1540; grey). Looking at all quantified peptides, abundance was reduced in the KO mice along the PDZ domain sequence. From the amino acid position 683 to the C-terminus, no further reduction in Shank3 peptide abundances was detected (Figure 17). The mass spectrometric analysis demonstrated, that Shank3

isoforms containing SPN to SH3 domains were absent in the mouse model and showed that the knockout is indeed isoform-specific.

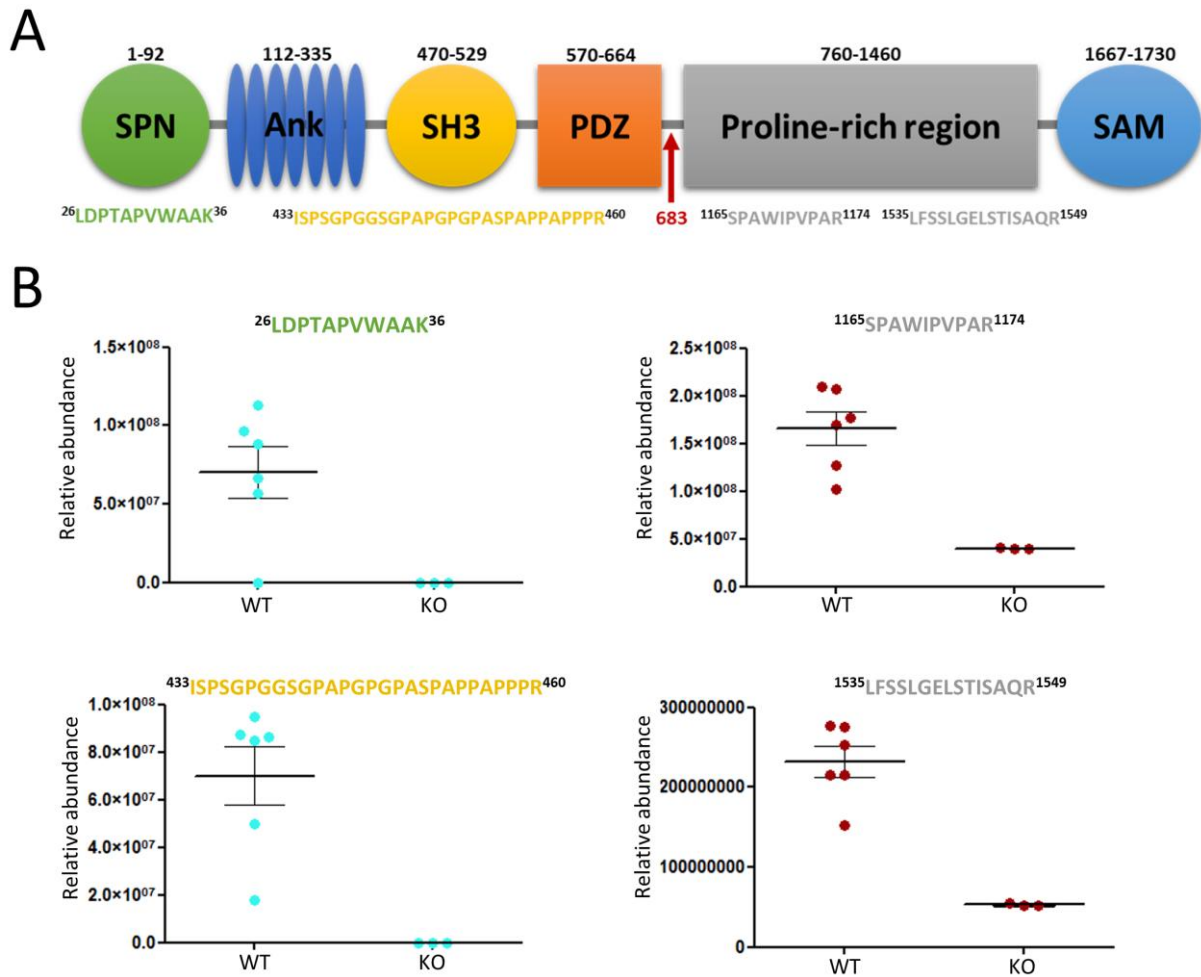


Figure 17: Analysis of peptides derived from different Shank3 domains. PSD fractions from forebrains of three *Shank3 $\alpha\beta$* -KO and six WT littermates were purified and analyzed by mass spectrometry. **(A)** Four peptides scattered across the domains of Shank3 were quantified separately to gain insight into the expression of Shank3 isoforms. The first peptide analyzed originated from the SPN domain (aa 26-36, green) and the second from the SH3 domain (aa 433-460, yellow). The third and fourth peptides were assigned to the proline-rich region (aa 1165-1174 and aa 1535-1540, grey). **(B)** Quantification of domain-specific peptides demonstrated the absence of peptides from the SPN and SH3 domains in the KO condition, while relative abundance of peptides from the proline-rich region was reduced to 10-20% compared with WT controls.

4.1.3.3. Knockout of *Shank1* and *Shank3 $\alpha\beta$* Alters the Postsynaptic Proteome

Linear PCA was applied to identify similarities and differences between PSD fractions of *Shank* knockout mice, evaluated in terms of purification specificity (see 4.1.3.1) and knockout efficiency (see 4.1.3.2). PCA was calculated using all significantly deregulated proteins based on a p-value of $p \leq 0.05$ determined by ANOVA between PSD fractions from KO mice (Figure 18, red) and their HZ (Figure 18, green) and WT littermates (Figure 18, blue). PSD samples from WT mice of both mouse lines clustered together closely, demonstrating high similarity among WT-PSDs among biological replicates. HZ- and KO-PSDs were more dispersed, indicating that postsynaptic protein composition was more variable due to heterozygous or homozygous knockout of *Shank1* or *Shank3* (Figure 18A-B). Interestingly, the data points of *Shank1*-HZ and -KO partially overlapped, suggesting some resemblance between them but not with the WT condition. Nevertheless, it should be emphasized that KO-PSDs clustered together relatively closely, while HZ-PSDs were more scattered (Figure 18A). This indicates that heterozygous knockout of *Shank1* lead to variable changes in PSD protein composition, whereas the homozygous knockout resulted in more uniform effects on postsynaptic protein abundances. The PCA of the *Shank3*

mice illustrated that the HZ-PSDs exhibited greater similarities to each other than the KO-PSDs (Figure 18B). In contrast to the Shank1 conditions, HZ and KO samples of the Shank3 line were more strongly separated from each other and did not overlap. This may indicate a stronger dose dependency of the effects of the Shank3 proteins on postsynaptic protein abundance compared with Shank1.

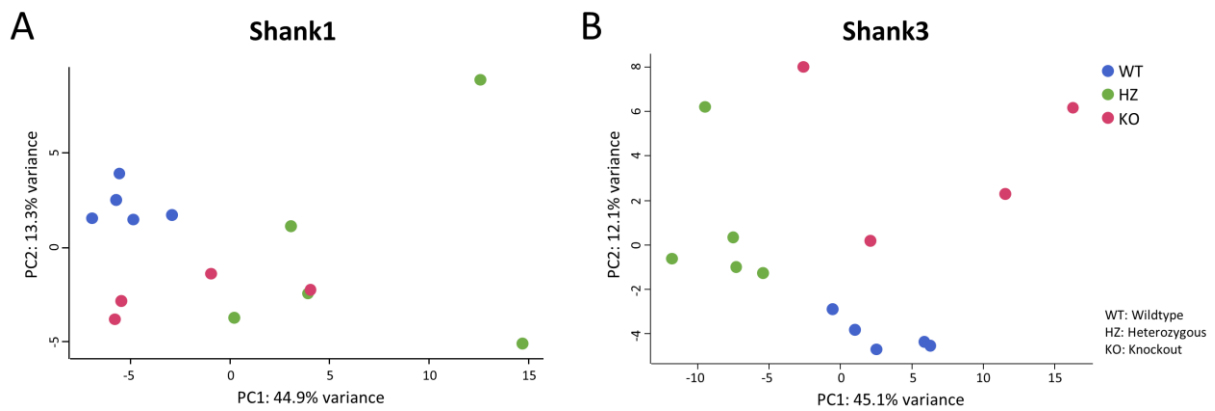


Figure 18: Analysis of the similarity of PSD fractions based on mass spectrometry. Linear PCA determined similarity of postsynaptic protein composition in PSD samples purified from *Shank1*-KO and *Shank3αβ*-KO mice compared to HZ and WT littermates. WT-PSDs clustered together. **(A)** Abundance of 56 proteins was significantly altered among PSD fractions of *Shank1*-KO, HZ and WT mice (ANOVA, $p \leq 0.05$). KO and HZ samples partially overlapped. HZ-PSDs scattered more compared to KO-PSDs. **(B)** In the PSD of the *Shank3αβ* line, 116 proteins were significantly deregulated between KO, HZ and WT conditions (ANOVA, $p \leq 0.05$). All three conditions formed separated subpopulations with most variability in the KO-PSDs.

Differentially abundant postsynaptic proteins between *Shank*-KO and WT were identified. Proteins with a p -value ≤ 0.05 and a fold change > 1.5 , represented as \log_{10} and $-\log_2$ transformations, were considered as significantly deregulated and the results were visualized in volcano plots (Figure 19). In the Shank1 analysis, 46 deregulated proteins were detected. Of these, 18 were decreased and 28 increased in abundance (Figure 19A). All differentially abundant proteins of *Shank1*-KO PSDs are listed in Table 50 in the appendix. Shank1 was most severely depleted, again demonstrating a complete knockout. Interestingly, the Actin-related protein 2/3 complex subunit 5 (*Arcp5*) was decreased. Since *Arcp5* is a subunit of the Arp2/3 complex, which generates branched actin networks through actin nucleation (Welch *et al.* 1997, Volkman *et al.* 2001), this result connects Shank1 to the regulation of actin dynamics. Comparison of KO- and WT-PSDs from the *Shank3αβ* line identified 67 significantly altered proteins (Figure 19B), listed in Table 51 in the appendix. Thus, *Shank3αβ* knockout resulted in stronger alterations of the PSD proteome compared to *Shank1* knockout. In the Shank3 analysis, 28 proteins were enriched and 39 decreased (Figure 19B). One of the reduced candidates was the Eukaryotic translation initiation factor 2A (*Eif2a*) that is directly connected to the regulation of translation. In both analyses, approximately 40% of deregulated proteins showed reduced postsynaptic abundance, whereas 60% were enriched (Shank1: 39.1% to 60.9%; Shank3: 41.8% to 58.2%). Remarkably, seven deregulated proteins overlapped between both analyses. The shared decreased candidates were *Rgs7bp* and *Gnb5*. The five proteins *L1cam*, *Prxl2a*, *Vps4a*, *Eno3* and *Rabep1* were enriched in both KO groups (see Table 50 and Table 51). Two candidates among the shared deregulated proteins were linked to G-protein-mediated signaling: the Rab GTPase-binding effector protein 1 (*Rabep1*) and the Regulator of G-protein signaling 7-binding protein (*Rgs7bp*). In summary, postsynaptic protein composition was altered in both mouse models. The *Shank3αβ* knockout resulted in more differentially abundant proteins compared to *Shank1*. The proteomics analysis indicated major Shank-specific effects on the postsynaptic proteome and moderate shared alterations.

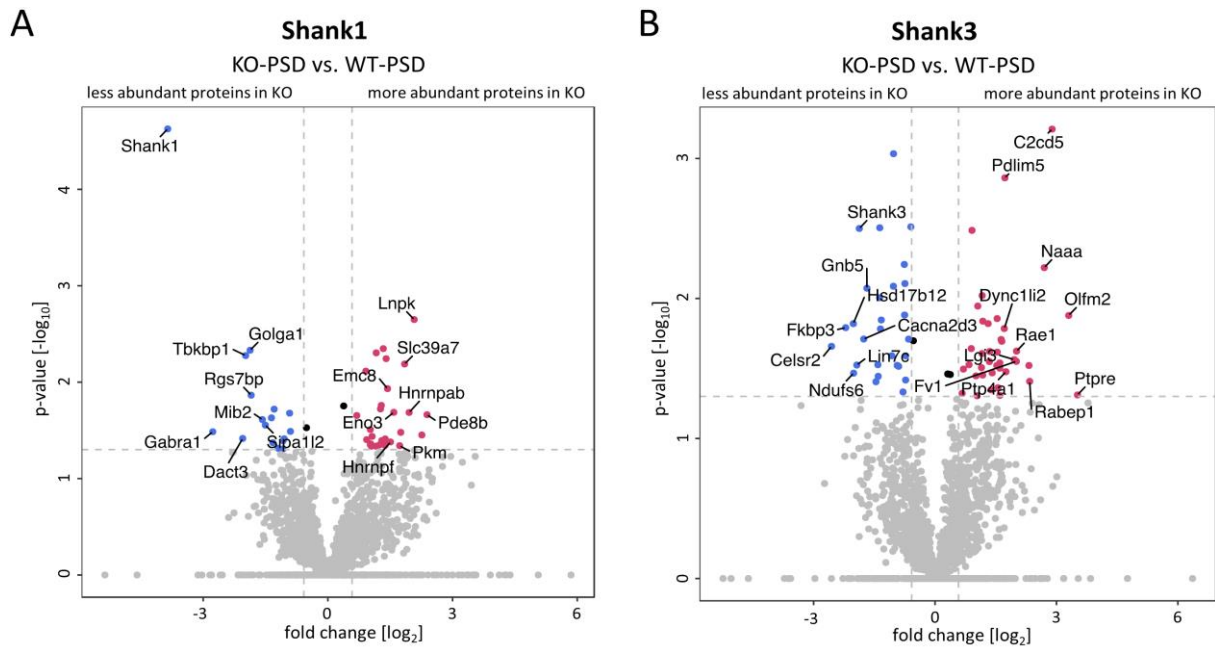


Figure 19: Differentially abundant proteins in PSD fractions of *Shank1*-KO and *Shank3αβ*-KO mice. Volcano plot visualization of two-sided, pairwise Student’s t-test results, comparing KO-PSD to WT. Proteins identified with a p-value ≤ 0.05 and a FC > 1.5 were considered significantly changed. Strongly altered proteins are highlighted by their gene symbol. **(A)** Comparison of the PSD proteome of the Shank1 mouse model determined 46 deregulated proteins of which 18 were decreased and 28 increased in abundance. **(B)** 67 deregulated proteins were quantified in the *Shank3* proteome analysis. 28 proteins were decreased and 39 enriched in KO-PSDs compared to WT.

To identify deregulated signaling pathways caused by an altered postsynaptic protein network, gene ontology (GO) analyses were performed using EnrichR (Chen *et al.* 2013, Kuleshov *et al.* 2016, Xie *et al.* 2021). Dependent on their known involvement in the corresponding biological processes (BPs), the contribution of all differentially abundant proteins from the PSD proteomic analyses to GO terms was determined. The 20 most affected BPs were visualized separately for Shank1 and Shank3 (Figure 20 and Figure 21). The highest enriched biological processes in PSD fractions of *Shank1*-KO mice were “negative regulation of tubulin acetylation” and “regulation of tubulin deacetylation”. BPs that were strongly downregulated included the regulation of (ion) transmembrane transport, to which the decrease in *Kcnj4* and *Nedd4* proteins contributed. The reduced abundance of *Arpc5* resulted in downregulation of Arp2/3 Complex-Mediated Actin Nucleation, according to the decreased combined score of the GO BP term (Figure 20). The deregulated processes in *Shank1*-KO and *Shank3αβ*-KO were compared. Five enriched biological processes overlapped between both analyses: carbohydrate catabolic process, glycolytic process, glycolytic process through glucose-6-phosphate, glucose catabolic process to pyruvate, and canonical glycolysis (Figure 20 and Figure 21). Enrichment of three proteins in each analysis contributed to these BP terms. Interestingly, *Eno3* was shared between both but the remaining two were Shank-specific. The proteins *Pkm* and *Eno1* were found to be increased in the Shank1 analysis, whereas enrichment of *Pfkl* and *Tpi1* contributed to the terms in the Shank3 analysis.

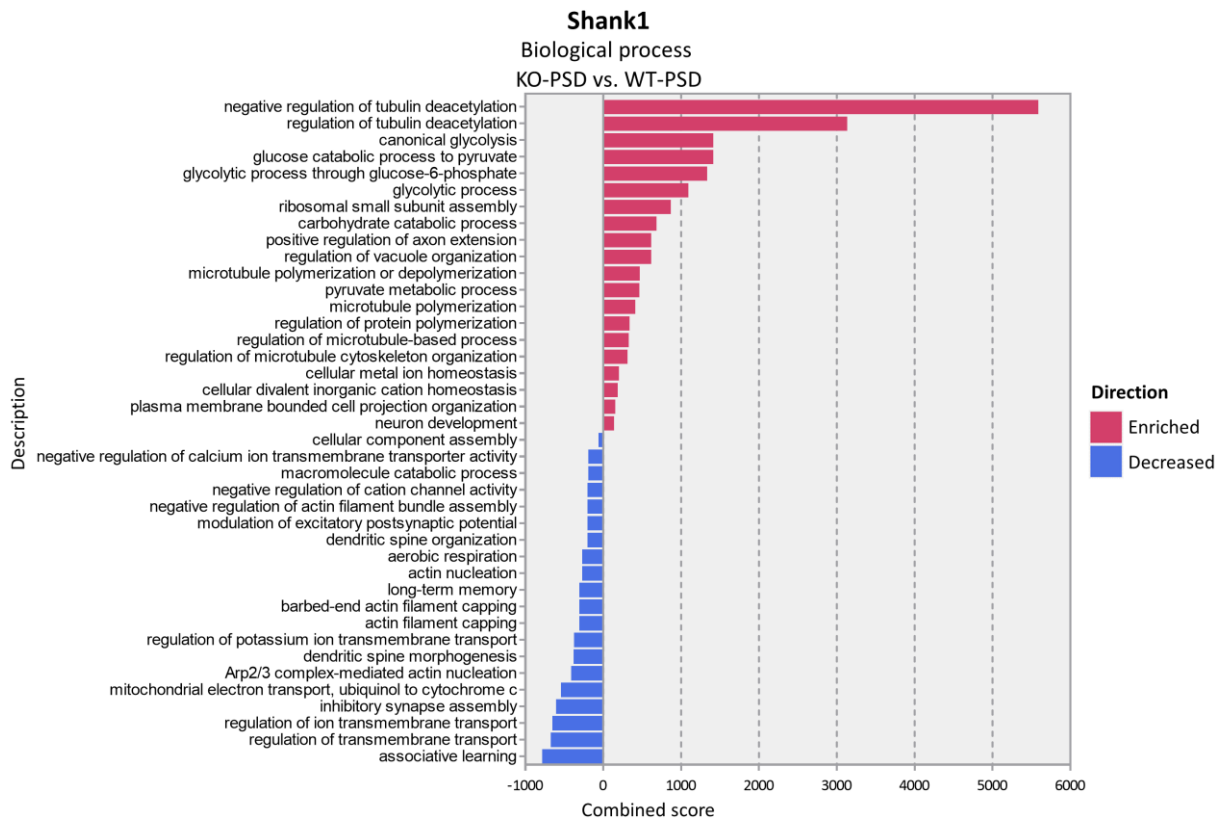


Figure 20: Gene ontology analysis of biological processes influenced by the altered proteome in the PSD of *Shank1*-KO mice. The entirety of significantly changed proteins ($FC > 1.5$, $p \leq 0.05$) was used for GO analysis. The combined score was visualized for the 20 most enriched (red) and decreased (blue) BPs. Strongest enrichment was determined for the negative regulation of tubulin acetylation and regulation of tubulin deacetylation. The most decreased term was associative learning.

In the analysis of biological processes in PSDs from *Shank3 $\alpha\beta$* -KO mice, the four highest enriched BPs were linked to glycolysis and shared with the *Shank1* analysis (Figure 20 and Figure 21). The most overrepresented BP in *Shank3 $\alpha\beta$* -KO that was specific for the *Shank3* analysis was “N-acylethanolamine metabolic process”, triggered by the reduction of the N-acylethanolamine-hydrolyzing acid amidase (Naaa). The “Regulation of AMPA Receptor Activity”, influenced by depletion of *Shisa6* and *Shank3* itself, was ranked highest among the downregulated biological processes (Figure 21).

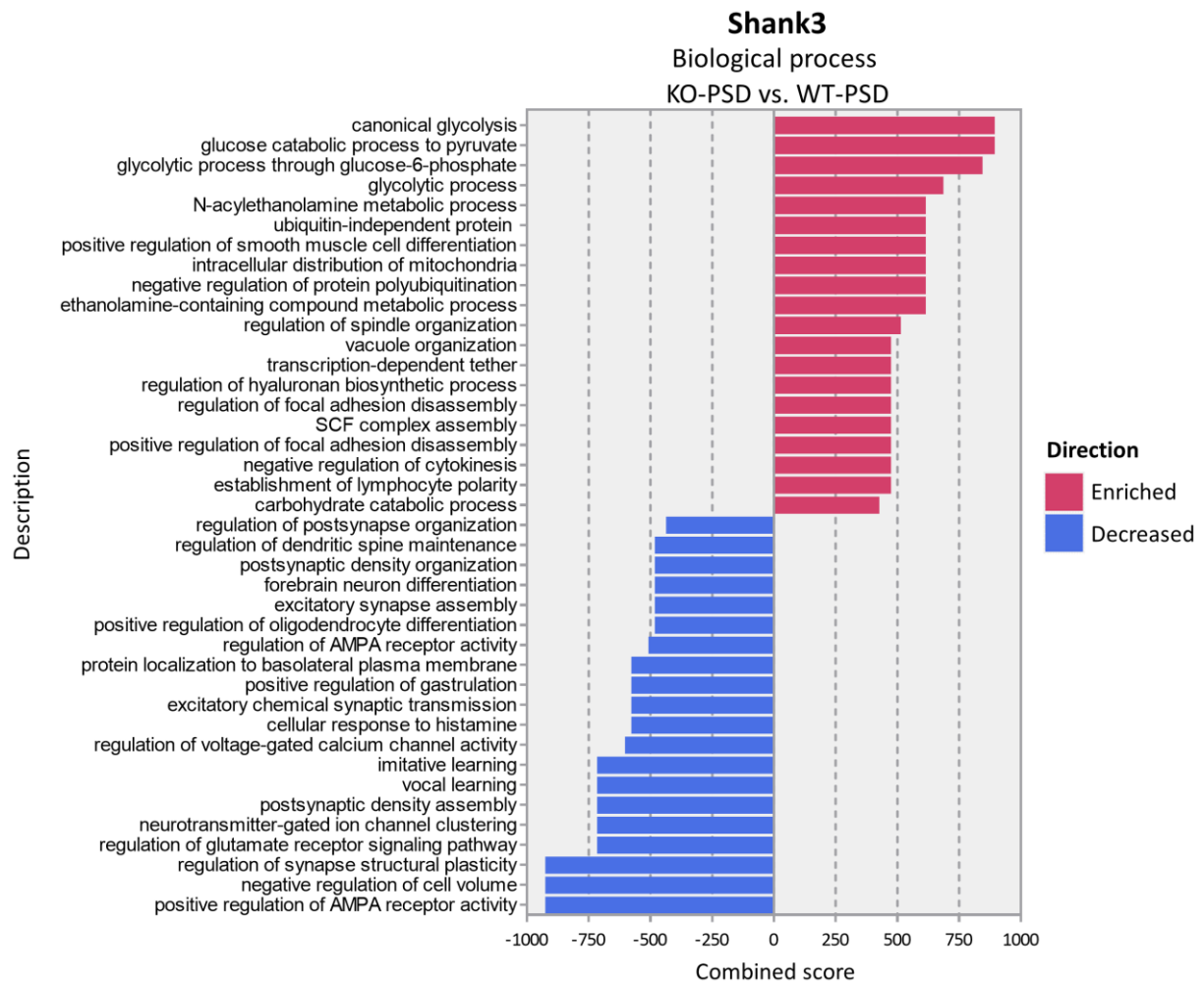


Figure 21: GO analysis of BPs affected by altered protein composition of the PSD of *Shank3αβ*-KO mice. All significantly altered proteins ($FC > 1.5$, $p \leq 0.05$) were submitted to GO analysis. The combined score was visualized for the 20 most enriched (red) and decreased (blue) BPs. The most enriched BP that was specific for the Shank3 analysis was N-acylethanolamine metabolic process. Strongest depletion was determined for the positive regulation of AMPA receptor activity.

The GO analyses of deregulated biological processes at the postsynapse of *Shank1* and *Shank3αβ* knockout mice indicated that depletion of Shank proteins might result in deregulation of a couple of common biological processes at the postsynapse, but Shank-specific consequences predominated and may contribute more to the pathogenicity of *SHANK* variants in ASD patients.

4.1.3.4. Knockout of *Shank1* and *Shank3αβ* Results in Increased Levels of *CaMKIIα* in the Postsynaptic Density

The *CaMKIIα* interacts with *Shank3* in its unphosphorylated, inactive state via an N-terminal linker region located between the SPN and ANK domains of *Shank3* (Cai *et al.* 2021). Missense variants of *SHANK3* found in ASD patients lead to alterations in the SPN-ANK conformation, thus preventing this interaction (Woike *et al.* 2022). Ca^{2+} -mediated neuronal depolarization and *CaMKII*-dependent signaling pathways link the reception of excitatory signals to regulation of transcription and translation, a mechanism indispensable for synaptic plasticity (Dolmetsch 2003, Flavell and Greenberg 2008, Lisman *et al.* 2012). I verified the interaction of T7-tagged *CaMKIIα* and RFP-tagged *Shank3* in a HEK293T-based overexpression and coimmunoprecipitation assay (see 3.2.3.2, Figure 22). RFP-*Shank1* and RFP-*Shank2* were included to decipher whether the *CaMKII* association is shared by all Shank proteins or is *Shank3*-specific. Efficient and specific binding of *Shank3* to *CaMKIIα* was detected that was significantly stronger compared to the interaction of *CaMKII* with *Shank1* and *Shank2* (Figure 22B).

A T7-CaMKII band of low intensity was detected for Shank1 in the IP sample, indicating a weak interaction with CaMKII, whereas no binding to CaMKII was detected for Shank2 (Figure 22A).

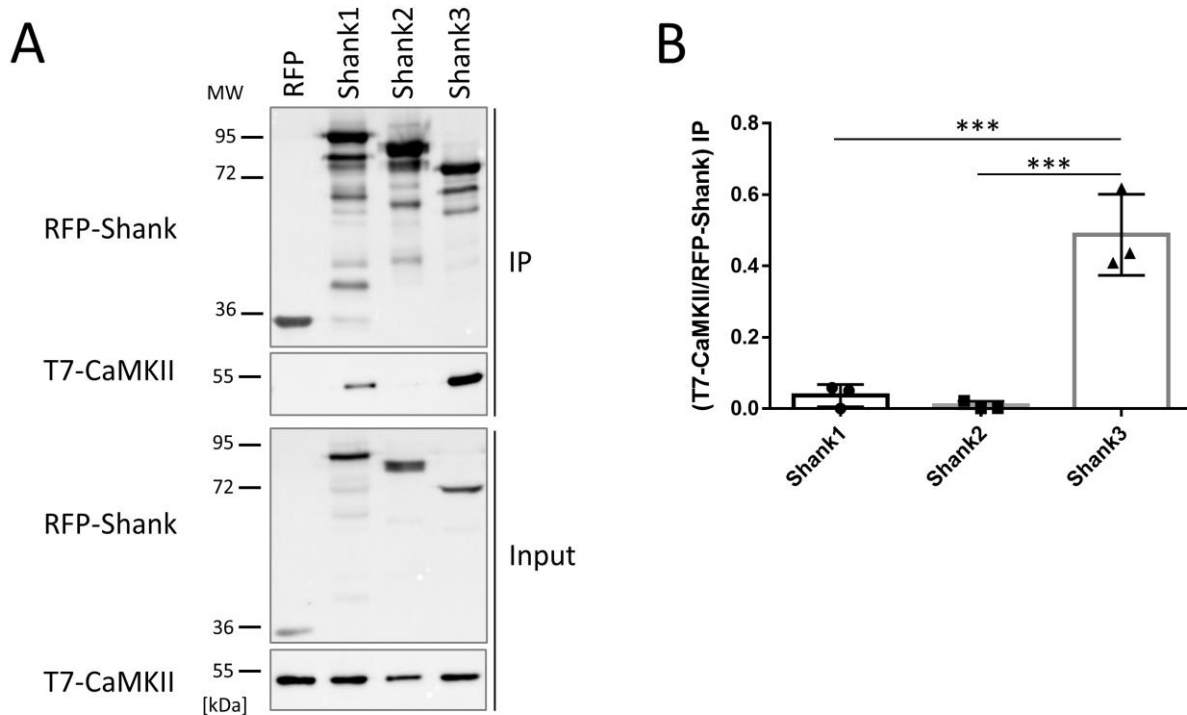


Figure 22: Analysis of the interaction of the CaMKII α with Shank proteins. (A) HEK292T cells were transfected with constructs encoding N-terminal fragments of the Shank proteins, comprising the SPN and ANK domains. RFP-tagged N-termini of Shank1, Shank2 and Shank3 were coexpressed with T7-CaMKII α . RFP alone was expressed as control. Coimmunoprecipitation was performed using RFP-trap and analyzed by western blot. Proteins were detected with antibodies recognizing the RFP or T7 tags. Uniform expression was confirmed in the whole cell lysates (Input). An efficient and specific binding of Shank3 and weak interaction of Shank1 to CaMKII α was determined. Shank2 did not interact with CaMKII α . (B) Quantitative analysis of the data shown in A. The ratios of T7 to mRFP IP signals are shown as mean with standard deviation. Statistical analysis: one-way ANOVA followed by Tukey's test ($p \leq 0.001 = ***$, $n = 3$).

In the proteomic approach to analyze the postsynaptic proteomes in *Shank1* and *Shank3 $\alpha\beta$* knockout mice, no changes in CaMKII α abundance were detected (see 4.1.3.2). This was surprising due to the interaction of CaMKII α with the N-termini of Shank3 and to lesser extent Shank1, which was confirmed here (Figure 22). Therefore, I determined the abundance of active phosphorylated CaMKII α relative to total amount of CaMKII α in PSD fractions prepared from cortices and hippocampi of *Shank-KO* and WT mice by western blot analyses. In addition to Shank and CaMKII, PSD-95 and tubulin were detected (Figure 23A). Upon loss of Shank1 and Shank3, an increase in phosphorylated CaMKII α was determined, which was more pronounced for Shank3 compared to Shank1 and greater in PSD fractions from the cortex compared to the hippocampus (Figure 23B). This enrichment of activated CaMKII α indicated that the N-terminal domains of Shank1 and Shank3 play a role in regulation of CaMKII-associated signaling pathways at the postsynapse.

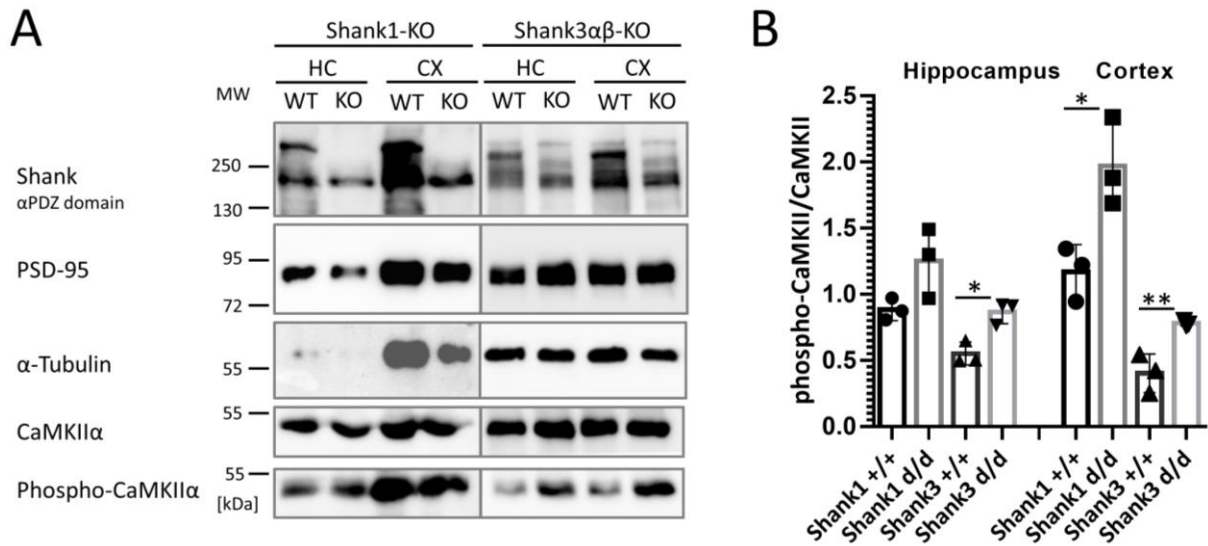


Figure 23: Loss of Shank1 and Shank3 resulted in enrichment of activated CaMKII α in PSD fractions. (A) PSD fractions were prepared from cortices and hippocampi of *Shank1*-KO and *Shank3 $\alpha\beta$* -KO mice and WT littermates to compare the activation status of CaMKII α in western blot analyses. Shank, PSD-95, tubulin, CaMKII α and phosphorylated CaMKII α (phospho-CaMKII α) were detected. **(B)** The abundance of active phospho-CaMKII α was quantified and normalized to the total CaMKII α amount. An increased activation of CaMKII α was detected upon loss of Shank. This change was more pronounced for Shank3 compared to Shank1 and stronger in the cortex compared to hippocampus. The mean with standard deviation was calculated and statistical significance determined by two-way ANOVA followed by Sidak's test ($p \leq 0.05 = *$, $p \leq 0.01 = **$). Tissues of five mice were pooled for one biological replicate ($n = 3$).

4.2. The Ago2 Patient Variant L192P Affects the miRNome and the miRNAs Bound to the RISC

Lessel *et al.* revealed that heterozygous missense variants in the *AGO2* gene, which encodes Argonaute-2 protein, are causative for a neurodevelopmental disorder termed Lessel-Kreienkamp syndrome (Lessel *et al.* 2020). The exact pathomechanism underlying LESKRES is currently unknown. As part of the RNA interference (RNAi) pathway, Ago2 binds to miRNAs to form the RNA-induced silencing complex (RISC) (Hammond *et al.* 2000, Hammond *et al.* 2001, Hutvagner and Zamore 2002, Peters and Meister 2007). By base pairing of RISC-incorporated miRNAs to mRNAs, translation is repressed (Hammond *et al.* 2000, Brennecke and Cohen 2003, He and Hannon 2004, Carthew and Sontheimer 2009). It was hypothesised that the Ago2 protein variants found in patients associate with different miRNAs compared to Ago2-WT. To test this hypothesis, I applied miRNA affinity purification (miRAP, see 3.2.3.5) (He 2012).

4.2.1. Validation of GFP-Ago2 Expression in AAV-transduced Primary Cortical Neurons

Primary cortical neurons were infected with AAVs to induce the expression of GFP-tagged Ago2 variants (WT and L192P) as well as GFP as negative control (see 3.2.2.3 and 3.2.2.4). Through usage of the hSyn1 promotor for control of expression of GFP-Ago2 variants, only the neuronal cell population was targeted (Hilfiker *et al.* 1999). GFP-tagged proteins were immunoprecipitated from cell lysates. The presence of GFP and GFP-tagged Ago2 variants in whole cell lysates (IC) and immunoprecipitates (IP) was confirmed via western blot analysis (Figure 24).

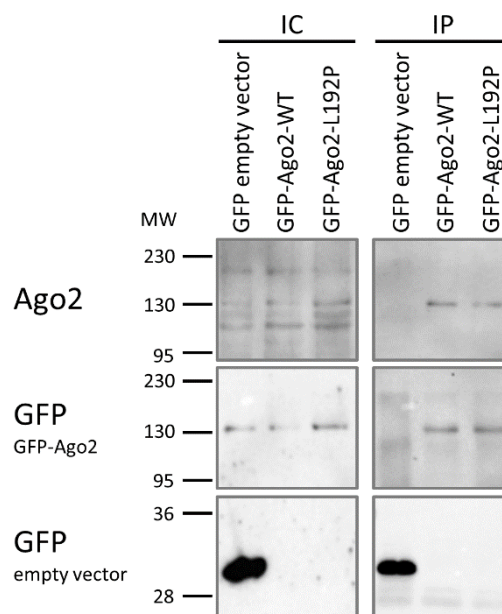


Figure 24: Verification of AAV-induced expression of GFP, GFP-Ago2-WT and GFP-Ago2-L192P in miRAP IC and IP prepared from primary neurons. Primary cultures of murine cortical neurons were transduced with AAVs at 1 DIV to express the GFP-tagged Ago2 variants WT and L192P, or GFP. At 12 DIV, cells were subjected to miRAP and lysate (IC) and IP of 1 million neurons per sample were subjected to western blot analysis. Expressed proteins were detected with antibodies that recognise Ago2 or the GFP-tag.

The viral expression of GFP-tagged Ago2-WT and Ago2-L192P in murine cortical neurons was validated using immunocytochemistry followed by confocal microscopy (Figure 25). Neurons were fixed at 12 DIV and stained for MAP2 as dendritic marker (Kosik and Finch 1987, Shiomura and Hirokawa 1987), as well as Dcp1a, a marker for p-bodies (Sheth and Parker 2003, Garneau et al. 2007) (see 3.1.3 and 3.2.3.4). Neurons expressing GFP were used as control. Transduction with AAVs induced expression of GFP-Ago2 or GFP in 95% of neurons. GFP-Ago2-WT and the L192P variant were localized in Dcp1a-

positive clusters throughout the soma and along the dendrites. Both Ago2 variants, L192P to a greater extent than WT, were also found in a diffuse pattern in the cytosol (Figure 25).

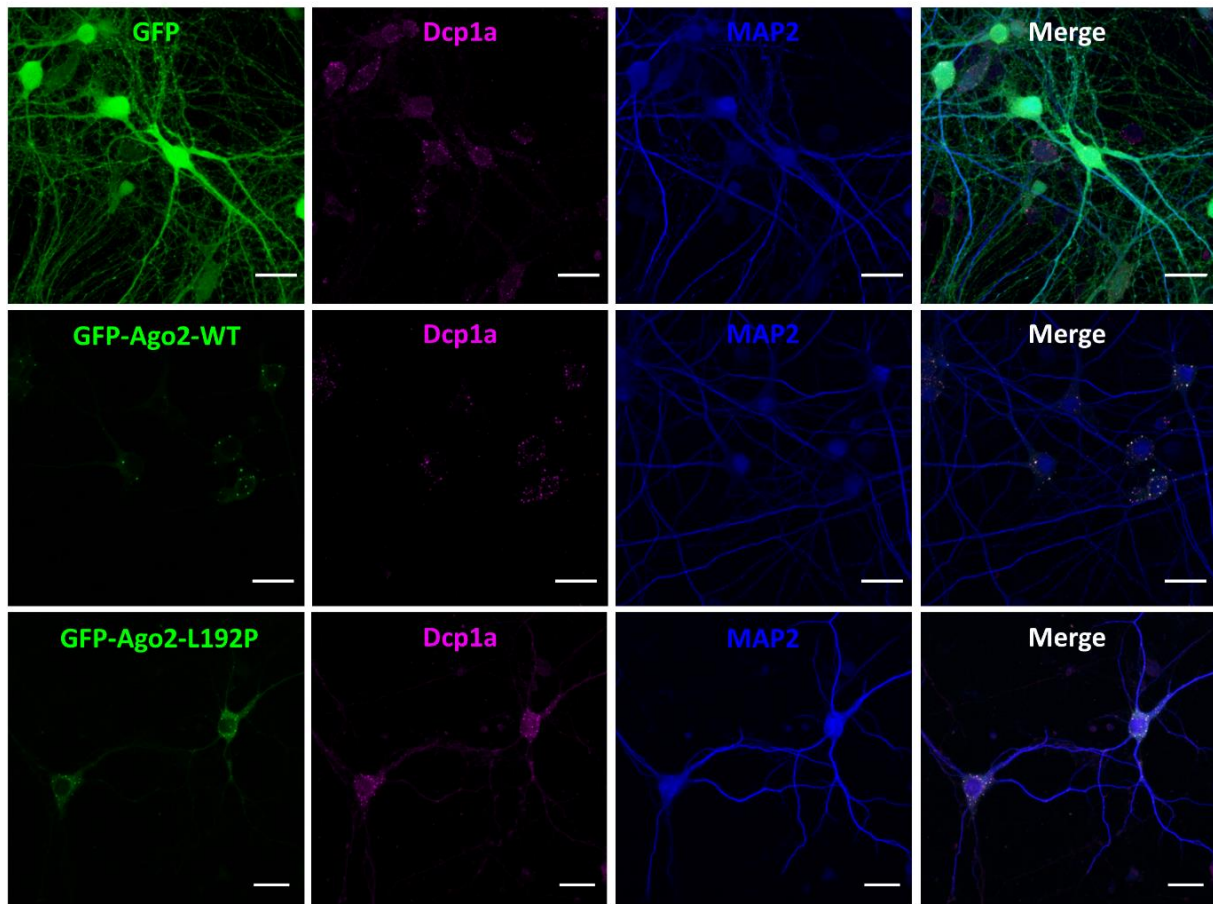


Figure 25: Analysis of the intracellular localization of virally expressed GFP and GFP-tagged Ago2-WT and Ago-L192P variants in cortical neurons. Cortical neurons from mice embryos (E18) were isolated and cultured and infected with AAVs to induce the expression of GFP-tagged Ago2 variants WT and L192P (green). GFP was used as control condition. At 12 DIV, cells were fixed and stained for MAP2 (A405, blue) as a dendritic markers as well as Dcp1a (A633, magenta) to visualise p-bodies. Ago2 was diffusely localized in the cytosol and enriched in Dcp1a-positive clusters in the cell soma and dendrites. Scale bar = 20 μ m.

4.2.2. The Ago2 Variant L192P Induces an Increased Occurrence of Dendritic P-Bodies

The localization of GFP-Ago2 variants in AAV-transduced cortical neurons was analyzed. In addition, the morphology of primary dendrites was assessed. Distal dendrites and cell bodies of fixed neurons stained for MAP2 and Dcp1a were imaged with a confocal microscope (Figure 26A). Dendritic and somatic clusters of Ago2 were quantified and the number of primary dendrites determined. The abundance of Ago2 clusters in the cell soma and the number of primary dendrites were similar between neurons expressing the Ago2 variants. In contrast, the occurrence of GFP-positive clusters that colocalized with Dcp1a-labelled p-bodies along distal dendrites was increased by expression of the Ago2-L192P variant compared to Ago2-WT. In the wildtype condition, 0.08 Ago2-positive p-bodies were found per μ m dendrite. This was increased 1.63-fold to 0.13/ μ m when Ago2-L192P was expressed. Statistical significance with $p \leq 0.031$ was calculated using Student's t test (Figure 26B). These results confirm those published by Lessel *et al.*, who, using a different model system with transfected rat hippocampal neurons, also observed an increased density of dendritic p-bodies for neurons expressing the L192P variant.

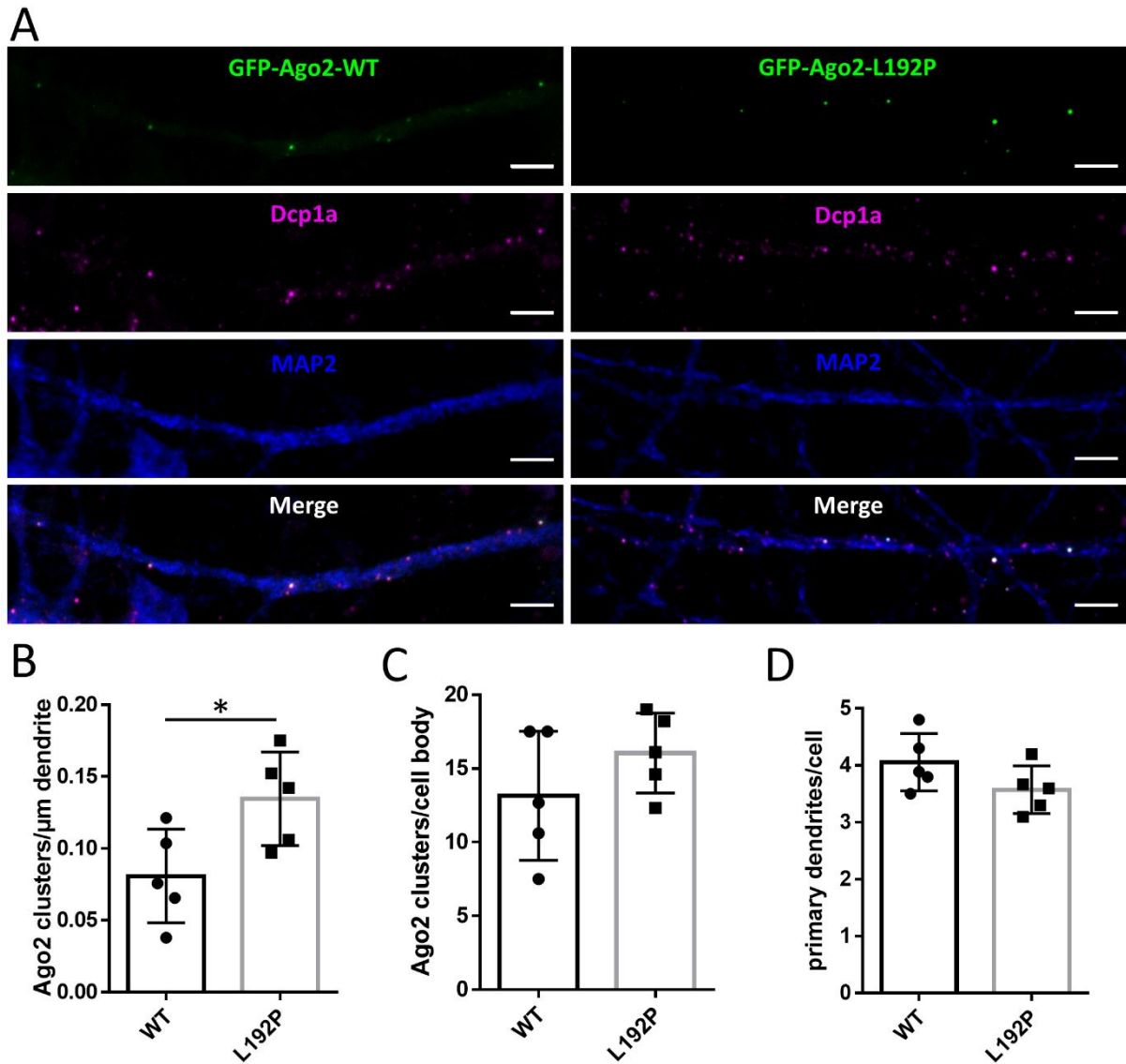


Figure 26: Analysis of primary dendrites and intracellular localization of GFP-Ago2-WT and GFP-Ago-L192P in AAV-infected neurons. (A) Sections of distal dendrites of AAV-infected neurons (E18) as shown in Fig. 2 (scale bar = 5 μ m). (B-D) Quantification of Ago2 clusters along dendrites (B) as well as in the cell body (C) and evaluation of the quantity of primary dendrites (D). In each repeat, five neurons were analyzed with three sections of distal dendrites per neuron. The arithmetic mean per replicate is shown with standard deviation. A two-tailed Student's t-test was calculated and revealed a statistically significant increase with $p \leq 0.031$ (*) in the abundance of dendritic p-bodies when the Ago2 variant L192P was expressed.

4.2.3. Evaluation of miRNA Concentration and Relative Enrichment of Neuron-specific miRNA-124 for Quality Assurance of the miRAP Assay

To investigate the effect of the Ago2 patient variant L192P on the miRNome and formation of the RISC, the miRAP method was applied on neurons that were AAV-infected to express GFP-tagged Ago2-WT and L192P under the control of the neuron-specific hSyn1 promoter. GFP-expressing neurons were used as control condition. To determine the entirety of miRNAs (miRNome), an input control sample (IC) was taken from the neuron lysate prior to immunoprecipitation. With an anti-GFP matrix, GFP-Ago2 variants and associated miRNAs were immunoprecipitated (IP). The miRNAs in IC and IP samples were purified and the concentration (c) determined (Figure 27). The miRNA concentrations in ICs ranged from 273 ng/ μ l in GFP-IC and 275 ng/ μ l in L192P-IC to 110 ng/ μ l in the WT-IC (arithmetic means, $n = 5$). The Ago2-WT-IP contained the highest amount of miRNA in IPs at $c = 41$ ng/ μ l. Compared to WT, the IP of Ago2-L192P contained 0.41-fold less miRNA with $c = 17$ ng/ μ l. The lowest miRNA amount ($c = 2$ ng/ μ l) was measured in the IP of the GFP control condition (Figure 27B).

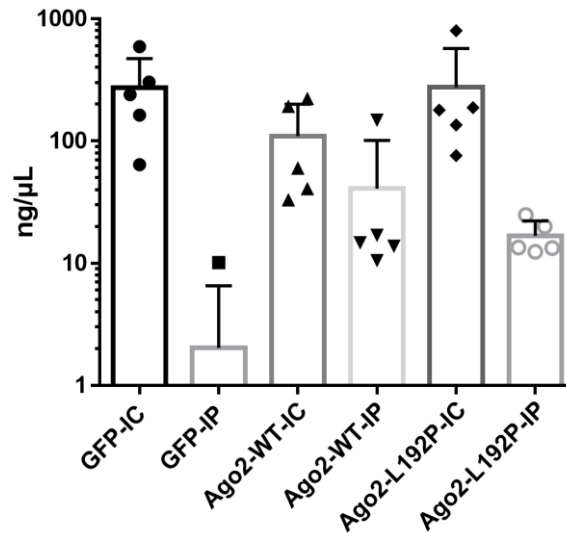


Figure 27: miRNA concentrations in IC and IP samples prepared via miRAP. Primary neurons were infected with AAVs at 1 DIV to induce expression of GFP-tagged Ago2 variants WT and L192P or GFP control. ICs were collected from neuron lysate and IPs were obtained by immunoprecipitation with an anti-GFP matrix via miRAP. The concentration of miRNA was determined using the Qubit microRNA Assay Kit (Thermo Fisher Scientific, Waltham, USA). The concentration in ng/μL is shown as arithmetic mean with standard deviation on a common logarithmic scale.

Next, I wanted to confirm the specificity of the miRAP procedure for GFP-tagged Ago2 variants. Since Ago2 variants were expressed under the control of the hSyn1 promoter, which targets the neuronal cell population, I expected an enrichment of neuronal miRNAs but not glia-specific miRNAs in IP samples of Ago2 variants. For this, I developed a quantitative PCR analysis of the miRNAs expressed in the primary culture. The abundance in IC (lighter color in Figure 28A-C) and IP (darker color in Figure 28A-C) of neuron-enriched miRNA-124 (miR-124, continuous lines in Figure 28A-C) was compared to miRNA-21 (miR-21, dotted lines in Figure 28A-C), which is typically expressed in glia cells (Lagos-Quintana et al. 2002, Akerblom et al. 2012, Zhang et al. 2012, Jovicic et al. 2013, Malmevik et al. 2015). miR-124 was enriched in IP compared to IC when GFP-tagged Ago2 variants were expressed, shown as a shift of the amplification curves towards less cycles (Figure 28B-C). This shift was more pronounced with Ago2-WT (Figure 28B). In the GFP control, the amount of miR-124 was reduced when comparing IP with IC (Figure 28A). The miR-21 was unaffected between Ago2-WT-IP and IC. In contrast, with the L192P variant, miR-21 was more abundant in the IP compared to IC (Figure 28B-C). When GFP was expressed, miR-21 was depleted from IC to IP (Figure 28C). As measure of efficiency and specificity, the relative enrichment in IP was calculated and normalized to the IC (Figure 28D). A two-way ANOVA with Sidak's multiple comparisons test showed a significant difference with $p \leq 0.0054$ for relative enrichment of miR-124 in Ago2-WT (mean = 16.22, $n = 5$) compared to GFP (mean = 0.01, $n = 5$). The relative enrichment of miR-124 with L192P (mean = 5.07, $n = 5$) was higher compared to GFP control, but this difference did not reach statistical significance after five replicates. Thus, the quantitative analysis showed that neuronal miRNAs were successfully enriched in the IP samples of neuronally expressed GFP-Ago2 variants, and that very little miRNAs were isolated in GFP control IPs. Based on these important quality control experiments, miRNAs in IC and IP samples from GFP-Ago2 expressing neurons were considered suitable for RNA-seq analysis.

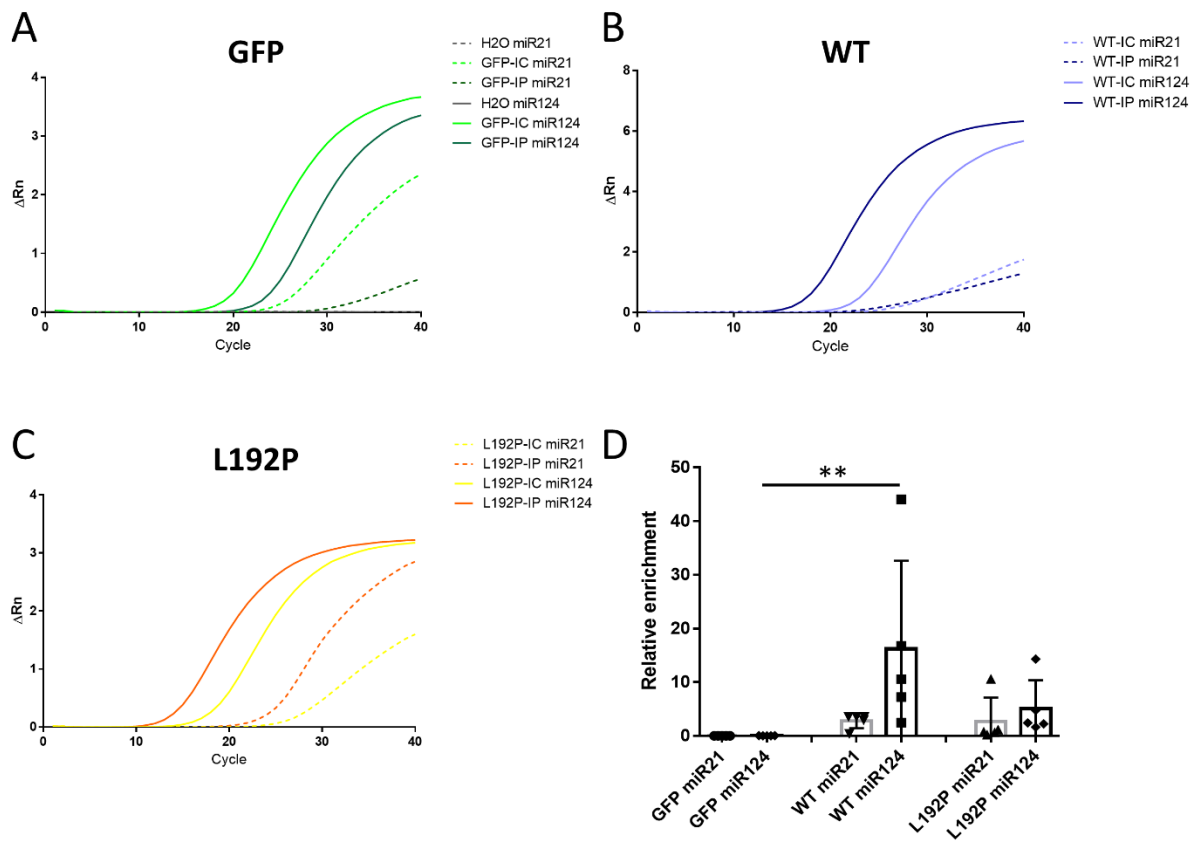


Figure 28: Abundance of miR-21 and miR-124 in IC and IP of the miRAP assay and relative enrichment of miR-124 in Ago2-WT condition. miRAP samples from cortical neurons expressing GFP, GFP-Ago2-WT or L192P were analyzed by qPCR using TaqMan probes. **(A-C)** Amplification of miR-21 (dotted lines) and miR-124 (continuous lines) in IC (lighter color) and IP (darker color) measured in GFP control (A), Ago2-WT (B) and Ago2-L192P (C). **(D)** The relative enrichment was calculated and normalized to the IC. A two-way ANOVA with Sidak's test determined a significant increase for the relative enrichment of miR-124 in the Ago2-WT condition compared to GFP control ($p \leq 0.01 = **$, $n = 5$).

4.2.4. The Ago2-L192P Variant Induces Changes in the miRNome and RISC-associated miRNAs

Next Generation Sequencing was employed to decode the miRNome and the identity of RISC-associated miRNAs in cortical neurons expressing GFP-tagged Ago2-WT and the L192P mutant (see 3.2.5.1). The miRAP samples were sequenced and bioinformatics were performed by Dr. Dr. Jan Broder Engler. To assess similarity between acquired RNA sequencing data from ICs and IPs, a principal component analysis (PCA, Figure 29A) was applied and a clustering dendrogram created (Figure 29B). All IPs clustered together in the PCA, indicating a high degree of similarity between Ago2-WT and Ago2-L192P IP samples. The ICs were scattered wider but still grouped together, suggesting resemblances between them, but to a lesser extent compared to the IPs (Figure 29A). A clustering dendrogram shows that, except for WT-IC2, the miRNA datasets hierarchically clustered together depending on sample type (IC vs. IP) and Ago2 variant (WT vs. L192P). It can be concluded that expression of the Ago2 mutant L192P influenced the entirety of miRNAs expressed, the miRNome, which was sampled in input controls. Moreover, the immunoprecipitates from Ago2-WT and Ago2-L192P clustered distinctly separately, suggesting that the miRNAs associated with mutant Ago2 in the L192P-RISC differed compared to the miRNAs present in the canonical WT-RISC (Figure 29B).

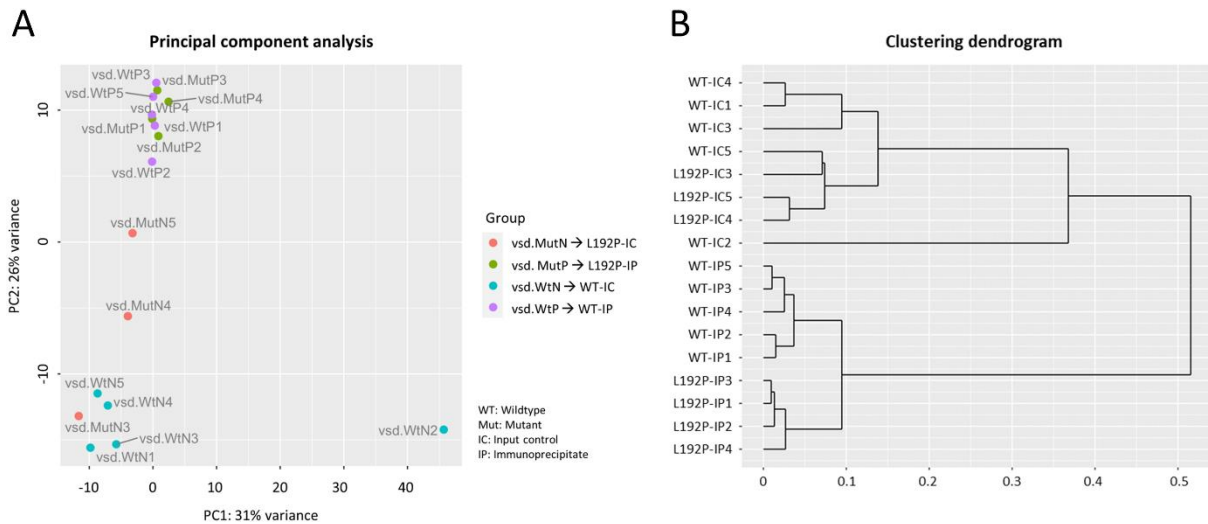


Figure 29: Analysis of similarity based on miRNA sequencing. Two ICs and one IP of the L192P mutant were excluded due to insufficient miRNA integrity. **(A)** PCA for illustration of similarities between miRAP IPs and ICs replicates from Ago2-WT and the Ago2-L192P expressing cortical neurons. **(B)** Dendrogram to depict clustering based on the RNA sequencing data between replicates and conditions.

Differential gene expression (DGE) analysis was performed to identify differentially abundant miRNAs (Figure 30A) and to determine alterations in RISC-associated miRNAs associated with the Ago2 variant L192P (Figure 30B). Differentially expressed or differentially RISC-bound miRNAs were appointed by having an adjusted p -value ≤ 0.05 and an absolute \log_2 fold change > 1 (see 3.2.5.1). The comparison of miRNomes, L192P-IC vs. WT-IC, showed 24 miRNAs significantly differing in abundance between cells expressing Ago2-WT and Ago2-L192P, of which 14 miRNAs were less frequently detected (Figure 30A, blue dots) and 10 miRNAs were more abundant (Figure 30B, red dots) when the Ago2 mutant was expressed (Figure 30A). Through comparison of L192P-IP with WT-IP, 23 miRNAs were detected that were differentially bound to Ago2-L192P, of which 14 miRNAs were less bound to the mutant Ago2 (Figure 30B, blue) and nine miRNAs were more associated with L192P-RISC compared to WT (Figure 30B, red dots). Between these two comparisons, eight miRNAs overlapped, indicating that sheer abundance of miRNAs can but does not always dictate the efficiency of incorporation into the RISC. All differentially expressed and RISC-bound miRNAs are listed in Table 52 in the appendix (see 7.2).

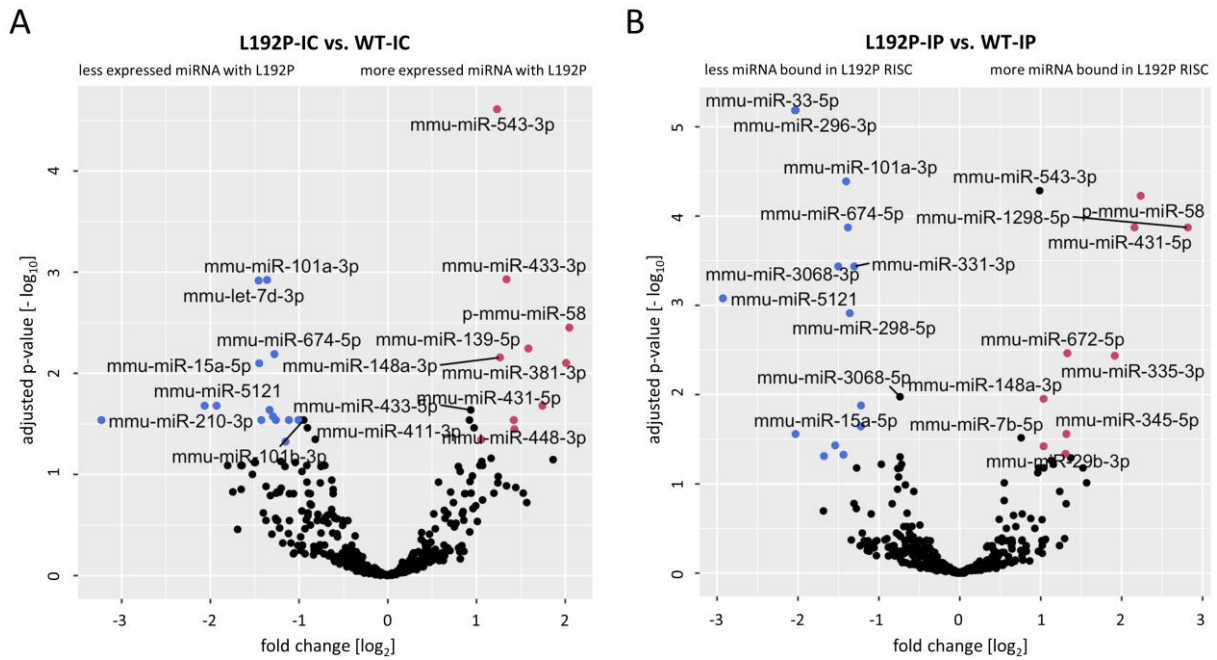


Figure 30: Differentially expressed or RISC-loaded miRNAs. Significant differences in expression of miRNAs or association with the RISC were determined using DESeq2. Significance was reached with an adjusted p-value of $p \leq 0.05$ plotted as $-\log_{10}$ and a \log_2 fold change > 1 . Decreased miRNAs are shown as blue dots and enriched miRNAs are depicted in red. **(A)** Comparison of L192P-IC vs. WT-IC showed 24 differentially expressed miRNAs. 14 miRNAs were expressed less with Ago2-L192P and 10 miRNAs were more abundant compared to the Ago2-WT condition. **(B)** 23 miRNAs were differentially associated with Ago2 in the L192P-IP vs. WT-IP comparison. 14 miRNAs were reduced in the L192P RISC whereas nine miRNAs were more strongly associated with the RISC of Ago2-L192P. A detailed list of all deregulated miRNAs is shown in Table 52.

4.2.5. Ago2 Variants Affect the Expression of Alternative miRNA Strands and Mediate miRNA Arm Switching Events in the RISC

Upon formation of the RISC, Ago2 receives a double-stranded miRNA duplex consisting of a 3p and 5p strand, one of which remains anchored at the Ago2 protein, whereas the other strand is ejected and degraded (Ma *et al.* 2004, Song *et al.* 2004, Ma *et al.* 2005, Wang *et al.* 2008, Frank *et al.* 2010). Typically, either the 3p or the 5p strand of a particular miRNA is preferentially incorporated into the RISC and is therefore named guide strand or miR. The discarded strand was termed passenger strand or miR* (Okamura *et al.* 2009, Ghildiyal *et al.* 2010). Since strand selection dictates the specificity for mRNA targets, a shift of the 3p/5p ratio can have manifold effects on regulation of translation. RNA-seq count data from the miRAP (see 4.2.4) was used to calculate 3p/5p ratios. 33 miRNAs with a significant difference ($p \leq 0.05$) of 3p/5p between Ago2-WT-IP with Ago-L192P-IP were identified. 3p and 5p strands were annotated as miR and miR* using the miRBase database (Release 22.1). Five miRNAs were excluded due to absence of annotation of guide and passenger strand. The remaining 28 miRNAs were assigned to different categories based on the proportion of miR to miR* expressed and bound to the RISC (Figure 35D). In the first category “WT miR*”, the seven miRNAs miR-124, miR-300, miR-342, miR-376a, miR-337, miR-381 and miR-3068 were grouped together. These miRNAs showed increased association of the miR* strand with Ago2-WT in the RISC (WT-IP) as well as elevated miR* expression levels (WT-IC) (Figure 31).

WT miR*

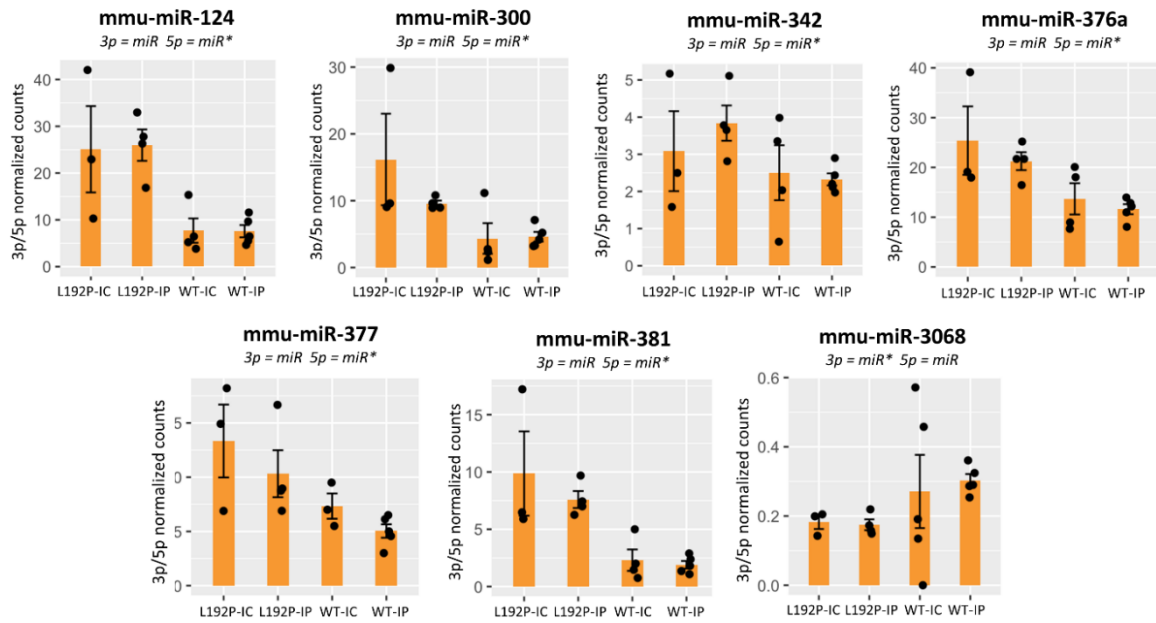


Figure 31: WT miR* category of seven miRNAs exhibiting higher expression of miR* and stronger association of miR* to the RISC with Ago2-WT. The normalized RNA-seq count data obtained from miRAP samples was used to calculate 3p to 5p strand ratios (3p/5p). 3p/5p are shown as arithmetic mean with standard deviation. All miRNAs with a statistically significant difference as $p \leq 0.05$ of 3p/5p in the Ago2-WT-IP compared to the Ago2-L192P-IP were selected and grouped into categories dependent on the 3p/5p pattern across the different samples and conditions. The passenger strand miR* of the miRNAs miR-124, miR-300, miR-342, miR-376a, miR-337, miR-381 and miR-3068 was more abundant in the WT-IC and in the WT-IP.

The seven miRNAs miR-9, miR-15a, miR-33, miR-101a, miR-125a, miR-335 and miR-337 were assigned to the second category “L192P miR*”. Here, the alternative strand miR* was more abundant in the input control and in the IP of the L192P variant compared to the wildtype conditions.

L192P miR*

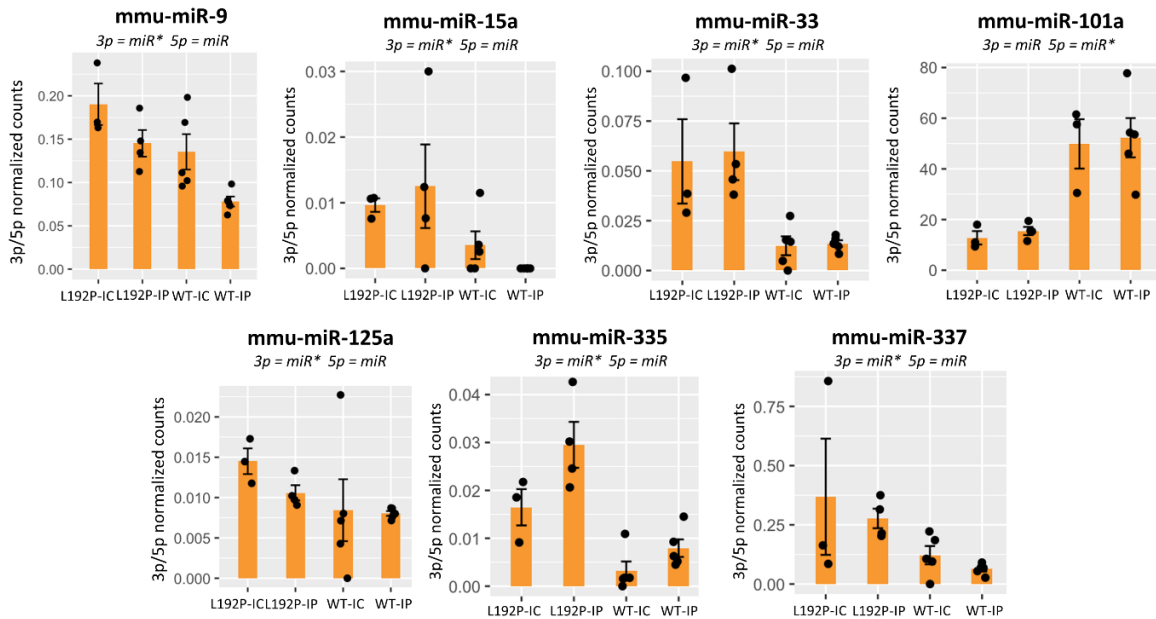


Figure 32: The L192P miR* group consists of seven miRNAs with higher abundance and RISC-association of miR* when the L192P variant was expressed. 3p/5p ratios were calculated with normalized count values. 3p/5p are shown as mean with standard deviation. The miRNAs with a significant difference ($p \leq 0.05$) of 3p/5p between the IPs were categorized dependent on the 3p/5p pattern. The miR* of miR-9, miR-15a, miR-33, miR-101a, miR-125a, miR-335 and miR-337 was expressed more (IC) and more associated more with the L192P-RISC (IP).

To determine the effect of the Ago2 variants on miRNA incorporation into the RISC, I focused on miRNAs for which the 3p/5p ratio showed a strong difference between the IPs of Ago2-WT and Ago2-L192P with comparable 3p/5p ratios in the ICs. After strand annotation, two miRNAs, miR-331 and miR-448, showed higher abundance of the miR strand in the WT-RISC compared to L192P-RISC, without being enriched in the IC. Therefore, these miRNAs were grouped into the category “WT-IP miR” (Figure 33A). Notably, the mean of normalized count values of the miR-331 was ≈ 105 , making it the most frequently detected miRNA among all miRNAs in the 3p/5p ratio analysis. The “WT-IP miR*” category with the miRNAs miR-330, miR-431 and let-7e was established following the same methodology. For miR-330 and miR-431, the alternative strand was more frequently detected only in Ago2-WT-IP compared to all other conditions. The miR* strand of let-7e was enriched in the IP of Ago2-WT although it was more expressed in the L192P-IC (Figure 33B).

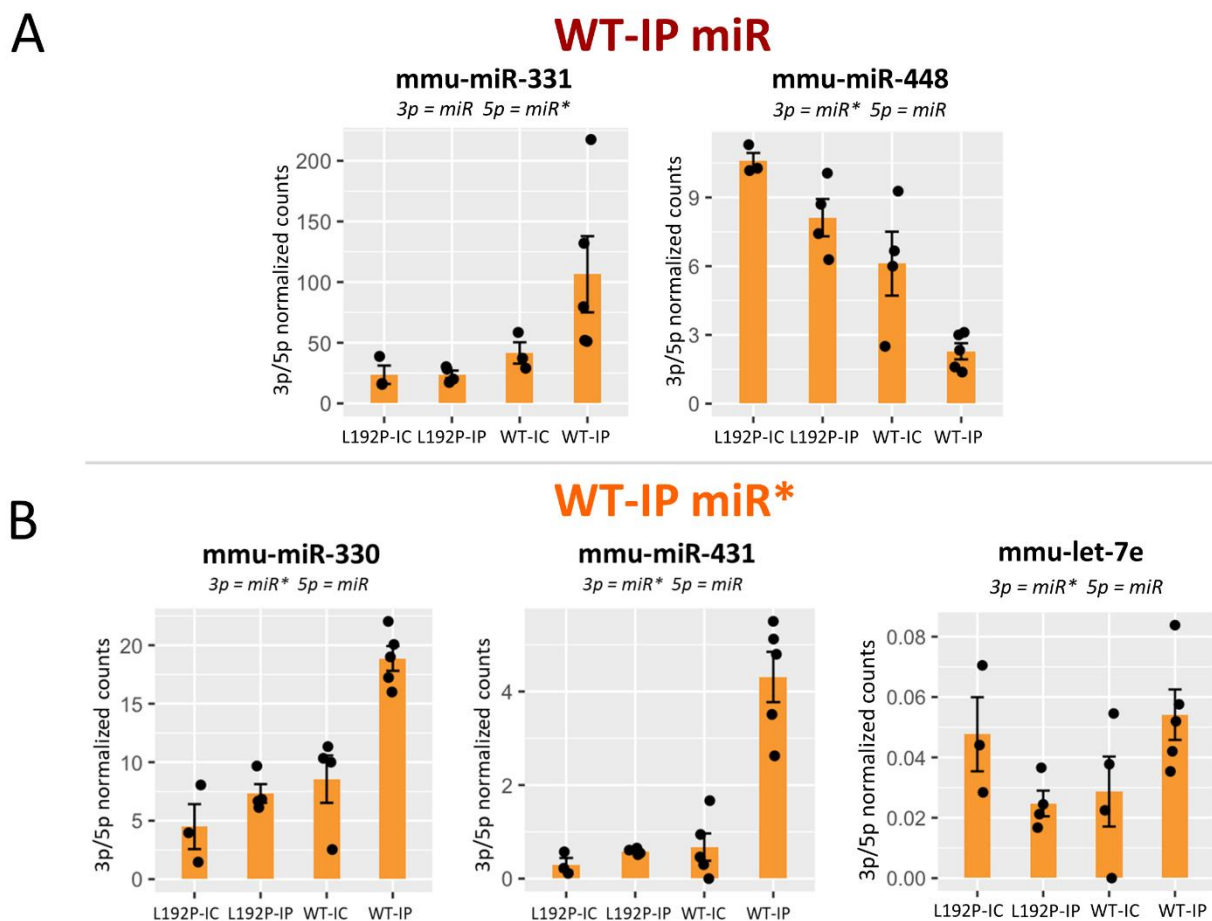


Figure 33: 3p/5p of miRNAs to detect miR and miR* strands enriched in the RISC of Ago2-WT. Using normalized count values from RNA-seq data obtained from miRAP samples, 3p/5p was calculated. Five miRNAs showed significant ($p \leq 0.05$) differences in the WT-IP compared to the L192P-IP without comparable changes in the respective ICs. 3p/5p are shown as mean with standard deviation. **(A)** Grouped into the WT-IP miR category, the miR strand of miR-331 and miR-448 was increased in WT-RISC compared to L192P-RISC, measured as 3p/5p in IP samples. **(B)** The WT-IP miR* group consists of three miRNAs, of which the two miRNAs miR-330 and miR-431 showed enrichment of the miR* in Ago2-WT-IP without higher abundance in the three remaining conditions. For let-7e, the miR* strand was more frequently detected in the WT-IP as well as in the L192P-IC.

In the last two categories, L192P-IP miR and L192P-IP miR*, the 3p/5p ratio in the L192P-IP differed considerably from all remaining conditions. The RISC-loaded miRNAs were altered in the L192P-RISC compared to the WT-RISC with no differences in the expression levels of these six miRNAs. The miR guide strand of miR-127, miR-543 and miR-672 was more frequently detected in the L192P-IP compared to Ago2-WT. Therefore, these three miRNAs were grouped into the category “L192P-IP miR” (Figure 34A). Among these, miR-543 showed the highest average 3p/5p in L192P-IP with $3p/5p \approx 45$. In the category “L192P-IP miR*”, the alternative strand of miR-149, miR-340 and miR-744 was more

abundant in the L192P-IP variant compared to the IP of Ago2-WT, which suggests an increased loading of the miR* into L192-RISC compared to WT-RISC (Figure 34B).

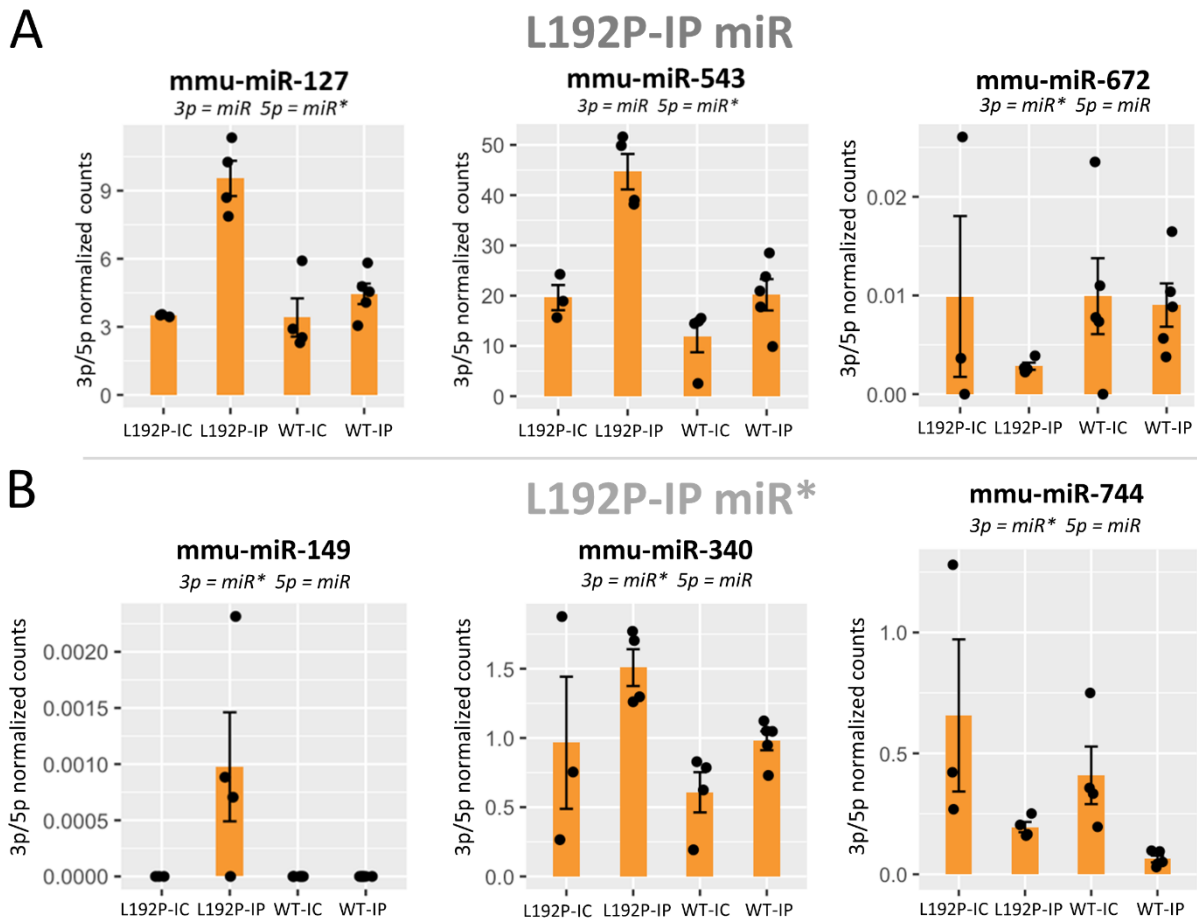


Figure 34: 3p/5p ratios determined three miR and miR* strands enriched in the L192P-RISC compared to Ago2-WT. 3p/5p were calculated using normalized count values from miRAP RNA-seq data and plotted as arithmetic mean with standard deviation. The miRNAs with statistically significant differences between Ago2-WT-IP and Ago2-L192P-IP were categorized dependent on the 3p/5p pattern. The miR or miR* strand of six miRNAs was enriched in the L192P-IP, without being differentially expressed (L192P-IC vs. WT-IC). **(A)** The three miRNAs miR-127, miR-543 and miR-672 showed higher abundance of the miR strand in the L192-IP. **(B)** The miR* of the three miRNAs miR-149, miR-340 and miR-744 was more strongly associated with the L192P-RISC compared to the RISC containing Ago2-WT.

To summarize the effects of Ago2 variants on 3p and 5p strand expression and incorporation into the RISC, the quantity of miRNAs in each category was illustrated (Figure 35A). In addition, the proportion of each category relative to the total of 28 3p/5p ratios analyzed was calculated (Figure 35B). The miR* of six miRNAs was expressed at higher levels and occurred more frequently in the IP when one of the Ago2 variants was expressed (Figure 35, L192P miR* and WT miR*). Three miRNAs were classified as L192P-IP miR and two as WT-IP miR. The incorporation of the alternative strand miR* in the RISC is an event often referred to as “arm switching” (Medley et al. 2021). Arm switching was observed here for three miRNAs in the IP of Ago2-L192P and for six miRNAs in the WT-IP, indicating differential effects of Ago2 variants on strand selection during RISC formation.

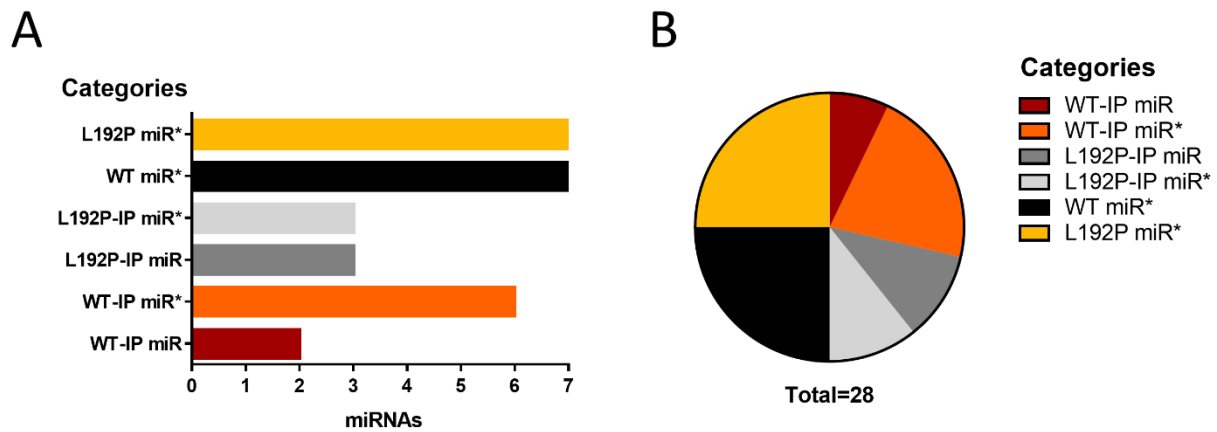


Figure 35. Analysis of 3p/5p ratios revealed distinct effects of Ago2 variants on miRNA strand expression and arm switching. 3p/5p ratios were calculated using normalized count values from RNA sequencing data obtained from miRAP samples. The miRNAs with statistically significant differences between Ago2-WT-IP and Ago2-L192P-IP were classified into six categories dependent on expression level in IC and association to the RISC, shown in IPs. **(A)** The quantity of miRNAs in each of the six categories. **(B)** The proportion of all categories in respect to a total of 28 3p/5p ratios of miRNAs analyzed.

4.2.6. The Ago2 Patient Variant L192P Induces Enhanced Incorporation of isomiRs into the RISC

To further decipher the miRNAs associated with the Ago2 mutant L192P, I analyzed the miRAP RNA sequencing data with regard to the abundance of isomiRs using the miRMaster tool (Fehlmann et al. 2017). IsomiRs are isomers of miRNAs that differ from the reference sequence of the corresponding canonical miRNA (Morin et al. 2008, Wang et al. 2008, Guo and Lu 2010). IsomiRs can be trimmed or extended at the 5' or 3' end, display nucleotide exchanges (nuc.ex, polymorphic isomiRs) or a combination of varying length and sequence (mixed isomiRs) (Nielsen et al. 2012, Wu et al. 2018) for thymine was used in miRMaster nomenclature although uracil (U) is used on RNA level at these positions. Notably, isomiRs can bind to Ago2 and change the identity of translationally downregulated target mRNAs, making them relevant for the specificity of RISC-mediated gene silencing (Cloonan et al. 2011, Londin et al. 2015, Haseeb et al. 2017). A total of 18,381 miRNAs, consisting of canonical sequences and all isomers, were detected in the IPs of Ago2-WT and L192P. 37 isomiRs were bound exclusively to the L192P variant. In contrast, none of the isomiRs were found to bind exclusively to the WT. From these, the 20 isomiRs with the highest average counts were selected. The four isomiRs miR-335-3p -3T, miR-409-3p -4T 17:C->A, miR-409 2T and miR-672-5p 22:A->T (for isomiR nomenclature see Figure 36A), were most frequently loaded into Ago2-L192P (Figure 36B). The 20 isomiRs were classified according to their sequence variability to the canonical miRNA sequence (Figure 36C). Table 53 in the appendix lists the 20 isomiRs sorted by category. 50% featured 3'-trimmed ends with exchange of a nucleotide (3'-trimmed nuc.ex in Figure 36B-D). Additionally, four 3'-trimmed isomiRs without nucleotide exchange were detected, making the 3'-trimmed isomiRs the most abundant. Three isomiRs were assigned to the 3'-extended category. For each of the categories 5'-extended + 3'-trimmed nuc.ex, polymorph, and 3'-extended + nuc.ex, one isomiR was identified. Notably, none of the isomiRs analyzed were 5'-edited isomiRs without variations at the 3'-end (5'-trimmed nuc.ex, 5'-trimmed, 5'-extended nuc.ex and 5'-extended in Figure 36C-D).

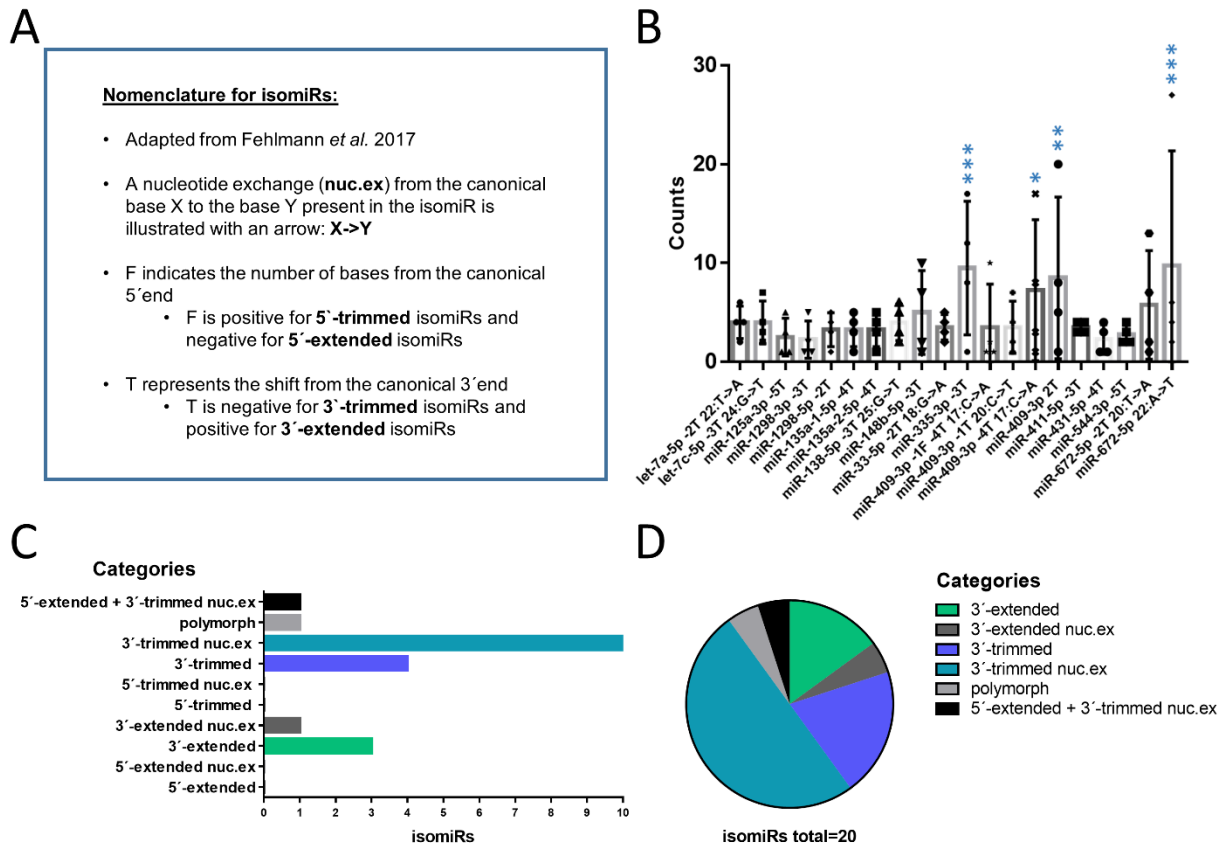


Figure 36: Increased association of isomiRs with the Ago2 variant L192P. The RNA sequencing data gathered from miRAP IPs was analyzed using the miRMaster tool to identify Ago2-loaded isomiRs. **(A)** An overview of nomenclature for isomiRs adapted from Fehlmann *et al.* 2017. Although uracil is used on RNA level, in the isomiR nomenclature from Fehlmann *et al.* a T (thymine) is used. **(B)** Out of 37 isomiRs which were bound exclusively to Ago2-L192P, the 20 isomiRs with highest average count values were selected and the count value of each replicate plotted against the respective isomiR. The mean with the coefficient of variation is shown. An ordinary two-way ANOVA followed by Sidak's multiple comparisons test determined the four isomiRs miR-335-3p -3T ($p \leq 0.0009$), miR-409-3p -4T 17:C→A ($p \leq 0.0321$), miR-409 2T ($p \leq 0.0049$) and miR-672-5p 22:A→T ($p \leq 0.0006$) as significantly enriched in the L192P-IP compared to WT-IP ($p \leq 0.05 = *$, $p \leq 0.01 = **$, $p \leq 0.001 = ***$) **(C)** The amount if isomiRs classified in each category. 10 isomiRs were 3'-trimmed with nucleotide exchange (nuc.ex) and 4 without nuc.ex. Three isomiRs had a 3'-extended end. One isomiR each belonged to the categories 5'-extended + 3'-trimmed nuc.ex, polymorph, and 3'-extended + nuc.ex. **(D)** The proportion of all isomiR categories in respect to a total of 20. 50% of the isomiRs were 3'-trimmed with nuc.ex. The remaining 50% included the other five categories in varying percentages.

4.2.7. Target Predictions for Deregulated miRNAs

The RISC silences translation of mRNA transcripts by targeting the complementary site of Ago2-loaded miRNA (Hammond *et al.* 2001, Hutvagner and Zamore 2002, Zeng *et al.* 2002). To estimate the impact of differential miRNA incorporation of the Ago2 variant L192P on mRNA targeting and ultimately protein composition, target predictions were performed using the bioinformatics tool miRTarget implemented in the miRDB database (Liu and Wang 2019, Chen and Wang 2020). Exemplary deregulated miRNAs were selected from the three aspects compared: IP vs. IP, 3p/5p ratios and isomiRs. Predicted targets were allocated prediction scores in the range of 0-100 and candidate transcripts were assigned target ranks of which the top five were selected to be presented in a tabular format (Table 44). Expression in the cortex was ensured using the Genotype-Tissue Expression (GTEx) portal (Version 05-08-15). Transcripts with ≤ 1 transcripts per million (TPM) in cortical tissue were counted as nonexpressed, excluded and replaced with next-ranked target.

First, two Ago2-loaded miRNAs from the L192P-IP vs. WT-IP comparison were analyzed. The miR-296-3p was severely decreased in the IP of Ago2-L192P whereas the miR-1298-3p was strongly enriched in the L192P-RISC (Figure 30). The top ranked cortical-expressed predicted target for the

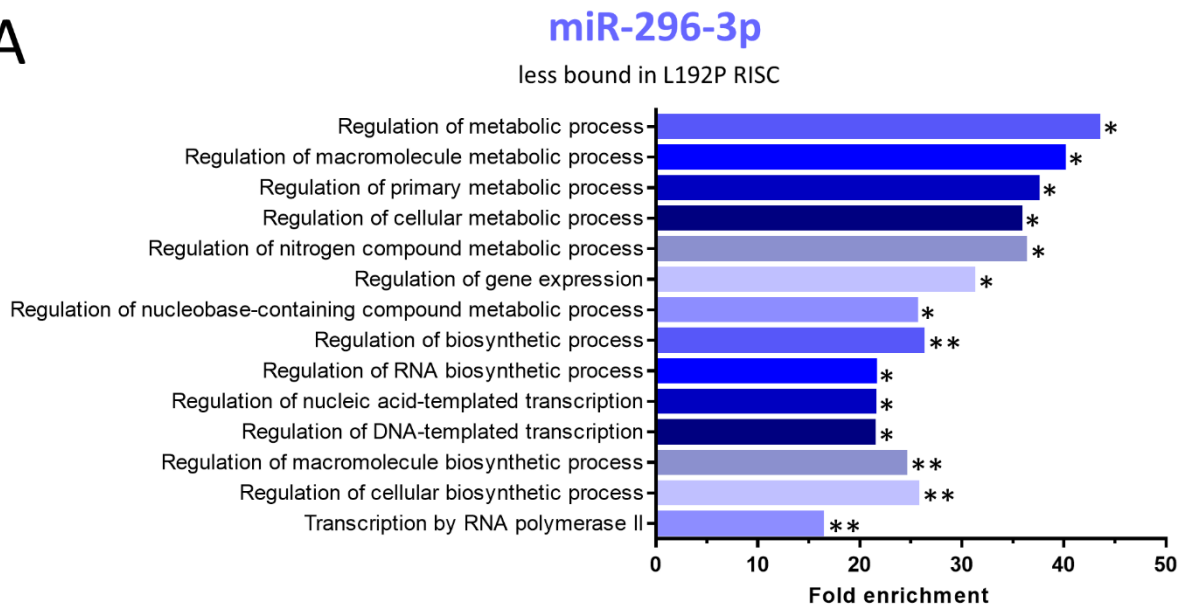
miR-296-3p was the sigma 1 subunit of the adaptor-related protein 5 complex (Ap5s1). For the miR-1298-5p, naked cuticle 1 (Nkd1) was allocated the highest target score (Table 44). Predicted targets with highest expression levels in the cortex were fibronectin type III domain containing 4 (Fndc4, TPM = 89.4) for the miR-296-3p and the copper chaperone cytochrome c oxidase assembly protein 17 as target of miR-1298-5p (Cox17, TPM = 22.2; see Table 44).

Table 44: Top five predicted target transcripts of deregulated miRNAs from the L192P-IP vs. WT-IP comparison. The mRNA targets of miR-296-3p (colored blue, reduced in L192P-IP) and miR-1298-5p (colored red, enriched in L192P-IP) were predicted using miRTarget implemented in miRDB. Target ranks and target scores as measure of prediction validity. The official gene symbol and gene description of predicted targets have been included. Expression values in transcripts per million (TPM) were extracted from the GTEx portal. Target transcripts with ≤ 1 TPM were excluded and replaced by the next target dependent on target rank and score.

Target rank	Target score	Gene symbol	Gene description	Expression [TPM]
miR-296-3p				
2	94	<i>Ap5s1</i>	adaptor-related protein 5 complex, sigma 1 subunit	4.7
5	93	<i>Itm2a</i>	integral membrane protein 2A	37.4
6	92	<i>Grm3</i>	glutamate receptor, metabotropic 3	31.8
7	90	<i>Cdo1</i>	cysteine dioxygenase 1, cytosolic	29.0
12	87	<i>Fndc4</i>	fibronectin type III domain containing 4	89.4
miR-1298-5p				
2	98	<i>Nkd1</i>	naked cuticle 1	2.2
4	95	<i>Tmem100</i>	transmembrane protein 100	2.2
5	95	<i>Eif4enif1</i>	eukaryotic translation initiation factor 4E nuclear import factor 1	17.9
6	92	<i>Vmp1</i>	vacuole membrane protein 1	13.9
7	91	<i>Cox17</i>	cytochrome c oxidase assembly protein 17, copper chaperone	22.2

Gene ontology analyses with all predicted targets of respective miRNAs were performed to elucidate biological processes deregulated by altered RISC function due to differentially associated miRNAs to Ago2-L192P compared with Ago2-WT. The PANTHER overrepresentation test connected to the GO database (DOI: 10.5281/zenodo.6799722; released 2022-10-13) was applied (Mi and Thomas 2009, Mi *et al.* 2019, Thomas *et al.* 2022). Predicted targets were assigned to GO terms dependent on their involvement in different BPs. The fold enrichment with FDR of BP GO terms was determined. For miR-296-3p, the top five enriched biological processes influenced by the predicted targeted transcripts were connected to metabolic processes: General metabolic processes, macromolecule, primary, cellular and nitrogen compound metabolic processes (FDR ≤ 0.05 , Figure 37A). Given that miR-296-3p was reduced in the L192P-RISC, silencing of the predicted targets would function less efficiently, suggesting that these biological processes were enhanced. Among the enriched BPs influenced by targets of miR-1298-5p, which was enriched in the L192P-RISC, the regulation of fibroblast migration stood out as most enriched GO term. Interestingly, two GO terms showed involvement in BPs connected to neurodevelopment: axon guidance and neuron projection guidance. Furthermore, five additional BPs were enriched with functions in development, for example tube development (FDR ≤ 0.05 , Figure 37B). Assuming that Ago2-L192P formed a functional RISC with miR-1298-5p, the silencing of the transcripts that contributed to these biological processes would be amplified under Ago2-L192P expression compared to Ago2-WT.

A



B

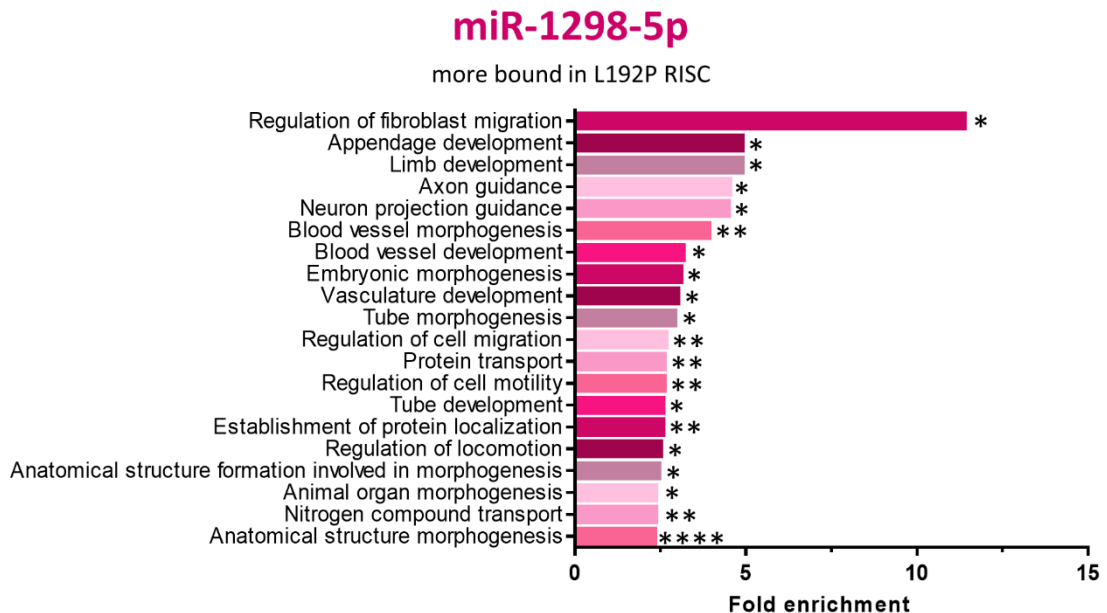


Figure 37: Gene ontology analysis of biological processes for predicted targets of (A) miR-296-3p and (B) miR-1298-5p. The entirety of miRDB-predicted targets was used for GO analysis with PANTHER. The fold enrichment was plotted against the GO terms. Statistical significance is illustrated by false discovery rate (FDR) with $FDR \leq 0.05 = *$, $FDR \leq 0.01 = **$ and $FDR \leq 0.0001 = ****$. Two miRNAs from the L192P-IP vs. WT-IP comparison were selected. **(A)** miR-296-3p was reduced in the L192P-RISC. Predicted targets showed enrichment in 14 GO terms. **(B)** miR-1298-5p was increased in the L192P-RISC. Predicted targets showed enrichment in 20 GO terms.

Secondly, the same approach of target predictions and GO analysis was applied to an miRNA that showed an altered 3p to 5p strand ratio between the Ago2 variants. The miR-543 was selected due to strong expression and Ago2 association. The 3p strand of miR-543 was significantly enriched, whereas the 5p strand displayed slightly less binding to Ago2-L192P compared to Ago2-WT (Figure 38).

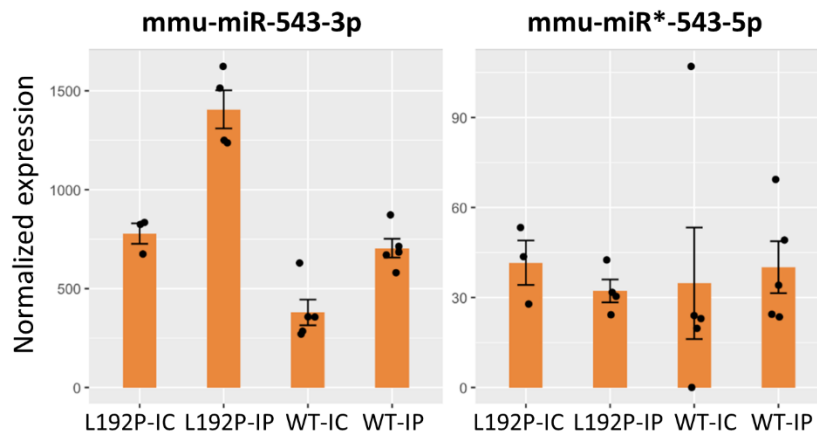


Figure 38: The 3p and 5p profiles of miR-543 illustrated strand selectivity of the Ago2 variants. Count values were taken from RNA-seq data obtained from the miRAP assay. Normalized expression values of miR-543-3p and miR-543-5p were plotted for the strand separately. The miR-543-3p showed 10- to 30-fold higher abundance across conditions compared to the 5p strand. 3p was strongly enriched in L192P-IP compared to WT-IP, while 5p displayed a slightly reversed distribution of strands.

The frizzled class receptor 4 (*Fzd4*) was the highest ranked target for the 5p strand of miR-543 but showed relatively low expression in the cortex (TPM = 6.2; Table 45). With a target score of 88, the secretory carrier membrane protein 5 (*Scamp5*) was ranked at the fourth place while being strongly expressed in cortical tissue (TPM = 211.5, Table 45). The miR-543-3p target with highest target score was the centriolar coiled coil protein 110 (*Ccp110*, Table 45). Scored with 98 on rank 5, the transcript of mitogen-activated protein kinase 1 (*Mapk1*) was most abundant in cortex among the 3p strand targets with TPM = 31.6 (Table 45). Importantly, there was no overlap between all predicted targets from 3p and 5p strand, indicating that arm switching events lead to differential targeting of transcripts by the RISC.

Table 45: The five highest ranked predicted targets of 3p and 5p strand of miR-543. Targets were predicted with miRDB, cortical expression validated with GTEx (TPM ≥ 1) and gene symbols sorted by target rank and score. (A) Target transcripts of miR-543-5p (blue) that was slightly less associated with Ago2-L192P than to Ago2-WT. (B) Predicted mRNA targets of miR-543-3p (red). This strand showed strong enrichment in L192P-IP compared to WT-IP.

Target rank	Target score	Gene symbol	Gene description	Expression [TPM]
miR-543-5p				
1	97	<i>Fzd4</i>	frizzled class receptor 4	6.2
2	93	<i>Slc25a5</i>	solute carrier family 25, member 5	190.4
3	89	<i>Vegfa</i>	vascular endothelial growth factor A	19.4
4	88	<i>Scamp5</i>	secretory carrier membrane protein 5	211.5
8	87	<i>Nemp2</i>	nuclear envelope integral membrane protein 2	1.4
miR-543-3p				
1	99	<i>Ccp110</i>	centriolar coiled coil protein 110	11.2
2	99	<i>Ss18l1</i>	SS18, nBAF chromatin remodeling complex subunit like 1	14.1
3	98	<i>Dmxl2</i>	Dmx-like 2	10.5
5	98	<i>Mapk1</i>	mitogen-activated protein kinase 1	31.6
6	98	<i>Adam9</i>	a disintegrin and metallopeptidase domain 9	8.0

GO analysis hinted towards different biological processes regulated by transcripts silenced by miR-543-5p or miR-543-3p. Astonishingly, the term “positive regulation of long-term neuronal synaptic plasticity” exhibited a severe fold enrichment (FE) of 43 (FDR ≤ 0.05; Figure 39A), while FEs of all other GO terms were ranging between 4.5 and 8.3. Additional BPs involved in neuronal cell homeostasis or development were enriched. Among these were: regulation of axon extension, neuron apoptotic

processes and of neurogenesis, as well as axon and neuron projection development. Hence, 50% of deregulated GO terms were BPs directly connected to neuronal mechanisms (Figure 39A). The fold enrichments of BP GO terms influenced by predicted targets of the 3p strand of miR-543 ranged between 3.3 (FDR \leq 0.05, adult locomotor behavior) and 7.2 (FDR \leq 0.05, histone H2A acetylation) and eight terms suggested involvement in acetylation pathways for predicted targets of miR-543-3p (Figure 39B). Not a single BP was present in both deregulated GO terms. Again, this result hinted towards distinct effects of transcripts targeted by 5p or 3p strand.

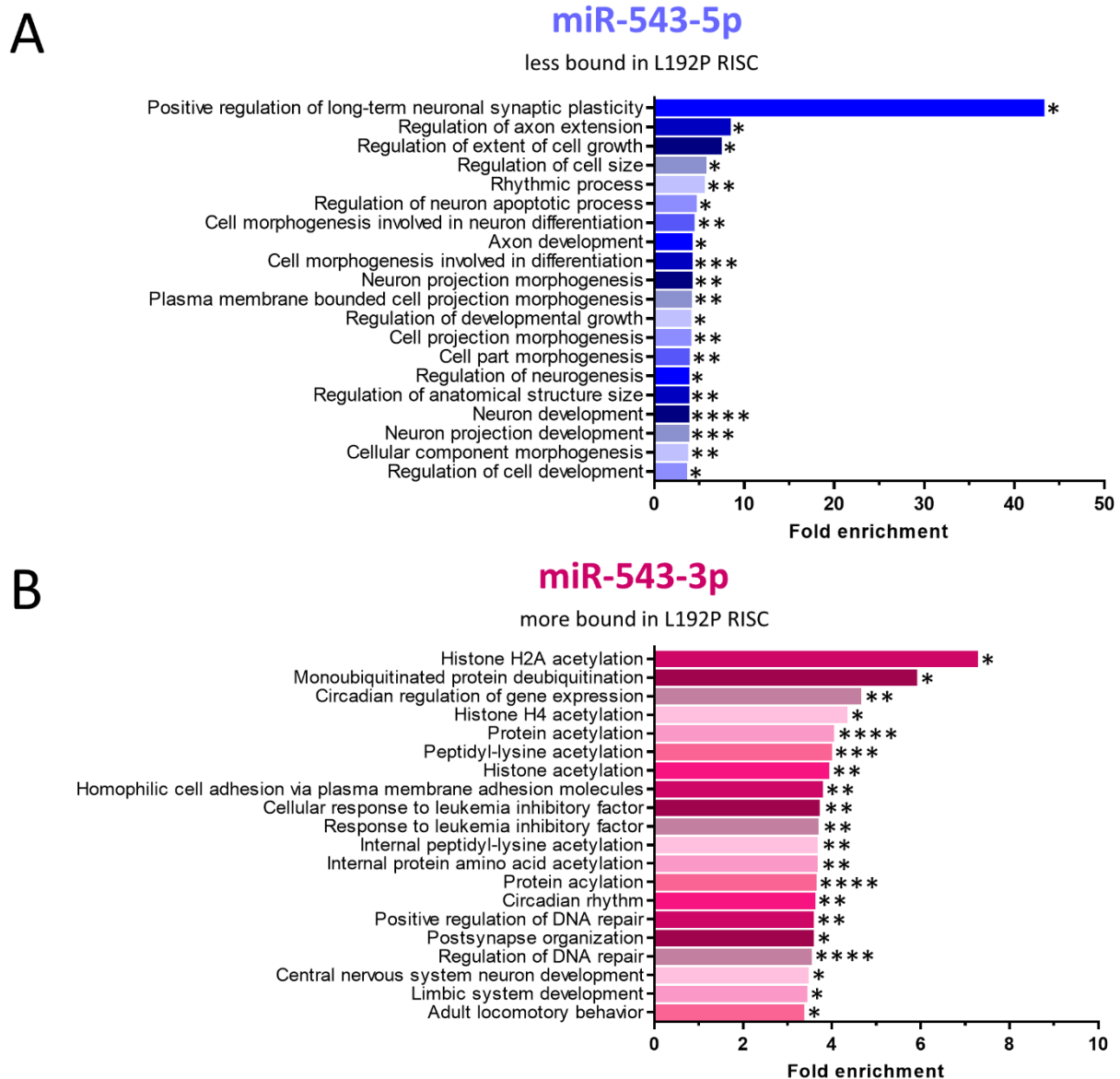


Figure 39: GO analyses of BPs for predicted targets of (A) miR-543-5p compared to (B) miR-543-3p. All miRDB-predicted targets were submitted to BP GO analyses using PANTHER. Fold enrichment for each GO term is shown with FDR \leq 0.05 = *, FDR \leq 0.01 = **, FDR \leq 0.001 = *** and FDR \leq 0.0001 = ****. 20 BP GO terms were enriched in both analyses. **(A)** miR-543-5p shown in blue exhibited less Ago2-binding so BPs were expected to be enhanced with Ago2-L192P compared to WT. **(B)** miR-543-3p was enriched in L192P-RISC, suggesting that the predicted targets contributing to the BPs were likely to be less silenced.

At last, the custom sequence submission in miRDB was used to predict targets of two isomiRs, miR-335-3p -3T and miR-672-5p 22:A->T, two miRNA variants that were exclusively incorporated into Ago2-L192P with highest count values among all L192P-specific isomiRs (Figure 36). The top target for the canonical miR-335-3p was synaptotagmin IV (*Syt4*) with highest expression in the cortex among the five highest scored targets with 32.3 TPM. This transcript was also a predicted target of the isomiR

miR-335-3p -3T, but with a lower target score (98 vs. 100) and rank (3 vs. 5, Table 46). The most reliable predicted target of the 3'-trimmed isomiR was *Thsd7a* (thrombospondin, type I, domain containing 7A) which was on third place in targets ranks of the canonical miR-335-3p. Three of the top five targets of canonical miRNA and isomiR overlapped, although allocated different targets ranks and scores. Two targeted transcripts were unique, DCN1 domain containing 1 (*Dcun1d1*) and the transmembrane protein 106B (*Tmem106b*) for the miR-335-3p and the transcripts coding for LIM domain only 7 (*Lmo7*) and inositol 1,3,4,5,6-pentakisphosphate 2-kinase (*lppk*) for the corresponding isomiR miR-335-3p -3T (Table 46).

Table 46: Comparison of the top five predicted targets between the canonical miR-335-3p and the isomiR-335-3p -3T. The targets that were predicted using miRDB were sorted by target score and allocated target ranks. Expression in the cortex was validated as TPM \geq 1 using the GTEx portal. The 3'-trimmed isomiR-335-3p -3T (red) was enriched in Ago2-L192P-IP and absent in Ago2-WT-IP. The gene symbols of shared targets between canonical miRNA and isomiR are indicated by blue color.

Target rank	Target score	Gene symbol	Gene description	Expression [TPM]
Canonical miR-335-3p				
1	100	<i>Syt4</i>	synaptotagmin IV	32.3
2	100	<i>Fam126b</i>	family with sequence similarity 126, member B	6.2
3	100	<i>Thsd7a</i>	thrombospondin, type I, domain containing 7A	1.7
4	99	<i>Dcun1d1</i>	DCN1, domain containing 1	6.0
5	99	<i>Tmem106b</i>	transmembrane protein 106B	4.9
isomiR miR-335-3p -3T				
1	99	<i>Thsd7a</i>	thrombospondin, type I, domain containing 7A	1.7
2	99	<i>Fam126b</i>	family with sequence similarity 126, member B	6.2
3	98	<i>Syt4</i>	synaptotagmin IV	32.3
5	98	<i>Lmo7</i>	LIM domain only 7	7.4
6	98	<i>lppk</i>	inositol 1,3,4,5,6-pentakisphosphate 2-kinase	5.7

The second isomiR for which targets were predicted was the isomiR miR-672-5p 22:A->T. This variant did not differ in length but contained a nucleotide exchange from the base adenine (A) to uracil (U). Although the modification was detected on RNA level, the altered base is represented by a T, which stands for thymine, following the Fehlmann *et al.* nomenclature. When targeted transcripts were compared between the canonical miR-672-5p and the polymorphic isomiR, the targets complement factor B (*Cfb*), transmembrane protein 167 (*Tmem167*), Argonaute RISC catalytic subunit 1 (*Ago1*) and the zinc finger protein 446 (*Zfp446*; human orthologue: ZNF446) overlapped with similar target ranks and scores (colored in blue, Table 47). The unique targets were ranked on fifth place. For miR-672-5p, the predicted target was nucleoporin 98 (*Nup98*), whereas perilipin 5 (*Plin5*) was found as transcript targeted by the isomiR miR-672-5p 22:A->T (Table 47).

Table 47: Comparison of the five highest ranked target transcripts between miR-672-5p and the isomiR miR-672-5p 22:A->T. miRDB-predicted targets were ranked by target score and cortical expression (TPM \geq 1) was confirmed via the GTEx portal. The isomiR miR-672-5p 22:A->T (red), was enriched in the IP of Ago2-L192P and absent in the Ago2-WT-IP.

Target rank	Target score	Gene symbol	Gene description	Expression [TPM]
Canonical miR-672-5p				
1	96	Cfb	complement factor B	3.4
2	94	Tmem167	transmembrane protein 167	29.6
3	94	Ago1	Argonaute RISC catalytic subunit 1	7.1
4	93	Zfp446	zinc finger protein 446	7.8
5	92	Nup98	nucleoporin 98	7.8
isomiR miR-672-5p 22:A->T				
1	96	Cfb	complement factor B	3.4
2	94	Tmem167	transmembrane protein 167	29.4
3	94	Ago1	Argonaute RISC catalytic subunit 1	7.1
4	93	Zfp446	zinc finger protein 446	7.8
5	92	Plin5	perilipin 5	4.8

The observation of shared predicted targets between canonical miRNAs and corresponding isomiRs indicated that the deregulation of translational silencing by Ago2-L192P may be more subtle compared to arm switching events but can still have distinct consequences on protein expression.

5. Discussion

5.1. Loss of Shank1 or Shank3 $\alpha\beta$ Affect Neuronal Protein Synthesis and the Postsynaptic Protein Network

In this thesis, I functionally analyzed and compared the pathomechanisms of two classes of NDD-linked genes. Mutations in the *SHANK* genes can cause ASDs and other NDDs. The association of *SHANK3* with ASDs is stronger and better characterized compared with *SHANK1* (Grabrucker *et al.* 2011, Sato *et al.* 2012). Shank1 and Shank3 are scaffold proteins that connect glutamate receptors to F-actin via a complex postsynaptic protein network (Boeckers *et al.* 1999, Sheng and Kim 2000, Kreienkamp 2008). Thus, *SHANK1* and *SHANK3* were analyzed as examples of NDD-associated genes that encode synaptic scaffold or cell adhesion proteins, whereas *AGO2* served as an example of an RBP-encoding gene. The N-terminus of Shank3 is a Ras association domain, which connects Shank proteins to MAPK signaling and deregulation of translation was proposed as a common pathomechanism in ASD (Kelleher and Bear 2008, Crino 2015, Lilja *et al.* 2017). The transcriptome in hippocampal neurons of the novel Lypd1-bacTRAPxShank3 $\alpha\beta$ mouse line was characterized to decipher the involvement of the N-terminal domains of Shank3 in the regulation of translation. The hippocampal proteome of PSD fractions from *Shank1* and *Shank3 $\alpha\beta$* knockout mice was assessed. In doing so, the effects of a loss of the Shank proteins on the composition of the postsynaptic protein network were determined.

5.1.1. Original and Novel *Shank1* and *Shank3 $\alpha\beta$* Knockout Mice Models Displayed an ASD-typical Phenotype

The open field behavioral test determined an ASD-typical phenotype in *Shank1* and *Shank3 $\alpha\beta$* knockout mice compared to littermates at 12 weeks of age. The PSD purification was performed subsequently to ensure an autistic phenotype at the time point of analyzing the proteome. Knockout of *Shank1* led to a severe reduction of body weight, while knockout of *Shank3 $\alpha\beta$* had no effect on body weight (Figure 5). Silverman *et al.* characterized the *Shank1*-KO mice compared to heterozygous and wildtype littermates. They reported no abnormalities in body weight but a slight increase in body temperature in knockouts compared to heterozygous mice at 10 weeks of age (Silverman *et al.* 2011). Another study found no differences in body weight and temperature in *Shank1*-KO pups between the postnatal day (PND) 2 and PND 12 (Wohr *et al.* 2011). Sungur *et al.* described a decrease of body weight in *Shank1*-KO pups (PND 12) and lower body temperature when compared to littermates (Sungur *et al.* 2014). It remains unclear why the severe decrease in body weight that I observed in the *Shank1*-KO mice did not occur in some studies and how this might be related to the reported changes in body temperature (Silverman *et al.* 2011, Wohr *et al.* 2011). It would be interesting to compare the body weight of *Shank1*-KO mice at different time points and to measure the body temperature in our experimental set up. Surprisingly, knockout mouse models regularly exhibit a reduction of body weight (Snell 1931, Reed *et al.* 2008). Reed *et al.* evaluated the body weight of 1977 knockout mouse models and found that 31.3% of viable knockout strains have reduced body weight (Birney *et al.* 2006, Reed *et al.* 2008). As the regulation of body weight is complex and not fully understood, the causal relationship between the knocked-out gene and the effect on body weight is often unknown. Same could be true for knockout of *Shank1* since no role of Shank1 in regulation of body weight has been published so far. The reduction of body weight might influence the motor capabilities of *Shank1*-KO mice. Interestingly, ASDs such as Rett syndrome are associated with impairments of motor skills and coordination (Clarke 1996, Phelan and McDermid 2012). During training sessions for a Morris water maze test, I observed that the *Shank1*-KO mice were unable to swim. This observation would fit the hypothesis of an impaired motor skill upon loss of Shank1. Motor deficits in *Shank1*-KO mice were described before, measured as reduced latencies in the rotarod test (Hung *et al.* 2008, Silverman *et al.* 2011). In contrast, the swimming ability of *Shank3 $\alpha\beta$* -KO mice is unimpaired (Vicidomini *et al.* 2017).

The *Shank3 $\Delta C/\Delta C$* ASD mouse model, which lacks expression of all major Shank3 isoforms (complete knockout), exhibits deficits in motor coordination determined by the rotarod test (Kouser *et al.* 2013). Interestingly, hypotonia and coordination deficits are regularly observed in patients with Phelan-McDermid syndrome, caused by haploinsufficiency of *SHANK3* (Phelan and McDermid 2012, Kouser *et al.* 2013). Shank1 is highly expressed in Purkinje cells in the cerebellum, whereas Shank3 is highly expressed in GABAergic neurons in the striatum (Bockers *et al.* 2004, Yoo *et al.* 2018). Both brain regions are of importance in controlling motor skills and coordination, which can be impaired in ASD (Clarke 1996, Peca *et al.* 2011, Cataldi *et al.* 2022). It would be interesting to investigate the function of Shank1 and Shank3 in the specific cell types and brain regions. This would allow conclusions about the contribution of these functions to the pathomechanism of ASD.

The open field test was performed to measure the locomotion of *Shank1*-KO and *Shank3 $\alpha\beta$* -KO mice. The knockouts of both lines exhibited reduced locomotion with the differences getting more pronounced over time (Figure 6 and Figure 7). It has been published before that *Shank1*-KO mice exhibit reduced activity during the open field test compared to WT littermates and the results here confirm this altered behavior (Hung *et al.* 2008, Silverman *et al.* 2011). In contrast, Duffney *et al.* tested heterozygous *Shank3*-KO (*Shank3 $+/ \Delta C$*) in the open field assay and did not observe differences in locomotion compared to WT controls (Duffney *et al.* 2015). The isoform-specific homozygous knockout of Shank3 $\alpha\beta$ results in decreased locomotion, whereas heterozygous knockout of all Shank3 isoforms does not. This may indicate a function of the N-terminal domains of Shank3 in a mechanism that affects locomotive behavior.

Knockout of *Shank1* and *Shank3 $\alpha\beta$* significantly increased the duration of self-grooming compared to their littermates (Figure 8). The extensive self-grooming was more pronounced in female *Shank1*-KO mice than in male *Shank1*-KO mice. In contrast, male *Shank3*-KO mice were more affected compared to female *Shank3*-KO mice. Repetitive behavior, measured as duration of self-grooming, has been studied in several *Shank* knockout mouse models as it is a core phenotype of ASD (Lord *et al.* 2000, Schmeisser *et al.* 2012, Sungur *et al.* 2014, Vicidomini *et al.* 2017). An increase in repetitive behavior was observed in KO mice of the *Shank1* and *Shank3* complete knockout lines, as well as in *Shank3 $\alpha\beta$* -KO mice (Schmeisser *et al.* 2012, Kouser *et al.* 2013, Sungur *et al.* 2014, Vicidomini *et al.* 2017). Notably, the study on *Shank3 $\Delta C/\Delta C$* mice reported increased self-grooming in older mice (10-13 months old) (Kouser *et al.* 2013). The interaction of Shank proteins with GKAP, also known as SAPAP, indirectly links Shank to AMPA and NMDA receptors (Boeckers *et al.* 1999, Naisbitt *et al.* 1999, Tu *et al.* 1999, Garner *et al.* 2000, Uchino *et al.* 2006, Kreienkamp 2008). *Sapap3* knockout mice also display severely increased duration and frequency in self-grooming (Welch *et al.* 2007). Thus, it has been presumed that loss of Shank might cause a reduction in postsynaptic GKAP/SAPAP, leading to a similar phenotype (Welch *et al.* 2007, Hung *et al.* 2008, Sungur *et al.* 2014). The rearing frequency of knockout mice from both lines was strikingly reduced (Figure 8). For the *Shank1*-KO mice, this result recapitulates those from Sungur *et al.*, whereas it is a novel finding that *Shank3 $\alpha\beta$* -KO mice exhibit increased rearing behavior.

Two novel mouse models were created by crossing *Lypd1*-bacTRAP mice, which express GFP-L10a in hippocampal neurons, with mice from the original *Shank1* and *Shank3 $\alpha\beta$* knockout lines. The novel *Lypd1*-bacTRAPx*Shank1*-KO and *Lypd1*-bacTRAPx*Shank3 $\alpha\beta$* -KO mice enable translatomic analyses using the bacTRAP method. The ASD-typical phenotype was validated in the novel mouse lines by the open field test (Figure 9). Due to restrictions in breeding capacities, these mice had to be tested in small cohorts. Nevertheless, KO mice from both lines exhibited decreased locomotion and the *Lypd1*-bacTRAPx*Shank3 $\alpha\beta$* -KO showed additional alterations in their behavior (less distance to the wall, less time spent in the center of the area), which were not observed for *Shank3 $\alpha\beta$* -KO of the original mouse model. Self-grooming and rearing behavior of *Lypd1*-bacTRAPx*Shank*-KO mice resembled the

phenotypes of the original lines, although the differences did not reach significance. Probably this was caused by higher variability due to testing of the mice in small cohorts on different days. In addition, several *Shank1*-KO mice were excluded from the open field test because they had to be housed in isolation due to aggressive behavior, which further negatively affected the results. Collectively, the behavior studies confirmed an autistic phenotype of original and novel mouse models for *SHANK*-associated forms of ASDs at the time point of transcriptome and proteome analyses.

5.1.2. Absence of the N-terminal Domains of Shank3 Lead to Subtle Alterations in the Transcriptome of Hippocampal Neurons

The consequences of *Shank3αβ* knockout on the hippocampal neuronal transcriptome of Lypd1-bacTRAPx*Shank3αβ*-KO mice were investigated. The expressed and actively translated mRNAs were determined by applying the bacTRAP method and transcriptomics. Similarities between conditions and biological replicates were assessed by PCA, which showed rather high variability (Figure 11). Expressed mRNAs (IC samples) were more similar to each other compared to the actively translated mRNAs (IP). This indicates that the expressed mRNAs were vastly different from the actively translated mRNAs and that expression of mRNAs was less variable compared to the regulation of translation. The differentially translated mRNAs were determined in a DEG analysis (Figure 12 and Figure 13). Statistical significance of differentially translated transcripts was appointed by having a FDR of ≤ 0.1 and a fold change of > 0.5 . By applying these rather mild cutoffs, 26 differentially translated mRNAs were determined, of which nine were translated less and 17 were translated more as a result of *Shank3αβ* knockout. Thus, absence of the N-terminal domains of Shank3 resulted in subtle alterations of translation of a subset of neuronal transcripts.

Interestingly, the DEG analysis of expressed yielded no differentially expressed transcripts. This indicates that differential translated mRNAs were present due to an altered regulation of translation and not caused by an altered abundance of transcripts. It should be considered that the transcripts measured in IC samples were not neuron-specific since no selective purification step for the neuronally expressed GFP-tagged L10a protein occurred, such as it was performed in the IP samples. The expressed mRNAs were combined from hippocampal neurons and all additional cell populations present in the hippocampus. This might have biased the results, as subtle neuron-specific changes in expression may not be detectable in the total mRNA expressed from all hippocampal cells. The first centrifugation step of the bacTRAP method separates the nuclei from the cytosol. Specific purification of expressed mRNAs from the neuronal cell population could be enabled by applying nuclei preparation and fluorescence activated cell sorting (FACS) of GFP-positive nuclei. These transcripts could be analyzed by RNA-seq, or expression of selected candidates could be verified by qPCR to determine whether differentially translated mRNAs were also differentially expressed. This approach should be pursued in future studies to confirm whether the N-terminus of Shank3 functions specifically in regulation of translation or also affects gene expression.

The translation of the mRNA encoding Ret was most strongly decreased by loss of *Shank3αβ*. Ret is a conserved receptor tyrosine kinase expressed in the CNS of vertebrates from early embryonic development through adulthood (Pachnis *et al.* 1993, Avantaggiato *et al.* 1994, Attie-Bitach *et al.* 1998). Receptor tyrosine kinases are transmembrane proteins which transduce extracellular signals into intracellular signaling cascades (Mahato and Sidorova 2020). Ret is activated by the glial cell line-derived neurotrophic factor (GDNF), which, despite its name, is expressed in neurons instead of glial cells (Durbec *et al.* 1996, Pascual *et al.* 2008, Gonzalez-Reyes *et al.* 2012, Mahato and Sidorova 2020). The activation is calcium dependent and induces autophosphorylation of the intracellular domains of Ret, which in turn triggers outgrowth of neurites and regulates neuronal survival (Durbec *et al.* 1996, Nozaki *et al.* 1998, Anders *et al.* 2001, Penttinen *et al.* 2018). Ret functions are mediated through several signaling cascades such as the phosphoinositide-3-kinase (PI3K), the MAPK, and Rac/c-Jun N-terminal kinase (JNK) pathways (van Weering and Bos 1998, Fukuda *et al.* 2002, Meka *et al.* 2015, Penttinen *et al.* 2018). Thus, reduced expression of Ret in hippocampal neurons of Lypd1-

bacTRAPx*Shank3αβ*-KO mice may result in diverse deregulated signaling pathways, altering neuronal migration and survival. This might contribute to a pathomechanism that leads to ID and ASD, as observed in patients harboring mutations in *SHANK3*. Interestingly, the isoform Ret9, which is expressed stronger in neurons compared to Ret51, harbors a PDZ ligand that binds to the Shank3 PDZ domain (Schuetz *et al.* 2004). The reduced translation of Ret in Lypd1-bacTRAPx*Shank3αβ*-KO mice might be indirectly connected to reduction of this specific interaction of Shank3. Shank3 connects glutamatergic signaling to F-actin dynamics and limits integrin activation through Ras- and Rap-dependent mechanisms (Du *et al.* 1998, Boeckers *et al.* 1999, Lim *et al.* 1999, Lilja *et al.* 2017, Salomaa *et al.* 2021). Loss of Ret also alters F-actin dynamics, mediated by altered MAPK, PI3K and Rac-dependent pathways and it has been suggested that Ret and integrins act in the same pathway to promote dendrite adhesion and growth (van Weering and Bos 1998, Fukuda *et al.* 2002, Soba *et al.* 2015). Thus, Shank3- and Ret-dependent regulation of the actin cytoskeleton and of integrins might be interconnected by small GTPases-dependent signaling pathways. Interestingly, *RET* is a known disease gene, as loss of function mutations are associated with Hirschsprungs disease, characterized by disrupted neural crest cell migration and developmental defects of the enteric nervous system (Knowles *et al.* 2006, Jiang *et al.* 2018, Wu *et al.* 2020).

One of the transcripts that showed enhanced translation following *Shank3αβ* knockout was the transcript coding for Rel, also known as c-Rel, which was initially identified as proto-oncogene in humans (Brownell *et al.* 1987). Rel proteins contain a nuclear targeting sequence and shuttle between the cytosol and the nucleus (Gilmore and Temin 1988). In the nucleus, Rel proteins function as transcription factors of the NF-κB family, which are involved in regulation of cellular differentiation and proliferation (Lenardo and Baltimore 1989, Ballard *et al.* 1990, Ip *et al.* 1991, Gerondakis *et al.* 2006, Mitchell *et al.* 2016). Deregulation of NF-κB-controlled transcription has detrimental consequences in neurons and is a characteristic of neuroinflammatory diseases such as Parkinson's disease (Courtois and Gilmore 2006, Mitchell *et al.* 2016, Singh *et al.* 2020). The activity of Rel is primarily regulated by its intracellular localization, rather than the level of transcription and translation. It would be crucial to determine the Rel protein levels in neuronal nuclei from Lypd1-bacTRAPx*Shank3αβ*-KO mice to conclude whether the activity of Rel is altered in absence of *Shank3αβ*. Taken together, Ret and Rel are interesting candidates for further studies deciphering the role of *Shank3αβ* in the pathomechanism of ASD.

However, focusing on selected candidate transcripts may oversimplify the molecular defects caused by the absence of *Shank3αβ* in hippocampal neurons. To interpret the entirety of deregulated biological processes and their relation to each other, a clustered gene ontology analysis of all differentially translated mRNAs is depicted in Figure 40. Three clusters of decreased biological processes in the knockout mice present interesting connections to molecular defects and behavioral impairments in ASDs. The interrelated terms "axon guidance" and "neuron projection guidance" formed the first cluster of deregulated molecular pathways that could have detrimental consequences for neurodevelopment. The same applies for the second cluster of decreased biological processes, which consisted of the four terms "axon ensheathment," "neuron ensheathment," "myelination," and "glial cell development." The third cluster consisted of the terms "learning," "associative learning," and "movement behavior," which fits well to typical behavior of ASD patients and mouse models. By far the largest cluster consisted of 15 highly enriched and interconnected biological processes. These processes included "ribosome biogenesis", "RNA splicing", and various terms of RNA modification, processing, and regulation of multiple RNA classes. The increased RNA metabolism and ribosome biogenesis hint towards higher rates of translation as an effect of *Shank3αβ* knockout. Interestingly, the biological process "positive regulation of translation" was also enriched.

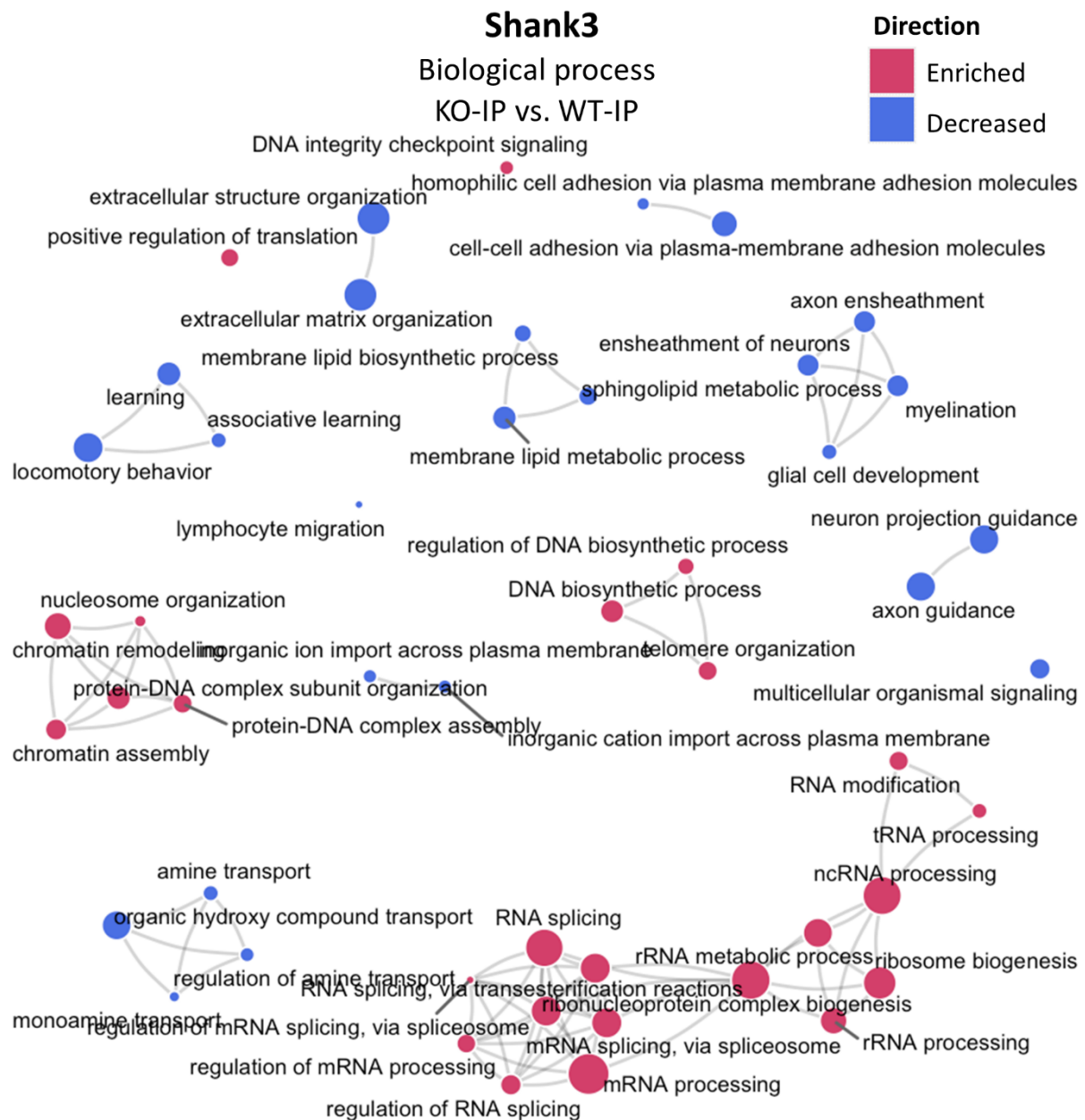


Figure 40: Clustered GO analysis of BPs influenced by differentially expressed mRNAs in *Shank3αβ*-KO hippocampal neurons. The contribution of differentially translated transcripts from the KO-IP vs. WT-IP comparison was assessed. The enriched (red) and decreased (blue) biological processes are shown as nodes. The node size illustrates the number of deregulated mRNAs contributing to the deregulated term. Lines connecting nodes indicate a functional relation of biological processes.

Fragile X syndrome (FXS) is a NDD characterized by ID and ASD-like behavior in varying degrees (Verkerk *et al.* 1991, Devys *et al.* 1993). FXS is caused by mutations in *FMR1* that encodes the fragile X mental retardation protein (FMRP) (Verkerk *et al.* 1991, Devys *et al.* 1993). FMRP is a RNA binding protein that acts as a negative regulator of translation in neurons (Zhang *et al.* 2001, Saffary and Xie 2011). Several of the known targets of FMRP have known functions in synaptogenesis, neuron morphology and function (Zhang *et al.* 2001, Huber *et al.* 2002, Bolduc *et al.* 2008, Darnell *et al.* 2011). Elevated translation was proposed as a key pathomechanism causing NDD-typical phenotypes in *Fmr1* knockout mice and was suggested to be a common pathomechanism in autism (Kelleher and Bear 2008, Richter *et al.* 2015, Prashad and Gopal 2021). Torossian *et al.* determined the rates of translation in adult male *Shank3αβ*-KO mice (*Shank3^{ex4-9}* mice, a neo cassette replaces exons 4-9, resulting in loss of Shank3 isoforms α and β) using L-[1-¹⁴C]-leucine quantitative autoradiography. *Shank3αβ*-KO mice had significantly elevated rates of translation in the brain when compared to littermate controls. This

effect was not observed in the liver and therefore might be brain specific, possibly due to the specific functions of Shank3 in neurons (Torossian *et al.* 2021).

The deregulated function of Shank3 results in reduced number and volume of spines and alters synaptic plasticity (Jiang and Ehlers 2013). The upregulation of translation might be a compensatory effect to counteract impaired synaptic function (Torossian *et al.* 2021). The clustered GO analysis of differentially translated hippocampal neurons of *Lypd1-bacTRAPxShank3 $\alpha\beta$ -KO* mice showed that several biological processes connected to RNA metabolism, ribosome biogenesis and translation were increased. This result supports the hypothesis that elevated rates of translation contribute to the pathomechanism of ASD. Nevertheless, the molecular defects observed here were distinct from a general upregulation of translation, such as it is caused by loss of function of FMRP in FXS.

5.1.3. Loss of Shank1 and Shank3 $\alpha\beta$ Causes Differences in the Postsynaptic Proteomes

I analyzed the postsynaptic proteome of *Shank1* and *Shank3 $\alpha\beta$* knockout mice. PSD fractions were purified from hippocampal tissue and the protein composition assessed by mass spectrometry. The efficiency of the purification method was validated by western blot (Figure 15). The knockout of *Shank1* and *Shank3 $\alpha\beta$* was further validated by mass spectrometry (Figure 16). There, complete loss of Shank1 protein was observed in *Shank1-KO* mice, whereas the abundance of other Shank proteins was not affected. A reduction but not a complete loss of Shank3 was determined in the PSD proteome of *Shank3 $\alpha\beta$ -KO* mice, consistent with the notion of an isoform-specific knockout. The absence of the SPN, ANK and SH3 domain of Shank3 was demonstrated by detection of peptides originating from the specific domains (Figure 17). It remains uncertain, why a peptide from the PDZ domain of Shank3 displayed an intermediate abundance between peptide from the N-terminal and C-terminal domains. The expression of Shank3 isoforms containing the PDZ domain could be assessed in future studies, to determine the exact effect of deletion of exon 11 in the ASD mouse model.

Mass spectrometry identified a total of 5176 different proteins across all conditions. The differential abundant proteins between *Shank-KO* and WT littermates were identified. Proteins with a p-value ≤ 0.05 and a fold change > 1.5 were considered significantly deregulated, which yielded a total of 113 deregulated proteins. Comparison of the cutoffs applied here ($p \leq 0.05$, $FC > 1.5$) with the cutoffs for significantly deregulated translated transcripts ($p \leq 0.1$, $FC > 0.5$) suggests that the alterations in the proteome were more severe and less variable compared to those in the transcriptome.

In the *Shank1* analysis, 46 deregulated proteins were determined, of which 28 were increased and 18 were decreased. One of the significantly decreased proteins was *Arpc5*, a scaffolding subunit of the actin filament nucleating *Arp2/3* complex (Molinie and Gautreau, 2018; Goley and Welch, 2006). This protein was especially interesting due to the known functions of Shank proteins in actin dynamics. The *Arp2/3* complex facilitates branching of actin networks by enhancing nucleation and growth of new actin filaments from the side of existing actin filaments (Welch *et al.* 1997, Blanchoin *et al.* 2000, Volkmann *et al.* 2001, Welch *et al.* 2007, Mullins *et al.* 2016). Decreased abundance of *Arpc5* might result in compromised regulation of actin branching with detrimental consequences for the stability and morphology of dendritic spines. The F-actin-capping protein subunit alpha-1 (*Capza1*) was also decreased, again highlighting the contribution of altered actin dynamics to *Shank*-associated pathomechanisms.

Qin *et al.* performed a study of the *SHANK1* gene in 613 ASD patients and compared *SHANK1* sequences to healthy controls. Six ASD-associated missense variants were found. One of these, the R874H variant, was chosen to generate the corresponding *Shank1-R882H* knockin mouse model (Qin *et al.* 2022). Proteomic analysis of PSD fractions from hippocampal tissue of these mice identified a total of 2081 proteins, of which 472 proteins were differentially abundant. Several less abundant proteins localize to postsynapses of glutamatergic synapses, such as ionotropic and metabotropic glutamate receptors (NMDAR and AMPAR subunits, GluN1/N2, GluA1/A2/A4, mGluR1) and Homer proteins. Remarkably,

all of the differentially abundant proteins interact direct or indirectly with Shank1 (Qin *et al.* 2022). None of the proteins that were deregulated in the postsynaptic proteome of *Shank1*-R882H knockin mice were affected by knockout of *Shank1* analyzed here. Hung *et al.*, who generated and characterized the *Shank1*-KO line, observed no changes in postsynaptic abundance of glutamate receptors, which validates the result obtained here (Hung *et al.* 2008). The differences in proteomic alterations in *Shank1*-R882H knockin mice compared to *Shank1*-KO mice suggest that the molecular defects caused by missense variants in *Shank1* are different to those resulting from a complete loss of *Shank1*.

The analysis of *Shank3αβ*-KO mice identified 67 significantly altered proteins, of which 28 proteins were enriched and 39 decreased. Thus, absence of Shank3αβ induced stronger differences in the postsynaptic proteome compared to Shank1. Homer proteins interact directly with Shank proteins and Homer 1 was significantly decreased upon *Shank3αβ* and *Shank1* knockout (Naisbitt *et al.* 1999, Tu *et al.* 1999, Uchino *et al.* 2006). In studies performed by Vicidomini *et al.*, no change in abundance of Homer in hippocampal PSD fractions was determined, contradicting the results from the proteomic analysis performed here. In contrast, reduced levels of Homer1 were detected in PSD fractions of knockout mice from four independent *Shank*-KO mouse models, the *Shank1*-KO, *Shank3αβ*-KO (*Shank3^{e11}*-KO), *Shank3^{e4-9}*-KO and *Shank3^{e13-16}*-KO lines (Peca *et al.* 2011, Wang *et al.* 2011). These results are consistent with the reduction in Homer1 observed here, although other differentially abundant proteins such as GKAP, GluA1, GluN2B, and mGlu5 did not overlap with any of the aforementioned studies (Peca *et al.* 2011, Wang *et al.* 2011, Vicidomini *et al.* 2017). The consistent reduction of postsynaptic Homer proteins in several independent knockout mouse lines suggests that reduced abundance of Homer in the PSD is a common molecular defect that may contribute to the ASD-typical phenotypes present in these models. Reim *et al.* performed proteomics on hippocampal PSD fractions from *Shank3αβ*-KO mice and identified a total of 2345 proteins of which 55 were significantly altered compared to littermate controls (Reim *et al.* 2017).

It is unknown whether mutations in *SHANK1* and *SHANK3* cause ASD by similar or different pathomechanisms. Compared with *SHANK1*, more ASD-associated mutations are known in the *SHANK3* gene, and mutations in *SHANK3* trigger ASD and ID of higher severity than *SHANK1* mutations (State 2010, Leblond *et al.* 2014). In this study, the behavioral phenotypes of the original *Shank1*-KO and *Shank3αβ*-KO lines were of similar severity. Proteomics showed that loss of major Shank3 isoforms resulted in more severe changes in postsynaptic protein composition than complete loss of Shank1. Shank3 localizes to the synapse early in embryonic development and is involved in signal transduction that initiates the formation of the postsynaptic scaffold (Grabrucker *et al.* 2011, Mossa *et al.* 2021). Shank1 localizes to the postsynapse at later stages of development and recruits several factors required for synaptic maturation. Therefore, it has been suggested that Shank3 facilitates the activation of intracellular signaling to recruit Shank1, which in turn is required for synapse stabilization (Naisbitt *et al.* 1999, Tu *et al.* 1999, Grabrucker *et al.* 2011, Mossa *et al.* 2021). This sequential arrival at the PSD may account for the stronger effect of the absence of Shank3 on the postsynaptic proteome compared with the loss of Shank1, as well as for the stronger association of *SHANK3* mutations with ASD than *SHANK1* mutations.

Deregulated biological processes influenced by deregulated proteins in the postsynaptic proteome of *Shank*-KO mice were determined (Figure 20 and Figure 21). In the *Shank1* analysis, the most enhanced BPs were “negative regulation of tubulin acetylation” and “regulation of tubulin deacetylation”. This hints towards a novel function of Shank1 in regulation of tubulin acetylation. tubulins form microtubules as part of the cytoskeleton in axons and function in intracellular transport processes, morphological changes, and motility (Amos and Klug 1974, Chaaban and Brouhard 2017, Nekooki-Machida and Hagiwara 2020). Acetylation of α-tubulin is associated with durable, stable microtubules, although the exact mechanism of how acetylation leads to increased stability is unknown (LeDizet and Piperno 1987, Palazzo *et al.* 2003, Kalebic *et al.* 2013). The acetylation induces a change of

conformation in α -tubulin that regulates neuronal function (Eshun-Wilson *et al.* 2019, Nekooki-Machida and Hagiwara 2020). Kinesin-dependent axonal transport of vesicles and protein complexes is more efficient along acetylated microtubules due to enhanced interaction of Kinesin-1 with acetylated α -tubulin compared with unacetylated α -tubulin (Reed *et al.* 2006, Dompierre *et al.* 2007, Even *et al.* 2019). Interestingly, tubulin acetylation is required for proper neurogenesis and malfunction of tubulin acetylation is associated with neurodegenerative diseases such as Parkinson's disease and Alzheimer's disease (Godena *et al.* 2014, Law *et al.* 2014, Selenica *et al.* 2014). Thus, deregulation of tubulin acetylation as a consequence of the absence of Shank1 may contribute to the pathomechanism of *SHANK1*-associated NDDs.

The four most enriched BPs in the Shank3 analysis were associated with glycolytic metabolism and were shared with the Shank1 analysis. Torossian *et al.*, who found that the rate of translation was increased in Shank3 $\alpha\beta$ -KO mice (see above), predicted an elevated energy metabolism to provide the energy required for the enhancement of translation (Torossian *et al.* 2021). This hypothesis aligns well with the changes in the transcriptome and proteome detected in hippocampal neurons from Shank3 $\alpha\beta$ -KO mice. Because the behavior and proteome of Shank1-KO mice were also altered, it would be very interesting to evaluate the transcriptome of this line and compare the results obtained with those of the Shank3 transcriptome analysis.

It has been hypothesized that ASD-associated mutations lead to either disruption of synaptic structure or deregulation of protein synthesis (Santini and Klann 2014). Analysis of deregulated biological processes in the proteome of Shank-KO mice was inconclusive regarding this hypothesis, although enhanced glycolytic metabolism suggested increased translation as a common pathomechanism. Hence, I performed hierarchical clustered GO analyses using Cytoscape Bingo to determine the molecular functions of the deregulated postsynaptic proteins from both mouse models (Shannon *et al.* 2003, Maere *et al.* 2005). Among the enriched molecular functions in the Shank1 analysis were "ATP binding" and "NAD or NADH binding", which might hint towards increased metabolic rates in postsynapses of Shank1-KO mice (Figure 41). The central decreased molecular function was "protein binding". The cluster comprised several terms of receptor binding, such as "ionotropic glutamate receptor binding" and "G-protein-coupled receptor binding". Furthermore, "small GTPase binding" and "Ral GTPase binding" were decreased molecular functions. This result connects the molecular defects induced by loss of Shank1 to deregulation of G-protein coupled signaling.

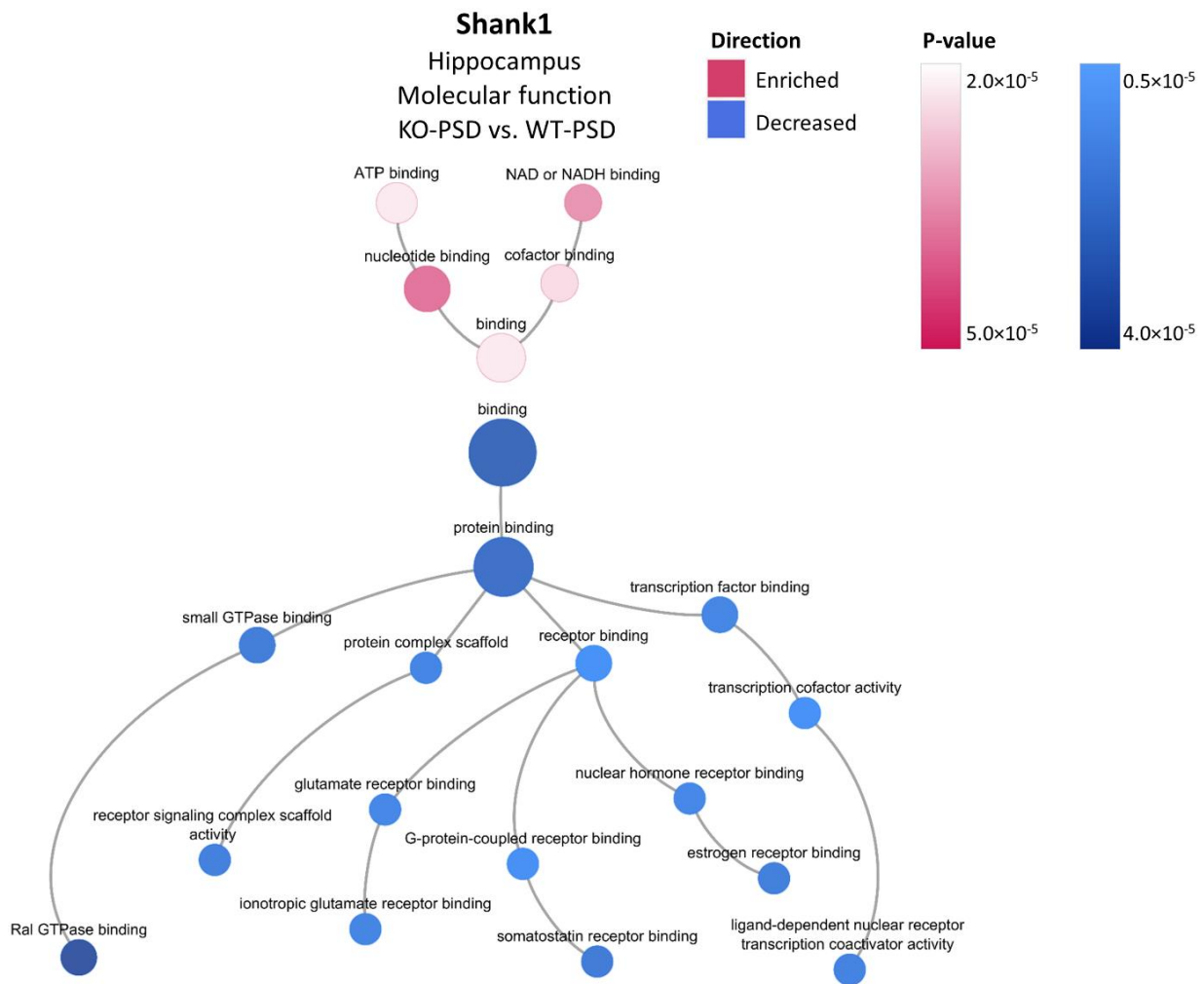


Figure 41: Hierarchical clustered GO analysis of affected molecular functions in the postsynaptic proteome of *Shank1*-KO mice. Deregulated terms are shown as nodes. The size of a node corresponds to the number of deregulated proteins that contributed to that term. Enriched molecular functions are shown in a red gradient and decreased molecular functions in a blue gradient. The intensity of the node color indicates the significance of the respective term, which was determined by an adjusted p-value. Functional dependencies between terms are represented as connecting lines.

Remarkably, the *Shank3* analysis determined that also for postsynaptic proteomes of *Shank3 $\alpha\beta$* -KO mice, the most reduced cluster of molecular functions was "binding," separated into "protein binding" and "RNA binding." Again, three terms related to G protein-coupled receptor binding and signaling appeared, emphasizing the importance of these molecular functions in the *Shank3*-associated pathomechanism. Notably, the term "small GTPase-mediated signal transduction" was enriched, whereas the terms "G-protein coupled receptor binding" and "type 5 metabotropic glutamate receptor binding" were decreased. GO analyses of deregulated molecular functions indicated a strong contribution of protein binding to the molecular defects in the proteome of both *Shank*-KO lines. This suggests reduced protein binding as a common molecular defect contributing to the pathomechanism in the ASD mouse models and demonstrates the importance of the Shank proteins as scaffold proteins for the formation of the postsynaptic protein network.

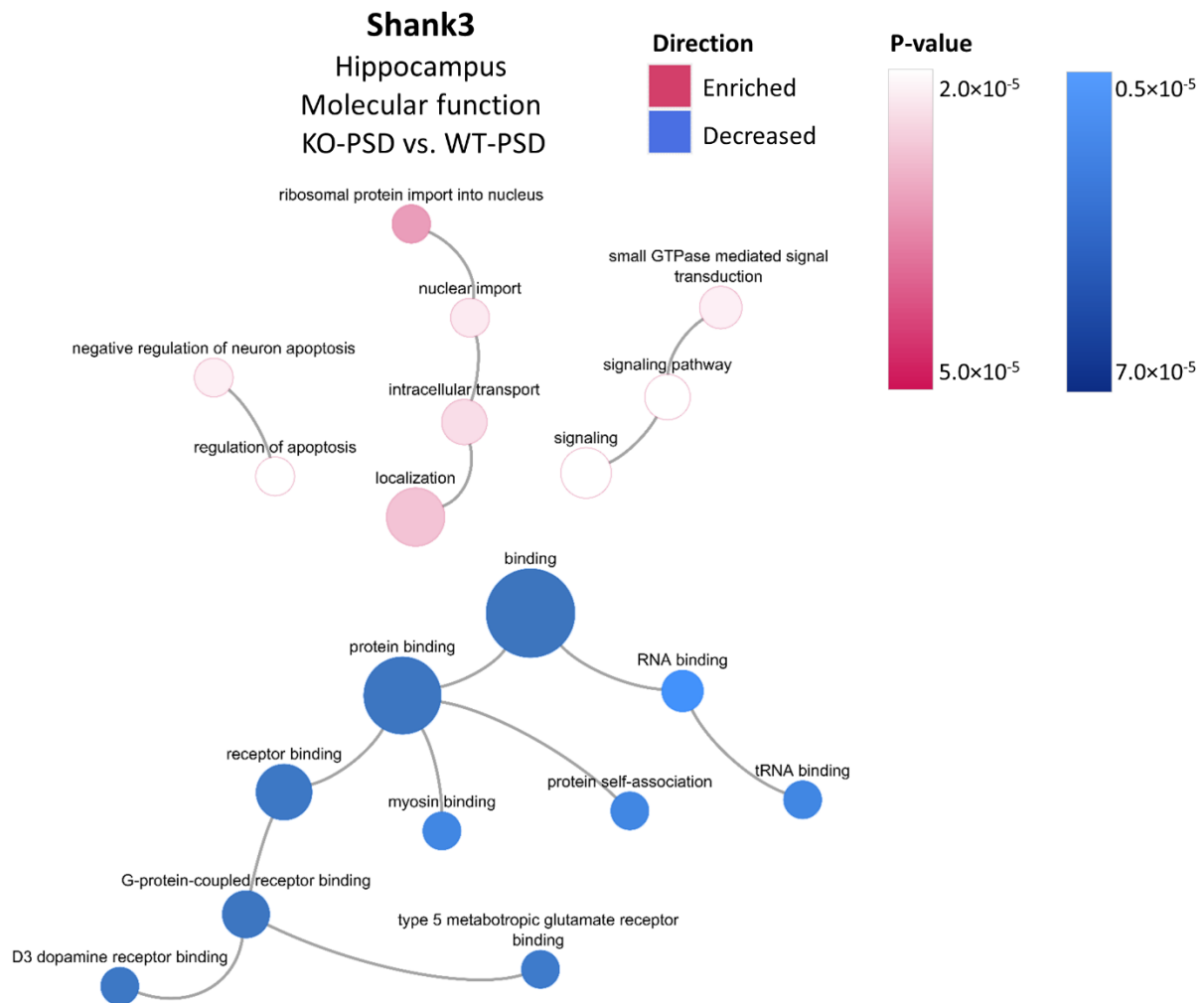


Figure 42: Hierarchical clustered GO analysis of affected molecular functions in the postsynaptic proteome of *Shank3αβ*-KO mice. Deregulated terms are shown as nodes. The size of a node corresponds to the number of deregulated proteins that contributed to that term. Enriched molecular functions are shown in a red gradient and decreased molecular functions in a blue gradient. The intensity of the node color indicates the significance of the respective term, which was determined by an adjusted p-value. Functional dependencies between terms are represented as connecting lines.

In summary, seven deregulated proteins were shared between the proteomes of *Shank1*-KO and *Shank3αβ*-KO mice. The converging biological processes were associated to increased glycolytic metabolism. The molecular functions of the deregulated proteins showed a strong contribution of reduced protein binding to the molecular defects triggered by the absence of Shank1 and Shank3αβ. The majority of the differentially abundant proteins, biological processes, and molecular functions were specific for postsynapses from either *Shank1*-KO or *Shank3αβ*-KO mice. Thus, the pathomechanisms causing *SHANK1*- and *SHANK3*-associated forms of ASD might also differ and may share only a few deregulated signaling pathways that could be related to small GTPases and G-protein-mediated signaling.

5.1.4. Absence of Shank1 and Shank3αβ Affect the Activation Status of the CaMKIIα at the Postsynapse

The N-terminus of Shank3 interacts with CaMKIIα in its unphosphorylated, inactive state (Cai *et al.* 2021). This interaction was verified by coimmunoprecipitation. The binding of N-terminal segments of Shank1, Shank2 and Shank3 to CaMKIIα was compared (Figure 22). The N-terminus of Shank3 displayed the most efficient interaction with CaMKIIα. Also the N-terminus of Shank1 interacts with CaMKIIα, although this interaction is weaker compared to Shank3. In the proteome analysis, no changes in

abundance of postsynaptic CaMKII α was determined in PSD fractions of *Shank1*-KO and *Shank3 $\alpha\beta$* -KO mice compared to controls. However, the absence of Shank1 and Shank3 $\alpha\beta$ increased the proportion of active phosphorylated CaMKII α in the PSD fractions of both brain regions. The change in CaMKII α activation status was more pronounced in the cortex than in the hippocampus. In addition, the effect of loss of Shank3 $\alpha\beta$ was stronger compared with Shank1. These results suggest that both Shank3 and Shank1 play a role in regulating CaMKII α -mediated signaling in postsynapses of the hippocampus and cortex. Autophosphorylation of CaMKII α at threonine 286, which was specifically detected in the western blot analysis, regulates critical functions for neuronal signaling and plasticity underlying learning and memory (Lisman *et al.* 2012, Hell 2014, Shonesy *et al.* 2014, Perfitt *et al.* 2020). CaMKII α is rapidly translocated from the soma to dendritic spines when postsynapses receive activating signals, leading to the accumulation of scaffold proteins such as PSD-95, SAPAP, Homer, and Shank, all of which stabilize the PSD (Shen and Meyer 1999, Dosemeci *et al.* 2001, Matsuzaki *et al.* 2004, Otmakhov *et al.* 2004, Lee *et al.* 2009, Bosch *et al.* 2014). Furthermore, CaMKII α shuttles between distinct subcompartments within the postsynapse (Cai *et al.* 2021). Most of the known interaction partners interact with CaMKII α in its active, phosphorylated form (Bayer *et al.* 2001, Baucum *et al.* 2015, Saneyoshi *et al.* 2019, Perfitt *et al.* 2020). Active CaMKII α binds to subunits of NMDA receptors (GluN2B), which are located at the postsynaptic membrane (Strack and Colbran 1998, Bayer *et al.* 2001, Bayer *et al.* 2006). In contrast, Shank proteins interact with the inactive form of CaMKII α and are localized in deeper layers of the PSD, located farther from the postsynaptic membrane (Cai *et al.* 2021). Subcompartments of the PSD are thought to generate through liquid-liquid phase separation (LLPS), driven by multivalent interactions of scaffold proteins that induce condensate formation (Zeng *et al.* 2016, Zeng *et al.* 2018, Zeng *et al.* 2019). Cai *et al.* showed that inactive CaMKII α is recruited to condensates that are enriched in Shank proteins, facilitated by the direct interaction of Shank to CaMKII α (Cai *et al.* 2021). Thus, the increase of activated CaMKII α in *Shank1*-KO and *Shank3 $\alpha\beta$* -KO mice might be caused by altered LLPS during synaptogenesis.

A model by Cai *et al.* suggested that Shank3 might retain inactive CaMKII α in deeper layers of the PSD to control shuttling and activation status of CaMKII α and connected signaling cascades. In addition, interaction of Shank3 to CaMKII α keeps the kinase close to the postsynapse, to ensure its presence upon reception of excitatory signals and rapid activation of CaMKII α -dependent signaling pathways (Tao-Cheng 2020, Cai *et al.* 2021). This hypothesis is supported by the results presented here, as absence of Shank3 $\alpha\beta$ altered the activation status of CaMKII α without affecting the overall abundance. Also, Shank1 appears to participate in this mechanism, as binding of Shank1 to CaMKII α was demonstrated and increased abundance of active CaMKII α was detected in PSD fractions of *Shank1*-KO mice. Notably, this effect was not only shared among the Shank proteins but also between the two brain regions hippocampus and cortex, indicating its importance in different brain areas. Future studies should aim to determine the shuttling mechanism of CaMKII α in *Shank1*-KO and *Shank3 $\alpha\beta$* -KO mice to show if absence of Shank1 and Shank3 $\alpha\beta$ indeed affect translocation of CaMKII α from the postsynaptic membrane to deeper layers of the PSD. Furthermore, the LLPS-dependent formation of condensates and their properties might be assessed in primary neurons from *Shank1*-KO and *Shank3 $\alpha\beta$* -KO mice using methods such as fluorescence recovery after photobleaching (FRAP). Collectively, the results presented here hint towards regulation of CaMKII α -dependent signaling by the N-termini of Shank1 and Shank3 that may contribute to the pathomechanism in *SHANK*-associated ASDs.

5.1.5. Comparison of the Translatome and Proteome in the Hippocampus of *Shank3 $\alpha\beta$* Knockout mice

I compared the determined alterations in the translatome and proteome in hippocampal tissue of *Shank3 $\alpha\beta$* -KO mice. The translatome analysis detected 26 differentially translated neuronal mRNAs, of which 35% were less translated and 65% more translated. The proteome analysis of PSD fractions

identified 67 differentially abundant proteins, of which 42% were decreased and 58% were enriched. No overlap between the deregulated candidates and biological processes of both analyses was observed. Thus, the alterations of the translome and proteome caused by absence of Shank3 $\alpha\beta$ did not converge in common molecular pathways. Qin *et al.* performed transcriptomics on hippocampal tissue from *Shank1*-R882H knockin mice. Of 23,718 expressed transcripts, only 14 showed significant changes between KO and WT conditions (Qin *et al.* 2022). Astonishingly, no overlap existed between differentially abundant postsynaptic proteins and the deregulated transcripts (Qin *et al.* 2022). This observation, made in *Shank1*-R882H knockin mice, is similar to the results obtained here in *Shank3 $\alpha\beta$* -knockout mice, indicating that expressed or translated mRNA do not correlate well with postsynaptic protein abundances in *Shank*-KO mouse models. Transcriptomics and translomics measure RNA abundance, which is dependent on rates of transcription, splicing, processing, modification and degradation (Wachutka and Gagneur 2017, Chappleboim *et al.* 2022). A growing number of studies suggest that the amount of transcripts in neurons does not correlate well with the amount of protein because mRNAs are transcribed at steady-state levels to allow rapid activation of translation by extracellular or intracellular signals (Morris *et al.* 2010, DeBoer *et al.* 2014, Kraushar *et al.* 2014, Hasin *et al.* 2017, Popovitchenko *et al.* 2020, Hoye and Silver 2021, Rotello and Veenstra 2021).

Synapses and the soma have different transcriptomes and translomes through distinct control of transport and translation of mRNAs (Rotello and Veenstra 2021). These changes occur during development and contribute to synaptic plasticity (Grunditz *et al.* 2008, Colgan and Yasuda 2014, Rotello and Veenstra 2021). Synaptic plasticity is defined as the strengthening or weakening of synapses dependent on the reception of neuronal activity. Regulation of translation and other posttranscriptional mechanisms contribute significantly to the development of the postsynaptic proteome (Vogel *et al.* 2010, Ghazalpour *et al.* 2011). Local translation enables changing the postsynaptic proteome of a specific dendritic spine and this may alter its properties such as size and synaptic strength (Klann and Dever 2004, Fuchs *et al.* 2006, Sutton and Schuman 2006, Twiss and van Minnen 2006). Thus, the discrepancy between translome and proteome candidates could be due to the importance of local translation in hippocampal neurons of *Shank3 $\alpha\beta$* -knockout mice. Furthermore, the results may suggest altered synaptic plasticity upon loss of Shank3 $\alpha\beta$. Interestingly, impaired synaptic plasticity was shown as a result of haploinsufficiency of Shank3 in a mouse model for Phelan-McDermid syndrome (Bozdagi *et al.* 2010).

Comprehensive investigation of neurodevelopmental disorders requires the understanding of several aspects of neuronal function such as the genome, epigenome, transcriptome, translome and proteome. Combined analyses of different types of macromolecules are called “multi-omics” approaches and yield indispensable insights to the understanding of pathomechanisms of NDDs (Subramanian *et al.* 2020). Integrative bioinformatics in a multi-omics approach of translome and proteome may decipher how the alterations in both analyses were connected to each other.

The lack of an overlap between candidates in translome and proteome may have been caused by differences in specificity of the bacTRAP method and the PSD purification. The proteome was assessed from biochemically purified PSD fractions that were separated from the remaining cellular components depending on the density of the postsynaptic protein network. The bacTRAP method targeted actively translated mRNAs that were generally present in the cytosol, as there was no selection for synaptic compartments. These differences in specificity for the cellular compartment may account for the differences in deregulated candidates in translome and proteome. Single-cell omics approaches would be appropriate to resolve this issue and should be the subject of future studies.

The hypothesis of this project was that absence of the N-terminal domains of Shank3 might result in altered translation, due to its interaction with Ras, connecting Shank3 to the MAPK signaling pathway (Lilja *et al.* 2017). It has been suggested that imbalance of translation contributes to the molecular defects underlying ASDs. Here, only subtle changes in the translome of hippocampal neurons from *Lypd1-bacTRAPxShank3 $\alpha\beta$ -KO* mice were observed, whereas the changes in the proteome were more severe and none of the candidates overlapped. These results suggest that subtly altered translation may contribute to the molecular defects but is not the main pathomechanism. Mutations in many genes encoding synaptic scaffold and cell-adhesion molecules have been identified in patients with ASD and ID (Jamain *et al.* 2003, Laumonnier *et al.* 2004, De Jaco *et al.* 2005, Kim *et al.* 2008, Betancur *et al.* 2009, Pinto *et al.* 2010). The proteins expressed by these disease genes participate in formation of the postsynaptic architecture and in the transduction of intracellular signals into intracellular signaling pathways (Sheng and Kim 2011). Mutations in *NRXNs* and *NLGNs* are associated with ASD, and the encoded Neurexin and Neuroligin proteins are located at the presynapse and postsynapse, respectively (Sudhof 2008). They influence the level of synaptic proteins and regulate synaptic homeostasis, which might lead to altered neuronal plasticity (Kwon *et al.* 2012). My results suggest that loss or malfunction of Shank3 primarily leads to alterations of the architecture of the postsynapse by altered connection of glutamatergic signaling to actin dynamics. An altered postsynaptic proteome might induce altered morphology of the synapses and therefore altered synaptic plasticity. This pathomechanism might be comparable to those induced by mutations in genes encoding other scaffold proteins or cell adhesion molecules. I hypothesize that an altered neuronal translome contributes to but is not the main cause of the arising of ASDs, whereas an altered postsynaptic proteome most strongly contributes to the *SHANK3*-associated pathomechanism of ASDs.

5.2. L192P-RISC Induces Deregulation of the RNA Interference Pathway

Neurodevelopmental disorders can result from mutations in different categories of genes (Wright *et al.* 2015, Clark *et al.* 2018, Srivastava *et al.* 2019). One category of NDD disease genes encodes for RNA-binding proteins (Kapur and Ackerman 2018, Lennox *et al.* 2018, McLachlan *et al.* 2019, Lessel *et al.* 2020, Schalk *et al.* 2022). In this work, the L192P missense variant in the *AGO2* gene, found in patients diagnosed with LESKRES, was functionally analyzed as an example of an NDD that results from dysregulation of an RNA-binding protein (Hammond *et al.* 2000, Lessel *et al.* 2020). Due to the capacity of Ago2 to bind miRNA and its function in RNA interference, it was hypothesized that LESKRES-causing missense variants could result in different miRNAs being loaded on mutant forms of the Ago2 protein, altering the properties of RISC-mediated RNAi. The exact pathomechanism of Ago2 missense variants, particularly in the context of RNAi, is currently unknown. Here, I performed the miRAP method followed by RNA-seq to determine the miRNome and the RISC-bound miRNAs in AAV-infected primary cortical neurons. I found that four different aspects of miRNA-mediated RNAi were affected by the expression of Ago2-L192P: (1) The miRNome, (2) RISC-bound miRNAs, (3) the strand selectivity, which resulted in arm switching events, (4) and the association to isomiRs (Figure 43).

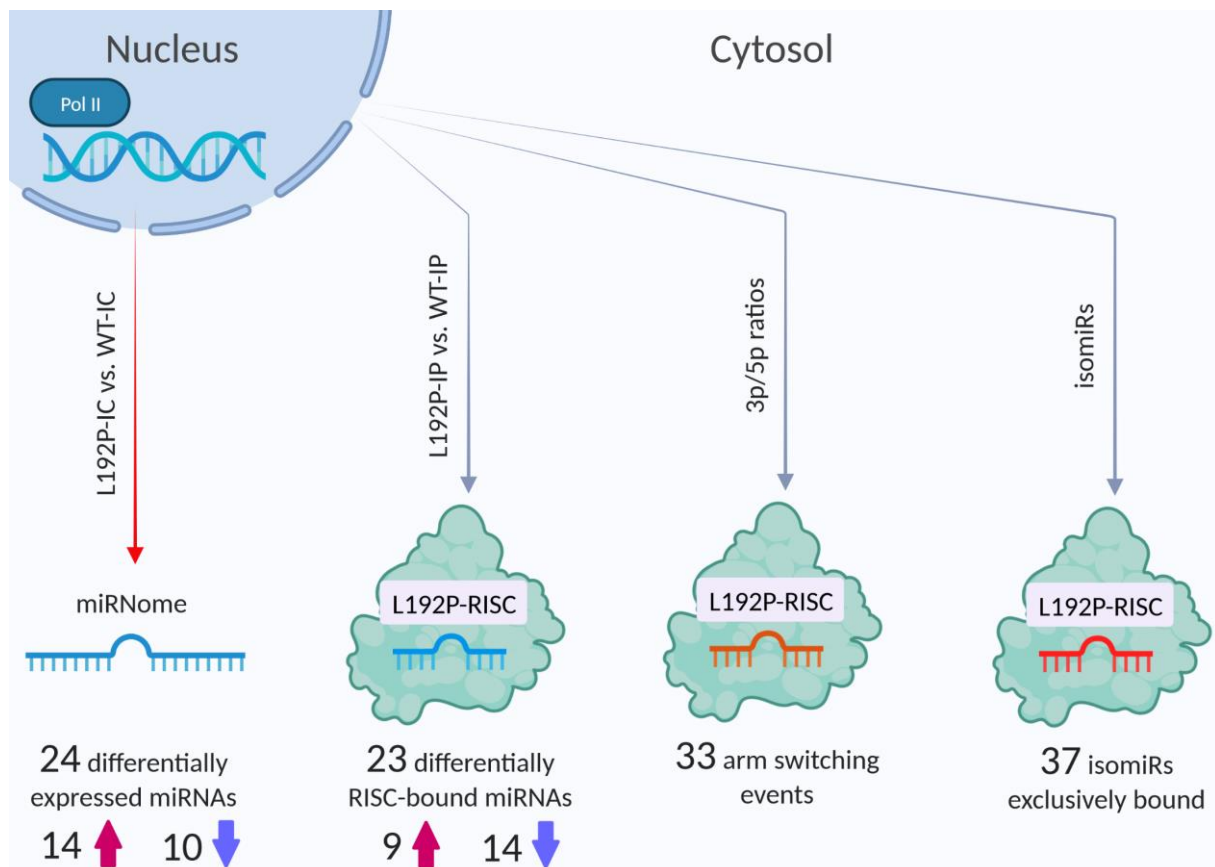


Figure 43: L192P-RISC induces alterations in the miRNome and deregulation of Ago2-mediated RNAi. The miRAP method followed by RNA-seq determined alterations in the miRNome and the RISC-bound miRNAs in AAV-infected primary cortical neurons expressing Ago2-L192P. Four different aspects were affected: (1) 24 miRNAs were differentially expressed, measured in the L192P-IC vs- WT-IC comparison, of which 14 were more (red) and 10 less (blue) expressed. (2) 23 miRNA were differentially bound in the L192P-RISC, of which nine were enriched and 13 decreased, determined by the L192P-IP vs. WT-IC comparison. (3) Arm switching events occurred for 33 miRNAs, analyzed by 3p/5p ratios. (4) The analysis of isomiRs determined 37 isomiRs which were exclusively bound to Ago2-L192P, whereas no isomiRs were exclusively bound to Ago2-WT. Created with BioRender.com.

5.2.1. The Expression of Ago2-L192P Altered Dynamics of P-Bodies

The efficiency and specificity of the miRAP method were validated using western blot, ICC and qPCR. The western blot analysis demonstrated that infection of primary neurons with AAVs induced the expression of GFP-tagged Ago2 under the control of the hSyn1 promoter. This specific promoter was chosen because it induces a mild expression level compared to regularly utilized strong promoters such as the human cytomegalovirus (CMV) promoter. The low band intensity of GFP-Ago2 detected by western blot confirmed the mild expression of Ago2 variants. In the IP condition, the bands of Ago2-WT and L192P had similarly low intensities, whereas no band was detected in the GFP negative control (Figure 24). It remains unclear why this band pattern was not observed in the total cell lysates, but I would speculate that without enrichment of GFP-Ago2 by immunoprecipitation, the protein abundance was below the detection limit. Thus, by usage of the hSyn1 promoter, artifacts of a strong overexpression were avoided. The expression of GFP-Ago2 variants was further validated by ICC and confocal microscopy (Figure 25). Ago2 localized to p-bodies together with Dcp1a, as it was described for Ago2-WT before (Eystathioy *et al.* 2002, Cougot *et al.* 2004, Liu *et al.* 2005). This shows that the intracellular localization of Ago2-WT and L192P is not affected by the GFP-tag, indicating full functionality of the expressed Ago2 protein. I quantified somatic and dendritic p-bodies and found that expression of Ago2-L192P increased the occurrence of p-bodies in distal dendrites. This result, obtained here in AAV-infected cortical neurons from mice confirmed results published by Lessel *et al.* who used transfected hippocampal neurons from rats. The independent confirmation of this result, using a different method of expression and a different species, demonstrates the robustness of this effect of the Ago2 mutant on p-body dynamics. To regulate translation, miRNAs accelerate the deadenylation of their mRNA targets (Behm-Ansmant *et al.* 2006, Behm-Ansmant *et al.* 2006, Giraldez *et al.* 2006, Wu *et al.* 2006). Argonaute proteins, the decapping complex Dcp1-Dcp2 and GW182 proteins are required for the deadenylation process and accelerated decay of mRNA, and all these proteins localize to p-bodies (Liu *et al.* 2005, Meister *et al.* 2005, Sen and Blau 2005, Behm-Ansmant *et al.* 2006). It has been shown that blocking of mRNA decay results in increased size and number of p-bodies (Sheth and Parker 2003, Cougot *et al.* 2004, Andrei *et al.* 2005, Teixeira *et al.* 2005). Accordingly, an increased occurrence of p-bodies hints towards blocked mRNA decay caused by the L192P mutant. The number of p-bodies was only elevated in dendrites and not in the cell soma, indicating that the hindered mRNA decay was specific for locally translated transcripts. Currently it remains unclear whether mRNA decay is restricted to p-bodies or also occurs in the cytoplasm. It has been proposed that initiation of the mRNA decay machinery takes place in the diffuse cytoplasm and that association of additional cofactors results in formation of p-bodies at later stages of the pathway (Chu and Rana 2006, Stoecklin *et al.* 2006). Interestingly, Ago2-L192P was detected diffuse in the cytoplasm to a greater extent than the WT, suggesting that initiation of mRNA decay might also be influenced by the mutant. Lessel *et al.* correlated a reduced phosphorylation of Ago2-L192P at the serine cluster 824-834, which is required for rapid release of targets, to increased occurrence of dendritic p-bodies (Golden *et al.* 2017, Quevillon Huberdeau *et al.* 2017, Lessel *et al.* 2020). Furthermore, they showed that the leucine substituted by the L192P missense variant is located in close spatial proximity to helix-7, thereby obstructing movement of the helix-7 during target binding and ejection (Schirle *et al.* 2014, Klum *et al.* 2018, Lessel *et al.* 2020). Taken together, a model can be proposed that Ago2-L192P exhibits slowed binding to and dissociation of mRNA targets, resulting in slowed or blocked mRNA decay in distal dendrites, linking the deregulation to local translation.

5.2.2. The miRAP Method Targeted RISC-bound miRNAs Specifically in Neurons

The miRNA concentration in total lysates and precipitated samples was measured to determine efficiency of the coprecipitation (Figure 27). The amount of miRNA expressed was unchanged by AAV-transduction and expression of different Ago2 variants or GFP control, seen as similar miRNA concentrations in input controls. Precipitation of RISC resulted in 30%-50% reduction of miRNA,

showing that more miRNAs are expressed than bound to the Ago2 protein. The low concentration of miRNA in the GFP-IP confirmed that no unspecific association of miRNA with the tag occurred. Consequently, the purified miRNA had been specifically loaded onto Ago2 to form functional RISCs, which were efficiently precipitated during the miRAP method. The specificity of the miRAP method to target the neuronal cell population, facilitated by usage of the hSyn1 promotor, was validated using qPCR (Figure 28). Enrichment of the neuron-specific miR-124 in immunoprecipitated samples compared to input controls was observed. Enrichment was more pronounced for Ago2-WT than for L192P. In contrast, the glia cell-specific miR-21 was depleted in precipitates. This showed that the expression of GFP-tagged Ago2 variants was induced specifically in neurons, while glia cells were not transduced, confirming the hSyn1 promotor specifically targeted the neuronal cell population. This was especially important when investigating miRNAs, because miRNAs can vastly differ between cell populations and play major roles in differentiation of cells (Londin *et al.* 2015). By employing the hSyn1 promotor, miRAP-generated RNA-seq data determined the neuronal miRNome only and was not biased by miRNAs originating from other cell types.

5.2.3. Ago2-L192P Affected the miRNome and the Formation of RISC

I investigated the effect of Ago2-L192P on miRNA expression and binding in primary neurons (Figure 30). The miRNome and RISC-associated miRNAs were decoded using RNA-seq. First, I compared the miRNomes of neurons expressing Ago2-WT and the L192P mutant. 24 miRNAs were differentially expressed, of which 14 were enriched and 10 were decreased in neurons expressing Ago2-L192P, indicating that no overall up- or down-regulation of transcription of miRNA-encoding genes caused the changes in miRNA abundance. 23 differentially RISC-bound miRNAs in IP samples were identified, of which nine were enriched and 14 were bound less in L192P-RSIC. Ago2 is essential for stabilizing miRNA upon incorporation into the RISC and protects miRNA from degradation, thereby modulating miRNA levels (Park *et al.* 2017, Reichholf *et al.* 2019). An insertion of the miRNA 3'-hydroxy end into a pocket in the PAZ domain of Ago2 is needed for this protection (Park *et al.* 2017). The domain structure of Ago2 was depicted using the crystal structure of human Argonaute-2 bound to a defined guide RNA (NDB: 4W5N, Schirle and MacRae 2012, Schirle *et al.* 2014) and the location of the L192 residue was indicated (Figure 44). Although L192 is not localized in the PAZ domain, the structure of Ago2 demonstrates that it lies in spatial proximity to the binding groove for miRNA, possibly altering the conformation of the binding pocket. Thus, deregulation of the neuronal miRNome might be explained by altered ability and selectivity of Ago2-L192P to stabilize miRNA. Additionally, the availability of mRNA targets has been shown to decrease or to elevate miRNA levels (Chatterjee *et al.* 2011). Expression of Ago2-L192P resulted in altered binding to miRNA, which probably altered the level of target transcripts, in turn influencing the miRNA levels. It becomes clear that deregulated Ago2 function might act at different stages of the RNA interference pathway, including feedback loops between miRNA and their targets.

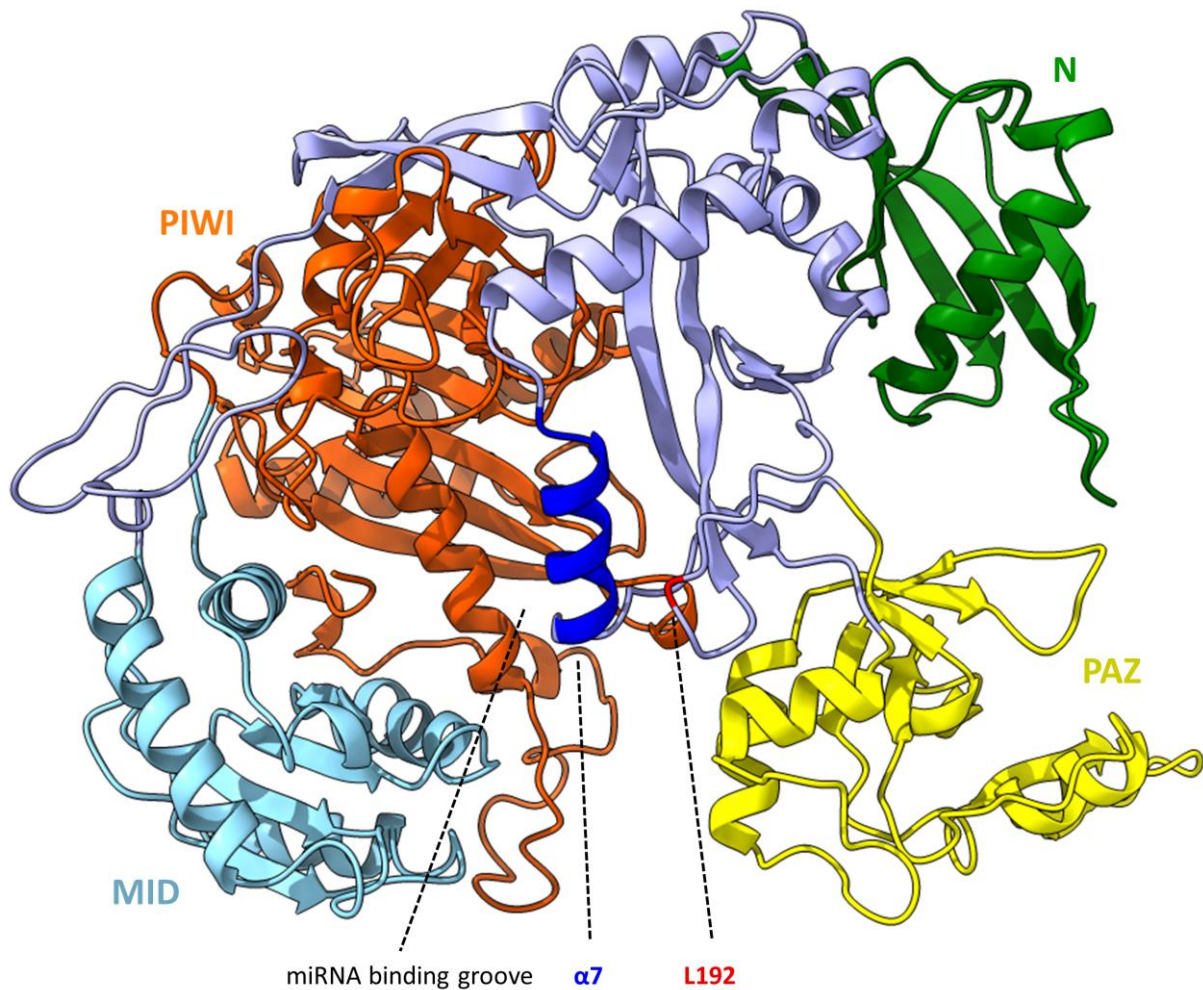


Figure 44: Location of the leucine 192 residue in Ago2. The tertiary structure of Ago2 was depicted using the crystal structure of human Argonaute-2 bound to a defined guide RNA (NDB: 4W5N, Schirle *et al.* 2014). The Ago2 domains and L192 (red) were visualized in UCSF ChimeraX (Pettersen *et al.* 2021, Huang *et al.* 2018). The RNA binding groove in between the PAZ and PIWI domain was indicated.

Ago2 functions in RNAi by associating with miRNAs. The detection of an altered complement of miRNAs in the RISC of the L192P mutant demonstrates that the variant alters RISC function. Many studies reported deregulation of Argonaute or PIWI proteins in human diseases, such as heart disease, infertility, and in several types of cancer (Vaksman *et al.* 2012, Zhang *et al.* 2013, Voller *et al.* 2016, Gou *et al.* 2017, Gao *et al.* 2018). In colon cancer, ovarian carcinoma, and gliomas, an overall upregulation of Ago2 activity was described. Thus, this pathomechanism differs from the deregulation of the L192P-RISC, since I determined enrichment and depletion of miRNAs expressed and bound to Ago2-L192P (Vaksman *et al.* 2012, Zhang *et al.* 2013, Feng *et al.* 2014). Nevertheless, the involvement of deregulated Ago2 in the pathogenesis of the aforementioned diseases supports the hypothesis that the differential association of Ago2-L192P with miRNA is an important factor in the manifestation of disease, in this case of LESKRES (Davis *et al.* 2008, Kawase-Koga *et al.* 2009, Hebert *et al.* 2010, McNeill and Van Vactor 2012, Nowakowski *et al.* 2018). But how might the deregulation of Ago2-L192P lead to the NDD LESKRES? The correct spatiotemporal regulation of translation is indispensable for proper neurodevelopment (Johnson *et al.* 2009, Kang *et al.* 2011, Popovitchenko and Rasin 2017, Cadwell *et al.* 2019, Telley *et al.* 2019). Alterations in these processes by deregulated RISC function can lead to the manifestation of NDDs (Gandal *et al.* 2018, Nowakowski *et al.* 2018, Lennox *et al.* 2020). Mutations in genes encoding for miRNA regulating proteins or miRNA targets have been reported in patients with various NDDs, such as FXS, Williams syndrome, Rett syndrome, and other ASDs (Hoogenraad *et al.*

2004, Jin *et al.* 2004, Klein *et al.* 2007, Abu-Elneel *et al.* 2008, Talebizadeh *et al.* 2008). In Williams syndrome, the translation and function of the LIM domain kinase 1, targeted by miR-134, is altered, which leads to cytoskeletal defects (Hoogenraad *et al.* 2004). The pathomechanism of Rett syndrome, an ASD with severe neurological symptoms such as ataxia and seizures, was linked to miR-132-mediated targeting of MECP2, encoding the methyl CpG binding protein 2 (Hagberg *et al.* 1983, Hagberg 1985, Klein *et al.* 2007). Neither miR-134 nor miR-132 were deregulated in any of the aspects analyzed following Ago2-L192P expression. This indicates that malfunction of specific miRNAs can lead to distinct NDDs with overlapping symptoms such as ID (Hoogenraad *et al.* 2004, Jin *et al.* 2004, Klein *et al.* 2007). Several studies investigated whether a connection exists between ASD and deregulated expression of miRNAs or RISC function (Abu-Elneel *et al.* 2008, Talebizadeh *et al.* 2008, Park *et al.* 2022). Abu-Elneel *et al.* applied a multiplex qPCR approach on miRNAs purified from postmortem cerebellar cortex tissue of 13 ASD patients. By comparison with healthy controls, they found 28 miRNAs to be differentially expressed (Abu-Elneel *et al.* 2008). In a study from Talebizadeh *et al.*, miRNAs were screened from lymphoblastoid cell lines generated from six ASD patients and compared to controls. Of the 470 miRNAs detected, nine miRNAs were found to be differentially expressed, of which six miRNAs were enriched and three decreased (Talebizadeh *et al.* 2008). One of these, miR-23a-3p, was also found in the L192P-IC vs. WT-IC comparison (Table 52). 24 miRNAs were differentially expressed in primary neurons expressing Ago2-L192P compared to the WT condition. Although different sample types and analytical methods were used, comparable numbers of deregulated miRNAs were determined (Abu-Elneel *et al.* 2008, Talebizadeh *et al.* 2008). These results suggest that even a relatively small group of differentially expressed miRNAs may contribute to the pathomechanisms of ASDs and also to LESKRES. In this project, I exclusively investigated the L192P variant. Therefore, it remains unknown whether the other *AGO2* variants found in LESKRES patients induce similar alterations in miRNA expression and binding. When I compared my findings with studies on other NDDs, I found that deregulation of the miRNome and Ago2-mediated RNAi is a common pathomechanism. However, miRNAs that are deregulated in these NDDs have minimal overlap with each other and with the differentially regulated miRNAs identified here, which would suggest significant differences in RISC function. I speculate that other Ago2 mutants expressed in LESKRES patients, except for complete loss-of-function variants such as G733R, might also result in altered miRNomes and RISC-bound miRNAs but that differentially regulated miRNAs differ dependent on the *AGO2* variant (Lessel *et al.* 2020). I hypothesize that the differentially regulated miRNAs might cause general deregulation of RISC-mediated RNAi with partial overlap to miRNAs altered by Ago2-L192P expression, rather than individual miRNAs contributing primarily to the pathomechanism. This hypothesis is supported by the patients' phenotypes described in Lessel *et al.* They described that the cohort of LESKRES patients share 50% of their symptoms, whereas other symptoms are only present in a subset of patients or are even specific for recurrent variants. The phenotype of central apnea in the postnatal period was exclusively found in the two LESKRES patients bearing the L192P variant (Lessel *et al.* 2020). This might be explained by distinct miRNAs expressed and bound to Ago2 mutants that target different mRNAs, leading to variant-specific molecular defects and to the manifestation of variant-specific phenotypes. It would be very interesting to investigate the miRNome and function of RISC of different Ago2 mutants derived from other patient variants to answer the open questions regarding overlapping or diverging pathways and genotype-phenotype correlations.

5.2.4. The Ago2 Mutant L192P Exhibited Altered Strand Selectivity

When Ago2 associates with a miRNA duplex to form the RISC, usually either the 3p or 5p strand is preferentially retained and is therefore named guide strand, whereas the other strand, the passenger strand, is discarded (Ma *et al.* 2004, Wang *et al.* 2008, Okamura *et al.* 2009). 3p/5p ratios were determined and 33 miRNAs exhibited altered strand-specific expression or arm switching events (Figure 31-Figure 35). The miRNAs were categorized dependent on their expression and association

with Ago2-L192P compared to Ago2-WT. Distinct arm switching events were observed between the Ago2 variants specific for respective miRNAs. No general tendency in binding preference to the passenger or guide strand was observed for either the mutant L192P or Ago2-WT (Figure 35). One driving factor for strand selectivity is the identity of the first 5'-nucleotide of each strand, for which an uracil is commonly favored (Mi *et al.* 2008, Ghildiyal and Zamore 2009, Hu *et al.* 2009). This preference is conveyed by a pocket formed by the MID domain (Hu *et al.* 2009, Frank *et al.* 2010, Suzuki *et al.* 2015). Furthermore, an excess of purines has been reported for 5'-terminal nucleotides of guide strands (Hu *et al.* 2009). This "purine bias" is mediated by the PAZ domain that initiates miRNA recognition and contains several aromatic residues, which stabilize purines via hydrophobic interactions (Song *et al.* 2004, Preall and Sontheimer 2005, Ming *et al.* 2007, Hu *et al.* 2009). To determine whether the strand selection of Ago2 variants was dictated by the 5'-uracil and by the purine bias, I quantified the abundance of 5'-terminal uracils and of purines in the first four nucleotides of 5'-termini (Figure 45). The differentially bound miRNAs from the L192P-IP vs. WT-IP and 3p/5p comparison were analyzed. Of the enriched miRNA in the L192P-IP, 75% possessed an uracil as the 5'-terminal nucleotide and 37.5% of the four nucleotides at the 5'-terminus were purines. Ago2-L192P exhibited stronger selectivity for the 5'-terminal uracil when compared to the WT control, whereas the selectivity for purines was impaired. The same aspects were quantified for miRNAs with altered 3p/5p ratios. Strands that were enriched upon expression of Ago2-L192P contained 63% 5'-terminal uracil and 50% purines. This result also suggests stronger association of the L192P mutant with 5'-uracil, possibly mediated by the binding pocket in the MID domain.

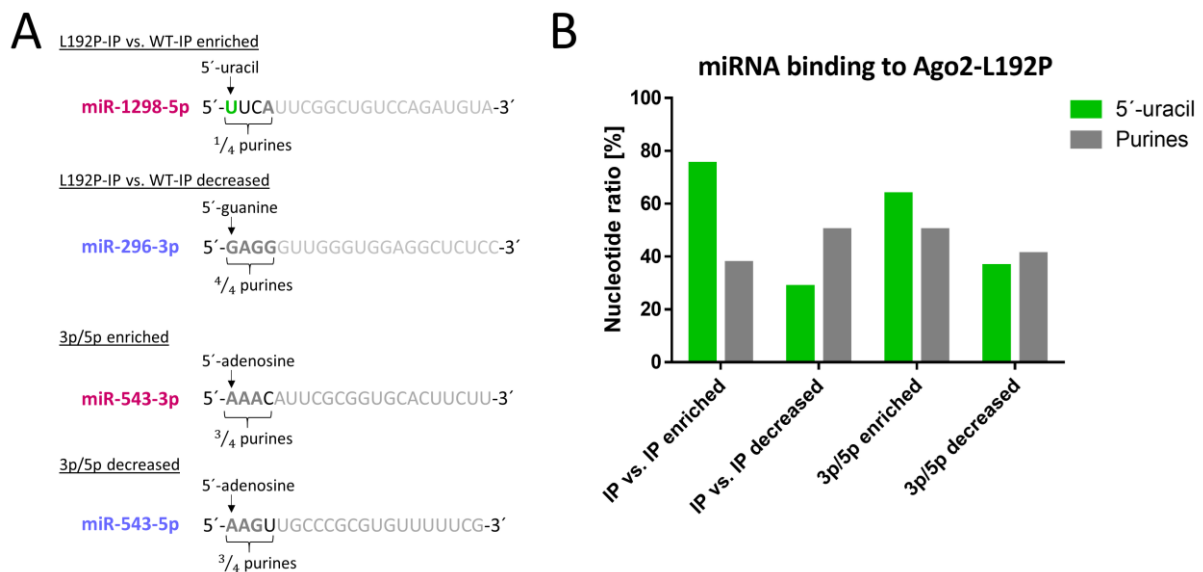


Figure 45: Ago2-L192P favored 5'-uracil but was less selective towards 5'-terminal purines. (A) The sequences of the differentially bound miRNAs found in the L192P-IP vs. WT-IP comparison and in the 3p/5p analysis were analyzed. **(B)** The identity of the 5'-nucleotide was determined and the ratio of uracil in respect to all 5'-nucleotides calculated. The proportion of purines among the four 5'-terminal nucleotides was calculated.

One could envision a model in which the substitution of leucine to proline at position 192 changes the conformation of the binding pocket within the MID domain, making it more affine to uracil. In contrast, the preference of the PAZ domain towards purines appeared to be compromised by the substitution. Since the residue 192 is not located in either the MID or PAZ domain, only a global change in the tertiary structure of Ago2 could indirectly influence the structure of these two domains (Figure 44). The L192 residue is located in proximity to the helix-7 and the RNA binding groove in the spatial center of the PAZ, MID and PIWI domains. Replacement of leucine 192 with the most rigid residue proline could cause general conformational changes in Ago2, perhaps leading to increased 5'-uracil binding and decreased purine bias. To elucidate the actual effects of the L192P variant on the conformation of

Ago2, a structural biology approach based on protein crystallization could be applied and should be the subject of future projects. Both Ago2 variants bound annotated passenger strands to a comparable extent. It remains unclear why the Ago2-WT protein did not show a clear preference for binding the canonical guide strand. (Figure 35). It has been described before that both strands of miRNA duplexes can be retained in the Ago2 protein to form a functional RISC (Ghildiyal and Zamore 2009, Okamura *et al.* 2009, Kim *et al.* 2020). The arm switching events were shown to be regulated dependent on cell type, but the molecular mechanisms to regulate the switch between canonical guide and passenger strand are subject of current research (Kim *et al.* 2020). For example, Kim *et al.* found that 14% of the miRNAs that they tested exhibited arm switching events. They further showed for miR-324 that arm switching is regulated by uridylation, but they also stated that this mechanism might be specific for miR-324 (Kim *et al.* 2020). Thus, the altered strand selectivity shown here could result from post-transcriptional modifications. Further studies will be needed to investigate the post-transcriptional modifications that dictate strand selectivity and to show if these are affected by expression of Ago2 mutants such as L192P. Interestingly, it has been described that in *Drosophila melanogaster* Ago1 and Ago2 display distinct preferences in loading of guide and passenger strands (Okamura *et al.* 2009). Okamura *et al.* described that guide strands were preferentially sorted into Ago2 compared to Ago1. This preference correlated with mismatches of the miRNA duplex at the 9th and 10th nucleotides and with modifications of the 3'-termini (Okamura *et al.* 2009). They inferred a pathway in which passenger strands fine-tune RNAi and are endogenous regulatory species, rather than being degraded by default (Okamura *et al.* 2008, Okamura *et al.* 2009). This hypothesis was supported by the observation that the passenger strands required canonical RNAi factors for loading into Ago2 (Okamura *et al.* 2009). Therefore, the sorting of miRNA strands to different Ago proteins might be crucial for their function and the reason why I observed arm switching events for Ago2-WT. Heterozygous missense variants in *AGO1* cause a severe NDD whose phenotype resembles the LESKRES (Lessel *et al.* 2020, Schalk *et al.* 2022). The L190 residue in Ago1, homologous to L192 in Ago2, is substituted to proline in a patient with the *AGO1*-associated NDD (Lessel *et al.* 2020, Schalk *et al.* 2022). It would be very interesting to test for arm switching events in Ago1-WT compared to Ago2-WT, as well as in Ago1-L190P compared to Ago2-L192P. In doing so, conclusions might be drawn about differences in strand selectivity of Ago1 and Ago2 in neurons and the contribution of arm switching events of the Ago2 mutant to the pathogenesis of LESKRES. It is also possible that the arm switching events of Ago2-L192P are caused by extrinsic factors, such as altered interaction with proteins involved in the loading of miRNA during RISC formation. The Integrator complex is a multiprotein complex that comprises an endonuclease activity and directly associates with miRNA (Wu *et al.* 2017, Albrecht *et al.* 2018, Kirstein *et al.* 2023). Kirstein *et al.* showed that Dicer, Ago2 and the Integrator subunit 11 (IntS11) interact in the cytoplasm of HEK293T cells. They hypothesized an assisting function of the Integrator complex in the loading of miRNA on Ago2 by stabilizing the strand of the miRNA duplex that is retained in the RISC. Absence of the Integrator complex led to decreased formation of RISCs and degradation of miRNAs, inferring a key role for the Integrator in regulation of miRNA loading and homeostasis (Kirstein *et al.* 2023). An altered interaction of the Integrator complex with Ago2 might result in deregulation of the assisting during RISC formation. An altered Integrator function might contribute to the changes in the miRNome and loading of miRNAs following Ago2-L192P expression. The interaction between the Integrator complex and Ago2-WT compared with Ago2-L192P could be investigated by performing coimmunoprecipitation experiments from cell lysates of transfected HEK293T cells to conclude whether an altered binding to Ago2-L192P could indeed cause arm switching events.

5.2.5. Increased Incorporation of isomiRs into the L192P-RISC

I analyzed the miRNAs bound to Ago2-L192P in terms of abundance of isomiRs, isomers of miRNA which differ in their sequence from the corresponding canonical miRNA (Morin *et al.* 2008, Wang *et al.* 2008, Guo and Lu 2010). 37 isomiRs bound exclusively to Ago2-L192P, whereas no isomiR associated exclusively with Ago2-WT. By classification of the 20 most abundant isomiRs, I found that 18 isomiRs exhibited altered 3'-termini (Figure 36). This result is in keeping with several studies about isomiRs which found that the abundance of 3'-isomiRs, with 40%-50% of total isomiRs, exceeds the abundance of 5'-isomiRs by far, which is approximately 5%-15% of all isomiRs expressed (Burroughs *et al.* 2010, Lee *et al.* 2010, Newman *et al.* 2011, Wyman *et al.* 2011, Tan *et al.* 2014). One could argue that isomiRs are experimental artefacts rather than a functional subclass of miRNA that is of physiological relevance. However, several studies convincingly demonstrated that the amount of detected isomiRs in small RNA-seq data far exceeds the expected rate of sequencing error. This was bioinformatically analyzed using small artificial RNAs, so called synthetic "spike in" controls (Linsen *et al.* 2009, Wyman *et al.* 2011, Neilsen *et al.* 2012, Tomasello *et al.* 2021). IsomiRs are expressed in various cell lines, cell populations, and tissues, among these HEK293T cells and human embryonic stem cells, and in different types of cancers, such as prostate cancer, breast cancer and leukaemia (Bar *et al.* 2008, Morin *et al.* 2008, Lipchina *et al.* 2011, Watahiki *et al.* 2011, Li *et al.* 2012, Voellenkle *et al.* 2012). The functional relevance of isomiRs was demonstrated by their ability to associate with Ago proteins, detected in coimmunoprecipitation assays, analogous to the isomiRs which I detected via the miRAP method (Cloonan *et al.* 2011, Londin *et al.* 2015, Haseeb *et al.* 2017). The modifications of isomiRs can affect their stability and specificity since variation of length and sequence can result in shifted selection of mRNA targets (Ameres and Zamore 2013, Loher *et al.* 2014, Zhang *et al.* 2016, Kim *et al.* 2020). It is uncertain whether the incorporation of IsomiRs into L192P-RISC was caused by intrinsic effects of Ago2-L192P, such as conformational changes and altered binding kinetics, or by extrinsic factors, such as enhanced generation of IsomiRs indirectly caused by expression of the mutant. This question could be answered by *in vitro* measurements of Ago2-L192P binding kinetics with isomiRs compared to the respective canonical miRNAs and to Ago2-WT. IsomiRs have gained interest due to their potential function in diagnostics as biomarkers (Bhardwaj *et al.* 2018, Scheper *et al.* 2022, Aiso and Ueda 2023). For example, Scheper *et al.* determined isomiRs as biomarkers for ID and ASD in Tuberous Sclerosis complex (TSC), a genetic disorder affecting several organs including the CNS (Curatolo *et al.* 2015, de Vries *et al.* 2020, Specchio *et al.* 2020, Northrup *et al.* 2021, Scheper *et al.* 2022). The phenotype of TSC patients includes a broad spectrum of symptoms such as epilepsy, malformations of the cortex, ADHD, ID, and ASD (Northrup *et al.* 2021, Scheper *et al.* 2022). On the molecular level, loss-of-function variants in the disease genes *TSC1* and *TSC2* result in deregulation of the mTOR pathway, a signaling pathway influencing cell proliferation and translation (Sancak *et al.* 2005, Muhlebauer *et al.* 2019). Scheper *et al.* used serum-derived isomiRs as biomarkers for ASD and ID in TSC patients. They identified 18,741 isomiRs in the serum of 29 TSC patients. Interestingly, this number matches the range of isomiRs and canonical miRNAs detected in the miRAP samples from AAV-induced primary cortical neurons (see 4.2.6). Furthermore, four differentially expressed isomiRs were identified for TSC patients with ASD and six in TSC patients with ID compared to controls. One of these ID biomarkers was the isomiR "miR-409 3prim AT" (Scheper *et al.* 2022), a 3'-isomiR with two non-templated nucleotides added at the 3'-terminus which do not match the pre-miRNA sequence (Wyman *et al.* 2011, Scheper *et al.* 2022). Although this exact isomiR was not detected in the L192P-RISC, four of the 20 most abundant isomiRs bound exclusively to the L192P mutant corresponded to the canonical miR-409-3p miRNA. Interestingly, all these isomiRs exhibited altered 3'-termini (one extended, three trimmed) and three of them contained a nucleotide exchange on the 3'-terminal side of the miRNA (17th-20th nt, see Table 53, colored blue). Considering that ID is a core symptom of LESKRES and that the isomiR of miR-

409-3p found by Scheper *et al.* was a specific marker for ID in TSC, the isomiRs of miR-409-3p are an interesting link between altered regulation of isomiRs and the manifestation of ID.

5.2.6. Ago2-L192P Induces Deregulation of miRNAs of the miR379-409 Cluster

Analyses of the miRNome and RISC-bound miRNAs, including 3p/5p ratios and isomiRs, revealed that eight of the deregulated miRNAs with Ago2-L192P originated from a genomic cluster of miRNAs, the miR379-410 cluster (Figure 46). The imprinted miR379-409 cluster is located on chromosome 14 in humans and chromosome 12 in mice, but the encoded miRNAs are highly conserved between the two species (da Rocha *et al.* 2008, Winter 2015). The large cluster is exclusively expressed from the maternal allele and encodes 38 miRNAs with brain-specific functions species (da Rocha *et al.* 2008, Winter 2015). Transcription of these miRNAs is increased by neuronal activity in primary neurons (Fiore *et al.* 2009, Winter 2015). The transcription factor myocyte enhancing factor 2 (Mef2) drives activity-dependent expression of miRNAs from the cluster which are required for adjustment of dendritic branching (Fiore *et al.* 2009). Thus, Mef2 acts as negative regulator of excitatory synaptogenesis (Flavell *et al.* 2006, Shalizi *et al.* 2006). The mechanism of local translation in dendrites connects neuronal activity to the expression of mRNAs in spatial proximity to synapses (Sutton and Schuman 2006, Fiore *et al.* 2009). Local translation is indispensable for proper neurodevelopment and morphological abnormalities of dendrites and aberrant dendritic branching are often observed in NDDs with ID such as the Fragile-X-syndrome (Bagni and Greenough 2005, Fiore *et al.* 2009). Three differentially expressed miRNAs from the miR379-409 cluster were found in the comparison of miRNomes, three from the 3p/5p strand ratio analysis and two from the analysis of isomiRs. Four of these miRNAs are enriched in the cerebellum of *Mecp2* knockout mice, a model for Rett syndrome (Wu *et al.* 2010). Two of these, miR-381-3p and miR-300, were enriched in miRNome of Ago-L192P expressing neurons. The miR-543, for which Ago-L192P showed altered strand selectivity and the canonical miR of isomiR miR-544-3p -5T were also found to be enriched in the Rett syndrome mouse model (Wu *et al.* 2010). The three miRNAs miR-380-3p, miR-381-3p, and miR-485-3p were enriched in neurons expressing Ago2-L192P. Two of these, miR-381-3p and miR-485-3p, have contrary roles in the regulation of dendritogenesis (Schratt *et al.* 2006, Fiore *et al.* 2009, Lavon *et al.* 2010, Cohen *et al.* 2011, Gardiner *et al.* 2012). Although these miRNAs were not enriched in the L192P-RISC, their enrichment in the miRNome of Ago-L192P expressing neurons indicates a deregulation of the activity-dependent expression of the miR379-409 cluster. Possibly, the increased expression was caused by altered synaptic activity in neurons upon expression of the Ago2 mutant. Electrophysiological measurements on AAV-transduced primary neurons expressing Ago2-L192P could test the electrical properties of neurons to draw conclusions about the synaptic activity. Three miRNAs of the miR379-409 cluster exhibited arm switching events with Ago2-L192P compared to WT. The canonical guide strands of miR-300 and miR-376a were more strongly expressed with and bound to Ago2-L192P, whereas miR-543 was exclusively enriched in the L192P-IP. Interestingly, miR-376a enhances neuronal differentiation of cultured rat cortical stem cells by silencing translation of the transcription factor Hes5 (Ohtsuka *et al.* 2001, Jovicic *et al.* 2013, Winter 2015). Furthermore, enrichment of miR-376a was detected in lymphoblastoid cell lines generated from patients diagnosed with ASD (Lavon *et al.* 2010, Sarachana *et al.* 2010, Jovicic *et al.* 2013). The miR-543-3p was enriched in the L192P-RISC (Figure 38). One of the main targets translationally silenced by miR-543-3p is the mRNA encoding the cell adhesion molecule N-cadherin (Rago *et al.* 2014). N-cadherin has several functions in the developing neocortex and is essential for cortical organization (Kadowaki *et al.* 2007, Zhang *et al.* 2010, Zhang *et al.* 2013, Rago *et al.* 2014). Fine-tuned expression of N-cadherin regulated by miR-543-3p has been shown to be required for proper neuronal migration as well as proper neurogenesis in the neocortex of mice (Kawauchi *et al.* 2010, Jossin and Cooper 2011, Rago *et al.* 2014). Deregulated miR-543-3p-mediated RNAi performed by the L192P-RISC might be a link between dysfunction of neuronal migration and differentiation and the pathomechanism of LESKRES. The miRNAs miR-409 and miR-544 also belong to

the miR379-409 cluster. In the analysis of isomiRs, four isomiRs exclusively bound to Ago2-L192P originated from the pre-miR-409 and one from the miR-544. In summary, the Ago2 variant L192P resulted in deregulation of the miR379-409 cluster, which encodes miRNAs that are indispensable fine-tuners of neurogenesis, neuronal migration, and synaptic function (Figure 46). Thus, deregulation of cluster miR379-409 likely contributes to the pathogenesis of LESKRES patients bearing the L192P variant. It remains unknown whether deregulation of the cluster is a shared molecular defect for all *AGO2* mutants or a variant-specific defect, and future studies investigating the remaining Ago2 mutants will be required to address this question.

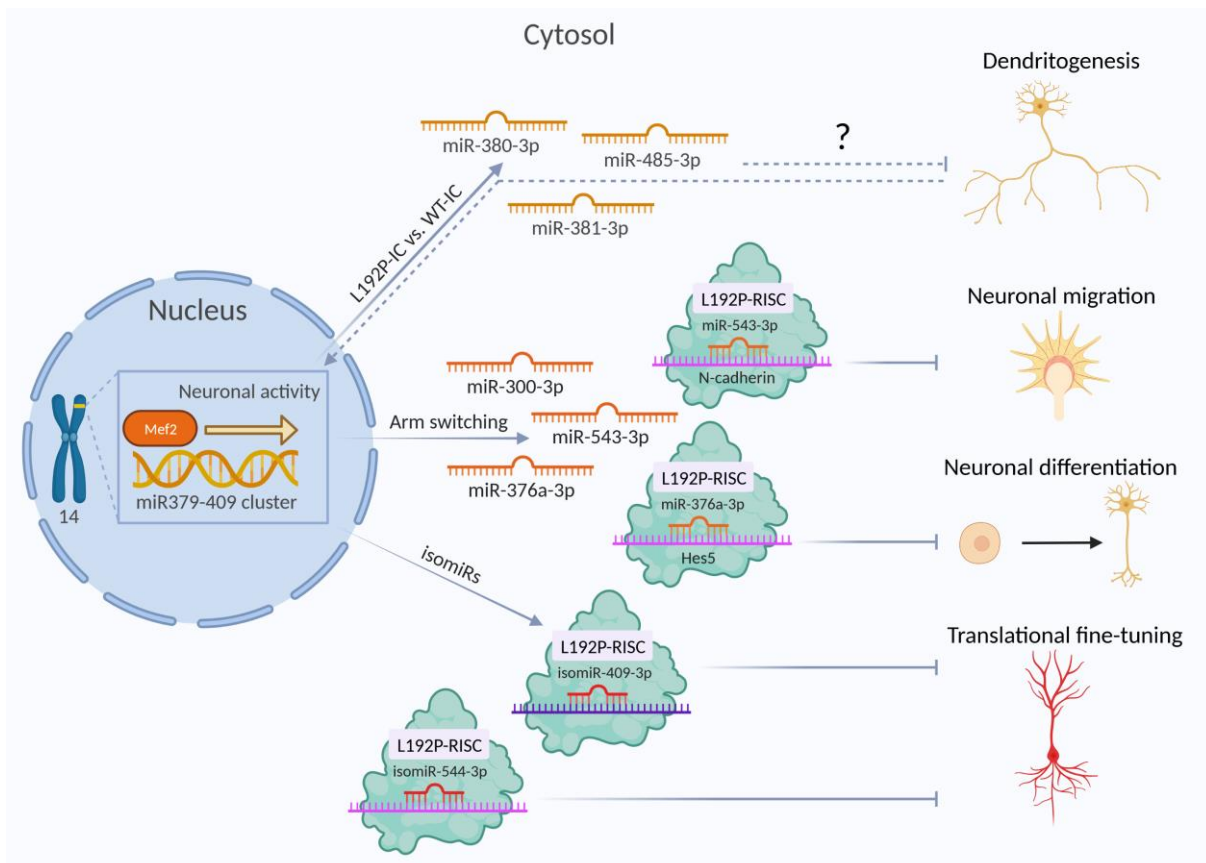


Figure 46: Ago2-L192P induces deregulation of specific miRNAs encoded by the miR379-409 cluster. The genomic miR379-409 cluster is located on chromosome 14 in humans (12 in mice) and encodes 38 miRNAs. The transcription factor Mef2 is activated by neuronal activity and enhances expression of the cluster. Three miRNAs, miR-380-3p, miR-409-3p, and miR-381-3p were differentially expressed and function in regulation dendritogenesis. Three miRNAs exhibited arm switching events: miR-300-3p, miR-543-3p and miR-376a-3p. The main target of miR-543-3p is encoding for N-cadherin, involved in neuronal migration. miR-376a-3p silences translation of the transcription factor Hes5, which induces neuronal differentiation. Four exclusively Ago2-L192P-bound isomiRs corresponded to miR-409-3p and one to miR-544-3p. Differential binding of isomiRs might alter fine-tuning of RNAi. Created with BioRender.com.

5.2.7. Gene Ontology Analyses with Predicted Targets of miRNAs Differentially Bound to the L192P-RISC

RISC functions through translational silencing of mRNA transcripts by binding of RISC-loaded miRNAs to partially complementary sequences in the 3'UTR of the target (Hammond *et al.* 2001, Hutvagner and Zamore 2002, Lai 2002, Zeng *et al.* 2002, Bartel 2004). Target predictions of differentially bound miRNAs in the L192P-RISC were performed to assess the effects of misdirected RISC function on translation (see 4.2.7). Lessel *et al.* investigated the transcriptome of primary dermal fibroblasts derived from patients bearing the L192P variant. They found 485 differentially expressed transcripts when transcriptomes of both patients were compared to an age-matched control (Lessel *et al.* 2020). I compared the predicted targets of the four most enriched and decreased miRNAs in the L192P

condition of the IC and IP comparison with the differentially expressed transcripts from primary fibroblasts to screen for a possible overlap. The mRNA encoding ABCA1, a protein involved in the transport of membrane lipids, was the highest ranked target of miR-33-5p, which was reduced in L192P-IC and IP. Interestingly, this transcript was also downregulated in the miRNomes of primary fibroblasts derived from LESKRES patients (Lessel *et al.* 2020). Unexpectedly, ABCA1 was the only shared target between the targets predicted here and the transcriptomes determined by Lessel *et al.* The prediction of miRNA targets remains a challenge in bioinformatics due to the short seed sequences of two to eight nucleotides (Nielsen *et al.* 2007, Friedman *et al.* 2009, Liu and Wang 2019). Partially complementary sequences to such short motifs occur numerously in the 3'UTR of mRNAs and are not sufficient for valid target prediction (Yue *et al.* 2009). Therefore, target prediction tools such as miRTarget integrate additional factors such as experimental data from miRNA overexpression studies and cross-linking and immunoprecipitation (CLIP) experiments to calculate prediction scores, but experimental data is not available for all miRNAs (Betel *et al.* 2010, Agarwal *et al.* 2015, Liu and Wang 2019). CLIP experiments can identify target transcripts by cross-linking miRNA to Ago2 and to RISC-targeted mRNAs (Chi *et al.* 2009). The predicted targets could be validated by transcriptome analysis of AAV-induced cortical neurons expressing Ago2-L192P or by CLIP experiments. Biological processes influenced by the predicted targets of differentially abundant miRNAs in the L192P-RISC were determined in gene ontology analyses. The miR-1298-5p was highly enriched in the L192P-IP and the predicted targets therefore would be silenced stronger compared to the WT-RISC. Interestingly, axon guidance and neuron projection guidance were among the biological processes that were most inhibited by L192P-RISC. In neurodevelopment, axons migrate to form connections to other neurons facilitated by the growth cone that reacts to extracellular signals to guide its navigation (Tessier-Lavigne and Goodman 1996, Lowery and Van Vactor 2009). The rapid adjustment of translation required for this process is enabled by local translation, which is regulated by RNAi (Brittis *et al.* 2002, Leung *et al.* 2006, Yao *et al.* 2006, Jung *et al.* 2014, Glock *et al.* 2017). Increased silencing of axon guidance might have detrimental consequences on neurodevelopment leading to the ID phenotype observed in LESKRES patients. Target predictions and GO analyses were performed for both strands of miR-543. The 3p strand of miR-543 was enriched in the L192P-RISC whereas the 5p strand was slightly less associated with Ago2-L192P compared to WT (Figure 38). Completely different targets were predicted for the 3p and 5p strands, highlighting the relevance of arm switching events and the effect on RISC function. Consequently, the GO analyses of the two strands resulted in no overlap of the regulated biological processes. The target predictions of four selected isomiRs and their corresponding canonical miRNAs, the five highest-ranked targets of two analyzed isomiRs are shown in Table 46 and Table 47, resulted in 75% overlap between the predicted targets of the isomiR and the corresponding canonical miRNA. This result indicates a function of isomiRs as additional fine-tuners of RISC-mediated silencing. Lessel *et al.* performed GO analyses with the transcriptome of primary fibroblasts bearing the L192P variant and determined an enrichment of biological processes involved in mitosis and control of the cell cycle (Lessel *et al.* 2020). None of these BPs were found in the GO analyses of the predicted targets of differentially regulated miRNAs in primary cortical neurons expressing Ago2-L192P. It is unclear whether this discrepancy was caused by invalid target prediction or use of different model systems, which differed in cell types (dermal fibroblasts vs. cortical neurons) and species (human vs. mouse). Neurons derived from patient-derived induced pluripotent stem cells could function as a valuable model system to form a bridge between both analyses. Among the limited number of target predictions and GO analyses that I performed here, altered RNAi by L192P-RISC did not seem to converge in distinct signaling cascades but rather results in a broad spectrum of deregulated biological processes, ranging from metabolic processes to neuronal migration and development.

5.3. Do Pathomechanisms of NDDs Converge in Common Pathways?

Despite the heterogeneity of NDD disease genes and the function of the proteins they encode, several studies have suggested that the molecular pathomechanisms underlying the different NDDs converge in a few common signaling pathways (Voineagu *et al.* 2011, Parikshak *et al.* 2013, Cristino *et al.* 2014, Hormozdiari *et al.* 2015, Sahin and Sur 2015). One example is the deregulation of the mTOR pathway in mTORopathies, NDDs characterized by abnormal cortical morphology and epileptic seizures (Crino 2015, Baulac 2016, Borrie *et al.* 2017, Winden *et al.* 2018). The evolutionarily conserved and ubiquitously expressed serine/threonine protein kinase mTOR controls signaling pathways implicated in neuronal proliferation, differentiation and migration by modulating translation (Lipton and Sahin 2014). Protein biosynthesis is regulated by a variety of mechanisms, including the MAPK signaling cascade. The MAPK pathway is activated by specific glutamate receptors and thus couples synaptic activity to the transcriptional and translational machinery. Malfunction of Ras proteins and consequently of the MAPK signaling pathway is causative for a group of diseases referred to as RASopathies (Kelleher and Bear 2008, Tidyman and Rauen 2009, Rauen 2013, Simanshu *et al.* 2017). Neither of these pathways were overrepresented in translome and proteome analyses of *Shank*-KO mice investigated here, nor in target predictions and GO analyses performed for miRNAs differentially bound to the L192P-RISC. Three statements can be concluded from these results:

(1) The molecular defects in *Shank*-KO mice are not mediated by a singular signaling cascade, but rather are characterized by subtle general deregulation of translation, severe alterations of the postsynaptic proteome, and altered activity of the CaMKII α . These alterations may contribute to a general dysregulation of neuronal signaling. (2) The LESKRES-causing *AGO2* variant L192P results in extensive deregulation of RISC-mediated silencing of translation. Differentially expressed and bound miRNAs might regulate various biological processes via RNAi rather than affecting a specific signaling pathway or a single aspect of cellular function. (3) When I compared molecular defects between *SHANK*-associated ASDs and LESKRES, neither the mTOR, nor the MAPK pathway, nor any other distinct signaling cascade was overrepresented.

Translatome, proteome and miRNome demonstrated a broad spectrum of alteration in translation, architecture of the postsynaptic density and miRNA-mediated RNAi. NDD-causing mutations were frequently found to lead to aberrant translation and to alter the homeostatic balance of protein synthesis during development (Scheper *et al.* 2007, Wang *et al.* 2016). Axons, dendrites, and individual synapses display distinct transcriptomes and translomes (Prashad and Gopal 2021). RNAi allows for precise adjustment of these transcript levels and dynamic fine-tuning of translational silencing (Holt and Schuman 2013). The length of neuronal projections, and the structural complexity and polarity of neurons present unique challenges for fulfilling exact control of translation in neurodevelopment and for synaptic plasticity (Sutton and Schuman 2006, Bramham and Wells 2007, Jung *et al.* 2014, Prashad and Gopal 2021). Thus, in neurons, the tolerance for errors is low and the requirements for properly regulated local translation are high. Alterations in translational regulation and RNAi during neurodevelopment have detrimental effects and lead to severe dysfunction in the brain compared with other tissues that may be able to compensate for deregulated translation or have less complex strategies for regulation of translation. Hence, altered control of gene expression and RNAi lead to more severe neurological phenotypes compared to the dysfunction in other tissues and organs, even though RBPs encoded by NDD disease genes such as *Ago2* are often ubiquitously expressed (Freilich *et al.* 2005, Ramskold *et al.* 2009, Prashad and Gopal 2021). This notion is supported by the association of NDDs with mutations in genes encoding for transcriptional regulators and chromatin remodellers such as *MECP2* (Ronan *et al.* 2013, Witteveen *et al.* 2016, Stessman *et al.* 2017, Fernandes *et al.* 2018, Suetterlin *et al.* 2018). Transcription factors and chromatin remodellers regulate transcript abundances and the exact spatiotemporal regulation of their function is especially important during

neurodevelopment. The pathomechanism of these proteins in NDD is linked to global deregulation of transcription (Ronan *et al.* 2013, Witteveen *et al.* 2016, Stessman *et al.* 2017, Fernandes *et al.* 2018, Suetterlin *et al.* 2018, Prashad and Gopal 2021). I propose that the global alteration of L192P-RISC function presented here is comparable to the molecular defects associated to malfunction of transcriptional regulators and chromatin remodellers. Thus, the pathomechanism of LESKRES could be similar to the pathomechanism of NDDs caused by mutations in genes encoding transcription factors and chromatin remodellers. In contrast to Ago2 and the LESKRES, the loss of *Shank3 $\alpha\beta$* in the ASD mouse model resulted in subtle alterations of the translome, whereas the postsynaptic proteome and synaptic signaling were severely affected in *Shank1*-KO and *Shank3 $\alpha\beta$* -KO mice. It remains unclear whether the changes in translation were due to direct function of Shank3 in regulation of translation or were caused by adaptational mechanisms such as feedback loops compensating for compromised postsynaptic architecture, signaling and plasticity (Mullins *et al.* 2016). Taken together, this study showed that the pathomechanisms of Shank-associated forms of ASD and the LESKRES syndrome do not converge in common pathways, but rather result in broad and gene-specific alterations of cellular functions.

6. References

- Abu-Elneel, K., T. Liu, F. S. Gazzaniga, Y. Nishimura, D. P. Wall, D. H. Geschwind, K. Lao, and K. S. Kosik. "Heterogeneous Dysregulation of Micrnas across the Autism Spectrum." *Neurogenetics* 9, no. 3 (Jul 2008): 153-61.
- Agarwal, V., G. W. Bell, J. W. Nam, and D. P. Bartel. "Predicting Effective MicroRNA Target Sites in Mammalian Mrnas." *Elife* 4 (Aug 12 2015).
- Aiso, T., and M. Ueda. "5'-Isomir Is the Most Abundant Sequence of Mir-1246, a Candidate Biomarker of Lung Cancer, in Serum." *Mol Med Rep* 27, no. 4 (Apr 2023).
- Akerblom, M., R. Sachdeva, I. Barde, S. Verp, B. Gentner, D. Trono, and J. Jakobsson. "MicroRNA-124 Is a Subventricular Zone Neuronal Fate Determinant." *J Neurosci* 32, no. 26 (Jun 27 2012): 8879-89.
- Albrecht, T. R., S. P. Shevtsov, Y. Wu, L. G. Mascibroda, N. J. Peart, K. L. Huang, I. A. Sawyer, *et al.* "Integrator Subunit 4 Is a 'Symplekin-Like' Scaffold That Associates with Ints9/11 to Form the Integrator Cleavage Module." *Nucleic Acids Res* 46, no. 8 (May 4 2018): 4241-55.
- Ameres, S. L., and P. D. Zamore. "Diversifying MicroRNA Sequence and Function." *Nat Rev Mol Cell Biol* 14, no. 8 (Aug 2013): 475-88.
- Amos, L., and A. Klug. "Arrangement of Subunits in Flagellar Microtubules." *J Cell Sci* 14, no. 3 (May 1974): 523-49.
- Anders, J., S. Kjar, and C. F. Ibanez. "Molecular Modeling of the Extracellular Domain of the Ret Receptor Tyrosine Kinase Reveals Multiple Cadherin-Like Domains and a Calcium-Binding Site." *J Biol Chem* 276, no. 38 (Sep 21 2001): 35808-17.
- Andrei, M. A., D. Ingelfinger, R. Heintzmann, T. Achsel, R. Rivera-Pomar, and R. Luhrmann. "A Role for Eif4e and Eif4e-Transporter in Targeting Mrnps to Mammalian Processing Bodies." *RNA* 11, no. 5 (May 2005): 717-27.
- Asperger, Hans. "Die „Autistischen Psychopathen“ Im Kindesalter." *Archiv für Psychiatrie und Nervenkrankheiten* 117, no. 1 (1944/06/01 1944): 76-136.
- Attie-Bitach, T., M. Abitbol, M. Gerard, A. L. Delezoide, J. Auge, A. Pelet, J. Amiel, *et al.* "Expression of the Ret Proto-Oncogene in Human Embryos." *Am J Med Genet* 80, no. 5 (Dec 28 1998): 481-6.
- Avantaggiato, V., N. A. Dathan, M. Grieco, N. Fabien, D. Lazzaro, A. Fusco, A. Simeone, and M. Santoro. "Developmental Expression of the Ret Protooncogene." *Cell Growth Differ* 5, no. 3 (Mar 1994): 305-11.
- Azlan, A., N. Dzaki, and G. Azzam. "Argonaute: The Executor of Small Rna Function." *J Genet Genomics* 43, no. 8 (Aug 20 2016): 481-94.
- Baek, D., J. Villen, C. Shin, F. D. Camargo, S. P. Gygi, and D. P. Bartel. "The Impact of Micrnas on Protein Output." *Nature* 455, no. 7209 (Sep 4 2008): 64-71.
- Bagni, C., and W. T. Greenough. "From Mrnp Trafficking to Spine Dymorphogenesis: The Roots of Fragile X Syndrome." *Nat Rev Neurosci* 6, no. 5 (May 2005): 376-87.

- Ballard, D. W., W. H. Walker, S. Doerre, P. Sista, J. A. Molitor, E. P. Dixon, N. J. Peffer, M. Hannink, and W. C. Greene. "The V-Rel Oncogene Encodes a Kappa B Enhancer Binding Protein That Inhibits Nf-Kappa B Function." *Cell* 63, no. 4 (Nov 16 1990): 803-14.
- Bar, M., S. K. Wyman, B. R. Fritz, J. Qi, K. S. Garg, R. K. Parkin, E. M. Kroh, *et al.* "MicroRNA Discovery and Profiling in Human Embryonic Stem Cells by Deep Sequencing of Small Rna Libraries." *Stem Cells* 26, no. 10 (Oct 2008): 2496-505.
- Barbee, S. A., P. S. Estes, A. M. Cziko, J. Hillebrand, R. A. Luedeman, J. M. Collier, N. Johnson, *et al.* "Staufen- and Fmrp-Containing Neuronal Rnps Are Structurally and Functionally Related to Somatic P Bodies." *Neuron* 52, no. 6 (Dec 21 2006): 997-1009.
- Baron, M. K., T. M. Boeckers, B. Vaida, S. Faham, M. Gingery, M. R. Sawaya, D. Salyer, E. D. Gundelfinger, and J. U. Bowie. "An Architectural Framework That May Lie at the Core of the Postsynaptic Density." *Science* 311, no. 5760 (Jan 27 2006): 531-5.
- Bartel, D. P. "MicroRNAs: Genomics, Biogenesis, Mechanism, and Function." *Cell* 116, no. 2 (Jan 23 2004): 281-97.
- Baucum, A. J., 2nd, B. C. Shonesy, K. L. Rose, and R. J. Colbran. "Quantitative Proteomics Analysis of Camkii Phosphorylation and the Camkii Interactome in the Mouse Forebrain." *ACS Chem Neurosci* 6, no. 4 (Apr 15 2015): 615-31.
- Baulac, S. "Mtor Signaling Pathway Genes in Focal Epilepsies." *Prog Brain Res* 226 (2016): 61-79.
- Bayer, K. U., P. De Koninck, A. S. Leonard, J. W. Hell, and H. Schulman. "Interaction with the Nmda Receptor Locks Camkii in an Active Conformation." *Nature* 411, no. 6839 (Jun 14 2001): 801-5.
- Bayer, K. U., E. LeBel, G. L. McDonald, H. O'Leary, H. Schulman, and P. De Koninck. "Transition from Reversible to Persistent Binding of Camkii to Postsynaptic Sites and Nr2b." *J Neurosci* 26, no. 4 (Jan 25 2006): 1164-74.
- Behm-Ansmant, I., J. Rehwinkel, T. Doerks, A. Stark, P. Bork, and E. Izaurralde. "Mrna Degradation by Mirnas and Gw182 Requires Both Ccr4:Not Deadenylase and Dcp1:Dcp2 Decapping Complexes." *Genes Dev* 20, no. 14 (Jul 15 2006): 1885-98.
- Behm-Ansmant, I., J. Rehwinkel, and E. Izaurralde. "MicroRNAs Silence Gene Expression by Repressing Protein Expression and/or by Promoting Mrna Decay." *Cold Spring Harb Symp Quant Biol* 71 (2006): 523-30.
- Berkel, S., C. R. Marshall, B. Weiss, J. Howe, R. Roeth, U. Moog, V. Endris, *et al.* "Mutations in the Shank2 Synaptic Scaffolding Gene in Autism Spectrum Disorder and Mental Retardation." *Nat Genet* 42, no. 6 (Jun 2010): 489-91.
- Berkel, S., W. Tang, M. Trevino, M. Vogt, H. A. Obenaus, P. Gass, S. W. Scherer, *et al.* "Inherited and De Novo Shank2 Variants Associated with Autism Spectrum Disorder Impair Neuronal Morphogenesis and Physiology." *Hum Mol Genet* 21, no. 2 (Jan 15 2012): 344-57.
- Bernstein, E., A. A. Caudy, S. M. Hammond, and G. J. Hannon. "Role for a Bidentate Ribonuclease in the Initiation Step of Rna Interference." *Nature* 409, no. 6818 (Jan 18 2001): 363-6.
- Betancur, C., T. Sakurai, and J. D. Buxbaum. "The Emerging Role of Synaptic Cell-Adhesion Pathways in the Pathogenesis of Autism Spectrum Disorders." *Trends Neurosci* 32, no. 7 (Jul 2009): 402-12.

- Betel, D., A. Koppal, P. Agius, C. Sander, and C. Leslie. "Comprehensive Modeling of MicroRNA Targets Predicts Functional Non-Conserved and Non-Canonical Sites." *Genome Biol* 11, no. 8 (2010): R90.
- Bhardwaj, A., H. Singh, C. M. Trinidad, C. T. Albarracin, K. K. Hunt, and I. Bedrosian. "The Isomir-140-3p-Regulated Mevalonic Acid Pathway as a Potential Target for Prevention of Triple Negative Breast Cancer." *Breast Cancer Res* 20, no. 1 (Dec 11 2018): 150.
- Birney, E., D. Andrews, M. Caccamo, Y. Chen, L. Clarke, G. Coates, T. Cox, *et al.* "Ensembl 2006." *Nucleic Acids Res* 34, no. Database issue (Jan 1 2006): D556-61.
- Blanchoin, L., K. J. Amann, H. N. Higgs, J. B. Marchand, D. A. Kaiser, and T. D. Pollard. "Direct Observation of Dendritic Actin Filament Networks Nucleated by Arp2/3 Complex and Wasp/Scar Proteins." *Nature* 404, no. 6781 (Apr 27 2000): 1007-11.
- Boccutto, L., M. Lauri, S. M. Sarasua, C. D. Skinner, D. Buccella, A. Dwivedi, D. Orteschi, *et al.* "Prevalence of Shank3 Variants in Patients with Different Subtypes of Autism Spectrum Disorders." *Eur J Hum Genet* 21, no. 3 (Mar 2013): 310-6.
- Bockers, T. M., M. G. Mameza, M. R. Kreutz, J. Bockmann, C. Weise, F. Buck, D. Richter, E. D. Gundelfinger, and H. J. Kreienkamp. "Synaptic Scaffolding Proteins in Rat Brain. Ankyrin Repeats of the Multidomain Shank Protein Family Interact with the Cytoskeletal Protein Alpha-Fodrin." *J Biol Chem* 276, no. 43 (Oct 26 2001): 40104-12.
- Bockers, T. M., M. Segger-Junius, P. Iglauer, J. Bockmann, E. D. Gundelfinger, M. R. Kreutz, D. Richter, S. Kindler, and H. J. Kreienkamp. "Differential Expression and Dendritic Transcript Localization of Shank Family Members: Identification of a Dendritic Targeting Element in the 3' Untranslated Region of Shank1 Mrna." *Mol Cell Neurosci* 26, no. 1 (May 2004): 182-90.
- Boeckers, T. M., M. R. Kreutz, C. Winter, W. Zuschratter, K. H. Smalla, L. Sanmarti-Vila, H. Wex, *et al.* "Proline-Rich Synapse-Associated Protein-1/Cortactin Binding Protein 1 (Prosap1/Cortbp1) Is a PdZ-Domain Protein Highly Enriched in the Postsynaptic Density." *J Neurosci* 19, no. 15 (Aug 1 1999): 6506-18.
- Boeckers, T. M., T. Liedtke, C. Spilker, T. Dresbach, J. Bockmann, M. R. Kreutz, and E. D. Gundelfinger. "C-Terminal Synaptic Targeting Elements for Postsynaptic Density Proteins Prosap1/Shank2 and Prosap2/Shank3." *J Neurochem* 92, no. 3 (Feb 2005): 519-24.
- Bohnsack, M. T., K. Czaplinski, and D. Gorlich. "Exportin 5 Is a RanGTP-Dependent Dsrna-Binding Protein That Mediates Nuclear Export of Pre-Mirnas." *RNA* 10, no. 2 (Feb 2004): 185-91.
- Boland, A., E. Huntzinger, S. Schmidt, E. Izaurralde, and O. Weichenrieder. "Crystal Structure of the Mid-Piwi Lobe of a Eukaryotic Argonaute Protein." *Proc Natl Acad Sci U S A* 108, no. 26 (Jun 28 2011): 10466-71.
- Bolduc, F. V., K. Bell, H. Cox, K. S. Broadie, and T. Tully. "Excess Protein Synthesis in Drosophila Fragile X Mutants Impairs Long-Term Memory." *Nat Neurosci* 11, no. 10 (Oct 2008): 1143-5.
- Bonaglia, M. C., R. Giorda, S. Beri, C. De Agostini, F. Novara, M. Fichera, L. Grillo, *et al.* "Molecular Mechanisms Generating and Stabilizing Terminal 22q13 Deletions in 44 Subjects with Phelan/Mcdermid Syndrome." *PLoS Genet* 7, no. 7 (Jul 2011): e1002173.

- Bonaglia, M. C., R. Giorda, R. Borgatti, G. Felisari, C. Gagliardi, A. Selicorni, and O. Zuffardi. "Disruption of the *Prosap2* Gene in a T(12;22)(Q24.1;Q13.3) Is Associated with the 22q13.3 Deletion Syndrome." *Am J Hum Genet* 69, no. 2 (Aug 2001): 261-8.
- Bonaglia, M. C., R. Giorda, R. Tenconi, M. Pessina, T. Pramparo, R. Borgatti, and O. Zuffardi. "A 2.3 Mb Duplication of Chromosome 8q24.3 Associated with Severe Mental Retardation and Epilepsy Detected by Standard Karyotype." *Eur J Hum Genet* 13, no. 5 (May 2005): 586-91.
- Borrie, S. C., H. Brems, E. Legius, and C. Bagni. "Cognitive Dysfunctions in Intellectual Disabilities: The Contributions of the Ras-Mapk and Pi3k-Akt-Mtor Pathways." *Annu Rev Genomics Hum Genet* 18 (Aug 31 2017): 115-42.
- Bosch, M., J. Castro, T. Saneyoshi, H. Matsuno, M. Sur, and Y. Hayashi. "Structural and Molecular Remodeling of Dendritic Spine Substructures During Long-Term Potentiation." *Neuron* 82, no. 2 (Apr 16 2014): 444-59.
- Bourgeron, T. "From the Genetic Architecture to Synaptic Plasticity in Autism Spectrum Disorder." *Nat Rev Neurosci* 16, no. 9 (Sep 2015): 551-63.
- Bozdagi, O., T. Sakurai, D. Papapetrou, X. Wang, D. L. Dickstein, N. Takahashi, Y. Kajiwara, *et al.* "Haploinsufficiency of the Autism-Associated *Shank3* Gene Leads to Deficits in Synaptic Function, Social Interaction, and Social Communication." *Mol Autism* 1, no. 1 (Dec 17 2010): 15.
- Bramham, C. R., and D. G. Wells. "Dendritic Mrna: Transport, Translation and Function." *Nat Rev Neurosci* 8, no. 10 (Oct 2007): 776-89.
- Brennecke, J., and S. M. Cohen. "Towards a Complete Description of the MicroRNA Complement of Animal Genomes." *Genome Biol* 4, no. 9 (2003): 228.
- Brittis, P. A., Q. Lu, and J. G. Flanagan. "Axonal Protein Synthesis Provides a Mechanism for Localized Regulation at an Intermediate Target." *Cell* 110, no. 2 (Jul 26 2002): 223-35.
- Brownell, E., B. Mathieson, H. A. Young, J. Keller, J. N. Ihle, and N. R. Rice. "Detection of C-Rel-Related Transcripts in Mouse Hematopoietic Tissues, Fractionated Lymphocyte Populations, and Cell Lines." *Mol Cell Biol* 7, no. 3 (Mar 1987): 1304-9.
- Burroughs, A. M., Y. Ando, M. J. de Hoon, Y. Tomaru, T. Nishibu, R. Ukekawa, T. Funakoshi, *et al.* "A Comprehensive Survey of 3' Animal Mirna Modification Events and a Possible Role for 3' Adenylation in Modulating Mirna Targeting Effectiveness." *Genome Res* 20, no. 10 (Oct 2010): 1398-410.
- Butler, M. G., M. J. Dasouki, X. P. Zhou, Z. Talebizadeh, M. Brown, T. N. Takahashi, J. H. Miles, *et al.* "Subset of Individuals with Autism Spectrum Disorders and Extreme Macrocephaly Associated with Germline *Pten* Tumour Suppressor Gene Mutations." *J Med Genet* 42, no. 4 (Apr 2005): 318-21.
- Cadwell, C. R., A. Bhaduri, M. A. Mostajo-Radji, M. G. Keefe, and T. J. Nowakowski. "Development and Arealization of the Cerebral Cortex." *Neuron* 103, no. 6 (Sep 25 2019): 980-1004.
- Cai, Q., M. Zeng, X. Wu, H. Wu, Y. Zhan, R. Tian, and M. Zhang. "Camkii α -Driven, Phosphatase-Checked Postsynaptic Plasticity Via Phase Separation." *Cell Res* 31, no. 1 (Jan 2021): 37-51.

- Cai, X., C. H. Hagedorn, and B. R. Cullen. "Human Micrnas Are Processed from Capped, Polyadenylated Transcripts That Can Also Function as Mrnas." *RNA* 10, no. 12 (Dec 2004): 1957-66.
- Cao, X., G. Yeo, A. R. Muotri, T. Kuwabara, and F. H. Gage. "Noncoding Rnas in the Mammalian Central Nervous System." *Annu Rev Neurosci* 29 (2006): 77-103.
- Capece, V., J. C. Garcia Vizcaino, R. Vidal, R. U. Rahman, T. Pena Centeno, O. Shomroni, I. Suberviola, A. Fischer, and S. Bonn. "Oasis: Online Analysis of Small Rna Deep Sequencing Data." *Bioinformatics* 31, no. 13 (Jul 1 2015): 2205-7.
- Carlisle, H. J., and M. B. Kennedy. "Spine Architecture and Synaptic Plasticity." *Trends Neurosci* 28, no. 4 (Apr 2005): 182-7.
- Carneiro, T. N., A. C. Krepischi, S. S. Costa, I. Tojal da Silva, A. M. Vianna-Morgante, R. Valieris, S. A. Ezquina, *et al.* "Utility of Trio-Based Exome Sequencing in the Elucidation of the Genetic Basis of Isolated Syndromic Intellectual Disability: Illustrative Cases." *Appl Clin Genet* 11 (2018): 93-98.
- Carninci, P., T. Kasukawa, S. Katayama, J. Gough, M. C. Frith, N. Maeda, R. Oyama, *et al.* "The Transcriptional Landscape of the Mammalian Genome." *Science* 309, no. 5740 (Sep 2 2005): 1559-63.
- Carthew, R. W., and E. J. Sontheimer. "Origins and Mechanisms of Mirnas and Sirnas." *Cell* 136, no. 4 (Feb 20 2009): 642-55.
- Cataldi, S., C. Lacefield, N. Shashaank, G. Kumar, S. Boumhaouad, and D. Sulzer. "Decreased Dorsomedial Striatum Direct Pathway Neuronal Activity Is Required for Learned Motor Coordination." *eNeuro* 9, no. 5 (Sep-Oct 2022).
- Caudy, A. A., M. Myers, G. J. Hannon, and S. M. Hammond. "Fragile X-Related Protein and Vig Associate with the Rna Interference Machinery." *Genes Dev* 16, no. 19 (Oct 1 2002): 2491-6.
- Chaaban, S., and G. J. Brouhard. "A Microtubule Bestiary: Structural Diversity in tubulin Polymers." *Mol Biol Cell* 28, no. 22 (Nov 1 2017): 2924-31.
- Chan, K. Y., M. J. Jang, B. B. Yoo, A. Greenbaum, N. Ravi, W. L. Wu, L. Sanchez-Guardado, *et al.* "Engineered Aavs for Efficient Noninvasive Gene Delivery to the Central and Peripheral Nervous Systems." *Nat Neurosci* 20, no. 8 (Aug 2017): 1172-79.
- Chappleboim, A., D. Joseph-Strauss, O. Gershon, and N. Friedman. "Transcription Feedback Dynamics in the Wake of Cytoplasmic Mrna Degradation Shutdown." *Nucleic Acids Res* 50, no. 10 (Jun 10 2022): 5864-80.
- Chatterjee, S., M. Fasler, I. Bussing, and H. Grosshans. "Target-Mediated Protection of Endogenous Micrnas in *C. Elegans*." *Dev Cell* 20, no. 3 (Mar 15 2011): 388-96.
- Chen, E. Y., C. M. Tan, Y. Kou, Q. Duan, Z. Wang, G. V. Meirelles, N. R. Clark, and A. Ma'ayan. "Enrichr: Interactive and Collaborative Htm15 Gene List Enrichment Analysis Tool." *BMC Bioinformatics* 14 (Apr 15 2013): 128.
- Chen, X., L. Vinade, R. D. Leapman, J. D. Petersen, T. Nakagawa, T. M. Phillips, M. Sheng, and T. S. Reese. "Mass of the Postsynaptic Density and Enumeration of Three Key Molecules." *Proc Natl Acad Sci U S A* 102, no. 32 (Aug 9 2005): 11551-6.

- Chen, Y., and X. Wang. "Mirdb: An Online Database for Prediction of Functional MicroRNA Targets." *Nucleic Acids Res* 48, no. D1 (Jan 8 2020): D127-D31.
- Chi, S. W., J. B. Zang, A. Mele, and R. B. Darnell. "Argonaute Hits-Clip Decodes MicroRNA-Mrna Interaction Maps." *Nature* 460, no. 7254 (Jul 23 2009): 479-86.
- Chklovskii, D. B. "Synaptic Connectivity and Neuronal Morphology: Two Sides of the Same Coin." *Neuron* 43, no. 5 (Sep 2 2004): 609-17.
- Chu, C. Y., and T. M. Rana. "Translation Repression in Human Cells by MicroRNA-Induced Gene Silencing Requires Rck/P54." *PLoS Biol* 4, no. 7 (Jul 2006): e210.
- Clark, M. M., Z. Stark, L. Farnaes, T. Y. Tan, S. M. White, D. Dimmock, and S. F. Kingsmore. "Meta-Analysis of the Diagnostic and Clinical Utility of Genome and Exome Sequencing and Chromosomal Microarray in Children with Suspected Genetic Diseases." *NPJ Genom Med* 3 (2018): 16.
- Clarke, A. "Rett Syndrome." *J Med Genet* 33, no. 8 (Aug 1996): 693-9.
- Cloonan, N., S. Wani, Q. Xu, J. Gu, K. Lea, S. Heater, C. Barbacioru, *et al.* "MicroRNAs and Their Isomirs Function Cooperatively to Target Common Biological Pathways." *Genome Biol* 12, no. 12 (Dec 30 2011): R126.
- Cohen, J. E., P. R. Lee, S. Chen, W. Li, and R. D. Fields. "MicroRNA Regulation of Homeostatic Synaptic Plasticity." *Proc Natl Acad Sci U S A* 108, no. 28 (Jul 12 2011): 11650-5.
- Colgan, L. A., and R. Yasuda. "Plasticity of Dendritic Spines: Subcompartmentalization of Signaling." *Annu Rev Physiol* 76 (2014): 365-85.
- Collins, M. O., H. Husi, L. Yu, J. M. Brandon, C. N. Anderson, W. P. Blackstock, J. S. Choudhary, and S. G. Grant. "Molecular Characterization and Comparison of the Components and Multiprotein Complexes in the Postsynaptic Proteome." *J Neurochem* 97 Suppl 1 (Apr 2006): 16-23.
- Constantino, J. N. "The Quantitative Nature of Autistic Social Impairment." *Pediatr Res* 69, no. 5 Pt 2 (May 2011): 55R-62R.
- Cougot, N., S. Babajko, and B. Seraphin. "Cytoplasmic Foci Are Sites of Mrna Decay in Human Cells." *J Cell Biol* 165, no. 1 (Apr 2004): 31-40.
- Courtois, G., and T. D. Gilmore. "Mutations in the Nf-Kappab Signaling Pathway: Implications for Human Disease." *Oncogene* 25, no. 51 (Oct 30 2006): 6831-43.
- Crino, P. B. "Mtor Signaling in Epilepsy: Insights from Malformations of Cortical Development." *Cold Spring Harb Perspect Med* 5, no. 4 (Apr 1 2015).
- Cristino, A. S., S. M. Williams, Z. Hawi, J. Y. An, M. A. Bellgrove, C. E. Schwartz, F. Costa Lda, and C. Claudianos. "Neurodevelopmental and Neuropsychiatric Disorders Represent an Interconnected Molecular System." *Mol Psychiatry* 19, no. 3 (Mar 2014): 294-301.
- Curatolo, P., R. Moavero, and P. J. de Vries. "Neurological and Neuropsychiatric Aspects of Tuberous Sclerosis Complex." *Lancet Neurol* 14, no. 7 (Jul 2015): 733-45.
- Czech, B., and G. J. Hannon. "Small Rna Sorting: Matchmaking for Argonautes." *Nat Rev Genet* 12, no. 1 (Jan 2011): 19-31.

- da Rocha, S. T., C. A. Edwards, M. Ito, T. Ogata, and A. C. Ferguson-Smith. "Genomic Imprinting at the Mammalian Dlk1-Dio3 Domain." *Trends Genet* 24, no. 6 (Jun 2008): 306-16.
- Darnell, J. C., S. J. Van Driesche, C. Zhang, K. Y. Hung, A. Mele, C. E. Fraser, E. F. Stone, *et al.* "Fmrp Stalls Ribosomal Translocation on Mrnas Linked to Synaptic Function and Autism." *Cell* 146, no. 2 (Jul 22 2011): 247-61.
- Davis, T. H., T. L. Cuellar, S. M. Koch, A. J. Barker, B. D. Harfe, M. T. McManus, and E. M. Ullian. "Conditional Loss of Dicer Disrupts Cellular and Tissue Morphogenesis in the Cortex and Hippocampus." *J Neurosci* 28, no. 17 (Apr 23 2008): 4322-30.
- De Jaco, A., Z. Kovarik, D. Comoletti, L. L. Jennings, G. Gaietta, M. H. Ellisman, and P. Taylor. "A Single Mutation near the C-Terminus in Alpha/Beta Hydrolase Fold Protein Family Causes a Defect in Protein Processing." *Chem Biol Interact* 157-158 (Dec 15 2005): 371-2.
- de Vries, P. J., E. Belousova, M. P. Benedik, T. Carter, V. Cottin, P. Curatolo, L. D'Amato, *et al.* "Natural Clusters of Tuberous Sclerosis Complex (Tsc)-Associated Neuropsychiatric Disorders (Tand): New Findings from the Tosca Tand Research Project." *J Neurodev Disord* 12, no. 1 (Sep 1 2020): 24.
- DeBoer, E. M., R. Azevedo, T. A. Vega, J. Brodtkin, W. Akamatsu, H. Okano, G. C. Wagner, and M. R. Rasin. "Prenatal Deletion of the Rna-Binding Protein Hud Disrupts Postnatal Cortical Circuit Maturation and Behavior." *J Neurosci* 34, no. 10 (Mar 5 2014): 3674-86.
- Denli, A. M., B. B. Tops, R. H. Plasterk, R. F. Ketting, and G. J. Hannon. "Processing of Primary Micrnas by the Microprocessor Complex." *Nature* 432, no. 7014 (Nov 11 2004): 231-5.
- Dent, E. W., E. B. Merriam, and X. Hu. "The Dynamic Cytoskeleton: Backbone of Dendritic Spine Plasticity." *Curr Opin Neurobiol* 21, no. 1 (Feb 2011): 175-81.
- Devys, D., Y. Lutz, N. Rouyer, J. P. Bellocq, and J. L. Mandel. "The Fmr-1 Protein Is Cytoplasmic, Most Abundant in Neurons and Appears Normal in Carriers of a Fragile X Premutation." *Nat Genet* 4, no. 4 (Aug 1993): 335-40.
- Djebali, S., C. A. Davis, A. Merkel, A. Dobin, T. Lassmann, A. Mortazavi, A. Tanzer, *et al.* "Landscape of Transcription in Human Cells." *Nature* 489, no. 7414 (Sep 6 2012): 101-8.
- Dobin, A., C. A. Davis, F. Schlesinger, J. Drenkow, C. Zaleski, S. Jha, P. Batut, M. Chaisson, and T. R. Gingeras. "Star: Ultrafast Universal Rna-Seq Aligner." *Bioinformatics* 29, no. 1 (Jan 1 2013): 15-21.
- Dolmetsch, R. "Excitation-Transcription Coupling: Signaling by Ion Channels to the Nucleus." *Sci STKE* 2003, no. 166 (Jan 21 2003): PE4.
- Dompierre, J. P., J. D. Godin, B. C. Charrin, F. P. Cordelieres, S. J. King, S. Humbert, and F. Saudou. "Histone Deacetylase 6 Inhibition Compensates for the Transport Deficit in Huntington's Disease by Increasing tubulin Acetylation." *J Neurosci* 27, no. 13 (Mar 28 2007): 3571-83.
- Dosemeci, A., J. H. Tao-Cheng, L. Vinade, C. A. Winters, L. Pozzo-Miller, and T. S. Reese. "Glutamate-Induced Transient Modification of the Postsynaptic Density." *Proc Natl Acad Sci U S A* 98, no. 18 (Aug 28 2001): 10428-32.
- Doxzen, K. W., and J. A. Doudna. "DNA Recognition by an Rna-Guided Bacterial Argonaute." *PLoS One* 12, no. 5 (2017): e0177097.

- Du, X., X. Gao, X. Liu, L. Shen, K. Wang, Y. Fan, Y. Sun, *et al.* "Genetic Diagnostic Evaluation of Trio-Based Whole Exome Sequencing among Children with Diagnosed or Suspected Autism Spectrum Disorder." *Front Genet* 9 (2018): 594.
- Du, Y., S. A. Weed, W. C. Xiong, T. D. Marshall, and J. T. Parsons. "Identification of a Novel Cortactin Sh3 Domain-Binding Protein and Its Localization to Growth Cones of Cultured Neurons." *Mol Cell Biol* 18, no. 10 (Oct 1998): 5838-51.
- Duffney, L. J., P. Zhong, J. Wei, E. Matas, J. Cheng, L. Qin, K. Ma, *et al.* "Autism-Like Deficits in Shank3-Deficient Mice Are Rescued by Targeting Actin Regulators." *Cell Rep* 11, no. 9 (Jun 9 2015): 1400-13.
- Durand, C. M., C. Betancur, T. M. Boeckers, J. Bockmann, P. Chaste, F. Fauchereau, G. Nygren, *et al.* "Mutations in the Gene Encoding the Synaptic Scaffolding Protein Shank3 Are Associated with Autism Spectrum Disorders." *Nat Genet* 39, no. 1 (Jan 2007): 25-7.
- Durbec, P., C. V. Marcos-Gutierrez, C. Kilkenny, M. Grigoriou, K. Wartiovaara, P. Suvanto, D. Smith, *et al.* "Gdnf Signalling through the Ret Receptor Tyrosine Kinase." *Nature* 381, no. 6585 (Jun 27 1996): 789-93.
- Ecker, C., W. Spooren, and D. G. Murphy. "Translational Approaches to the Biology of Autism: False Dawn or a New Era?" *Mol Psychiatry* 18, no. 4 (Apr 2013): 435-42.
- Elkayam, E., C. R. Faehnle, M. Morales, J. Sun, H. Li, and L. Joshua-Tor. "Multivalent Recruitment of Human Argonaute by Gw182." *Mol Cell* 67, no. 4 (Aug 17 2017): 646-58 e3.
- Eshun-Wilson, L., R. Zhang, D. Portran, M. V. Nachury, D. B. Toso, T. Lohr, M. Vendruscolo, *et al.* "Effects of Alpha-tubulin Acetylation on Microtubule Structure and Stability." *Proc Natl Acad Sci U S A* 116, no. 21 (May 21 2019): 10366-71.
- Eulalio, A., I. Behm-Ansmant, D. Schweizer, and E. Izaurralde. "P-Body Formation Is a Consequence, Not the Cause, of Rna-Mediated Gene Silencing." *Mol Cell Biol* 27, no. 11 (Jun 2007): 3970-81.
- Even, A., G. Morelli, L. Broix, C. Scaramuzzino, S. Turchetto, I. Gladwyn-Ng, R. Le Bail, *et al.* "Atat1-Enriched Vesicles Promote Microtubule Acetylation Via Axonal Transport." *Sci Adv* 5, no. 12 (Dec 2019): eaax2705.
- Eystathioy, T., E. K. Chan, S. A. Tenenbaum, J. D. Keene, K. Griffith, and M. J. Fritzler. "A Phosphorylated Cytoplasmic Autoantigen, Gw182, Associates with a Unique Population of Human Mrnas within Novel Cytoplasmic Speckles." *Mol Biol Cell* 13, no. 4 (Apr 2002): 1338-51.
- Faehnle, C. R., and L. Joshua-Tor. "Argonautes Confront New Small Rnas." *Curr Opin Chem Biol* 11, no. 5 (Oct 2007): 569-77.
- Fehlmann, T., C. Backes, M. Kahraman, J. Haas, N. Ludwig, A. E. Posch, M. L. Wurstle, *et al.* "Web-Based Ngs Data Analysis Using Mirmaster: A Large-Scale Meta-Analysis of Human Mirnas." *Nucleic Acids Res* 45, no. 15 (Sep 6 2017): 8731-44.
- Feng, B., P. Hu, S. J. Lu, J. B. Chen, and R. L. Ge. "Increased Argonaute 2 Expression in Gliomas and Its Association with Tumor Progression and Poor Prognosis." *Asian Pac J Cancer Prev* 15, no. 9 (2014): 4079-83.
- Fernandes, I. R., A. C. P. Cruz, A. Ferrasa, D. Phan, R. H. Herai, and A. R. Muotri. "Genetic Variations on Setd5 Underlying Autistic Conditions." *Dev Neurobiol* 78, no. 5 (May 2018): 500-18.

- Filipowicz, W. "Rnai: The Nuts and Bolts of the Risc Machine." *Cell* 122, no. 1 (Jul 15 2005): 17-20.
- Fiore, R., S. Khudayberdiev, M. Christensen, G. Siegel, S. W. Flavell, T. K. Kim, M. E. Greenberg, and G. Schratt. "Mef2-Mediated Transcription of the Mir379-410 Cluster Regulates Activity-Dependent Dendritogenesis by Fine-Tuning Pumilio2 Protein Levels." *EMBO J* 28, no. 6 (Mar 18 2009): 697-710.
- Fischer, M., S. Kaech, D. Knutti, and A. Matus. "Rapid Actin-Based Plasticity in Dendritic Spines." *Neuron* 20, no. 5 (May 1998): 847-54.
- Flavell, S. W., C. W. Cowan, T. K. Kim, P. L. Greer, Y. Lin, S. Paradis, E. C. Griffith, *et al.* "Activity-Dependent Regulation of Mef2 Transcription Factors Suppresses Excitatory Synapse Number." *Science* 311, no. 5763 (Feb 17 2006): 1008-12.
- Flavell, S. W., and M. E. Greenberg. "Signaling Mechanisms Linking Neuronal Activity to Gene Expression and Plasticity of the Nervous System." *Annu Rev Neurosci* 31 (2008): 563-90.
- Foxe, J. J., S. Molholm, V. A. Del Bene, H. P. Frey, N. N. Russo, D. Blanco, D. Saint-Amour, and L. A. Ross. "Severe Multisensory Speech Integration Deficits in High-Functioning School-Aged Children with Autism Spectrum Disorder (Asd) and Their Resolution During Early Adolescence." *Cereb Cortex* 25, no. 2 (Feb 2015): 298-312.
- Frank, F., N. Sonenberg, and B. Nagar. "Structural Basis for 5'-Nucleotide Base-Specific Recognition of Guide Rna by Human Ago2." *Nature* 465, no. 7299 (Jun 10 2010): 818-22.
- Freilich, S., T. Massingham, S. Bhattacharyya, H. Ponsting, P. A. Lyons, T. C. Freeman, and J. M. Thornton. "Relationship between the Tissue-Specificity of Mouse Gene Expression and the Evolutionary Origin and Function of the Proteins." *Genome Biol* 6, no. 7 (2005): R56.
- Friedman, R. C., K. K. Farh, C. B. Burge, and D. P. Bartel. "Most Mammalian Mrnas Are Conserved Targets of Micrnas." *Genome Res* 19, no. 1 (Jan 2009): 92-105.
- Fuchs, E., G. Flugge, and B. Czeh. "Remodeling of Neuronal Networks by Stress." *Front Biosci* 11 (Sep 1 2006): 2746-58.
- Fukuda, T., K. Kiuchi, and M. Takahashi. "Novel Mechanism of Regulation of Rac Activity and Lamellipodia Formation by Ret Tyrosine Kinase." *J Biol Chem* 277, no. 21 (May 24 2002): 19114-21.
- Gandal, M. J., P. Zhang, E. Hadjimichael, R. L. Walker, C. Chen, S. Liu, H. Won, *et al.* "Transcriptome-Wide Isoform-Level Dysregulation in Asd, Schizophrenia, and Bipolar Disorder." *Science* 362, no. 6420 (Dec 14 2018).
- Gao, C. L., R. Sun, D. H. Li, and F. Gong. "Piwi-Like Protein 1 Upregulation Promotes Gastric Cancer Invasion and Metastasis." *Oncotargets Ther* 11 (2018): 8783-89.
- Gardiner, E., N. J. Beveridge, J. Q. Wu, V. Carr, R. J. Scott, P. A. Tooney, and M. J. Cairns. "Imprinted Dlk1-Dio3 Region of 14q32 Defines a Schizophrenia-Associated Mirna Signature in Peripheral Blood Mononuclear Cells." *Mol Psychiatry* 17, no. 8 (Jul 2012): 827-40.
- Garneau, N. L., J. Wilusz, and C. J. Wilusz. "The Highways and Byways of Mrna Decay." *Nat Rev Mol Cell Biol* 8, no. 2 (Feb 2007): 113-26.

- Garner, C. C., J. Nash, and R. L. Huganir. "PdZ Domains in Synapse Assembly and Signalling." *Trends Cell Biol* 10, no. 7 (Jul 2000): 274-80.
- Gauthier, J., D. Spiegelman, A. Piton, R. G. Lafreniere, S. Laurent, J. St-Onge, L. Lapointe, *et al.* "Novel De Novo Shank3 Mutation in Autistic Patients." *Am J Med Genet B Neuropsychiatr Genet* 150B, no. 3 (Apr 5 2009): 421-4.
- Gerondakis, S., R. Grumont, R. Gugasyan, L. Wong, I. Isomura, W. Ho, and A. Banerjee. "Unravelling the Complexities of the Nf-Kappab Signalling Pathway Using Mouse Knockout and Transgenic Models." *Oncogene* 25, no. 51 (Oct 30 2006): 6781-99.
- Gerstberger, S., M. Hafner, and T. Tuschl. "A Census of Human Rna-Binding Proteins." *Nat Rev Genet* 15, no. 12 (Dec 2014): 829-45.
- Ghazalpour, A., B. Bennett, V. A. Petyuk, L. Orozco, R. Hagopian, I. N. Mungrue, C. R. Farber, *et al.* "Comparative Analysis of Proteome and Transcriptome Variation in Mouse." *PLoS Genet* 7, no. 6 (Jun 2011): e1001393.
- Ghildiyal, M., J. Xu, H. Seitz, Z. Weng, and P. D. Zamore. "Sorting of Drosophila Small Silencing Rnas Partitions Microrna* Strands into the Rna Interference Pathway." *RNA* 16, no. 1 (Jan 2010): 43-56.
- Ghildiyal, M., and P. D. Zamore. "Small Silencing Rnas: An Expanding Universe." *Nat Rev Genet* 10, no. 2 (Feb 2009): 94-108.
- Gillberg, C. "The Essence in Child Psychiatry: Early Symptomatic Syndromes Eliciting Neurodevelopmental Clinical Examinations." *Res Dev Disabil* 31, no. 6 (Nov-Dec 2010): 1543-51.
- Gilmore, T. D., and H. M. Temin. "V-Rel Oncoproteins in the Nucleus and in the Cytoplasm Transform Chicken Spleen Cells." *J Virol* 62, no. 3 (Mar 1988): 703-14.
- Giraldez, A. J., Y. Mishima, J. Rihel, R. J. Grocock, S. Van Dongen, K. Inoue, A. J. Enright, and A. F. Schier. "Zebrafish Mir-430 Promotes Deadenylation and Clearance of Maternal Mrnas." *Science* 312, no. 5770 (Apr 7 2006): 75-9.
- Glock, C., M. Heumuller, and E. M. Schuman. "Mrna Transport & Local Translation in Neurons." *Curr Opin Neurobiol* 45 (Aug 2017): 169-77.
- Godena, V. K., N. Brookes-Hocking, A. Moller, G. Shaw, M. Oswald, R. M. Sancho, C. C. Miller, A. J. Whitworth, and K. J. De Vos. "Increasing Microtubule Acetylation Rescues Axonal Transport and Locomotor Deficits Caused by Lrrk2 Roc-Cor Domain Mutations." *Nat Commun* 5 (Oct 15 2014): 5245.
- Golden, R. J., B. Chen, T. Li, J. Braun, H. Manjunath, X. Chen, J. Wu, *et al.* "An Argonaute Phosphorylation Cycle Promotes Microrna-Mediated Silencing." *Nature* 542, no. 7640 (Feb 9 2017): 197-202.
- Gonzalez-Reyes, L. E., M. Verbitsky, J. Blesa, V. Jackson-Lewis, D. Paredes, K. Tillack, S. Phani, *et al.* "Sonic Hedgehog Maintains Cellular and Neurochemical Homeostasis in the Adult Nigrostriatal Circuit." *Neuron* 75, no. 2 (Jul 26 2012): 306-19.

- Gou, L. T., J. Y. Kang, P. Dai, X. Wang, F. Li, S. Zhao, M. Zhang, *et al.* "Ubiquitination-Deficient Mutations in Human Piwi Cause Male Infertility by Impairing Histone-to-Protamine Exchange During Spermiogenesis." *Cell* 169, no. 6 (Jun 1 2017): 1090-104 e13.
- Grabrucker, A. M., M. J. Knight, C. Proepper, J. Bockmann, M. Joubert, M. Rowan, G. U. Nienhaus, *et al.* "Concerted Action of Zinc and Prosap/Shank in Synaptogenesis and Synapse Maturation." *EMBO J* 30, no. 3 (Feb 2 2011): 569-81.
- Grabrucker, A. M., M. J. Schmeisser, M. Schoen, and T. M. Boeckers. "Postsynaptic Prosap/Shank Scaffolds in the Cross-Hair of Synaptopathies." *Trends Cell Biol* 21, no. 10 (Oct 2011): 594-603.
- Gregory, R. I., K. P. Yan, G. Amuthan, T. Chendrimada, B. Doratotaj, N. Cooch, and R. Shiekhattar. "The Microprocessor Complex Mediates the Genesis of Micrnas." *Nature* 432, no. 7014 (Nov 11 2004): 235-40.
- Grishok, A., A. E. Pasquinelli, D. Conte, N. Li, S. Parrish, I. Ha, D. L. Baillie, *et al.* "Genes and Mechanisms Related to Rna Interference Regulate Expression of the Small Temporal Rnas That Control C. Elegans Developmental Timing." *Cell* 106, no. 1 (Jul 13 2001): 23-34.
- Grunditz, A., N. Holbro, L. Tian, Y. Zuo, and T. G. Oertner. "Spine Neck Plasticity Controls Postsynaptic Calcium Signals through Electrical Compartmentalization." *J Neurosci* 28, no. 50 (Dec 10 2008): 13457-66.
- Gundelfinger, E. D., T. M. Boeckers, M. K. Baron, and J. U. Bowie. "A Role for Zinc in Postsynaptic Density Assambly and Plasticity?". *Trends Biochem Sci* 31, no. 7 (Jul 2006): 366-73.
- Guo, L., and Z. Lu. "Global Expression Analysis of Mirna Gene Cluster and Family Based on Isomirs from Deep Sequencing Data." *Comput Biol Chem* 34, no. 3 (Jun 2010): 165-71.
- Hagberg, B. "Rett Syndrome: Swedish Approach to Analysis of Prevalence and Cause." *Brain Dev* 7, no. 3 (1985): 276-80.
- Hagberg, B., J. Aicardi, K. Dias, and O. Ramos. "A Progressive Syndrome of Autism, Dementia, Ataxia, and Loss of Purposeful Hand Use in Girls: Rett's Syndrome: Report of 35 Cases." *Ann Neurol* 14, no. 4 (Oct 1983): 471-9.
- Hallmayer, J., S. Cleveland, A. Torres, J. Phillips, B. Cohen, T. Torigoe, J. Miller, *et al.* "Genetic Heritability and Shared Environmental Factors among Twin Pairs with Autism." [In eng]. *Arch Gen Psychiatry* 68, no. 11 (Nov 2011): 1095-102.
- Hammond, S. M., E. Bernstein, D. Beach, and G. J. Hannon. "An Rna-Directed Nuclease Mediates Post-Transcriptional Gene Silencing in Drosophila Cells." *Nature* 404, no. 6775 (Mar 16 2000): 293-6.
- Hammond, S. M., S. Boettcher, A. A. Caudy, R. Kobayashi, and G. J. Hannon. "Argonaute2, a Link between Genetic and Biochemical Analyses of Rnai." *Science* 293, no. 5532 (Aug 10 2001): 1146-50.
- Han, J., Y. Lee, K. H. Yeom, Y. K. Kim, H. Jin, and V. N. Kim. "The Drosha-Dgcr8 Complex in Primary Microrna Processing." *Genes Dev* 18, no. 24 (Dec 15 2004): 3016-27.
- Haseeb, A., M. S. Makki, N. M. Khan, I. Ahmad, and T. M. Haqqi. "Deep Sequencing and Analyses of Mirnas, Isomirs and Mirna Induced Silencing Complex (Mirisc)-Associated Mirnome in Primary Human Chondrocytes." *Sci Rep* 7, no. 1 (Nov 9 2017): 15178.

- Hasin, Y., M. Seldin, and A. Lusic. "Multi-Omics Approaches to Disease." *Genome Biol* 18, no. 1 (May 5 2017): 83.
- Hayashi, M. K., C. Tang, C. Verpelli, R. Narayanan, M. H. Stearns, R. M. Xu, H. Li, C. Sala, and Y. Hayashi. "The Postsynaptic Density Proteins Homer and Shank Form a Polymeric Network Structure." *Cell* 137, no. 1 (Apr 3 2009): 159-71.
- He, L., and G. J. Hannon. "MicroRNAs: Small Rnas with a Big Role in Gene Regulation." *Nat Rev Genet* 5, no. 7 (Jul 2004): 522-31.
- He, M. "Mirna Tagging and Affinity-Purification (Mirap)." *Bio Protoc* 2, no. 19 (Oct 5 2012).
- Heaton, P., and G. L. Wallace. "Annotation: The Savant Syndrome." *J Child Psychol Psychiatry* 45, no. 5 (Jul 2004): 899-911.
- Hebert, S. S., A. S. Papadopoulou, P. Smith, M. C. Galas, E. Planel, A. N. Silahdaroglu, N. Sergeant, L. Buee, and B. De Strooper. "Genetic Ablation of Dicer in Adult Forebrain Neurons Results in Abnormal Tau Hyperphosphorylation and Neurodegeneration." *Hum Mol Genet* 19, no. 20 (Oct 15 2010): 3959-69.
- Heiman, M., R. Kulicke, R. J. Fenster, P. Greengard, and N. Heintz. "Cell Type-Specific Mrna Purification by Translating Ribosome Affinity Purification (Trap)." *Nat Protoc* 9, no. 6 (2014): 1282-91.
- Hell, J. W. "Camkii: Claiming Center Stage in Postsynaptic Function and Organization." *Neuron* 81, no. 2 (Jan 22 2014): 249-65.
- Higley, M. J., and B. L. Sabatini. "Calcium Signaling in Dendritic Spines." *Cold Spring Harb Perspect Biol* 4, no. 4 (Apr 1 2012): a005686.
- Hilfiker, S., V. A. Pieribone, A. J. Czernik, H. T. Kao, G. J. Augustine, and P. Greengard. "Synapsins as Regulators of Neurotransmitter Release." *Philos Trans R Soc Lond B Biol Sci* 354, no. 1381 (Feb 28 1999): 269-79.
- Hirose, T., Y. Mishima, and Y. Tomari. "Elements and Machinery of Non-Coding Rnas: Toward Their Taxonomy." *EMBO Rep* 15, no. 5 (May 2014): 489-507.
- Hobert, O. "Gene Regulation by Transcription Factors and MicroRNAs." *Science* 319, no. 5871 (Mar 28 2008): 1785-6.
- Hock, J., and G. Meister. "The Argonaute Protein Family." *Genome Biol* 9, no. 2 (2008): 210.
- Holt, C. E., and E. M. Schuman. "The Central Dogma Decentralized: New Perspectives on Rna Function and Local Translation in Neurons." *Neuron* 80, no. 3 (Oct 30 2013): 648-57.
- Hoogenraad, C. C., A. Akhmanova, N. Galjart, and C. I. De Zeeuw. "Limk1 and Clip-115: Linking Cytoskeletal Defects to Williams Syndrome." *Bioessays* 26, no. 2 (Feb 2004): 141-50.
- Hormozdiari, F., O. Penn, E. Borenstein, and E. E. Eichler. "The Discovery of Integrated Gene Networks for Autism and Related Disorders." *Genome Res* 25, no. 1 (Jan 2015): 142-54.
- Hotulainen, P., and C. C. Hoogenraad. "Actin in Dendritic Spines: Connecting Dynamics to Function." *J Cell Biol* 189, no. 4 (May 17 2010): 619-29.

- Hoye, M. L., and D. L. Silver. "Decoding Mixed Messages in the Developing Cortex: Translational Regulation of Neural Progenitor Fate." *Curr Opin Neurobiol* 66 (Feb 2021): 93-102.
- Hu, H. Y., Z. Yan, Y. Xu, H. Hu, C. Menzel, Y. H. Zhou, W. Chen, and P. Khaitovich. "Sequence Features Associated with MicroRNA Strand Selection in Humans and Flies." *BMC Genomics* 10 (Sep 4 2009): 413.
- Huber, K. M., S. M. Gallagher, S. T. Warren, and M. F. Bear. "Altered Synaptic Plasticity in a Mouse Model of Fragile X Mental Retardation." *Proc Natl Acad Sci U S A* 99, no. 11 (May 28 2002): 7746-50.
- Hughes, C. S., S. Moggridge, T. Muller, P. H. Sorensen, G. B. Morin, and J. Krijgsveld. "Single-Pot, Solid-Phase-Enhanced Sample Preparation for Proteomics Experiments." *Nat Protoc* 14, no. 1 (Jan 2019): 68-85.
- Hung, A. Y., K. Futai, C. Sala, J. G. Valtschanoff, J. Ryu, M. A. Woodworth, F. L. Kidd, *et al.* "Smaller Dendritic Spines, Weaker Synaptic Transmission, but Enhanced Spatial Learning in Mice Lacking Shank1." *J Neurosci* 28, no. 7 (Feb 13 2008): 1697-708.
- Hutvagner, G., J. McLachlan, A. E. Pasquinelli, E. Balint, T. Tuschl, and P. D. Zamore. "A Cellular Function for the Rna-Interference Enzyme Dicer in the Maturation of the Let-7 Small Temporal Rna." *Science* 293, no. 5531 (Aug 3 2001): 834-8.
- Hutvagner, G., and P. D. Zamore. "A MicroRNA in a Multiple-Turnover Rnai Enzyme Complex." *Science* 297, no. 5589 (Sep 20 2002): 2056-60.
- Ip, Y. T., R. Kraut, M. Levine, and C. A. Rushlow. "The Dorsal Morphogen Is a Sequence-Specific DNA-Binding Protein That Interacts with a Long-Range Repression Element in Drosophila." *Cell* 64, no. 2 (Jan 25 1991): 439-46.
- Iwasaki, S., T. Kawamata, and Y. Tomari. "Drosophila Argonaute1 and Argonaute2 Employ Distinct Mechanisms for Translational Repression." *Mol Cell* 34, no. 1 (Apr 10 2009): 58-67.
- Jamain, S., H. Quach, C. Betancur, M. Rastam, C. Colineaux, I. C. Gillberg, H. Soderstrom, *et al.* "Mutations of the X-Linked Genes Encoding Neuroligins Nlgn3 and Nlgn4 Are Associated with Autism." *Nat Genet* 34, no. 1 (May 2003): 27-9.
- Jaramillo, T. C., H. E. Speed, Z. Xuan, J. M. Reimers, C. O. Escamilla, T. P. Weaver, S. Liu, I. Filonova, and C. M. Powell. "Novel Shank3 Mutant Exhibits Behaviors with Face Validity for Autism and Altered Striatal and Hippocampal Function." *Autism Res* 10, no. 1 (Jan 2017): 42-65.
- Jiang, Q., F. Liu, C. Miao, Q. Li, Z. Zhang, P. Xiao, L. Su, *et al.* "Ret Somatic Mutations Are Underrecognized in Hirschsprung Disease." *Genet Med* 20, no. 7 (Jul 2018): 770-77.
- Jiang, Y. H., and M. D. Ehlers. "Modeling Autism by Shank Gene Mutations in Mice." *Neuron* 78, no. 1 (Apr 10 2013): 8-27.
- Jin, P., D. C. Zarnescu, S. Ceman, M. Nakamoto, J. Mowrey, T. A. Jongens, D. L. Nelson, K. Moses, and S. T. Warren. "Biochemical and Genetic Interaction between the Fragile X Mental Retardation Protein and the MicroRNA Pathway." *Nat Neurosci* 7, no. 2 (Feb 2004): 113-7.
- Jinek, M., and J. A. Doudna. "A Three-Dimensional View of the Molecular Machinery of Rna Interference." *Nature* 457, no. 7228 (Jan 22 2009): 405-12.

- Johnson, M. B., Y. I. Kawasawa, C. E. Mason, Z. Krsnik, G. Coppola, D. Bogdanovic, D. H. Geschwind, *et al.* "Functional and Evolutionary Insights into Human Brain Development through Global Transcriptome Analysis." *Neuron* 62, no. 4 (May 28 2009): 494-509.
- Jossin, Y., and J. A. Cooper. "Reelin, Rap1 and N-Cadherin Orient the Migration of Multipolar Neurons in the Developing Neocortex." *Nat Neurosci* 14, no. 6 (Jun 2011): 697-703.
- Jovicic, A., R. Roshan, N. Moisoj, S. Pradervand, R. Moser, B. Pillai, and R. Luthi-Carter. "Comprehensive Expression Analyses of Neural Cell-Type-Specific Mirnas Identify New Determinants of the Specification and Maintenance of Neuronal Phenotypes." *J Neurosci* 33, no. 12 (Mar 20 2013): 5127-37.
- Jung, H., C. G. Gkogkas, N. Sonenberg, and C. E. Holt. "Remote Control of Gene Function by Local Translation." *Cell* 157, no. 1 (Mar 27 2014): 26-40.
- Kadowaki, M., S. Nakamura, O. Machon, S. Krauss, G. L. Radice, and M. Takeichi. "N-Cadherin Mediates Cortical Organization in the Mouse Brain." *Dev Biol* 304, no. 1 (Apr 1 2007): 22-33.
- Kalebic, N., S. Sorrentino, E. Perlas, G. Bolasco, C. Martinez, and P. A. Heppenstall. "Alphata1 Is the Major Alpha-tubulin Acetyltransferase in Mice." *Nat Commun* 4 (2013): 1962.
- Kang, H. J., Y. I. Kawasawa, F. Cheng, Y. Zhu, X. Xu, M. Li, A. M. Sousa, *et al.* "Spatio-Temporal Transcriptome of the Human Brain." *Nature* 478, no. 7370 (Oct 26 2011): 483-9.
- Kanner, L. "Autistic Disturbances of Affective Contact." *Acta Paedopsychiatr* 35, no. 4 (1968): 100-36.
- Kapur, M., and S. L. Ackerman. "Mrna Translation Gone Awry: Translation Fidelity and Neurological Disease." *Trends Genet* 34, no. 3 (Mar 2018): 218-31.
- Kawase-Koga, Y., G. Otaegi, and T. Sun. "Different Timings of Dicer Deletion Affect Neurogenesis and Gliogenesis in the Developing Mouse Central Nervous System." *Dev Dyn* 238, no. 11 (Nov 2009): 2800-12.
- Kawauchi, T., K. Sekine, M. Shikanai, K. Chihama, K. Tomita, K. Kubo, K. Nakajima, Y. Nabeshima, and M. Hoshino. "Rab Gtpases-Dependent Endocytic Pathways Regulate Neuronal Migration and Maturation through N-Cadherin Trafficking." *Neuron* 67, no. 4 (Aug 26 2010): 588-602.
- Kelleher, R. J., 3rd, and M. F. Bear. "The Autistic Neuron: Troubled Translation?". *Cell* 135, no. 3 (Oct 31 2008): 401-6.
- Ketting, R. F. "The Many Faces of Rnai." *Dev Cell* 20, no. 2 (Feb 15 2011): 148-61.
- Ketting, R. F., S. E. Fischer, E. Bernstein, T. Sijen, G. J. Hannon, and R. H. Plasterk. "Dicer Functions in Rna Interference and in Synthesis of Small Rna Involved in Developmental Timing in *C. Elegans*." *Genes Dev* 15, no. 20 (Oct 15 2001): 2654-9.
- Khvorova, A., A. Reynolds, and S. D. Jayasena. "Functional Sirnas and Mirnas Exhibit Strand Bias." *Cell* 115, no. 2 (Oct 17 2003): 209-16.
- Kim, H., J. Kim, S. Yu, Y. Y. Lee, J. Park, R. J. Choi, S. J. Yoon, S. G. Kang, and V. N. Kim. "A Mechanism for MicroRNA Arm Switching Regulated by Uridylation." *Mol Cell* 78, no. 6 (Jun 18 2020): 1224-36 e5.

- Kim, J., S. Y. Jung, Y. K. Lee, S. Park, J. S. Choi, C. J. Lee, H. S. Kim, *et al.* "Neuroigin-1 Is Required for Normal Expression of Ltp and Associative Fear Memory in the Amygdala of Adult Animals." *Proc Natl Acad Sci U S A* 105, no. 26 (Jul 1 2008): 9087-92.
- Kirstein, N., S. Dokaneheifard, P. R. Cingaram, M. G. Valencia, F. Beckedorff, H. Gomes Dos Santos, E. Blumenthal, *et al.* "The Integrator Complex Regulates Microrna Abundance through Risc Loading." *Sci Adv* 9, no. 6 (Feb 10 2023): eadf0597.
- Klann, E., and T. E. Dever. "Biochemical Mechanisms for Translational Regulation in Synaptic Plasticity." *Nat Rev Neurosci* 5, no. 12 (Dec 2004): 931-42.
- Klein, M. E., D. T. Lioy, L. Ma, S. Impey, G. Mandel, and R. H. Goodman. "Homeostatic Regulation of Mecp2 Expression by a Creb-Induced Microrna." *Nat Neurosci* 10, no. 12 (Dec 2007): 1513-4.
- Klemmer, P., R. M. Meredith, C. D. Holmgren, O. I. Klychnikov, J. Stahl-Zeng, M. Loos, R. C. van der Schors, *et al.* "Proteomics, Ultrastructure, and Physiology of Hippocampal Synapses in a Fragile X Syndrome Mouse Model Reveal Presynaptic Phenotype." *J Biol Chem* 286, no. 29 (Jul 22 2011): 25495-504.
- Klum, S. M., S. D. Chandradoss, N. T. Schirle, C. Joo, and I. J. MacRae. "Helix-7 in Argonaute2 Shapes the Microrna Seed Region for Rapid Target Recognition." *EMBO J* 37, no. 1 (Jan 4 2018): 75-88.
- Knight, S. W., and B. L. Bass. "A Role for the Rnase Iii Enzyme Dcr-1 in Rna Interference and Germ Line Development in Caenorhabditis Elegans." *Science* 293, no. 5538 (Sep 21 2001): 2269-71.
- Knowles, P. P., J. Murray-Rust, S. Kjaer, R. P. Scott, S. Hanrahan, M. Santoro, C. F. Ibanez, and N. Q. McDonald. "Structure and Chemical Inhibition of the Ret Tyrosine Kinase Domain." *J Biol Chem* 281, no. 44 (Nov 3 2006): 33577-87.
- Kobayashi, H., and Y. Tomari. "Risc Assembly: Coordination between Small Rnas and Argonaute Proteins." *Biochim Biophys Acta* 1859, no. 1 (Jan 2016): 71-81.
- Kong, A., M. L. Frigge, G. Masson, S. Besenbacher, P. Sulem, G. Magnusson, S. A. Gudjonsson, *et al.* "Rate of De Novo Mutations and the Importance of Father's Age to Disease Risk." *Nature* 488, no. 7412 (Aug 23 2012): 471-5.
- Kosik, K. S., and E. A. Finch. "Map2 and Tau Segregate into Dendritic and Axonal Domains after the Elaboration of Morphologically Distinct Neurites: An Immunocytochemical Study of Cultured Rat Cerebrum." *J Neurosci* 7, no. 10 (Oct 1987): 3142-53.
- Kouser, M., H. E. Speed, C. M. Dewey, J. M. Reimers, A. J. Widman, N. Gupta, S. Liu, *et al.* "Loss of Predominant Shank3 Isoforms Results in Hippocampus-Dependent Impairments in Behavior and Synaptic Transmission." *J Neurosci* 33, no. 47 (Nov 20 2013): 18448-68.
- Kraushar, M. L., K. Thompson, H. R. Wijeratne, B. Viljetic, K. Sakers, J. W. Marson, D. L. Kontoyiannis, *et al.* "Temporally Defined Neocortical Translation and Polysome Assembly Are Determined by the Rna-Binding Protein Hu Antigen R." *Proc Natl Acad Sci U S A* 111, no. 36 (Sep 9 2014): E3815-24.
- Kreienkamp, H. J. "Scaffolding Proteins at the Postsynaptic Density: Shank as the Architectural Framework." *Handb Exp Pharmacol*, no. 186 (2008): 365-80.

- Krol, J., K. Sobczak, U. Wilczynska, M. Drath, A. Jasinska, D. Kaczynska, and W. J. Krzyzosiak. "Structural Features of Microna (Mirna) Precursors and Their Relevance to Mirna Biogenesis and Small Interfering Rna/Short Hairpin Rna Design." *J Biol Chem* 279, no. 40 (Oct 1 2004): 42230-9.
- Kuhn, C. D., and L. Joshua-Tor. "Eukaryotic Argonautes Come into Focus." *Trends Biochem Sci* 38, no. 5 (May 2013): 263-71.
- Kuleshov, M. V., M. R. Jones, A. D. Rouillard, N. F. Fernandez, Q. Duan, Z. Wang, S. Koplev, *et al.* "Enrichr: A Comprehensive Gene Set Enrichment Analysis Web Server 2016 Update." *Nucleic Acids Res* 44, no. W1 (Jul 8 2016): W90-7.
- Kwak, P. B., and Y. Tomari. "The N Domain of Argonaute Drives Duplex Unwinding During Risc Assembly." *Nat Struct Mol Biol* 19, no. 2 (Jan 10 2012): 145-51.
- Kwon, H. B., Y. Kozorovitskiy, W. J. Oh, R. T. Peixoto, N. Akhtar, J. L. Saulnier, C. Gu, and B. L. Sabatini. "Neuroigin-1-Dependent Competition Regulates Cortical Synaptogenesis and Synapse Number." *Nat Neurosci* 15, no. 12 (Dec 2012): 1667-74.
- Lagos-Quintana, M., R. Rauhut, A. Yalcin, J. Meyer, W. Lendeckel, and T. Tuschl. "Identification of Tissue-Specific Micrnas from Mouse." *Curr Biol* 12, no. 9 (Apr 30 2002): 735-9.
- Lai, E. C. "Micro Rnas Are Complementary to 3' Utr Sequence Motifs That Mediate Negative Post-Transcriptional Regulation." *Nat Genet* 30, no. 4 (Apr 2002): 363-4.
- Lai, M. C., M. V. Lombardo, and S. Baron-Cohen. "Autism." *Lancet* 383, no. 9920 (Mar 8 2014): 896-910.
- Laumonier, F., F. Bonnet-Brilhault, M. Gomot, R. Blanc, A. David, M. P. Moizard, M. Raynaud, *et al.* "X-Linked Mental Retardation and Autism Are Associated with a Mutation in the Nlgn4 Gene, a Member of the Neuroigin Family." *Am J Hum Genet* 74, no. 3 (Mar 2004): 552-7.
- Lavon, I., D. Zrihan, A. Granit, O. Einstein, N. Fainstein, M. A. Cohen, M. A. Cohen, *et al.* "Gliomas Display a Microna Expression Profile Reminiscent of Neural Precursor Cells." *Neuro Oncol* 12, no. 5 (May 2010): 422-33.
- Law, B. M., V. A. Spain, V. H. Leinster, R. Chia, A. Beilina, H. J. Cho, J. M. Taymans, *et al.* "A Direct Interaction between Leucine-Rich Repeat Kinase 2 and Specific Beta-tubulin Isoforms Regulates tubulin Acetylation." *J Biol Chem* 289, no. 2 (Jan 10 2014): 895-908.
- Leblond, C. S., C. Nava, A. Polge, J. Gauthier, G. Huguet, S. Lumbroso, F. Giuliano, *et al.* "Meta-Analysis of Shank Mutations in Autism Spectrum Disorders: A Gradient of Severity in Cognitive Impairments." *PLoS Genet* 10, no. 9 (Sep 2014): e1004580.
- LeDizet, M., and G. Piperno. "Identification of an Acetylation Site of Chlamydomonas Alpha-tubulin." *Proc Natl Acad Sci U S A* 84, no. 16 (Aug 1987): 5720-4.
- Lee, J., C. Chung, S. Ha, D. Lee, D. Y. Kim, H. Kim, and E. Kim. "Shank3-Mutant Mice Lacking Exon 9 Show Altered Excitation/Inhibition Balance, Enhanced Rearing, and Spatial Memory Deficit." *Front Cell Neurosci* 9 (2015): 94.
- Lee, L. W., S. Zhang, A. Etheridge, L. Ma, D. Martin, D. Galas, and K. Wang. "Complexity of the Microna Repertoire Revealed by Next-Generation Sequencing." *RNA* 16, no. 11 (Nov 2010): 2170-80.

- Lee, R. C., R. L. Feinbaum, and V. Ambros. "The C. Elegans Heterochronic Gene Lin-4 Encodes Small Rnas with Antisense Complementarity to Lin-14." *Cell* 75, no. 5 (Dec 3 1993): 843-54.
- Lee, S. J., Y. Escobedo-Lozoya, E. M. Szatmari, and R. Yasuda. "Activation of Camkii in Single Dendritic Spines During Long-Term Potentiation." *Nature* 458, no. 7236 (Mar 19 2009): 299-304.
- Lee, Y., C. Ahn, J. Han, H. Choi, J. Kim, J. Yim, J. Lee, *et al.* "The Nuclear Rnase Iii Drosha Initiates MicroRNA Processing." *Nature* 425, no. 6956 (Sep 25 2003): 415-9.
- Lee, Y., K. Jeon, J. T. Lee, S. Kim, and V. N. Kim. "MicroRNA Maturation: Stepwise Processing and Subcellular Localization." *EMBO J* 21, no. 17 (Sep 2 2002): 4663-70.
- Lee, Y., M. Kim, J. Han, K. H. Yeom, S. Lee, S. H. Baek, and V. N. Kim. "MicroRNA Genes Are Transcribed by Rna Polymerase Ii." *EMBO J* 23, no. 20 (Oct 13 2004): 4051-60.
- Leibovitch, M., and I. Topisirovic. "Dysregulation of Mrna Translation and Energy Metabolism in Cancer." *Adv Biol Regul* 67 (Jan 2018): 30-39.
- Lenardo, M. J., and D. Baltimore. "Nf-Kappa B: A Pleiotropic Mediator of Inducible and Tissue-Specific Gene Control." *Cell* 58, no. 2 (Jul 28 1989): 227-9.
- Lennox, A. L., M. L. Hoye, R. Jiang, B. L. Johnson-Kerner, L. A. Suit, S. Venkataramanan, C. J. Sheehan, *et al.* "Pathogenic Ddx3x Mutations Impair Rna Metabolism and Neurogenesis During Fetal Cortical Development." *Neuron* 106, no. 3 (May 6 2020): 404-20 e8.
- Lennox, A. L., H. Mao, and D. L. Silver. "Rna on the Brain: Emerging Layers of Post-Transcriptional Regulation in Cerebral Cortex Development." *Wiley Interdiscip Rev Dev Biol* 7, no. 1 (Jan 2018).
- Lessel, D., D. M. Zeitler, M. R. F. Reijnders, A. Kazantsev, F. Hassani Nia, A. Bartholomaeus, V. Martens, *et al.* "Germline Ago2 Mutations Impair Rna Interference and Human Neurological Development." *Nat Commun* 11, no. 1 (Nov 16 2020): 5797.
- Leung, K. M., F. P. van Horck, A. C. Lin, R. Allison, N. Standart, and C. E. Holt. "Asymmetrical Beta-Actin Mrna Translation in Growth Cones Mediates Attractive Turning to Netrin-1." *Nat Neurosci* 9, no. 10 (Oct 2006): 1247-56.
- Leuschner, P. J., S. L. Ameres, S. Kueng, and J. Martinez. "Cleavage of the Sirna Passenger Strand During Risc Assembly in Human Cells." *EMBO Rep* 7, no. 3 (Mar 2006): 314-20.
- Li, S. C., Y. L. Liao, M. R. Ho, K. W. Tsai, C. H. Lai, and W. C. Lin. "Mirna Arm Selection and Isomir Distribution in Gastric Cancer." *BMC Genomics* 13 Suppl 1, no. Suppl 1 (2012): S13.
- Liao, Y., G. K. Smyth, and W. Shi. "Featurecounts: An Efficient General Purpose Program for Assigning Sequence Reads to Genomic Features." *Bioinformatics* 30, no. 7 (Apr 1 2014): 923-30.
- Lilja, J., T. Zacharchenko, M. Georgiadou, G. Jacquemet, N. De Franceschi, E. Peuhu, H. Hamidi, *et al.* "Shank Proteins Limit Integrin Activation by Directly Interacting with Rap1 and R-Ras." *Nat Cell Biol* 19, no. 4 (Apr 2017): 292-305.
- Lim, S., S. Naisbitt, J. Yoon, J. I. Hwang, P. G. Suh, M. Sheng, and E. Kim. "Characterization of the Shank Family of Synaptic Proteins. Multiple Genes, Alternative Splicing, and Differential Expression in Brain and Development." *J Biol Chem* 274, no. 41 (Oct 8 1999): 29510-8.

- Linsen, S. E., E. de Wit, G. Janssens, S. Heater, L. Chapman, R. K. Parkin, B. Fritz, *et al.* "Limitations and Possibilities of Small Rna Digital Gene Expression Profiling." *Nat Methods* 6, no. 7 (Jul 2009): 474-6.
- Lipchina, I., Y. Elkabetz, M. Hafner, R. Sheridan, A. Mihailovic, T. Tuschl, C. Sander, L. Studer, and D. Betel. "Genome-Wide Identification of MicroRNA Targets in Human Es Cells Reveals a Role for Mir-302 in Modulating Bmp Response." *Genes Dev* 25, no. 20 (Oct 15 2011): 2173-86.
- Lipton, J. O., and M. Sahin. "The Neurology of Mtor." *Neuron* 84, no. 2 (Oct 22 2014): 275-91.
- Lisitskaya, L., A. A. Aravin, and A. Kulbachinskiy. "DNA Interference and Beyond: Structure and Functions of Prokaryotic Argonaute Proteins." *Nat Commun* 9, no. 1 (Dec 4 2018): 5165.
- Lisman, J., R. Yasuda, and S. Raghavachari. "Mechanisms of Camkii Action in Long-Term Potentiation." *Nat Rev Neurosci* 13, no. 3 (Feb 15 2012): 169-82.
- Liu, J., M. A. Carmell, F. V. Rivas, C. G. Marsden, J. M. Thomson, J. J. Song, S. M. Hammond, L. Joshua-Tor, and G. J. Hannon. "Argonaute2 Is the Catalytic Engine of Mammalian Rnai." *Science* 305, no. 5689 (Sep 3 2004): 1437-41.
- Liu, J., M. A. Valencia-Sanchez, G. J. Hannon, and R. Parker. "MicroRNA-Dependent Localization of Targeted Mrnas to Mammalian P-Bodies." *Nat Cell Biol* 7, no. 7 (Jul 2005): 719-23.
- Liu, W., and X. Wang. "Prediction of Functional MicroRNA Targets by Integrative Modeling of MicroRNA Binding and Target Expression Data." *Genome Biol* 20, no. 1 (Jan 22 2019): 18.
- Livak, K. J., and T. D. Schmittgen. "Analysis of Relative Gene Expression Data Using Real-Time Quantitative Pcr and the 2(-Delta Delta C(T)) Method." *Methods* 25, no. 4 (Dec 2001): 402-8.
- Loher, P., E. R. Londin, and I. Rigoutsos. "Isomir Expression Profiles in Human Lymphoblastoid Cell Lines Exhibit Population and Gender Dependencies." *Oncotarget* 5, no. 18 (Sep 30 2014): 8790-802.
- Londin, E., P. Loher, A. G. Telonis, K. Quann, P. Clark, Y. Jing, E. Hatzimichael, *et al.* "Analysis of 13 Cell Types Reveals Evidence for the Expression of Numerous Novel Primate- and Tissue-Specific MicroRNAs." *Proc Natl Acad Sci U S A* 112, no. 10 (Mar 10 2015): E1106-15.
- Lord, C., S. Risi, L. Lambrecht, E. H. Cook, Jr., B. L. Leventhal, P. C. DiLavore, A. Pickles, and M. Rutter. "The Autism Diagnostic Observation Schedule-Generic: A Standard Measure of Social and Communication Deficits Associated with the Spectrum of Autism." *J Autism Dev Disord* 30, no. 3 (Jun 2000): 205-23.
- Love, M. I., W. Huber, and S. Anders. "Moderated Estimation of Fold Change and Dispersion for Rna-Seq Data with Deseq2." *Genome Biol* 15, no. 12 (2014): 550.
- Lowery, L. A., and D. Van Vactor. "The Trip of the Tip: Understanding the Growth Cone Machinery." *Nat Rev Mol Cell Biol* 10, no. 5 (May 2009): 332-43.
- Lugli, G., J. Larson, M. E. Martone, Y. Jones, and N. R. Smalheiser. "Dicer and Eif2c Are Enriched at Postsynaptic Densities in Adult Mouse Brain and Are Modified by Neuronal Activity in a Calpain-Dependent Manner." *J Neurochem* 94, no. 4 (Aug 2005): 896-905.
- Lund, E., S. Guttinger, A. Calado, J. E. Dahlberg, and U. Kutay. "Nuclear Export of MicroRNA Precursors." *Science* 303, no. 5654 (Jan 2 2004): 95-8.

- Ma, J. B., K. Ye, and D. J. Patel. "Structural Basis for Overhang-Specific Small Interfering Rna Recognition by the Paz Domain." *Nature* 429, no. 6989 (May 20 2004): 318-22.
- Ma, J. B., Y. R. Yuan, G. Meister, Y. Pei, T. Tuschl, and D. J. Patel. "Structural Basis for 5'-End-Specific Recognition of Guide Rna by the A. Fulgidus Piwi Protein." *Nature* 434, no. 7033 (Mar 31 2005): 666-70.
- Maere, S., K. Heymans, and M. Kuiper. "Bingo: A Cytoscape Plugin to Assess Overrepresentation of Gene Ontology Categories in Biological Networks." *Bioinformatics* 21, no. 16 (Aug 15 2005): 3448-9.
- Mahato, A. K., and Y. A. Sidorova. "Ret Receptor Tyrosine Kinase: Role in Neurodegeneration, Obesity, and Cancer." *Int J Mol Sci* 21, no. 19 (Sep 26 2020).
- Malmevik, J., R. Petri, T. Klussendorf, P. Knauff, M. Akerblom, J. Johansson, S. Soneji, and J. Jakobsson. "Identification of the Mirna Targetome in Hippocampal Neurons Using Rip-Seq." *Sci Rep* 5 (Jul 28 2015): 12609.
- Manning, M. A., S. B. Cassidy, C. Clericuzio, A. M. Cherry, S. Schwartz, L. Hudgins, G. M. Enns, and H. E. Hoyme. "Terminal 22q Deletion Syndrome: A Newly Recognized Cause of Speech and Language Disability in the Autism Spectrum." *Pediatrics* 114, no. 2 (Aug 2004): 451-7.
- Margulies, M., M. Egholm, W. E. Altman, S. Attiya, J. S. Bader, L. A. Bemben, J. Berka, *et al.* "Genome Sequencing in Microfabricated High-Density Picolitre Reactors." *Nature* 437, no. 7057 (Sep 15 2005): 376-80.
- Matranga, C., Y. Tomari, C. Shin, D. P. Bartel, and P. D. Zamore. "Passenger-Strand Cleavage Facilitates Assembly of Sirna into Ago2-Containing Rnai Enzyme Complexes." *Cell* 123, no. 4 (Nov 18 2005): 607-20.
- Matsuzaki, M., N. Honkura, G. C. Ellis-Davies, and H. Kasai. "Structural Basis of Long-Term Potentiation in Single Dendritic Spines." *Nature* 429, no. 6993 (Jun 17 2004): 761-6.
- McCombie, W. R., J. D. McPherson, and E. R. Mardis. "Next-Generation Sequencing Technologies." *Cold Spring Harb Perspect Med* 9, no. 11 (Nov 1 2019).
- McLachlan, F., A. M. Sires, and C. M. Abbott. "The Role of Translation Elongation Factor Eef1 Subunits in Neurodevelopmental Disorders." *Hum Mutat* 40, no. 2 (Feb 2019): 131-41.
- McNeill, E., and D. Van Vactor. "MicroRNAs Shape the Neuronal Landscape." *Neuron* 75, no. 3 (Aug 9 2012): 363-79.
- Medley, J. C., G. Panzade, and A. Y. Zinovyeva. "MicroRNA Strand Selection: Unwinding the Rules." *Wiley Interdiscip Rev RNA* 12, no. 3 (May 2021): e1627.
- Meister, G., M. Landthaler, L. Peters, P. Y. Chen, H. Urlaub, R. Luhrmann, and T. Tuschl. "Identification of Novel Argonaute-Associated Proteins." *Curr Biol* 15, no. 23 (Dec 6 2005): 2149-55.
- Meka, D. P., A. K. Muller-Rischart, P. Nidadavolu, B. Mohammadi, E. Motori, S. K. Ponna, H. Aboutaleb, *et al.* "Parkin Cooperates with Gdnf/Ret Signaling to Prevent Dopaminergic Neuron Degeneration." *J Clin Invest* 125, no. 5 (May 2015): 1873-85.

- Mi, H., A. Muruganujan, X. Huang, D. Ebert, C. Mills, X. Guo, and P. D. Thomas. "Protocol Update for Large-Scale Genome and Gene Function Analysis with the Panther Classification System (V.14.0)." *Nat Protoc* 14, no. 3 (Mar 2019): 703-21.
- Mi, H., and P. Thomas. "Panther Pathway: An Ontology-Based Pathway Database Coupled with Data Analysis Tools." *Methods Mol Biol* 563 (2009): 123-40.
- Mi, S., T. Cai, Y. Hu, Y. Chen, E. Hodges, F. Ni, L. Wu, *et al.* "Sorting of Small Rnas into Arabidopsis Argonaute Complexes Is Directed by the 5' Terminal Nucleotide." *Cell* 133, no. 1 (Apr 4 2008): 116-27.
- Ming, D., M. E. Wall, and K. Y. Sanbonmatsu. "Domain Motions of Argonaute, the Catalytic Engine of Rna Interference." *BMC Bioinformatics* 8 (Nov 30 2007): 470.
- Mitchell, S., J. Vargas, and A. Hoffmann. "Signaling Via the Nfkappab System." *Wiley Interdiscip Rev Syst Biol Med* 8, no. 3 (May 2016): 227-41.
- Moessner, R., C. R. Marshall, J. S. Sutcliffe, J. Skaug, D. Pinto, J. Vincent, L. Zwaigenbaum, *et al.* "Contribution of Shank3 Mutations to Autism Spectrum Disorder." *Am J Hum Genet* 81, no. 6 (Dec 2007): 1289-97.
- Moreno-De-Luca, A., S. M. Myers, T. D. Challman, D. Moreno-De-Luca, D. W. Evans, and D. H. Ledbetter. "Developmental Brain Dysfunction: Revival and Expansion of Old Concepts Based on New Genetic Evidence." *Lancet Neurol* 12, no. 4 (Apr 2013): 406-14.
- Moreno, J. A., H. Radford, D. Peretti, J. R. Steinert, N. Verity, M. G. Martin, M. Halliday, *et al.* "Sustained Translational Repression by Eif2alpha-P Mediates Prion Neurodegeneration." *Nature* 485, no. 7399 (May 6 2012): 507-11.
- Morin, R. D., M. D. O'Connor, M. Griffith, F. Kuchenbauer, A. Delaney, A. L. Prabhu, Y. Zhao, *et al.* "Application of Massively Parallel Sequencing to Microrna Profiling and Discovery in Human Embryonic Stem Cells." *Genome Res* 18, no. 4 (Apr 2008): 610-21.
- Morris, A. R., N. Mukherjee, and J. D. Keene. "Systematic Analysis of Posttranscriptional Gene Expression." *Wiley Interdiscip Rev Syst Biol Med* 2, no. 2 (Mar-Apr 2010): 162-80.
- Morris, K. V., and J. S. Mattick. "The Rise of Regulatory Rna." *Nat Rev Genet* 15, no. 6 (Jun 2014): 423-37.
- Mossa, A., J. Pagano, L. Ponzoni, A. Tozzi, E. Vezzoli, M. Sciacaluga, C. Costa, *et al.* "Developmental Impaired Akt Signaling in the Shank1 and Shank3 Double Knock-out Mice." *Mol Psychiatry* 26, no. 6 (Jun 2021): 1928-44.
- Muhlebner, A., A. Bongaarts, H. B. Sarnat, T. Scholl, and E. Aronica. "New Insights into a Spectrum of Developmental Malformations Related to Mtor Dysregulations: Challenges and Perspectives." *J Anat* 235, no. 3 (Sep 2019): 521-42.
- Mullins, C., G. Fishell, and R. W. Tsien. "Unifying Views of Autism Spectrum Disorders: A Consideration of Autoregulatory Feedback Loops." *Neuron* 89, no. 6 (Mar 16 2016): 1131-56.
- Murphy, D., and W. Spooren. "Eu-Aims: A Boost to Autism Research." *Nat Rev Drug Discov* 11, no. 11 (Nov 2012): 815-6.

- Naisbitt, S., E. Kim, J. C. Tu, B. Xiao, C. Sala, J. Valtchanoff, R. J. Weinberg, P. F. Worley, and M. Sheng. "Shank, a Novel Family of Postsynaptic Density Proteins That Binds to the Nmda Receptor/Psd-95/Gkap Complex and Cortactin." *Neuron* 23, no. 3 (Jul 1999): 569-82.
- Neilsen, C. T., G. J. Goodall, and C. P. Bracken. "Isomirs--the Overlooked Repertoire in the Dynamic Micronaome." *Trends Genet* 28, no. 11 (Nov 2012): 544-9.
- Nekooki-Machida, Y., and H. Hagiwara. "Role of tubulin Acetylation in Cellular Functions and Diseases." *Med Mol Morphol* 53, no. 4 (Dec 2020): 191-97.
- Newman, M. A., V. Mani, and S. M. Hammond. "Deep Sequencing of MicroRNA Precursors Reveals Extensive 3' End Modification." *RNA* 17, no. 10 (Oct 2011): 1795-803.
- Nielsen, C. B., N. Shomron, R. Sandberg, E. Hornstein, J. Kitzman, and C. B. Burge. "Determinants of Targeting by Endogenous and Exogenous MicroRNAs and Sirnas." *RNA* 13, no. 11 (Nov 2007): 1894-910.
- Niemi, M. E. K., H. C. Martin, D. L. Rice, G. Gallone, S. Gordon, M. Kelemen, K. McAloney, *et al.* "Common Genetic Variants Contribute to Risk of Rare Severe Neurodevelopmental Disorders." *Nature* 562, no. 7726 (Oct 2018): 268-71.
- Noguchi, J., M. Matsuzaki, G. C. Ellis-Davies, and H. Kasai. "Spine-Neck Geometry Determines Nmda Receptor-Dependent Ca²⁺ Signaling in Dendrites." *Neuron* 46, no. 4 (May 19 2005): 609-22.
- Northrup, H., M. E. Aronow, E. M. Bebin, J. Bissler, T. N. Darling, P. J. de Vries, M. D. Frost, *et al.* "Updated International Tuberous Sclerosis Complex Diagnostic Criteria and Surveillance and Management Recommendations." *Pediatr Neurol* 123 (Oct 2021): 50-66.
- Nowakowski, T. J., N. Rani, M. Golkaram, H. R. Zhou, B. Alvarado, K. Huch, J. A. West, *et al.* "Regulation of Cell-Type-Specific Transcriptomes by MicroRNA Networks During Human Brain Development." *Nat Neurosci* 21, no. 12 (Dec 2018): 1784-92.
- Nozaki, C., N. Asai, H. Murakami, T. Iwashita, Y. Iwata, K. Horibe, R. D. Klein, A. Rosenthal, and M. Takahashi. "Calcium-Dependent Ret Activation by Gdnf and Neurturin." *Oncogene* 16, no. 3 (Jan 22 1998): 293-9.
- O'Connor, N., and B. Hermelin. "The Memory Structure of Autistic Idiot-Savant Mnemonists." *Br J Psychol* 80 (Pt 1) (Feb 1989): 97-111.
- Oh, P., Y. Li, J. Yu, E. Durr, K. M. Krasinska, L. A. Carver, J. E. Testa, and J. E. Schnitzer. "Subtractive Proteomic Mapping of the Endothelial Surface in Lung and Solid Tumours for Tissue-Specific Therapy." *Nature* 429, no. 6992 (Jun 10 2004): 629-35.
- Ohtsuka, T., M. Sakamoto, F. Guillemot, and R. Kageyama. "Roles of the Basic Helix-Loop-Helix Genes Hes1 and Hes5 in Expansion of Neural Stem Cells of the Developing Brain." *J Biol Chem* 276, no. 32 (Aug 10 2001): 30467-74.
- Okamura, K., N. Liu, and E. C. Lai. "Distinct Mechanisms for MicroRNA Strand Selection by Drosophila Argonautes." *Mol Cell* 36, no. 3 (Nov 13 2009): 431-44.
- Okamura, K., M. D. Phillips, D. M. Tyler, H. Duan, Y. T. Chou, and E. C. Lai. "The Regulatory Activity of MicroRNA* Species Has Substantial Influence on MicroRNA and 3' Utr Evolution." *Nat Struct Mol Biol* 15, no. 4 (Apr 2008): 354-63.

- Olina, A. V., A. V. Kulbachinskiy, A. A. Aravin, and D. M. Esyunina. "Argonaute Proteins and Mechanisms of Rna Interference in Eukaryotes and Prokaryotes." *Biochemistry (Mosc)* 83, no. 5 (May 2018): 483-97.
- Otmakhov, N., J. H. Tao-Cheng, S. Carpenter, B. Asrican, A. Dosemeci, T. S. Reese, and J. Lisman. "Persistent Accumulation of Calcium/Calmodulin-Dependent Protein Kinase II in Dendritic Spines after Induction of NMDA Receptor-Dependent Chemical Long-Term Potentiation." *J Neurosci* 24, no. 42 (Oct 20 2004): 9324-31.
- Pachnis, V., B. Mankoo, and F. Costantini. "Expression of the C-Ret Proto-Oncogene During Mouse Embryogenesis." *Development* 119, no. 4 (Dec 1993): 1005-17.
- Palazzo, A., B. Ackerman, and G. G. Gundersen. "Cell Biology: tubulin Acetylation and Cell Motility." *Nature* 421, no. 6920 (Jan 16 2003): 230.
- Parenti, I., L. G. Rabaneda, H. Schoen, and G. Novarino. "Neurodevelopmental Disorders: From Genetics to Functional Pathways." *Trends Neurosci* 43, no. 8 (Aug 2020): 608-21.
- Parikshak, N. N., R. Luo, A. Zhang, H. Won, J. K. Lowe, V. Chandran, S. Horvath, and D. H. Geschwind. "Integrative Functional Genomic Analyses Implicate Specific Molecular Pathways and Circuits in Autism." *Cell* 155, no. 5 (Nov 21 2013): 1008-21.
- Park, J. H., S. Y. Shin, and C. Shin. "Non-Canonical Targets Destabilize MicroRNAs in Human Argonautes." *Nucleic Acids Res* 45, no. 4 (Feb 28 2017): 1569-83.
- Park, Y., N. Page, I. Salamon, D. Li, and M. R. Rasin. "Making Sense of mRNA Landscapes: Translation Control in Neurodevelopment." *Wiley Interdiscip Rev RNA* 13, no. 1 (Jan 2022): e1674.
- Parker, R., and U. Sheth. "P Bodies and the Control of mRNA Translation and Degradation." *Mol Cell* 25, no. 5 (Mar 9 2007): 635-46.
- Pascual, A., M. Hidalgo-Figueroa, J. I. Piruat, C. O. Pintado, R. Gomez-Diaz, and J. Lopez-Barneo. "Absolute Requirement of GDNF for Adult Catecholaminergic Neuron Survival." *Nat Neurosci* 11, no. 7 (Jul 2008): 755-61.
- Peca, J., C. Feliciano, J. T. Ting, W. Wang, M. F. Wells, T. N. Venkatraman, C. D. Lascola, Z. Fu, and G. Feng. "Shank3 Mutant Mice Display Autistic-Like Behaviours and Striatal Dysfunction." *Nature* 472, no. 7344 (Apr 28 2011): 437-42.
- Pennington, K., P. Dicker, M. J. Dunn, and D. R. Cotter. "Proteomic Analysis Reveals Protein Changes within Layer 2 of the Insular Cortex in Schizophrenia." *Proteomics* 8, no. 23-24 (Dec 2008): 5097-107.
- Penttinen, A. M., I. Parkkinen, M. H. Voutilainen, M. Koskela, S. Back, A. Their, C. T. Richie, *et al.* "Pre-Alpha-Pro-GDNF and Pre-Beta-Pro-GDNF Isoforms Are Neuroprotective in the 6-Hydroxydopamine Rat Model of Parkinson's Disease." *Front Neurol* 9 (2018): 457.
- Perfitt, T. L., X. Wang, M. T. Dickerson, J. R. Stephenson, T. Nakagawa, D. A. Jacobson, and R. J. Colbran. "Neuronal L-Type Calcium Channel Signaling to the Nucleus Requires a Novel CamkII α -Shank3 Interaction." *J Neurosci* 40, no. 10 (Mar 4 2020): 2000-14.
- Peters, L., and G. Meister. "Argonaute Proteins: Mediators of RNA Silencing." *Mol Cell* 26, no. 5 (Jun 8 2007): 611-23.

- Pfaff, J., J. Hennig, F. Herzog, R. Aebersold, M. Sattler, D. Niessing, and G. Meister. "Structural Features of Argonaute-Gw182 Protein Interactions." *Proc Natl Acad Sci U S A* 110, no. 40 (Oct 1 2013): E3770-9.
- Phelan, K., and H. E. McDermid. "The 22q13.3 Deletion Syndrome (Phelan-Mcdermid Syndrome)." *Mol Syndromol* 2, no. 3-5 (Apr 2012): 186-201.
- Phelan, M. C. "Deletion 22q13.3 Syndrome." *Orphanet J Rare Dis* 3 (May 27 2008): 14.
- Phillips, J. R., T. Dalmay, and D. Bartels. "The Role of Small Rnas in Abiotic Stress." *FEBS Lett* 581, no. 19 (Jul 31 2007): 3592-7.
- Pillai, R. S., S. N. Bhattacharyya, and W. Filipowicz. "Repression of Protein Synthesis by Mirnas: How Many Mechanisms?." *Trends Cell Biol* 17, no. 3 (Mar 2007): 118-26.
- Pinto, D., A. T. Pagnamenta, L. Klei, R. Anney, D. Merico, R. Regan, J. Conroy, *et al.* "Functional Impact of Global Rare Copy Number Variation in Autism Spectrum Disorders." *Nature* 466, no. 7304 (Jul 15 2010): 368-72.
- Popovitchenko, T., Y. Park, N. F. Page, X. Luo, Z. Krsnik, Y. Liu, I. Salamon, *et al.* "Translational Derepression of Elavl4 Isoforms at Their Alternative 5' Utrs Determines Neuronal Development." *Nat Commun* 11, no. 1 (Apr 3 2020): 1674.
- Popovitchenko, T., and M. R. Rasin. "Transcriptional and Post-Transcriptional Mechanisms of the Development of Neocortical Lamination." *Front Neuroanat* 11 (2017): 102.
- Prashad, S., and P. P. Gopal. "Rna-Binding Proteins in Neurological Development and Disease." *RNA Biol* 18, no. 7 (Jul 2021): 972-87.
- Preall, J. B., and E. J. Sontheimer. "Rnai: Risc Gets Loaded." *Cell* 123, no. 4 (Nov 18 2005): 543-5.
- Proepper, C., S. Johannsen, S. Liebau, J. Dahl, B. Vaida, J. Bockmann, M. R. Kreutz, E. D. Gundelfinger, and T. M. Boeckers. "Abelson Interacting Protein 1 (Abi-1) Is Essential for Dendrite Morphogenesis and Synapse Formation." *EMBO J* 26, no. 5 (Mar 7 2007): 1397-409.
- Qin, Y., Y. Du, L. Chen, Y. Liu, W. Xu, Y. Liu, Y. Li, *et al.* "A Recurrent Shank1 Mutation Implicated in Autism Spectrum Disorder Causes Autistic-Like Core Behaviors in Mice Via Downregulation of Mglur1-Ip3r1-Calcium Signaling." *Mol Psychiatry* 27, no. 7 (Jul 2022): 2985-98.
- Quevillon Huberdeau, M., D. M. Zeitler, J. Hauptmann, A. Bruckmann, L. Fressigne, J. Danner, S. Piquet, *et al.* "Phosphorylation of Argonaute Proteins Affects Mrna Binding and Is Essential for Microrna-Guided Gene Silencing in Vivo." *EMBO J* 36, no. 14 (Jul 14 2017): 2088-106.
- Raghuram, V., Y. Sharma, and M. R. Kreutz. "Ca(2+) Sensor Proteins in Dendritic Spines: A Race for Ca(2+)." *Front Mol Neurosci* 5 (2012): 61.
- Rago, L., R. Beattie, V. Taylor, and J. Winter. "Mir379-410 Cluster Mirnas Regulate Neurogenesis and Neuronal Migration by Fine-Tuning N-Cadherin." *EMBO J* 33, no. 8 (Apr 16 2014): 906-20.
- Ramskold, D., E. T. Wang, C. B. Burge, and R. Sandberg. "An Abundance of Ubiquitously Expressed Genes Revealed by Tissue Transcriptome Sequence Data." *PLoS Comput Biol* 5, no. 12 (Dec 2009): e1000598.

- Rand, T. A., S. Petersen, F. Du, and X. Wang. "Argonaute2 Cleaves the Anti-Guide Strand of siRNA During RISC Activation." *Cell* 123, no. 4 (Nov 18 2005): 621-9.
- Rauen, Katherine A. "The Rasopathies." *Annual Review of Genomics and Human Genetics* 14, no. 1 (2013): 355-69.
- Reed, D. R., M. P. Lawler, and M. G. Tordoff. "Reduced Body Weight Is a Common Effect of Gene Knockout in Mice." *BMC Genet* 9 (Jan 8 2008): 4.
- Reed, N. A., D. Cai, T. L. Blasius, G. T. Jih, E. Meyhofer, J. Gaertig, and K. J. Verhey. "Microtubule Acetylation Promotes Kinesin-1 Binding and Transport." *Curr Biol* 16, no. 21 (Nov 7 2006): 2166-72.
- Reichholf, B., V. A. Herzog, N. Fasching, R. A. Manzenreither, I. Sowemimo, and S. L. Ameres. "Time-Resolved Small RNA Sequencing Unravels the Molecular Principles of miRNA Homeostasis." *Mol Cell* 75, no. 4 (Aug 22 2019): 756-68 e7.
- Reim, D., U. Distler, S. Halbedl, C. Verpelli, C. Sala, J. Bockmann, S. Tenzer, T. M. Boeckers, and M. J. Schmeisser. "Proteomic Analysis of Post-Synaptic Density Fractions from Shank3 Mutant Mice Reveals Brain Region Specific Changes Relevant to Autism Spectrum Disorder." *Front Mol Neurosci* 10 (2017): 26.
- Richter, J. D., G. J. Bassell, and E. Klann. "Dysregulation and Restoration of Translational Homeostasis in Fragile X Syndrome." *Nat Rev Neurosci* 16, no. 10 (Oct 2015): 595-605.
- Rivas, F. V., N. H. Tolia, J. J. Song, J. P. Aragon, J. Liu, G. J. Hannon, and L. Joshua-Tor. "Purified Argonaute2 and an siRNA Form Recombinant Human RISC." *Nat Struct Mol Biol* 12, no. 4 (Apr 2005): 340-9.
- Ronald, A., and R. A. Hoekstra. "Autism Spectrum Disorders and Autistic Traits: A Decade of New Twin Studies." *Am J Med Genet B Neuropsychiatr Genet* 156B, no. 3 (Apr 2011): 255-74.
- Ronan, J. L., W. Wu, and G. R. Crabtree. "From Neural Development to Cognition: Unexpected Roles for Chromatin." *Nat Rev Genet* 14, no. 5 (May 2013): 347-59.
- Rotello, R. J., and T. D. Veenstra. "Mass Spectrometry Techniques: Principles and Practices for Quantitative Proteomics." *Curr Protein Pept Sci* 22, no. 2 (2021): 121-33.
- Roussignol, G., F. Ango, S. Romorini, J. C. Tu, C. Sala, P. F. Worley, J. Bockaert, and L. Fagni. "Shank Expression Is Sufficient to Induce Functional Dendritic Spine Synapses in Spiny Neurons." *J Neurosci* 25, no. 14 (Apr 6 2005): 3560-70.
- Saffary, R., and Z. Xie. "Fmrp Regulates the Transition from Radial Glial Cells to Intermediate Progenitor Cells During Neocortical Development." *J Neurosci* 31, no. 4 (Jan 26 2011): 1427-39.
- Sahin, M., and M. Sur. "Genes, Circuits, and Precision Therapies for Autism and Related Neurodevelopmental Disorders." *Science* 350, no. 6263 (Nov 20 2015).
- Salomaa, S. I., M. Miihkinen, E. Kremneva, I. Paatero, J. Lilja, G. Jacquemet, J. Vuorio, *et al.* "Shank3 Conformation Regulates Direct Actin Binding and Crosstalk with Rap1 Signaling." *Curr Biol* 31, no. 22 (Nov 22 2021): 4956-70 e9.

- Sancak, O., M. Nellist, M. Goedbloed, P. Elfferich, C. Wouters, A. Maat-Kievit, B. Zonnenberg, *et al.* "Mutational Analysis of the Tsc1 and Tsc2 Genes in a Diagnostic Setting: Genotype--Phenotype Correlations and Comparison of Diagnostic DNA Techniques in Tuberous Sclerosis Complex." *Eur J Hum Genet* 13, no. 6 (Jun 2005): 731-41.
- Sandin, S., P. Lichtenstein, R. Kuja-Halkola, H. Larsson, C. M. Hultman, and A. Reichenberg. "The Familial Risk of Autism." *JAMA* 311, no. 17 (May 7 2014): 1770-7.
- Saneyoshi, T., H. Matsuno, A. Suzuki, H. Murakoshi, N. G. Hedrick, E. Agnello, R. O'Connell, *et al.* "Reciprocal Activation within a Kinase-Effector Complex Underlying Persistence of Structural Ltp." *Neuron* 102, no. 6 (Jun 19 2019): 1199-210 e6.
- Sanger, F., S. Nicklen, and A. R. Coulson. "DNA Sequencing with Chain-Terminating Inhibitors." *Proc Natl Acad Sci U S A* 74, no. 12 (Dec 1977): 5463-7.
- Santini, E., and E. Klann. "Reciprocal Signaling between Translational Control Pathways and Synaptic Proteins in Autism Spectrum Disorders." *Sci Signal* 7, no. 349 (Oct 28 2014): re10.
- Sarachana, T., R. Zhou, G. Chen, H. K. Manji, and V. W. Hu. "Investigation of Post-Transcriptional Gene Regulatory Networks Associated with Autism Spectrum Disorders by MicroRNA Expression Profiling of Lymphoblastoid Cell Lines." *Genome Med* 2, no. 4 (Apr 7 2010): 23.
- Sasaki, T., A. Shiohama, S. Minoshima, and N. Shimizu. "Identification of Eight Members of the Argonaute Family in the Human Genome." *Genomics* 82, no. 3 (Sep 2003): 323-30.
- Sato, D., A. C. Lionel, C. S. Leblond, A. Prasad, D. Pinto, S. Walker, I. O'Connor, *et al.* "Shank1 Deletions in Males with Autism Spectrum Disorder." *Am J Hum Genet* 90, no. 5 (May 4 2012): 879-87.
- Satoh, K., M. Takeuchi, Y. Oda, M. Deguchi-Tawarada, Y. Sakamoto, K. Matsubara, T. Nagasu, and Y. Takai. "Identification of Activity-Regulated Proteins in the Postsynaptic Density Fraction." *Genes Cells* 7, no. 2 (Feb 2002): 187-97.
- Schalk, A., M. A. Cousin, N. R. Dsouza, T. D. Challman, K. E. Wain, Z. Powis, K. Minks, *et al.* "De Novo Coding Variants in the Ago1 Gene Cause a Neurodevelopmental Disorder with Intellectual Disability." *J Med Genet* 59, no. 10 (Oct 2022): 965-75.
- Scheper, G. C., M. S. van der Knaap, and C. G. Proud. "Translation Matters: Protein Synthesis Defects in Inherited Disease." *Nat Rev Genet* 8, no. 9 (Sep 2007): 711-23.
- Scheper, M., A. Romagnolo, Z. M. Besharat, A. M. Iyer, R. Moavero, C. Hertzberg, B. Weschke, *et al.* "Mirnas and Isomirs: Serum-Based Biomarkers for the Development of Intellectual Disability and Autism Spectrum Disorder in Tuberous Sclerosis Complex." *Biomedicine* 10, no. 8 (Jul 29 2022).
- Schirle, N. T., and I. J. MacRae. "The Crystal Structure of Human Argonaute2." *Science* 336, no. 6084 (May 25 2012): 1037-40.
- Schirle, N. T., J. Sheu-Gruttadauria, and I. J. MacRae. "Structural Basis for MicroRNA Targeting." *Science* 346, no. 6209 (Oct 31 2014): 608-13.
- Schmeisser, M. J. "Translational Neurobiology in Shank Mutant Mice--Model Systems for Neuropsychiatric Disorders." *Ann Anat* 200 (Jul 2015): 115-7.

- Schmeisser, M. J., E. Ey, S. Wegener, J. Bockmann, A. V. Stempel, A. Kuebler, A. L. Janssen, *et al.* "Autistic-Like Behaviours and Hyperactivity in Mice Lacking Prosap1/Shank2." *Nature* 486, no. 7402 (Apr 29 2012): 256-60.
- Schratt, G. "MicroRNAs at the Synapse." *Nat Rev Neurosci* 10, no. 12 (Dec 2009): 842-9.
- Schratt, G. M., F. Tuebing, E. A. Nigh, C. G. Kane, M. E. Sabatini, M. Kiebler, and M. E. Greenberg. "A Brain-Specific MicroRNA Regulates Dendritic Spine Development." *Nature* 439, no. 7074 (Jan 19 2006): 283-9.
- Schuetz, G., M. Rosario, J. Grimm, T. M. Boeckers, E. D. Gundelfinger, and W. Birchmeier. "The Neuronal Scaffold Protein Shank3 Mediates Signaling and Biological Function of the Receptor Tyrosine Kinase Ret in Epithelial Cells." *J Cell Biol* 167, no. 5 (Dec 6 2004): 945-52.
- Schwarz, D. S., G. Hutvagner, T. Du, Z. Xu, N. Aronin, and P. D. Zamore. "Asymmetry in the Assembly of the Rnai Enzyme Complex." *Cell* 115, no. 2 (Oct 17 2003): 199-208.
- Selbach, M., B. Schwanhauser, N. Thierfelder, Z. Fang, R. Khanin, and N. Rajewsky. "Widespread Changes in Protein Synthesis Induced by MicroRNAs." *Nature* 455, no. 7209 (Sep 4 2008): 58-63.
- Selenica, M. L., L. Benner, S. B. Housley, B. Manchec, D. C. Lee, K. R. Nash, J. Kalin, *et al.* "Histone Deacetylase 6 Inhibition Improves Memory and Reduces Total Tau Levels in a Mouse Model of Tau Deposition." *Alzheimers Res Ther* 6, no. 1 (2014): 12.
- Selevsek, N., C. Y. Chang, L. C. Gillet, P. Navarro, O. M. Bernhardt, L. Reiter, L. Y. Cheng, O. Vitek, and R. Aebersold. "Reproducible and Consistent Quantification of the *Saccharomyces Cerevisiae* Proteome by Swath-Mass Spectrometry." *Mol Cell Proteomics* 14, no. 3 (Mar 2015): 739-49.
- Sen, G. L., and H. M. Blau. "Argonaute 2/Risc Resides in Sites of Mammalian Mrna Decay Known as Cytoplasmic Bodies." *Nat Cell Biol* 7, no. 6 (Jun 2005): 633-6.
- Shalizi, A., B. Gaudilliere, Z. Yuan, J. Stegmuller, T. Shirogane, Q. Ge, Y. Tan, *et al.* "A Calcium-Regulated Mef2 Sumoylation Switch Controls Postsynaptic Differentiation." *Science* 311, no. 5763 (Feb 17 2006): 1012-7.
- Shannon, P., A. Markiel, O. Ozier, N. S. Baliga, J. T. Wang, D. Ramage, N. Amin, B. Schwikowski, and T. Ideker. "Cytoscape: A Software Environment for Integrated Models of Biomolecular Interaction Networks." *Genome Res* 13, no. 11 (Nov 2003): 2498-504.
- Shen, K., and T. Meyer. "Dynamic Control of Camkii Translocation and Localization in Hippocampal Neurons by Nmda Receptor Stimulation." *Science* 284, no. 5411 (Apr 2 1999): 162-6.
- Sheng, M., and C. C. Hoogenraad. "The Postsynaptic Architecture of Excitatory Synapses: A More Quantitative View." *Annu Rev Biochem* 76 (2007): 823-47.
- Sheng, M., and E. Kim. "The Postsynaptic Organization of Synapses." *Cold Spring Harb Perspect Biol* 3, no. 12 (Dec 1 2011).
- Sheng, M., E. Kim. "The Shank Family of Scaffold Proteins." *J Cell Sci* 113 (Pt 11) (Jun 2000): 1851-6.
- Sheth, U., and R. Parker. "Decapping and Decay of Messenger Rna Occur in Cytoplasmic Processing Bodies." *Science* 300, no. 5620 (May 2 2003): 805-8.

- Shiomura, Y., and N. Hirokawa. "Colocalization of Microtubule-Associated Protein 1a and Microtubule-Associated Protein 2 on Neuronal Microtubules in Situ Revealed with Double-Label Immunoelectron Microscopy." *J Cell Biol* 104, no. 6 (Jun 1987): 1575-8.
- Shonesy, B. C., N. Jalan-Sakrikar, V. S. Cavener, and R. J. Colbran. "Camkii: A Molecular Substrate for Synaptic Plasticity and Memory." *Prog Mol Biol Transl Sci* 122 (2014): 61-87.
- Silverman, J. L., S. M. Turner, C. L. Barkan, S. S. Tolu, R. Saxena, A. Y. Hung, M. Sheng, and J. N. Crawley. "Sociability and Motor Functions in Shank1 Mutant Mice." *Brain Res* 1380 (Mar 22 2011): 120-37.
- Simanshu, D. K., D. V. Nissley, and F. McCormick. "Ras Proteins and Their Regulators in Human Disease." *Cell* 170, no. 1 (Jun 29 2017): 17-33.
- Simon, B., J. P. Kirkpatrick, S. Eckhardt, M. Reuter, E. A. Rocha, M. A. Andrade-Navarro, P. Sehr, R. S. Pillai, and T. Carlomagno. "Recognition of 2'-O-Methylated 3'-End of Pirna by the Paz Domain of a Piwi Protein." *Structure* 19, no. 2 (Feb 9 2011): 172-80.
- Singh, S. S., S. N. Rai, H. Birla, W. Zahra, A. S. Rathore, and S. P. Singh. "Nf-Kappab-Mediated Neuroinflammation in Parkinson's Disease and Potential Therapeutic Effect of Polyphenols." *Neurotox Res* 37, no. 3 (Mar 2020): 491-507.
- Skuse, D. H., W. Mandy, C. Steer, L. L. Miller, R. Goodman, K. Lawrence, A. Emond, and J. Golding. "Social Communication Competence and Functional Adaptation in a General Population of Children: Preliminary Evidence for Sex-by-Verbal Iq Differential Risk." *J Am Acad Child Adolesc Psychiatry* 48, no. 2 (Feb 2009): 128-37.
- Snell, G. D. "Inheritance in the House Mouse, the Linkage Relations of Short-Ear, Hairless, and Naked." *Genetics* 16, no. 1 (Jan 1931): 42-74.
- Soba, P., C. Han, Y. Zheng, D. Perea, I. Miguel-Aliaga, L. Y. Jan, and Y. N. Jan. "The Ret Receptor Regulates Sensory Neuron Dendrite Growth and Integrin Mediated Adhesion." *Elife* 4 (Mar 12 2015).
- Soltau, M., D. Richter, and H. J. Kreienkamp. "The Insulin Receptor Substrate Irs53 Links Postsynaptic Shank1 to the Small G-Protein Cdc42." *Mol Cell Neurosci* 21, no. 4 (Dec 2002): 575-83.
- Song, G., H. Chen, G. Sheng, Y. Wang, and J. Lou. "Argonaute Facilitates the Lateral Diffusion of the Guide Along Its Target and Prevents the Guide from Being Pushed Away by the Ribosome." *Biochemistry* 57, no. 15 (Apr 17 2018): 2179-83.
- Song, J. J., S. K. Smith, G. J. Hannon, and L. Joshua-Tor. "Crystal Structure of Argonaute and Its Implications for Risc Slicer Activity." *Science* 305, no. 5689 (Sep 3 2004): 1434-7.
- Sorra, K. E., and K. M. Harris. "Overview on the Structure, Composition, Function, Development, and Plasticity of Hippocampal Dendritic Spines." *Hippocampus* 10, no. 5 (2000): 501-11.
- Specchio, N., N. Pietrafusa, M. Trivisano, R. Moavero, L. De Palma, A. Ferretti, F. Vigeveno, and P. Curatolo. "Autism and Epilepsy in Patients with Tuberous Sclerosis Complex." *Front Neurol* 11 (2020): 639.

- Srivastava, S., J. A. Love-Nichols, K. A. Dies, D. H. Ledbetter, C. L. Martin, W. K. Chung, H. V. Firth, *et al.* "Meta-Analysis and Multidisciplinary Consensus Statement: Exome Sequencing Is a First-Tier Clinical Diagnostic Test for Individuals with Neurodevelopmental Disorders." *Genet Med* 21, no. 11 (Nov 2019): 2413-21.
- State, M. W. "Another Piece of the Autism Puzzle." *Nat Genet* 42, no. 6 (Jun 2010): 478-9.
- Stessman, H. A., B. Xiong, B. P. Coe, T. Wang, K. Hoekzema, M. Fenckova, M. Kvarnung, *et al.* "Targeted Sequencing Identifies 91 Neurodevelopmental-Disorder Risk Genes with Autism and Developmental-Disability Biases." *Nat Genet* 49, no. 4 (Apr 2017): 515-26.
- Stoecklin, G., T. Mayo, and P. Anderson. "Are-Mrna Degradation Requires the 5'-3' Decay Pathway." *EMBO Rep* 7, no. 1 (Jan 2006): 72-7.
- Strack, S., and R. J. Colbran. "Autophosphorylation-Dependent Targeting of Calcium/ Calmodulin-Dependent Protein Kinase II by the NR2B Subunit of the N-Methyl- D-Aspartate Receptor." *J Biol Chem* 273, no. 33 (Aug 14 1998): 20689-92.
- Subramanian, I., S. Verma, S. Kumar, A. Jere, and K. Anamika. "Multi-Omics Data Integration, Interpretation, and Its Application." *Bioinform Biol Insights* 14 (2020): 1177932219899051.
- Sudhof, T. C. "Neuroligins and Neurexins Link Synaptic Function to Cognitive Disease." *Nature* 455, no. 7215 (Oct 16 2008): 903-11.
- Sudhof, T. C. "Towards an Understanding of Synapse Formation." *Neuron* 100, no. 2 (Oct 24 2018): 276-93.
- Suetterlin, P., S. Hurley, C. Mohan, K. L. H. Riegman, M. Pagani, A. Caruso, J. Ellegood, *et al.* "Altered Neocortical Gene Expression, Brain Overgrowth and Functional over-Connectivity in Chd8 Haploinsufficient Mice." *Cereb Cortex* 28, no. 6 (Jun 1 2018): 2192-206.
- Sugiyama, Y., I. Kawabata, K. Sobue, and S. Okabe. "Determination of Absolute Protein Numbers in Single Synapses by a Gfp-Based Calibration Technique." *Nat Methods* 2, no. 9 (Sep 2005): 677-84.
- Sungur, A. O., K. J. Vorckel, R. K. Schwarting, and M. Wohn. "Repetitive Behaviors in the Shank1 Knockout Mouse Model for Autism Spectrum Disorder: Developmental Aspects and Effects of Social Context." *J Neurosci Methods* 234 (Aug 30 2014): 92-100.
- Sutton, M. A., and E. M. Schuman. "Dendritic Protein Synthesis, Synaptic Plasticity, and Memory." *Cell* 127, no. 1 (Oct 6 2006): 49-58.
- Suzuki, H. I., A. Katsura, T. Yasuda, T. Ueno, H. Mano, K. Sugimoto, and K. Miyazono. "Small-Rna Asymmetry Is Directly Driven by Mammalian Argonautes." *Nat Struct Mol Biol* 22, no. 7 (Jul 2015): 512-21.
- Swarts, D. C., K. Makarova, Y. Wang, K. Nakanishi, R. F. Ketting, E. V. Koonin, D. J. Patel, and J. van der Oost. "The Evolutionary Journey of Argonaute Proteins." *Nat Struct Mol Biol* 21, no. 9 (Sep 2014): 743-53.
- Talebizadeh, Z., M. G. Butler, and M. F. Theodoro. "Feasibility and Relevance of Examining Lymphoblastoid Cell Lines to Study Role of MicroRNAs in Autism." *Autism Res* 1, no. 4 (Aug 2008): 240-50.

- Tan, G. C., E. Chan, A. Molnar, R. Sarkar, D. Alexieva, I. M. Isa, S. Robinson, *et al.* "5' Isomir Variation Is of Functional and Evolutionary Importance." *Nucleic Acids Res* 42, no. 14 (Aug 2014): 9424-35.
- Tao-Cheng, J. H. "Activity-Dependent Redistribution of Camkii in the Postsynaptic Compartment of Hippocampal Neurons." *Mol Brain* 13, no. 1 (Apr 1 2020): 53.
- Tarlungeanu, D. C., and G. Novarino. "Genomics in Neurodevelopmental Disorders: An Avenue to Personalized Medicine." *Exp Mol Med* 50, no. 8 (Aug 7 2018): 1-7.
- Teixeira, D., U. Sheth, M. A. Valencia-Sanchez, M. Brengues, and R. Parker. "Processing Bodies Require Rna for Assembly and Contain Nontranslating Mrnas." *RNA* 11, no. 4 (Apr 2005): 371-82.
- Telley, L., G. Agirman, J. Prados, N. Amberg, S. Fievre, P. Oberst, G. Bartolini, *et al.* "Temporal Patterning of Apical Progenitors and Their Daughter Neurons in the Developing Neocortex." *Science* 364, no. 6440 (May 10 2019).
- Tessier-Lavigne, M., and C. S. Goodman. "The Molecular Biology of Axon Guidance." *Science* 274, no. 5290 (Nov 15 1996): 1123-33.
- Thomas, P. D., D. Ebert, A. Muruganujan, T. Mushayahama, L. P. Albou, and H. Mi. "Panther: Making Genome-Scale Phylogenetics Accessible to All." *Protein Sci* 31, no. 1 (Jan 2022): 8-22.
- Tian, Y., D. K. Simanshu, J. B. Ma, and D. J. Patel. "Structural Basis for Pirna 2'-O-Methylated 3'-End Recognition by Piwi Paz (Piwi/Argonaute/Zwille) Domains." *Proc Natl Acad Sci U S A* 108, no. 3 (Jan 18 2011): 903-10.
- Tidyman, W. E., and K. A. Rauen. "The Rasopathies: Developmental Syndromes of Ras/Mapk Pathway Dysregulation." *Curr Opin Genet Dev* 19, no. 3 (Jun 2009): 230-6.
- Tolia, N. H., and L. Joshua-Tor. "Slicer and the Argonautes." *Nat Chem Biol* 3, no. 1 (Jan 2007): 36-43.
- Tomasello, L., R. Distefano, G. Nigita, and C. M. Croce. "The MicroRNA Family Gets Wider: The Isomirs Classification and Role." *Front Cell Dev Biol* 9 (2021): 668648.
- Torossian, A., R. M. Sare, I. Loutaev, and C. B. Smith. "Increased Rates of Cerebral Protein Synthesis in Shank3 Knockout Mice: Implications for a Link between Synaptic Protein Deficit and Dysregulated Protein Synthesis in Autism Spectrum Disorder/Intellectual Disability." *Neurobiol Dis* 148 (Jan 2021): 105213.
- Tsuboyama, K., H. Tadakuma, and Y. Tomari. "Conformational Activation of Argonaute by Distinct yet Coordinated Actions of the Hsp70 and Hsp90 Chaperone Systems." *Mol Cell* 70, no. 4 (May 17 2018): 722-29 e4.
- Tu, J. C., B. Xiao, S. Naisbitt, J. P. Yuan, R. S. Petralia, P. Brakeman, A. Doan, *et al.* "Coupling of Mglur/Homer and Psd-95 Complexes by the Shank Family of Postsynaptic Density Proteins." *Neuron* 23, no. 3 (Jul 1999): 583-92.
- Tuli, L., and H. W. Ressom. "Lc-Ms Based Detection of Differential Protein Expression." *J Proteomics Bioinform* 2 (Oct 2 2009): 416-38.
- Twiss, J. L., and J. van Minnen. "New Insights into Neuronal Regeneration: The Role of Axonal Protein Synthesis in Pathfinding and Axonal Extension." *J Neurotrauma* 23, no. 3-4 (Mar-Apr 2006): 295-308.

- Uchino, S., H. Wada, S. Honda, Y. Nakamura, Y. Ondo, T. Uchiyama, M. Tsutsumi, *et al.* "Direct Interaction of Post-Synaptic Density-95/Dlg/Zo-1 Domain-Containing Synaptic Molecule Shank3 with Glur1 Alpha-Amino-3-Hydroxy-5-Methyl-4-Isoxazole Propionic Acid Receptor." *J Neurochem* 97, no. 4 (May 2006): 1203-14.
- Vagin, V. V., A. Sigova, C. Li, H. Seitz, V. Gvozdev, and P. D. Zamore. "A Distinct Small Rna Pathway Silences Selfish Genetic Elements in the Germline." *Science* 313, no. 5785 (Jul 21 2006): 320-4.
- Vaksman, O., T. E. Hetland, C. G. Trope, R. Reich, and B. Davidson. "Argonaute, Dicer, and Drosha Are up-Regulated Along Tumor Progression in Serous Ovarian Carcinoma." *Hum Pathol* 43, no. 11 (Nov 2012): 2062-9.
- van Bokhoven, H. "Genetic and Epigenetic Networks in Intellectual Disabilities." *Annu Rev Genet* 45 (2011): 81-104.
- van Dijk, E., N. Cougot, S. Meyer, S. Babajko, E. Wahle, and B. Seraphin. "Human Dcp2: A Catalytically Active Mrna Decapping Enzyme Located in Specific Cytoplasmic Structures." *EMBO J* 21, no. 24 (Dec 16 2002): 6915-24.
- Van Stry, M., T. H. Oguin, 3rd, S. Cheloufi, P. Vogel, M. Watanabe, M. R. Pillai, P. Dash, *et al.* "Enhanced Susceptibility of Ago1/3 Double-Null Mice to Influenza a Virus Infection." *J Virol* 86, no. 8 (Apr 2012): 4151-7.
- van Weering, D. H., and J. L. Bos. "Signal Transduction by the Receptor Tyrosine Kinase Ret." *Recent Results Cancer Res* 154 (1998): 271-81.
- Verkerk, A. J., M. Pieretti, J. S. Sutcliffe, Y. H. Fu, D. P. Kuhl, A. Pizzuti, O. Reiner, *et al.* "Identification of a Gene (Fmr-1) Containing a Cgg Repeat Coincident with a Breakpoint Cluster Region Exhibiting Length Variation in Fragile X Syndrome." *Cell* 65, no. 5 (May 31 1991): 905-14.
- Vicidomini, C., L. Ponzoni, D. Lim, M. J. Schmeisser, D. Reim, N. Morello, D. Orellana, *et al.* "Pharmacological Enhancement of Mglu5 Receptors Rescues Behavioral Deficits in Shank3 Knock-out Mice." *Mol Psychiatry* 22, no. 5 (May 2017): 689-702.
- Voellenkle, C., Jv Rooij, A. Guffanti, E. Brini, P. Fasanaro, E. Isaia, L. Croft, *et al.* "Deep-Sequencing of Endothelial Cells Exposed to Hypoxia Reveals the Complexity of Known and Novel Micrnas." *RNA* 18, no. 3 (Mar 2012): 472-84.
- Vogel, C., S. Abreu Rde, D. Ko, S. Y. Le, B. A. Shapiro, S. C. Burns, D. Sandhu, *et al.* "Sequence Signatures and Mrna Concentration Can Explain Two-Thirds of Protein Abundance Variation in a Human Cell Line." *Mol Syst Biol* 6 (Aug 24 2010): 400.
- Voineagu, I., X. Wang, P. Johnston, J. K. Lowe, Y. Tian, S. Horvath, J. Mill, *et al.* "Transcriptomic Analysis of Autistic Brain Reveals Convergent Molecular Pathology." *Nature* 474, no. 7351 (May 25 2011): 380-4.
- Volkman, N., K. J. Amann, S. Stoilova-McPhie, C. Egile, D. C. Winter, L. Hazelwood, J. E. Heuser, *et al.* "Structure of Arp2/3 Complex in Its Activated State and in Actin Filament Branch Junctions." *Science* 293, no. 5539 (Sep 28 2001): 2456-9.
- Voller, D., L. Linck, A. Bruckmann, J. Hauptmann, R. Deutzmann, G. Meister, and A. K. Bosserhoff. "Argonaute Family Protein Expression in Normal Tissue and Cancer Entities." *PLoS One* 11, no. 8 (2016): e0161165.

- Wachutka, L., and J. Gagneur. "Measures of Rna Metabolism Rates: Toward a Definition at the Level of Single Bonds." *Transcription* 8, no. 2 (Mar 15 2017): 75-80.
- Walikonis, R. S., O. N. Jensen, M. Mann, D. W. Provance, Jr., J. A. Mercer, and M. B. Kennedy. "Identification of Proteins in the Postsynaptic Density Fraction by Mass Spectrometry." *J Neurosci* 20, no. 11 (Jun 1 2000): 4069-80.
- Wang, E. T., R. Sandberg, S. Luo, I. Khrebtkova, L. Zhang, C. Mayr, S. F. Kingsmore, G. P. Schroth, and C. B. Burge. "Alternative Isoform Regulation in Human Tissue Transcriptomes." *Nature* 456, no. 7221 (Nov 27 2008): 470-6.
- Wang, E. T., J. M. Taliaferro, J. A. Lee, I. P. Sudhakaran, W. Rossoll, C. Gross, K. R. Moss, and G. J. Bassell. "Dysregulation of Mrna Localization and Translation in Genetic Disease." *J Neurosci* 36, no. 45 (Nov 9 2016): 11418-26.
- Wang, H. W., C. Noland, B. Siridechadilok, D. W. Taylor, E. Ma, K. Felderer, J. A. Doudna, and E. Nogales. "Structural Insights into Rna Processing by the Human Risc-Loading Complex." *Nat Struct Mol Biol* 16, no. 11 (Nov 2009): 1148-53.
- Wang, X., A. L. Bey, B. M. Katz, A. Badea, N. Kim, L. K. David, L. J. Duffney, *et al.* "Altered Mglur5-Homer Scaffolds and Corticostriatal Connectivity in a Shank3 Complete Knockout Model of Autism." *Nat Commun* 7 (May 10 2016): 11459.
- Wang, X., P. A. McCoy, R. M. Rodriguiz, Y. Pan, H. S. Je, A. C. Roberts, C. J. Kim, *et al.* "Synaptic Dysfunction and Abnormal Behaviors in Mice Lacking Major Isoforms of Shank3." *Hum Mol Genet* 20, no. 15 (Aug 1 2011): 3093-108.
- Wang, Y., S. Juranek, H. Li, G. Sheng, T. Tuschl, and D. J. Patel. "Structure of an Argonaute Silencing Complex with a Seed-Containing Guide DNA and Target Rna Duplex." *Nature* 456, no. 7224 (Dec 18 2008): 921-6.
- Wang, Y., G. Sheng, S. Juranek, T. Tuschl, and D. J. Patel. "Structure of the Guide-Strand-Containing Argonaute Silencing Complex." *Nature* 456, no. 7219 (Nov 13 2008): 209-13.
- Warf, M. B., W. E. Johnson, and B. L. Bass. "Improved Annotation of C. Elegans Micrnas by Deep Sequencing Reveals Structures Associated with Processing by Drosha and Dicer." *RNA* 17, no. 4 (Apr 2011): 563-77.
- Watahiki, A., Y. Wang, J. Morris, K. Dennis, H. M. O'Dwyer, M. Gleave, P. W. Gout, and Y. Wang. "Micrnas Associated with Metastatic Prostate Cancer." *PLoS One* 6, no. 9 (2011): e24950.
- Welch, J. M., J. Lu, R. M. Rodriguiz, N. C. Trotta, J. Peca, J. D. Ding, C. Feliciano, *et al.* "Cortico-Striatal Synaptic Defects and Ocd-Like Behaviours in Sapap3-Mutant Mice." *Nature* 448, no. 7156 (Aug 23 2007): 894-900.
- Welch, M. D., A. H. DePace, S. Verma, A. Iwamatsu, and T. J. Mitchison. "The Human Arp2/3 Complex Is Composed of Evolutionarily Conserved Subunits and Is Localized to Cellular Regions of Dynamic Actin Filament Assembly." *J Cell Biol* 138, no. 2 (Jul 28 1997): 375-84.
- Wesseling, H., P. C. Guest, C. M. Lee, E. H. Wong, H. Rahmoune, and S. Bahn. "Integrative Proteomic Analysis of the Nmda Nr1 Knockdown Mouse Model Reveals Effects on Central and Peripheral Pathways Associated with Schizophrenia and Autism Spectrum Disorders." *Mol Autism* 5 (2014): 38.

- Wightman, B., I. Ha, and G. Ruvkun. "Posttranscriptional Regulation of the Heterochronic Gene Lin-14 by Lin-4 Mediates Temporal Pattern Formation in *C. Elegans*." *Cell* 75, no. 5 (Dec 3 1993): 855-62.
- Wilson, H. L., A. C. Wong, S. R. Shaw, W. Y. Tse, G. A. Stapleton, M. C. Phelan, S. Hu, J. Marshall, and H. E. McDermid. "Molecular Characterisation of the 22q13 Deletion Syndrome Supports the Role of Haploinsufficiency of Shank3/Prosap2 in the Major Neurological Symptoms." *J Med Genet* 40, no. 8 (Aug 2003): 575-84.
- Winden, K. D., D. Ebrahimi-Fakhari, and M. Sahin. "Abnormal Mtor Activation in Autism." *Annu Rev Neurosci* 41 (Jul 8 2018): 1-23.
- Wingett, S. W., and S. Andrews. "Fastq Screen: A Tool for Multi-Genome Mapping and Quality Control." *F1000Res* 7 (2018): 1338.
- Winter, J. "MicroRNAs of the Mir379-410 Cluster: New Players in Embryonic Neurogenesis and Regulators of Neuronal Function." *Neurogenesis (Austin)* 2, no. 1 (2015): e1004970.
- Witteveen, J. S., M. H. Willemsen, T. C. Dombroski, N. H. van Bakel, W. M. Nillesen, J. A. van Hulten, E. J. Jansen, *et al.* "Haploinsufficiency of Mecp2-Interacting Transcriptional Co-Repressor Sin3a Causes Mild Intellectual Disability by Affecting the Development of Cortical Integrity." *Nat Genet* 48, no. 8 (Aug 2016): 877-87.
- Wiznitzer, M. "Autism and Tuberous Sclerosis." *J Child Neurol* 19, no. 9 (Sep 2004): 675-9.
- Wohr, M., F. I. Rouillet, A. Y. Hung, M. Sheng, and J. N. Crawley. "Communication Impairments in Mice Lacking Shank1: Reduced Levels of Ultrasonic Vocalizations and Scent Marking Behavior." *PLoS One* 6, no. 6 (2011): e20631.
- Woike, D., E. Wang, D. Tibbe, F. Hassani Nia, A. V. Failla, M. Kibaek, T. M. Overgard, *et al.* "Mutations Affecting the N-Terminal Domains of Shank3 Point to Different Pathomechanisms in Neurodevelopmental Disorders." *Sci Rep* 12, no. 1 (Jan 18 2022): 902.
- Wright, C. F., T. W. Fitzgerald, W. D. Jones, S. Clayton, J. F. McRae, M. van Kogelenberg, D. A. King, *et al.* "Genetic Diagnosis of Developmental Disorders in the Ddd Study: A Scalable Analysis of Genome-Wide Research Data." *Lancet* 385, no. 9975 (Apr 4 2015): 1305-14.
- Wu, C. W., J. M. Evans, S. Huang, D. W. Mahoney, B. A. Dukek, W. R. Taylor, T. C. Yab, *et al.* "A Comprehensive Approach to Sequence-Oriented Isomir Annotation (Casmir): Demonstration with Isomir Profiling in Colorectal Neoplasia." *BMC Genomics* 19, no. 1 (May 25 2018): 401.
- Wu, H., J. Tao, P. J. Chen, A. Shahab, W. Ge, R. P. Hart, X. Ruan, Y. Ruan, and Y. E. Sun. "Genome-Wide Analysis Reveals Methyl-Cpg-Binding Protein 2-Dependent Regulation of MicroRNAs in a Mouse Model of Rett Syndrome." *Proc Natl Acad Sci U S A* 107, no. 42 (Oct 19 2010): 18161-6.
- Wu, H., C. Ye, D. Ramirez, and N. Manjunath. "Alternative Processing of Primary MicroRNA Transcripts by Drosha Generates 5' End Variation of Mature MicroRNA." *PLoS One* 4, no. 10 (Oct 27 2009): e7566.
- Wu, J., J. Yang, W. C. Cho, and Y. Zheng. "Argonaute Proteins: Structural Features, Functions and Emerging Roles." *J Adv Res* 24 (Jul 2020): 317-24.
- Wu, L., J. Fan, and J. G. Belasco. "MicroRNAs Direct Rapid Deadenylation of Mrna." *Proc Natl Acad Sci U S A* 103, no. 11 (Mar 14 2006): 4034-9.

- Wu, L., P. Xiao, Q. Li, Z. Zhang, H. Wang, Q. Jiang, and L. Li. "Altered Expression of Akt1 and P38a in the Colons of Patients with Hirschsprung's Disease." *Pediatr Surg Int* 36, no. 6 (Jun 2020): 719-25.
- Wu, Y., T. R. Albrecht, D. Baillat, E. J. Wagner, and L. Tong. "Molecular Basis for the Interaction between Integrator Subunits Ints9 and Ints11 and Its Functional Importance." *Proc Natl Acad Sci U S A* 114, no. 17 (Apr 25 2017): 4394-99.
- Wyman, S. K., E. C. Knouf, R. K. Parkin, B. R. Fritz, D. W. Lin, L. M. Dennis, M. A. Krouse, P. J. Webster, and M. Tewari. "Post-Transcriptional Generation of Mirna Variants by Multiple Nucleotidyl Transferases Contributes to Mirna Transcriptome Complexity." *Genome Res* 21, no. 9 (Sep 2011): 1450-61.
- Xie, Z., A. Bailey, M. V. Kuleshov, D. J. B. Clarke, J. E. Evangelista, S. L. Jenkins, A. Lachmann, *et al.* "Gene Set Knowledge Discovery with Enrichr." *Curr Protoc* 1, no. 3 (Mar 2021): e90.
- Yang, J. S., and E. C. Lai. "Alternative Mirna Biogenesis Pathways and the Interpretation of Core Mirna Pathway Mutants." *Mol Cell* 43, no. 6 (Sep 16 2011): 892-903.
- Yao, J., Y. Sasaki, Z. Wen, G. J. Bassell, and J. Q. Zheng. "An Essential Role for Beta-Actin Mrna Localization and Translation in Ca²⁺-Dependent Growth Cone Guidance." *Nat Neurosci* 9, no. 10 (Oct 2006): 1265-73.
- Yi, R., Y. Qin, I. G. Macara, and B. R. Cullen. "Exportin-5 Mediates the Nuclear Export of Pre-Micrnas and Short Hairpin Rnas." *Genes Dev* 17, no. 24 (Dec 15 2003): 3011-6.
- Yoo, T., H. Cho, J. Lee, H. Park, Y. E. Yoo, E. Yang, J. Y. Kim, H. Kim, and E. Kim. "Gaba Neuronal Deletion of Shank3 Exons 14-16 in Mice Suppresses Striatal Excitatory Synaptic Input and Induces Social and Locomotor Abnormalities." *Front Cell Neurosci* 12 (2018): 341.
- Yoshimura, Y., Y. Yamauchi, T. Shinkawa, M. Taoka, H. Donai, N. Takahashi, T. Isobe, and T. Yamauchi. "Molecular Constituents of the Postsynaptic Density Fraction Revealed by Proteomic Analysis Using Multidimensional Liquid Chromatography-Tandem Mass Spectrometry." *J Neurochem* 88, no. 3 (Feb 2004): 759-68.
- Yue, D., H. Liu, and Y. Huang. "Survey of Computational Algorithms for Microrna Target Prediction." *Curr Genomics* 10, no. 7 (Nov 2009): 478-92.
- Zeng, M., X. Chen, D. Guan, J. Xu, H. Wu, P. Tong, and M. Zhang. "Reconstituted Postsynaptic Density as a Molecular Platform for Understanding Synapse Formation and Plasticity." *Cell* 174, no. 5 (Aug 23 2018): 1172-87 e16.
- Zeng, M., J. Diaz-Alonso, F. Ye, X. Chen, J. Xu, Z. Ji, R. A. Nicoll, and M. Zhang. "Phase Separation-Mediated Tarp/Maguk Complex Condensation and Ampa Receptor Synaptic Transmission." *Neuron* 104, no. 3 (Nov 6 2019): 529-43 e6.
- Zeng, M., Y. Shang, T. Guo, Q. He, W. H. Yung, K. Liu, and M. Zhang. "A Binding Site Outside the Canonical PdZ Domain Determines the Specific Interaction between Shank and Sapap and Their Function." *Proc Natl Acad Sci U S A* 113, no. 22 (May 31 2016): E3081-90.
- Zeng, Y., E. J. Wagner, and B. R. Cullen. "Both Natural and Designed Micro Rnas Can Inhibit the Expression of Cognate Mrnas When Expressed in Human Cells." *Mol Cell* 9, no. 6 (Jun 2002): 1327-33.




- Zhang, J., X. S. Fan, C. X. Wang, B. Liu, Q. Li, and X. J. Zhou. "Up-Regulation of Ago2 Expression in Gastric Carcinoma." *Med Oncol* 30, no. 3 (2013): 628.
- Zhang, J., J. R. Shemezis, E. R. McQuinn, J. Wang, M. Sverdllov, and A. Chenn. "Akt Activation by N-Cadherin Regulates Beta-Catenin Signaling and Neuronal Differentiation During Cortical Development." *Neural Dev* 8 (Apr 25 2013): 7.
- Zhang, J., G. J. Woodhead, S. K. Swaminathan, S. R. Noles, E. R. McQuinn, A. J. Pisarek, A. M. Stocker, *et al.* "Cortical Neural Precursors Inhibit Their Own Differentiation Via N-Cadherin Maintenance of Beta-Catenin Signaling." *Dev Cell* 18, no. 3 (Mar 16 2010): 472-9.
- Zhang, K., X. Zhang, Z. Cai, J. Zhou, R. Cao, Y. Zhao, Z. Chen, *et al.* "A Novel Class of MicroRNA-Recognition Elements That Function Only within Open Reading Frames." *Nat Struct Mol Biol* 25, no. 11 (Nov 2018): 1019-27.
- Zhang, L., L. Y. Dong, Y. J. Li, Z. Hong, and W. S. Wei. "Mir-21 Represses FasI in Microglia and Protects against Microglia-Mediated Neuronal Cell Death Following Hypoxia/Ischemia." *Glia* 60, no. 12 (Dec 2012): 1888-95.
- Zhang, Y. Q., A. M. Bailey, H. J. Matthies, R. B. Renden, M. A. Smith, S. D. Speese, G. M. Rubin, and K. Broadie. "Drosophila Fragile X-Related Gene Regulates the Map1b Homolog Futsch to Control Synaptic Structure and Function." *Cell* 107, no. 5 (Nov 30 2001): 591-603.
- Zhang, Y., Q. Zang, B. Xu, W. Zheng, R. Ban, H. Zhang, Y. Yang, *et al.* "Isomir Bank: A Research Resource for Tracking Isomirs." *Bioinformatics* 32, no. 13 (Jul 1 2016): 2069-71.
- Zitzer, H., D. Richter, and H. J. Kreienkamp. "Agonist-Dependent Interaction of the Rat Somatostatin Receptor Subtype 2 with Cortactin-Binding Protein 1." *J Biol Chem* 274, no. 26 (Jun 25 1999): 18153-6.
- Zoghbi, H. Y. "Postnatal Neurodevelopmental Disorders: Meeting at the Synapse?". *Science* 302, no. 5646 (Oct 31 2003): 826-30.

7. Appendix

7.1. Hazardous Substances

Table 48: Hazardous Substances. List of all hazardous substances used according to GHS (hazard pictograms, H and P statements). GHS, H and P statements taken from GESTIS substance database of the IFA, retrieved on the 4th of June 2023. Ordered by appearance in the materials section.

Substance	Pictogram	Hazard (H) statements	Precautionary (P) statements
KOH		290-302-314	234-260-280-301+312-303+361+353-305+351+338
CHX		300-341-360D-411	201-280-301+330+331+310-308+313
DTT		302-315-318	264-270-280-301+312-302+352-305+351+338
PFA		228-302+332-315-317-318-335-341-350	210-280-301+312-304+340+312-305+351+338-308+313
HCl		290-314-335	280-303+361+353-305+351+338+310
NP-40		318+412	280+273+305+351+338+310+501
EDTA		319-332-373	280-304+340-312-305+351+338-337+313
Ketamine		302-336	301+312+330
SDS		228-302+332-315-318-335-412	210-261-280-301+312+330-305+351+338+310-370+378
CaCl ₂		319	305+351+338
PMSF		280+260+270+264	304+340+310-301+330+331-303+361+353-363-305+351+338-311+501
Leupeptin		302+312+332+361	203-261-264-270-271-280-301+317-302+352-304+340-317-318-321-330-362+364-409+501
Pepstatin A		300	264-270-301+316-321-330-405+501
Triton X-100		301+318+400+410	270-273-280-305+351+338+310

Substance	Pictogram	Hazard (H) statements	Precautionary (P) statements
Acrylamide		301-312-332-315-317-319-340-350-361f-372	201-280-301+310-302+352+312-304+340+312-305+351+338
TEMED		225-332-302-314	210-280-301+330+331-303+361+353-304+340+312-305+351+338
Methanol		225-301+311+331-370	210-233-280-301+310-303+361+353-304+340+311

7.2. Tables

Table 49: Differentially translated mRNAs in hippocampal neurons of *Shank3 $\alpha\beta$ -KO* mice. RNA was purified from samples prepared with the bacTRAP method. DEG analysis was performed to determine differentially translated transcripts. Significance was appointed by adjusted p-value ≤ 0.1 and a FC of > 0.5 . A \log_2 transformation was calculated for the FC values. 26 mRNAs were deregulated of which nine were less translated and 17 exhibited enhanced translation.

No.	Gene symbol	Ensembl ID	P-value (adj)	FC (\log_2)
1	Gm12912	ENSMUSG00000081067	0.098	1.26
2	Gm15697	ENSMUSG00000081670	0.079	1.17
3	Fam83h	ENSMUSG00000046761	0.032	1.13
4	Rel	ENSMUSG00000020275	0.046	1.12
5	Wdr89	ENSMUSG00000045690	0.080	1.05
6	Gm11652	ENSMUSG00000083465	0.073	0.98
7	Gm37795	ENSMUSG00000102813	0.073	0.95
8	Syce1	ENSMUSG00000025480	0.072	0.84
9	Irf4	ENSMUSG00000021356	0.046	0.83
10	BC018473	ENSMUSG00000056032	0.073	0.78
11	Pkn3	ENSMUSG00000026785	0.066	0.78
12	Gm7964	ENSMUSG00000063902	0.008	0.76
13	Gucy2f	ENSMUSG00000042282	0.098	0.75
14	Sntg2	ENSMUSG00000020672	0.098	0.71
15	Rnf144a	ENSMUSG00000020642	0.098	0.58
16	Gm15663	ENSMUSG00000085282	0.098	0.56
17	1700003M07Rik	ENSMUSG00000085389	0.098	0.55
18	Abcg2	ENSMUSG00000029802	0.080	-0.57
19	Abcb4	ENSMUSG00000042476	0.046	-0.64
20	Enpp6	ENSMUSG00000038173	0.098	-0.91
21	Cd180	ENSMUSG00000021624	0.098	-0.96
22	4930488L21Rik	ENSMUSG00000097520	0.079	-1.00
23	Htr1f	ENSMUSG00000050783	0.098	-1.01
24	Gm17491	ENSMUSG00000097042	0.009	-1.14
25	Gm26799	ENSMUSG00000097579	0.073	-1.22
26	Ret	ENSMUSG00000030110	0.007	-1.24

Table 50: Deregulated proteins in the PSD of *Shank1*-KO mice determined by a mass spectrometry-based proteomics approach. Postsynaptic proteins that were decreased or enriched in KO-PSDs compared to WT-PSDs. Student's t-testing determined statistical significance and a p-value cutoff of $p \leq 0.05$ was applied. A \log_2 transformation was performed and a fold change (FC) cutoff of > 0.58 and < -0.58 applied, to include candidates which were at least 1.5 times higher or less abundant in KO compared to WT. 46 proteins were found to be deregulated, 18 of which showed decreased and 28 increased abundances in KO-PSDs. Proteins found to be deregulated in the analyses of both mouse lines are colored blue.

No.	Gene symbol	Description	P-value	FC (\log_2)
1	Shank1	SH3 and multiple ankyrin repeat domains protein 1	0.00002	3.85
2	Gabra1	Gamma-aminobutyric acid receptor subunit alpha-1	0.033	2.77
3	Dact3	Dapper homolog 3	0.038	2.05
4	Tbkbp1	TANK-binding kinase 1-binding protein 1	0.005	1.98
5	Golga1	Golgin subfamily A member 1	0.005	1.87
6	Rgs7bp	Regulator of G-protein signaling 7-binding protein	0.014	1.85
7	Mib2	E3 ubiquitin-protein ligase MIB2	0.024	1.58
8	Sipa1l2	Signal-induced proliferation-associated 1-like protein 2	0.028	1.51
9	Arpc5	Actin-related protein 2/3 complex subunit 5	0.023	1.36
10	Plekha6	Pleckstrin homology domain-containing family A member 6	0.042	1.32
11	Dcaf7	DDB1- and CUL4-associated factor 7	0.019	1.29
12	Kcnj4	Inward rectifier potassium channel 4	0.049	1.20
13	Efr3a	Protein EFR3 homolog A	0.049	1.08
14	Capza1	F-actin-capping protein subunit alpha-1	0.040	1.08
15	Gnb5	Guanine nucleotide-binding protein subunit beta-5	0.039	1.05
16	Nedd4	E3 ubiquitin-protein ligase NEDD4	0.021	0.92
17	Uqcrc1	Cytochrome b-c1 complex subunit 1, mitochondrial	0.032	0.90
18	Atp1a3	Sodium/potassium-transporting ATPase subunit alpha-3	0.022	-0.69
19	Vapb	Vesicle-associated membrane protein-associated protein B	0.008	-0.91
20	L1cam	Neural cell adhesion molecule L1	0.039	-0.93
21	Hmgb1	High mobility group protein B1	0.031	-1.02
22	Eno1	Alpha-enolase	0.045	-1.02
23	Nlgn4l	Neuroigin 4-like	0.044	-1.03
24	Abi1	Abl interactor 1	0.046	-1.04
25	Mapt	Microtubule-associated protein tau	0.037	-1.06
26	Prxl2a	Peroxiredoxin-like 2A	0.046	-1.16
27	Rps5	40S ribosomal protein S5	0.005	-1.16
28	Vps4a	Vacuolar protein sorting-associated protein 4A	0.045	-1.23
29	Crmp1	Dihydropyrimidinase-related protein 1	0.019	-1.27
30	Sv2a	Synaptic vesicle glycoprotein 2A	0.017	-1.28
31	Crocc	Rootletin	0.040	-1.29
32	Sh3glb2	Endophilin-B2	0.004	-1.33
33	Rpsa	40S ribosomal protein SA	0.042	-1.34
34	Pik3r4	Phosphoinositide 3-kinase regulatory subunit 4	0.045	-1.37
35	Tppp	tubulin polymerization-promoting protein	0.039	-1.38
36		Uncharacterized protein C8orf34 homolog	0.006	-1.40
37	Emc8	ER membrane protein complex subunit 8	0.012	-1.43

No.	Gene symbol	Description	P-value	FC (log ₂)
38	Hnrnpf	Heterogeneous nuclear ribonucleoprotein F	0.042	-1.51
39	Eno3	Beta-enolase	0.021	-1.58
40	Pkm	Pyruvate kinase PKM	0.046	-1.73
41	Rabep1	Rab GTPase-binding effector protein 1	0.033	-1.75
42	Slc39a7	Zinc transporter SLC39A7	0.006	-1.85
43	Hnrnpab	Heterogeneous nuclear ribonucleoprotein A/B	0.021	-1.95
44	Lnk	Endoplasmic reticulum junction formation protein lunapark	0.002	-2.07
45	Atp2a2	Sarcoplasmic/endoplasmic reticulum calcium ATPase 2	0.035	-2.26
46	Pde8b	High affinity cAMP-specific and IBMX-insensitive 3',5'-cyclic phosphodiesterase 8B	0.022	-2.38

Table 51: Deregulated proteins in the PSD of *Shank3αβ*-KO mice determined by proteomics. Postsynaptic proteins decreased or enriched in KO-PSDs compared to WT-PSDs. Student's t-testing determined statistical significance with p-value cutoff of $p \leq 0.05$. A log₂ transformation was performed and an 1.5 FC cutoff applied. 67 deregulated proteins were quantified. The abundance of 28 proteins was decreased and 39 were increased in KO-PSDs. Proteins found to be deregulated PSD fractions of both mouse lines are colored blue

No.	Gene symbol	Description	P-value	FC (log ₂)
1	Celsr2	Cadherin EGF LAG seven-pass G-type receptor 2	0.022	2.56
2	Fkbp3	Peptidyl-prolyl cis-trans isomerase FKBP3	0.016	2.21
3	Hsd17b12	Very-long-chain 3-oxoacyl-CoA reductase	0.015	2.02
4	Ndufs6	NADH dehydrogenase [ubiquinone] iron-sulfur protein 6, mitochondrial	0.034	2.01
5	Lin7c	Protein lin-7 homolog C	0.030	1.93
6	Shank3	SH3 and multiple ankyrin repeat domains protein 3	0.003	1.87
7	Cacna2d3	Voltage-dependent calcium channel subunit alpha-2/delta-3	0.019	1.76
8	Gnb5	Guanine nucleotide-binding protein subunit beta-5	0.008	1.68
9	Atp5me	ATP synthase subunit e, mitochondrial	0.039	1.46
10	Xkr4	XK-related protein 4	0.030	1.41
11	Rgs7bp	Regulator of G-protein signaling 7-binding protein	0.036	1.41
12	Lmtk2	Serine/threonine-protein kinase LMTK2	0.010	1.37
13	Spata2l	Spermatogenesis-associated protein 2-like protein	0.003	1.37
14	Fundc2	FUN14 domain-containing protein 2	0.016	1.35
15	Nacad	NAC-alpha domain-containing protein 1	0.014	1.33
16	Sipa1l3	Signal-induced proliferation-associated 1-like protein 3	0.026	1.07
17	Cacnb1	Voltage-dependent L-type calcium channel subunit beta-1	0.008	1.03
18	Gabrg2	Gamma-aminobutyric acid receptor subunit gamma-2	0.001	1.03
19	Scamp5	Secretory carrier-associated membrane protein 5	0.030	0.94
20	Homer1	Homer protein homolog 1	0.031	0.90
21	Tenm4	Teneurin-4	0.046	0.79
22	Numbl	Numb-like protein	0.006	0.76
23	Rpl19	60S ribosomal protein L19	0.013	0.75
24	Mtdh	Protein LYRIC	0.008	0.75
25	Shisa6	Protein shisa-6	0.026	0.73
26	Cct3	T-complex protein 1 subunit gamma	0.038	0.73

No.	Gene symbol	Description	P-value	FC (log ₂)
27	Sptan1	Spectrin alpha chain, non-erythrocytic 1	0.019	0.65
28	Elmo2	Engulfment and cell motility protein 2	0.003	0.60
29	Ppia	Peptidyl-prolyl cis-trans isomerase A	0.048	-0.67
30	Taok2	Serine/threonine-protein kinase TAO2	0.032	-0.70
31	Dnajb14	DnaJ homolog subfamily B member 14	0.030	-0.84
32	Zdhhc8	Palmitoyltransferase ZDHHC8	0.023	-0.89
33	Unc5a	Netrin receptor UNC5A	0.003	-0.91
34	Skp1	S-phase kinase-associated protein 1	0.036	-1.01
35	Prxl2a	Peroxiredoxin-like 2A	0.050	-1.04
36	Tpi1	Triosephosphate isomerase	0.011	-1.05
37	Arhgef12	Rho guanine nucleotide exchange factor 12	0.031	-1.14
38	L1cam	Neural cell adhesion molecule L1	0.025	-1.16
39	Snx27	Sorting nexin-27	0.010	-1.16
40	Pik3r1	Phosphatidylinositol 3-kinase regulatory subunit alpha	0.035	-1.18
41	Dnaja4	DnaJ homolog subfamily A member 4	0.015	-1.18
42	Dnm1l	Dynamin-1-like protein	0.015	-1.31
43	Ndrg2	Protein NDRG2	0.028	-1.34
44	Cltc	Clathrin heavy chain 1	0.024	-1.35
45	Pfkl	ATP-dependent 6-phosphofructokinase, liver type	0.045	-1.38
46	Spata2	Spermatogenesis-associated protein 2	0.034	-1.41
47	Pacsin1	Protein kinase C and casein kinase substrate in neurons protein 1	0.030	-1.53
48	Pja1	E3 ubiquitin-protein ligase Praja-1	0.014	-1.53
49	Vps4a	Vacuolar protein sorting-associated protein 4A	0.024	-1.54
50	Eno3	Beta-enolase	0.043	-1.55
51	Tmem126a	Transmembrane protein 126A	0.029	-1.60
52	Suclg1	Succinate--CoA ligase [ADP/GDP-forming] subunit alpha, mitochondrial	0.031	-1.60
53	Eif2a	Eukaryotic translation initiation factor 2A	0.049	-1.60
54	Dnajc6	Putative tyrosine-protein phosphatase auxilin	0.020	-1.63
55	Cwc25	Pre-mRNA-splicing factor CWC25 homolog	0.020	-1.65
56	Dync1li2	Cytoplasmic dynein 1 light intermediate chain 2	0.016	-1.71
57	Pdlim5	PDZ and LIM domain protein 5	0.001	-1.72
58	Ptp4a1	Protein tyrosine phosphatase type IVA 1	0.033	-1.75
59	Lgi3	Leucine-rich repeat LGI family member 3	0.027	-1.96
60	Fv1	Friend virus susceptibility protein 1	0.028	-2.01
61	Rae1	mRNA export factor	0.024	-2.01
62	Cadps	Calcium-dependent secretion activator 1	0.030	-2.32
63	Rabep1	Rab GTPase-binding effector protein 1	0.039	-2.34
64	Naaa	N-acyl ethanolamine-hydrolyzing acid amidase	0.006	-2.70
65	C2cd5	C2 domain-containing protein 5	0.001	-2.89
66	Olfm2	Noelin-2	0.013	-3.30
67	Ptpre	Receptor-type tyrosine-protein phosphatase epsilon	0.049	-3.52

Table 52: Differentially expressed and RISC-bound miRNAs analyzed in the miRAP assay. Comparisons of miRNAs in input controls (IC) and immunoprecipitates (IP) of the miRAP assay obtained from AAV-infected primary murine neuron cultures. The species *mus musculus* (mmu), the identity of miRNA (miR) and the strand (3p or 5p) are listed. The miRNAs found in both comparisons are colored blue.

No.	L192P-IC vs. WT-IC	L192-IP vs. WT-IP
1	mmu-let-7d-3p	mmu-let-7g-3p
2	mmu-miR-15a-5p	mmu-miR-15a-5p
3	mmu-miR-23a-3p	mmu-miR-33-5p
4	mmu-miR-30a-3p	p-mmu-miR-58
5	mmu-miR-33-5p	mmu-miR-101a-3p
6	p-mmu-miR-58	mmu-miR-148a-3p
7	mmu-miR-101a-3p	mmu-miR-296-3p
8	mmu-miR-129-1-3p	mmu-miR-298-5p
9	mmu-miR-139-5p	mmu-miR-29b-3p
10	mmu-miR-145a-5p	mmu-miR-331-3p
11	mmu-miR-148a-3p	mmu-miR-335-3p
12	mmu-miR-210-3p	mmu-miR-344g-3p
13	mmu-miR-301a-3p	mmu-miR-345-5p
14	mmu-miR-322-5p	mmu-miR-351-5p
15	mmu-miR-335-5p	mmu-miR-431-5p
16	mmu-miR-380-3p	mmu-miR-497a-5p
17	mmu-miR-381-3p	mmu-miR-672-5p
18	mmu-miR-431-5p	mmu-miR-674-5p
19	mmu-miR-433-3p	mmu-miR-744-3p
20	mmu-miR-448-3p	mmu-miR-1298-5p
21	mmu-miR-485-3p	mmu-miR-3068-3p
22	mmu-miR-543-3p	mmu-miR-5121
23	mmu-miR-674-5p	mmu-miR-5099
24	mmu-miR-5121	-

Table 53: Classification of selected isomiRs identified as Ago2-L192P-associated. The RNA sequencing data of miRAP IP samples from Ago2-WT and Ago2-L192P were analyzed using the miRMaster tool to identify Ago2-loaded isomiRs. 37 isomiRs were bound exclusively to the L192P variant. The 20 isomiRs with highest count values were classified as different types of isomiRs. Nucleotide exchanges (nuc.ex) are indicated as position: original base -> isomiR base. The four isomiRs originating from the same strand of the same pre-miR-409 are colored blue. The two isomiRs generated from the 5p strand of miR-672 are indicated in orange.

No.	3'-extended	3'-extended nuc.ex	3'-trimmed	3'-trimmed nuc.ex	Polymorph	5'-extended + 3'-trimmed nuc.ex
1	miR-409-3p 2T	let-7a-5p -2T 22:T->A	miR-125a-3p -5T	miR-33-5p -2T 18:G->A	miR-672-5p 22:A->T	miR-409-3p -1F -4T 17:C->A
2	-	let-7c-5p -3T 24:G->T	miR-1298-3p -3T	miR-409-3p -1T 20:C->T	-	-
3	-	miR-138-5p -3T 25:G->T	miR-1298-5p -2T	miR-409-3p -4T 17:C->A	-	-
4	-	-	miR-135a-1- 5p-4T	miR-672-5p -2T 20:T->A	-	-
5	-	-	miR-135a-2- 5p -4T	-	-	-
6	-	-	miR-148b-5p -3T	-	-	-
7	-	-	miR-335-3p -3T	-	-	-
8	-	-	miR-411-5p -3T	-	-	-
9	-	-	miR-431-5p -4T	-	-	-
10	-	-	miR-544-3p -5T	-	-	-

7.3. List of Figures

Figure 1: Domains of the Shank proteins. The domains are highly conserved among all Shank proteins, though individual domains may be missing in some transcript variants. The numbers indicate the length and position of the amino acid sequence of the respective domain of Shank3 in full length. From the N- to the C-terminus: Shank/ProSAP N-terminal (SPN) domain, the ankyrin repeats (ANK), the SRC homology 3 (SH3) domain, the PSD-95/Discs large/ZO-1 (PDZ) domain, the proline-rich region (PRR) and the sterile alpha motif (SAM). Adapted from Lilja et al. 2017 and the PhD thesis of D. Woike 2022. 6

Figure 2: Shank proteins function as scaffold of the postsynapse. Shanks localize at excitatory, glutamatergic synapses on dendritic spines. Shanks links F-actin to neurotransmitter receiving receptors at the postsynaptic membrane. Shank is either directly or indirectly connected with ionotropic and metabotropic glutamate receptors. AMPARs either interact with the PDZ domain of Shank or indirectly associate with Shank via the Shank-GKAP-PSD-95-Stargazin-AMPA complex. GKAP and PSD-95 connect Shank to NMDARs. Shank proteins are connected to cell adhesion molecule Neuroligin (NLGN) via GKAP. Neuroligin interacts with presynaptic neuroligin in the synaptic cleft. Shank binds mGluR5 indirectly via Homer. Zn²⁺-dependent self-association of the C-terminal SAM domain allows Shank proteins to multimerize. Shank facilitates regulation of F-actin via binding to actin-regulating proteins such as α -fodrin, Abi1 and cortactin. The N-terminal domains link Shank to CaMKII α and Ras/Rap1-mediated signaling. 7

Figure 3: Domains of the Argonaute proteins. The numbers indicate the length and position of the amino acid sequence of the respective domain of human Argonaute-2. Folded in a two-lobed configuration, an Argonaute protein comprises the following domains from N- to C-terminus: the N-terminal domain (N) linked by linker 1 (L1) to the PIWI/Argonaute/Zwille (PAZ) domain, connected by linker 2 (L2), which includes the α -helix-7 (α 7), the middle (MID) and the PIWI domains. Adapted from Lessel et al. 2020 10

Figure 4: Biogenesis of miRNA and RISC-mediated RNAi. RNA polymerase II (Pol II) transcribes pri-miRNA from the genome. The microprocessor complex, including DGCR8 and Drosha, generates the pre-miRNA. Nuclear export of the pre-miRNA into the cytosol is facilitated by Exportin 5 via a RanGTP-dependent pathway. Dicer processes the pre-miRNA and generates a miRNA duplex. The RISC is formed by incorporation of the guide strand into Ago2, assisted by the Hsc70/Hsp90 multichaperone machinery. The passenger strand is degraded. RISC silences translation of specific mRNA targets by binding of partially complementary sequences in the 3'UTR of the mRNA. After prolonged silencing, the mRNA is degraded. Unsilenced mRNAs can be translated into proteins by the translation machinery. Created with BioRender.com. 11

Figure 5: Knockout of *Shank1* resulted in reduced body weight in mice. The body weight of *Shank1* and *Shank3αβ* knockout mice and their WT littermates was measured. **(A)** The body weight of male and female *Shank1*-KO mice was reduced. **(B)** *Shank3αβ*-KO mice had no change in body weight compared to the controls. The body weight of each sampled mouse at 12 weeks of age is shown as mean with standard deviation of each group. Statistical significance was determined by two-tailed Student's t-test ($p \leq 0.01 = **$, $p \leq 0.001 = ***$). 36

Figure 6: *Shank1* knockout induced altered locomotion behavior in the open field test. Locomotion of *Shank1*-KO mice and the WT littermates was measured in an established open field experimental set up to assess distance travelled (A), the distance to the wall of the field (B) and the time spent in the center of the testing area (C). The mean with standard deviation of each group at each time point is shown (left panels). Female (middle panels) and male cohorts (right panels) differed in their behavior. **(A)** *Shank1*-KO mice moved less distance compared to WT. **(B)** Female *Shank1*-KO mice (KO-F) showed a smaller distance to the field wall at 20 min. **(C)** KO-F mice spent significantly less time in the center. Statistical significance was calculated with two-way ANOVA, with genotype and sex as the two factors tested, followed by Sidak's multiple comparisons tests ($p \leq 0.05 = *$, $p \leq 0.01 = **$, $p \leq 0.001 = ***$). 37

Figure 7: *Shank3αβ* knockout mice moved less during the open field test. Locomotor parameters of *Shank3αβ*-KO mice and littermate controls were quantified using an open field test. The distance travelled (A), the distance to the wall (B) and the time spent in the center (C) were determined. The mean and standard deviation of each group at each time point is shown (left panels). Female (middle panels) and male cohorts (right panels) are shown separately for each parameter. **(A)** *Shank3αβ*-KO mice moved less distance compared to WT. For males, the difference occurred after 20 min whereas females moved less distance at each time point measured. **(B)** No alterations in distance to the wall were observed. **(C)** The time spent in the center did not significantly change with *Shank3αβ* knockout. The KO-F mice displayed a tendency to spend less time in the center at 20 min. Statistical significance was calculated with two-way ANOVA followed by Sidak's tests ($p \leq 0.05 = *$, $p \leq 0.01 = **$). 38

Figure 8: *Shank*-KO mouse models displayed altered self-grooming and rearing behavior. Video footage of the open field experiment with *Shank1*-KO (left panels) and *Shank3αβ*-KO (right panels) mice was analyzed to evaluate self-grooming (A) and rearing (B). **(A)** Self-grooming was quantified as time spent for self-grooming during the first 5 min (0-5) and the last 5 min (15-20) of the open field test. Both mouse models showed a tendency towards increased duration of self-grooming during the second measuring period. **(B)** *Shank*-KO mice exhibited decreased rearing behavior, measured as frequency of rearing events. Male and female mice of both lines were affected to the same degree. Mean with standard deviation of each group is shown with statistical significance determined between WT and KO of male and female mice by two-way ANOVAs followed by Sidak's tests ($p \leq 0.01 = **$). 39

Figure 9: Validation of an autistic phenotype in the novel *Lypd1*-bacTRAP-*Shank1*-KO and *Lypd1*-bacTRAP-*Shank3αβ* -KO mouse lines. Separate groups of mice were tested at 12 weeks of age in an open field test. Distance moved (A), distance to the wall (B), time in center (C), self-grooming (D) and rearing behavior (E) were analyzed. Shown is the mean with standard deviation. Two-tailed Student's t-tests revealed significant differences in several parameters tested. **(A)** In both mouse models, knockout mice moved less distance. **(B)** *Shank3αβ* knockout resulted in reduced distance to the field wall. **(C)** *Shank3αβ*-KO mice spent less time in the center of the area. **(D)** Assessment of self-grooming behavior demonstrated a trend toward increased self-grooming in the *Shank3αβ*-KO mice. **(E)** Knockout mice of both lines exhibited a tendency to reduced rearing behavior ($p \leq 0.05 = *$). 41

Figure 10: The qPCR detected enrichment of GFP and neuron-specific transcripts in bacTRAP IP samples. **(A)** IC and IP bacTRAP samples were analyzed for the relative abundance of cell type-specific transcripts. *Cnp*, *Dsp* and *Gfap* were analyzed as markers for oligodendrocytes, astrocytes, and neurons respectively. GFP-encoding transcripts were analyzed to verify the expression and precipitation of the GFP-tagged ribosomal protein L10a. A region of the *Lypd1* promoter was detected. *Tbp* was used as a ubiquitously expressed control. **(B)** The relative enrichment was calculated as transcript abundance in IP normalized to IC. GFP and *Dsp* showed higher relative enrichment compared to the *Tbp* control, while the abundance of the remaining transcripts was reduced. Tissue from three mice was combined and reverse transcriptase qPCR performed in technical triplicates. Shown is the mean of technical replicates. As no biological replicates were measured, no standard deviation was calculated. 42

Figure 11: Analysis of similarity based on RNA sequencing. BacTRAP samples were prepared from *Lypd1*-bacTRAPx*Shank3αβ*-KO mice and WT littermates. RNA purified from ICs and IPs was sequenced. The PCA illustrates the similarities between five biological replicates ($n = 5$). IC and IP samples formed separate subpopulation. 43

Figure 12: Differentially translated mRNAs in hippocampal neurons of *Shank3αβ*-KO mice. Differential gene expression analysis was performed using DEseq2. Significance was defined by p-value ≤ 0.1 and a fold change of > 0.5 , plotted as $-\log_{10}$ and \log_2 transformed values. Significantly less translated mRNAs are shown in blue and more translated mRNAs are shown in red. The mRNAs of both categories are highlighted by their gene symbols. 26 mRNAs were differentially translated under loss of *Shank3αβ* of which nine were less and 17 were more translated compared to the WT control. A detailed list of all deregulated mRNAs is shown in Table 49. 44

Figure 13: Expression and translation of selected mRNAs from hippocampal neurons of *Shank3αβ*-KO mice. Expression values, determined with RNA-seq, of a subset of mRNAs in IC and IP samples generated with the bacTRAP method. Expression (IC) and active translation (IP) of transcripts were compared between *Shank3αβ*-KO mice and WT littermates. The mean with standard deviation of five biological replicates is shown (n = 5). Gm accession numbers annotate transcripts, for which it is unknown whether they encode functional proteins.45

Figure 14: GO analysis of biological processes altered by differentially translated mRNAs in hippocampal neurons of *Shank3αβ*-KO mice. Statistical significance of altered translation was appointed by a p-value ≤ 0.1 and a fold change of > 0.5 . All differentially translated mRNAs found in the KO-IP to WT-IP comparison were submitted to a GO analysis for biological processes. The normalized enrichment scores (NES) of the 20 most enriched (red) and decreased (blue) terms are shown.46

Figure 15: Validation of PSD purification from hippocampal tissue of two ASD mouse models. PSD fractions were prepared from hippocampi of *Shank1*-KO (E), *Shank3αβ*-KO (I) mice, and WT littermates. (A) Samples of the postnuclear fraction (P1), the membrane fraction (P2) and the PSD fraction (P3) were prepared. Shank, PSD-95 and tubulin were detected via immunoblot (A, E and I). Band intensities were quantified (B-D, F-H, J-L). The postsynaptic marker PSD-95 and Shank proteins were enriched from P1 to P3 fractions (C-D, G-H, K-L), whereas tubulin decreased during PSD purification (B, F, J). A reduction of band intensities was detected by the Shank PDZ domain antibody, indicating specific reduction of Shank proteins. The mean with standard deviation was calculated and statistical significance determined by one-way ANOVA followed by Tukey's test ($p \leq 0.05 = *$, $p \leq 0.01 = **$, $p \leq 0.0001 = ****$). Tissues of five mice were pooled for one biological replicate (n = 5).47

Figure 16: Relative protein abundances of Shank1, Shank3 and CaMKII in postsynaptic density fractions of two ASD mouse models. Postsynaptic density purification was performed using hippocampal tissue from *Shank1*-KO and *Shank3αβ*-KO mice. WT and HZ littermates were used as controls. Two KO samples had to be excluded from the analyses due to low protein concentration, resulting in four biological repeats for both KO conditions. The relative abundance of Shank1 (blue), Shank3 (green) and CaMKII (orange) was compared to all quantified proteins (grey lines) in PSDs of the two mouse models. (A) *Shank1*-KO resulted in a complete loss of Shank1 protein in the PSD of KO mice without affecting the relative abundances Shank3 and CaMKII. HZ and WT mice showed no significant reduction of Shank1 protein. (B) *Shank3αβ*-KO induced a modest reduction of Shank3 protein only in the KO mice, but not in WT and HZ mice. Shank1 and CaMKII protein levels were unchanged across conditions.48

Figure 17: Analysis of peptides derived from different Shank3 domains. PSD fractions from forebrains of three *Shank3αβ*-KO and six WT littermates were purified and analyzed by mass spectrometry. (A) Four peptides scattered across the domains of Shank3 were quantified separately to gain insight into the expression of Shank3 isoforms. The first peptide analyzed originated from the SPN domain (aa 26-36, green) and the second from the SH3 domain (aa 433-460, yellow). The third and fourth peptides were assigned to the proline-rich region (aa 1165-1174 and aa 1535-1540, grey). (B) Quantification of domain-specific peptides demonstrated the absence of peptides from the SPN and SH3 domains in the KO condition, while relative abundance of peptides from the proline-rich region was reduced to 10-20% compared with WT controls.49

Figure 18: Analysis of the similarity of PSD fractions based on mass spectrometry. Linear PCA determined similarity of postsynaptic protein composition in PSD samples purified from *Shank1*-KO and *Shank3αβ*-KO mice compared to HZ and WT littermates. WT-PSDs clustered together. (A) Abundance of 56 proteins was significantly altered among PSD fractions of *Shank1*-KO, HZ and WT mice (ANOVA, $p \leq 0.05$). KO and HZ samples partially overlapped. HZ-PSDs scattered more compared to KO-PSDs. (B) In the PSD of the *Shank3αβ* line, 116 proteins were significantly deregulated between KO, HZ and WT conditions (ANOVA, $p \leq 0.05$). All three conditions formed separated subpopulations with most variability in the KO-PSDs.50

Figure 19: Differentially abundant proteins in PSD fractions of *Shank1*-KO and *Shank3αβ*-KO mice. Volcano plot visualization of two-sided, pairwise Student's t-test results, comparing KO-PSD to WT. Proteins identified with a p-value ≤ 0.05 and a FC > 1.5 were considered significantly changed. Strongly altered proteins are highlighted by their gene symbol. (A) Comparison of the PSD proteome of the *Shank1* mouse model determined 46 deregulated proteins of which 18 were decreased and 28 increased in abundance. (B) 67 deregulated proteins were quantified in the *Shank3* proteome analysis. 28 proteins were decreased and 39 enriched in KO-PSDs compared to WT.51

Figure 20: Gene ontology analysis of biological processes influenced by the altered proteome in the PSD of *Shank1*-KO mice. The entirety of significantly changed proteins (FC > 1.5 , $p \leq 0.05$) was used for GO analysis. The combined score was visualized for the 20 most enriched (red) and decreased (blue) BPs. Strongest enrichment was determined for the negative regulation of tubulin acetylation and regulation of tubulin deacetylation. The most decreased term was associative learning.52

Figure 21: GO analysis of BPs affected by altered protein composition of the PSD of *Shank3αβ*-KO mice. All significantly altered proteins (FC > 1.5 , $p \leq 0.05$) were submitted to GO analysis. The combined score was visualized for the 20 most enriched (red) and decreased (blue) BPs. The most enriched BP that was specific for the *Shank3* analysis was N-acylethanolamine metabolic process. Strongest depletion was determined for the positive regulation of AMPA receptor activity.53

Figure 22: Analysis of the interaction of the CaMKII α with Shank proteins. (A) HEK292T cells were transfected with constructs encoding N-terminal fragments of the Shank proteins, comprising the SPN and ANK domains. RFP-tagged N-termini of Shank1, Shank2 and Shank3 were coexpressed with T7-CaMKII α . RFP alone was expressed as control. Coimmunoprecipitation was performed using RFP-trap and analyzed by western blot. Proteins were detected with antibodies recognizing the RFP or T7 tags. Uniform expression was confirmed in the whole cell lysates (Input). An efficient and specific binding of Shank3 and weak interaction of Shank1 to CaMKII α was determined. Shank2 did not interact with CaMKII α . (B) Quantitative analysis of the data shown in A. The ratios of T7 to mRFP IP signals are shown as mean with standard deviation. Statistical analysis: one-way ANOVA followed by Tukey's test ($p \leq 0.001 = ***$, $n = 3$).....54

Figure 23: Loss of Shank1 and Shank3 resulted in enrichment of activated CaMKII α in PSD fractions. (A) PSD fractions were prepared from cortices and hippocampi of *Shank1*-KO and *Shank3 $\alpha\beta$* -KO mice and WT littermates to compare the activation status of CaMKII α in western blot analyses. Shank, PSD-95, tubulin, CaMKII α and phosphorylated CaMKII α (phospho-CaMKII α) were detected. (B) The abundance of active phospho-CaMKII α was quantified and normalized to the total CaMKII α amount. An increased activation of CaMKII α was detected upon loss of Shank. This change was more pronounced for Shank3 compared to Shank1 and stronger in the cortex compared to hippocampus. The mean with standard deviation was calculated and statistical significance determined by two-way ANOVA followed by Sidak's test ($p \leq 0.05 = *$, $p \leq 0.01 = **$). Tissues of five mice were pooled for one biological replicate ($n = 3$).....55

Figure 24: Verification of AAV-induced expression of GFP, GFP-Ago2-WT and GFP-Ago2-L192P in miRAP IC and IP prepared from primary neurons. Primary cultures of murine cortical neurons were transduced with AAVs at 1 DIV to express the GFP-tagged Ago2 variants WT and L192P, or GFP. At 12 DIV, cells were subjected to miRAP and lysate (IC) and IP of 1 million neurons per sample were subjected to western blot analysis. Expressed proteins were detected with antibodies that recognise Ago2 or the GFP-tag.....56

Figure 25: Analysis of the intracellular localization of virally expressed GFP and GFP-tagged Ago2-WT and Ago-L192P variants in cortical neurons. Cortical neurons from mice embryos (E18) were isolated, cultured and infected with AAVs to induce the expression of GFP-tagged Ago2 variants WT and L192P (green). GFP was used as control condition. At 12 DIV, cells were fixed and stained for MAP2 (A405, blue) as a dendritic marker as well as Dcp1a (A633, magenta) to visualise p-bodies. Ago2 was diffusely localized in the cytosol and enriched in Dcp1a-positive clusters in the cell soma and dendrites. Scale bar = 20 μm . 57

Figure 26: Analysis of primary dendrites and intracellular localization of GFP-Ago2-WT and GFP-Ago-L192P in AAV-infected neurons. (A) Sections of distal dendrites of AAV-infected neurons (E18) as shown in Fig. 2 (scale bar = 5 μm). (B-D) Quantification of Ago2 clusters along dendrites (B) as well as in the cell body (C) and evaluation of the quantity of primary dendrites (D). In each repeat, five neurons were analyzed with three sections of distal dendrites per neuron. The arithmetic mean per replicate is shown with standard deviation. A two-tailed Student's t-test was calculated and revealed a statistically significant increase with $p \leq 0.031 (*)$ in the abundance of dendritic p-bodies when the Ago2 variant L192P was expressed.58

Figure 27: miRNA concentrations in IC and IP samples prepared via miRAP. Primary murine neurons were infected with AAVs at 1 DIV to induce expression of GFP-tagged Ago2 variants WT and L192P or GFP control. ICs were collected from neuron lysate and IPs were obtained by immunoprecipitation with an anti-GFP matrix via miRAP. The concentration of miRNA was determined using the Qubit microRNA Assay Kit (Thermo Fisher Scientific, Waltham, USA). The concentration in ng/ μl is shown as arithmetic mean with standard deviation on a common logarithmic scale.....59

Figure 28: Abundance of miR-21 and miR-124 in IC and IP of the miRAP assay and relative enrichment of miR-124 in Ago2-WT condition. miRAP samples from cortical neurons expressing GFP, GFP-Ago2-WT or L192P were analyzed by qPCR using TaqMan probes. (A-C) Amplification of miR-21 (dotted lines) and miR-124 (continuous lines) in IC (lighter color) and IP (darker color) measured in GFP control (A), Ago2-WT (B) and Ago2-L192P (C). (D) The relative enrichment was calculated and normalized to the IC. A two-way ANOVA with Sidak's test determined a significant increase for the relative enrichment of miR-124 in the Ago2-WT condition compared to GFP control ($p \leq 0.01 = **$, $n = 5$).....60

Figure 29: Analysis of similarity based on miRNA sequencing. Two ICs and one IP of the L192P mutant were excluded due to insufficient miRNA integrity. (A) PCA for illustration of similarities between miRAP IPs and ICs replicates from Ago2-WT and the Ago2-L192P expressing cortical neurons. (B) Dendrogram to depict clustering based on the RNA sequencing data between replicates and conditions.....61

Figure 30: Differentially expressed or RISC-loaded miRNAs. Significant differences in expression of miRNAs or association with the RISC were determined using DEseq2. Significance was reached with an adjusted p-value of $p \leq 0.05$ plotted as $-\log_{10}$ and a \log_2 fold change > 1 . Decreased miRNAs are shown as blue dots and enriched miRNAs are depicted in red. (A) Comparison of L192P-IC vs. WT-IC showed 24 differentially expressed miRNAs. 14 miRNAs were expressed less with Ago2-L192P and 10 miRNAs were more abundant compared to the Ago2-WT condition. (B) 23 miRNAs were differentially associated with Ago2 in the L192P-IP vs. WT-IP comparison. 14 miRNAs were reduced in the L192P RISC whereas nine miRNAs were more strongly associated with the RISC of Ago2-L192P. A detailed list of all deregulated miRNAs is shown in Table 52.62

Figure 31: WT miR* category of seven miRNAs exhibiting higher expression of miR* and stronger association of miR* to the RISC with Ago2-WT. The normalized RNA-seq count data obtained from miRAP samples was used to calculate 3p to 5p strand ratios (3p/5p). 3p/5p are shown as arithmetic mean with standard deviation. All miRNAs with a statistically significant difference as $p \leq 0.05$ of 3p/5p in the Ago2-WT-IP compared to the Ago2-L192P-IP were selected and grouped into categories dependent on the 3p/5p pattern across the different samples and conditions. The passenger strand miR* of the miRNAs miR-124, miR-300, miR-342, miR-376a, miR-337, miR-381 and miR-3068 was more abundant in the WT-IC and in the WT-IP. 63

Figure 32: The L192P miR* group consists of seven miRNAs with higher abundance and RISC-association of miR* when the L192P variant was expressed. 3p/5p ratios were calculated with normalized count values. 3p/5p are shown as mean with standard deviation. The miRNAs with a significant difference ($p \leq 0.05$) of 3p/5p between the IPs were categorized dependent on the 3p/5p pattern. The miR* of miR-9, miR-15a, miR-33, miR-101a, miR-125a, miR-335 and miR-337 was expressed more (IC) and more associated more with the L192P-RISC (IP). 63

Figure 33: 3p/5p of miRNAs to detect miR and miR* strands enriched in the RISC of Ago2-WT. Using normalized count values from RNA-seq data obtained from miRAP samples, 3p/5p was calculated. Five miRNAs showed significant ($p \leq 0.05$) differences in the WT-IP compared to the L192P-IP without comparable changes in the respective ICs. 3p/5p are shown as mean with standard deviation. **(A)** Grouped into the WT-IP miR category, the miR strand of miR-331 and miR-448 was increased in WT-RISC compared to L192P-RISC, measured as 3p/5p in IP samples. **(B)** The WT-IP miR* group consists of three miRNAs, of which the two miRNAs miR-330 and miR-431 showed enrichment of the miR* in Ago2-WT-IP without higher abundance in the three remaining conditions. For let-7e, the miR* strand was more frequently detected in the WT-IP as well as in the L192P-IC. 64

Figure 34: 3p/5p ratios determined three miR and miR* strands enriched in the L192P-RISC compared to Ago2-WT. 3p/5p were calculated using normalized count values from miRAP RNA-seq data and plotted as arithmetic mean with standard deviation. The miRNAs with statistically significant differences between Ago2-WT-IP and Ago2-L192P-IP were categorized dependent on the 3p/5p pattern. The miR or miR* strand of six miRNAs was enriched in the L192P-IP, without being differentially expressed (L192P-IC vs. WT-IC). **(A)** The three miRNAs miR-127, miR-543 and miR-672 showed higher abundance of the miR strand in the L192P-IP. **(B)** The miR* of the three miRNAs miR-149, miR-340 and miR-744 was more strongly associated with the L192P-RISC compared to the RISC containing Ago2-WT. 65

Figure 35. Analysis of 3p/5p ratios revealed distinct effects of Ago2 variants on miRNA strand expression and arm switching. 3p/5p ratios were calculated using normalized count values from RNA sequencing data obtained from miRAP samples. The miRNAs with statistically significant differences between Ago2-WT-IP and Ago2-L192P-IP were classified into six categories dependent on expression level in IC and association to the RISC, shown in IPs. **(A)** The quantity of miRNAs in each of the six categories. **(B)** The proportion of all categories in respect to a total of 28 3p/5p ratios of miRNAs analyzed. 66

Figure 36: Increased association of isomiRs with the Ago2 variant L192P. The RNA sequencing data gathered from miRAP IPs was analyzed using the miRMaster tool to identify Ago2-loaded isomiRs. **(A)** An overview of nomenclature for isomiRs adapted from Fehlmann et al. 2017. Although uracil is used on RNA level, in the isomiR nomenclature from Fehlmann et al. a T (thymine) is used. **(B)** Out of 37 isomiRs which were bound exclusively to Ago2-L192P, the 20 isomiRs with highest average count values were selected and the count value of each replicate plotted against the respective isomiR. The mean with the coefficient of variation is shown. An ordinary two-way ANOVA followed by Sidak's multiple comparisons test determined the four isomiRs miR-335-3p -3T ($p \leq 0.0009$), miR-409-3p -4T 17:C->A ($p \leq 0.0321$), miR-409 2T ($p \leq 0.0049$) and miR-672-5p 22:A->T ($p \leq 0.0006$) as significantly enriched in the L192P-IP compared to WT-IP ($p \leq 0.05 = *$, $p \leq 0.01 = **$, $p \leq 0.001 = ***$) **(C)** The amount if isomiRs classified in each category. 10 isomiRs were 3'-trimmed with nucleotide exchange (nuc.ex) and 4 without nuc.ex. Three isomiRs had a 3'-extended end. One isomiR each belonged to the categories 5'-extended + 3'-trimmed nuc.ex, polymorph, and 3'-extended + nuc.ex. **(D)** The proportion of all isomiR categories in respect to a total of 20. 50% of the isomiRs were 3'-trimmed with nuc.ex. The remaining 50% included the other five categories in varying percentages. 67

Figure 37: Gene ontology analysis of biological processes for predicted targets of (A) miR-296-3p and (B) miR-1298-5p. The entirety of miRDB-predicted targets was used for GO analysis with PANTHER. The fold enrichment was plotted against the GO terms. Statistical significance is illustrated by false discovery rate (FDR) with $FDR \leq 0.05 = *$, $FDR \leq 0.01 = **$ and $FDR \leq 0.0001 = ***$. Two miRNAs from the L192P-IP vs. WT-IP comparison were selected. **(A)** miR-296-3p was reduced in the L192P-RISC. Predicted targets showed enrichment in 14 GO terms. **(B)** miR-1298-5p was increased in the L192P-RISC. Predicted targets showed enrichment in 20 GO terms. 69

Figure 38: The 3p and 5p profiles of miR-543 illustrated strand selectivity of the Ago2 variants. Count values were taken from RNA-seq data obtained from the miRAP assay. Normalized expression values of miR-543-3p and miR-543-5p were plotted for the strand separately. The miR-543-3p showed 10- to 30-fold higher abundance across conditions compared to the 5p strand. 3p was strongly enriched in L192P-IP compared to WT-IP, while 5p displayed a slightly reversed distribution of strands. 70

Figure 39: GO analyses of BPs for predicted targets of (A) miR-543-5p compared to (B) miR-543-3p. All miRDB-predicted targets were submitted to BP GO analyses using PANTHER. Fold enrichment for each GO term is shown with $FDR \leq 0.05 = *$, $FDR \leq 0.01 = **$, $FDR \leq 0.001 = ***$ and $FDR \leq 0.0001 = ****$. 20 BP GO terms were enriched in both analyses. **(A)** miR-543-5p shown in blue exhibited less Ago2-binding so BPs were expected to be enhanced with Ago2-L192P compared to WT. **(B)** miR-543-3p was enriched in L192P-RISC, suggesting that the predicted targets contributing to the BPs were likely to be less silenced. 71

Figure 40: Clustered GO analysis of BPs influenced by differentially expressed mRNAs in *Shank3aβ*-KO hippocampal neurons. The contribution of differentially translated transcripts from the KO-IP vs. WT-IP comparison was assessed. The enriched (red) and decreased (blue) biological processes are shown as nodes. The node size illustrates the number of deregulated mRNAs contributing to the deregulated term. Lines connecting nodes indicate a functional relation of biological processes. 78

Figure 41: Hierarchical clustered GO analysis of affected molecular functions in the postsynaptic proteome of *Shank1*-KO mice. Deregulated terms are shown as nodes. The size of a node corresponds to the number of deregulated proteins that contributed to that term. Enriched molecular functions are shown in a red gradient and decreased molecular functions in a blue gradient. The intensity of the node color indicates the significance of the respective term, which was determined by an adjusted p-value. Functional dependencies between terms are represented as connecting lines. 82

Figure 42: Hierarchical clustered GO analysis of affected molecular functions in the postsynaptic proteome of *Shank3aβ*-KO mice. Deregulated terms are shown as nodes. The size of a node corresponds to the number of deregulated proteins that contributed to that term. Enriched molecular functions are shown in a red gradient and decreased molecular functions in a blue gradient. The intensity of the node color indicates the significance of the respective term, which was determined by an adjusted p-value. Functional dependencies between terms are represented as connecting lines. 83

Figure 43: L192P-RISC induces alterations in the miRNome and deregulation of Ago2-mediated RNAi. The miRAP method followed by RNA-seq determined alterations in the miRNome and the RISC-bound miRNAs in AAV-infected primary cortical neurons expressing Ago2-L192P. Four different aspects were affected: (1) 24 miRNAs were differentially expressed, measured in the L192P-IC vs- WT-IC comparison, of which 14 were more (red) and 10 less (blue) expressed. (2) 23 miRNA were differentially bound in the L192P-RISC, of which nine were enriched and 13 decreased, determined by the L192P-IP vs. WT-IC comparison. (3) Arm switching events occurred for 33 miRNAs, analyzed by 3p/5p ratios. (4) The analysis of isomiRs determined 37 isomiRs which were exclusively bound to Ago2-L192P, whereas no isomiRs were exclusively bound to Ago2-WT. Created with BioRender.com. 87

Figure 44: Location of the leucine 192 residue in Ago2. The tertiary structure of Ago2 was depicted using the crystal structure of human Argonaute-2 bound to a defined guide RNA (NDB: 4W5N, Schirle et al. 2014). The Ago2 domains and L192 (red) were visualized in UCSF ChimeraX (Pettersen et al. 2021, Huang et al. 2018). The RNA binding groove in between the PAZ and PIWI domain was indicated. 90

Figure 45: Ago2-L192P favored 5'-uracil but was less selective towards 5'-terminal purines. (A) The sequences of the differentially bound miRNAs found in the L192P-IP vs. WT-IP comparison and in the 3p/5p analysis were analyzed. **(B)** The identity of the 5'-nucleotide was determined and the ratio of uracil in respect to all 5'-nucleotides calculated. The proportion of purines among the four 5'-terminal nucleotides was calculated. 92

Figure 46: Ago2-L192P induces deregulation of specific miRNAs encoded by the miR379-409 cluster. The genomic miR379-409 cluster is located on chromosome 14 in humans (12 in mice) and encodes 38 miRNAs. The transcription factor Mef2 is activated by neuronal activity and enhances expression of the cluster. Three miRNAs, miR-380-3p, miR-409-3p, and miR-381-3p were differentially expressed and function in regulation dendritogenesis. Three miRNAs exhibited arm switching events: miR-300-3p, miR-543-3p and miR-376a-3p. The main target of miR-543-3p is encoding for N-cadherin, involved in neuronal migration. miR-376a-3p silences translation of the transcription factor Hes5, which induces neuronal differentiation. Four exclusively Ago2-L192P-bound isomiRs corresponded to miR-409-3p and one to miR-544-3p. Differential binding of isomiRs might alter fine-tuning of RNAi. Created with BioRender.com. 96

7.4. List of Tables

Table 1: Overview of Omics Approaches.....	12
Table 2: Laboratory mice.....	14
Table 3: Suppliers of bacterial strains and cell lines.....	14
Table 4: Primary antibodies used in western blot analyses.....	14

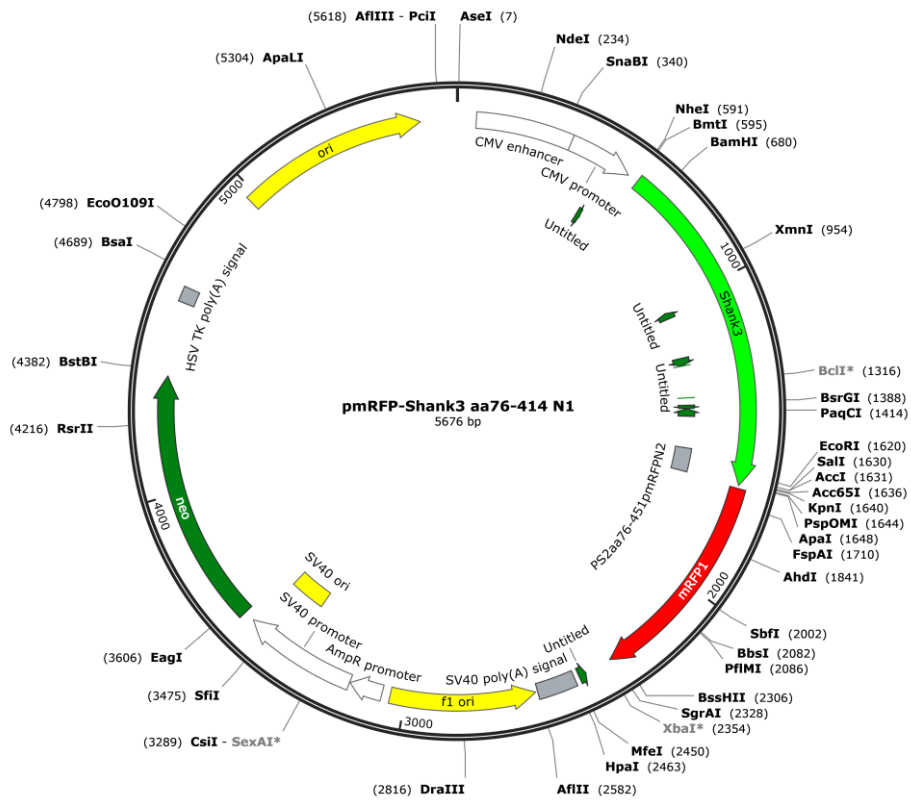
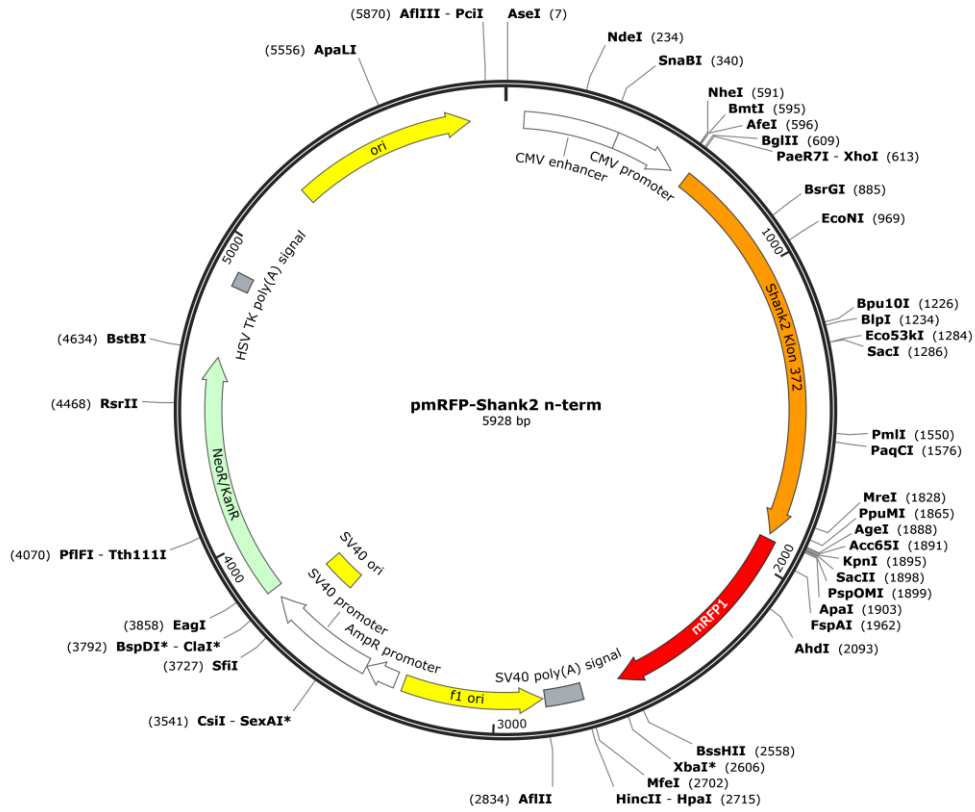
Table 5: Primary antibodies used for immunocytochemistry.....	15
Table 6: HRP-coupled secondary antibodies used in western blot analyses.	15
Table 7: Secondary antibodies used in ICC experiments.	15
Table 8: Primers used for genotyping.	15
Table 9: Oligonucleotides for sequencing of plasmids coding for GFP-tagged Ago2.....	15
Table 10: Oligonucleotides used for cloning.....	16
Table 11: Primers for mutagenesis.....	16
Table 12: Plasmids from the stock of the Kreienkamp research group.	16
Table 13: Purchased or generated plasmids.....	16
Table 14: Commercial kits used.....	16
Table 15: Buffers, solutions, and supplements.....	17
Table 16: Culture media for bacteria, HEK293T cells and primary neurons.	19
Table 17: Antibiotics used for bacteria and cell culture.	19
Table 18: Software and tools.....	19
Table 19: PCR reaction for site directed mutagenesis.....	21
Table 20: Thermal cycler program for site-directed mutagenesis.	22
Table 21: Reaction mixture of a sequencing PCR.....	22
Table 22: Thermal cycler program for sequencing.	22
Table 23: Reaction mixture for 3'-poly(A) tailing of miRNA.	26
Table 24: Thermal cycler program for 3'-poly(A) tailing.....	26
Table 25: Components of a 5'-ligation reaction following 3'-poly(A) tailing.	26
Table 26: Reverse transcription reaction of polyadenylated miRNA ligation products.....	26
Table 27: Thermal cycler program for reverse transcription of polyadenylated miRNA.	26
Table 28: Components for miRNA-originated cDNA amplification.	27
Table 29: Thermal cycler program for amplification of miRNA-originated cDNA.....	27
Table 30: The qPCR reaction for miRAP quality control.....	27
Table 31: Chosen Advanced miRNA Assays for marker miRNAs in miRAP quality control.	27
Table 32: Thermal cycler settings for qPCR for miRAP quality control.....	27
Table 33: PCR reaction for genotyping of Shank1-KO mice.....	28
Table 34: PCR reaction for genotyping of Shank3 $\alpha\beta$ -KO mice.	29

Table 35: Thermal cycler temperature program for Shank1 or Shank3 genotyping via PCR.....	29
Table 36: Components of the PCR reaction for verification of the Lypd1-bacTRAP transgene.....	29
Table 37: PCR program for genotyping of Lypd1-bacTRAP transgene.....	30
Table 38: Expected PCR product band sizes in genotyping.....	30
Table 39: Components for a reverse transcription reaction.....	32
Table 40: Temperature program for cDNA synthesis.....	32
Table 41: Chosen marker genes for TaqMan Gene Expression Assays.....	32
Table 42: The qPCR reaction with TaqMan Gene Expression Assays.....	32
Table 43: Thermal cycler program used for qPCR.....	33
Table 44: Top five predicted target transcripts of deregulated miRNAs from the L192P-IP vs. WT-IP comparison. The mRNA targets of miR-296-3p (colored blue, reduced in L192P-IP) and miR-1298-5p (colored red, enriched in L192P-IP) were predicted using miRTarget implemented in miRDB. Target ranks and target scores as measure of prediction validity. The official gene symbol and gene description of predicted targets have been included. Expression values in transcripts per million (TPM) were extracted from the GTEx portal. Target transcripts with ≤ 1 TPM were excluded and replaced by the next target dependent on target rank and score.	68
Table 45: The five highest ranked predicted targets of 3p and 5p strand of miR-543. Targets were predicted with miRDB, cortical expression validated with GTEx (TPM ≥ 1) and gene symbols sorted by target rank and score. (A) Target transcripts of miR-543-5p (blue) that was slightly less associated with Ago2-L192P than to Ago2-WT. (B) Predicted mRNA targets of miR-543-3p (red). This strand showed strong enrichment in L192P-IP compared to WT-IP.....	70
Table 46: Comparison of the top five predicted targets between the canonical miR-335-3p and the isomiR-335-3p -3T. The targets that were predicted using miRDB were sorted by target score and allocated target ranks. Expression in the cortex was validated as TPM ≥ 1 using the GTEx portal. The 3'-trimmed isomiR-335-3p -3T (red) was enriched in Ago2-L192P-IP and absent in Ago2-WT-IP. The gene symbols of shared targets between canonical miRNA and isomiR are indicated by blue color.....	72
Table 47: Comparison of the five highest ranked target transcripts between miR-672-5p and the isomiR miR-672-5p 22:A->T. miRDB-predicted targets were ranked by target score and cortical expression (TPM ≥ 1) was confirmed via the GTEx portal. The isomiR miR-672-5p 22:A->T (red), was enriched in the IP of Ago2-L192P and absent in the Ago2-WT-IP.....	72
Table 48: Hazardous Substances. List of all hazardous substances used according to GHS (hazard pictograms, H and P statements). GHS, H and P statements taken from GESTIS substance database of the IFA, retrieved on the 4 th of June 2023. Ordered by appearance in the materials section.	134
Table 49: Differentially translated mRNAs in hippocampal neurons of Shank3$\alpha\beta$-KO mice. RNA was purified from samples prepared with the bacTRAP method. DEG analysis was performed to determine differentially translated transcripts. Significance was appointed by adjusted p-value ≤ 0.1 and a FC of > 0.5 . A \log_2 transformation was calculated for the FC values. 26 mRNAs were deregulated of which nine were less translated and 17 exhibited enhanced translation.....	135
Table 50: Deregulated proteins in the PSD of Shank1-KO mice determined by a mass spectrometry-based proteomics approach. Postsynaptic proteins that were decreased or enriched in KO-PSDs compared to WT-PSDs. Student's t-testing determined statistical significance and a p-value cutoff of $p \leq 0.05$ was applied. A \log_2 transformation was performed and a fold change (FC) cutoff of > 0.58 and < -0.58 applied, to include candidates which were at least 1.5 times higher or less abundant in KO compared to WT. 46 proteins were found to be deregulated, 18 of which showed decreased and 28 increased abundances in KO-PSDs. Proteins found to be deregulated in the analyses of both mouse lines are colored blue.	136

Table 51: Deregulated proteins in the PSD of *Shank3αβ*-KO mice determined by proteomics. Postsynaptic proteins decreased or enriched in KO-PSDs compared to WT-PSDs. Student's t-testing determined statistical significance with p-value cutoff of $p \leq 0.05$. A \log_2 transformation was performed and an 1.5 FC cutoff applied. 67 deregulated proteins were quantified. The abundance of 28 proteins was decreased and 39 were increased in KO-PSDs. Proteins found to be deregulated PSD fractions of both mouse lines are colored blue137

Table 52: Differentially expressed and RISC-bound miRNAs analyzed in the miRAP assay. Comparisons of miRNAs in input controls (IC) and immunoprecipitates (IP) of the miRAP assay obtained from AAV-infected primary murine neuron cultures. The species *mus musculus* (mmu), the identity of miRNA (miR) and the strand (3p or 5p) are listed. The miRNAs found in both comparisons are colored blue.139

Table 53: Classification of selected isomiRs identified as Ago2-L192P-associated. The RNA sequencing data of miRAP IP samples from Ago2-WT and Ago2-L192P were analyzed using the miRMaster tool to identify Ago2-loaded isomiRs. 37 isomiRs were bound exclusively to the L192P variant. The 20 isomiRs with highest count values were classified as different types of isomiRs. Nucleotide exchanges (nux.ex) are indicated as position: original base -> isomiR base. The four isomiRs originating from the same strand of the same pre-miR-409 are colored blue. The two isomiRs generated from the 5p strand of miR-672 are indicated in orange.....140



8. Curriculum Vitae

Der Lebenslauf wurde aufgrund von datenschutzrechtlichen Gründen auf den beruflichen Werdegang verkürzt.

Debora Tibbe

EDUCATION

- 06.2020 – 09.2023 Doctor rerum naturalium in Chemistry
Hamburg University, Institute for Human Genetics at the UKE, Hamburg.
Thesis: Omics Approaches for the Analysis of Shank1/3-associated Autism Spectrum Disorders and the Lessel-Kreienkamp syndrome
- 10.2017 – 10.2019 M. Sc. in Cellular Biochemistry
Bielefeld University, Final grade: 1.3
Thesis: Analysis of mutations in the CaM kinase domain of the calcium/calmodulin-dependent serine protein kinase CASK. Grade: 1.0
- 10.2014 – 09.2017 B. Sc. in Biochemistry
Bielefeld University, Final grade: 2.7
Thesis: Effect of hypoxia on the intracellular localization of NDRG3. Grade: 1.0

LABORATORY EXPERIENCE

- 03.2020 – 05.2020 Research assistant in the Institute for Human Genetics at the UKE, Hamburg.
Project: Functional analyses of Shank-associated synaptopathies caused by patient missense variants affecting the N-terminal domains of SHANK3 or in key domains of SHANK2.
- 10.2019 – 02.2020 Research assistant in the Institute for Human Genetics at the UKE, Hamburg.
Project: Establishment of assays for the analysis of the kinase activity of the calcium/calmodulin-dependent serine protein kinase CASK
Methods: FACS, split-YFP assay, ³²P-ATP kinase assay
- 04.2019 – 10.2019 Master's student in the Institute for Human Genetics at the UKE, Hamburg.
Project: Functional analysis of mutations in the CaM kinase domain of CASK
Methods: Immunocytochemistry, confocal fluorescence microscopy, preparation of primary cultures of embryonic rat hippocampal neurons, cell culture with primary cells and cell lines (HEK293-T), transient transfection, GST-fusion protein purification, SDS-PAGE, western blotting, site-directed mutagenesis
- 01.2019 – 03.2019 Research intern in the Institute for Human Genetics at the UKE, Hamburg.
Project: Analysis of transcript variants of CASK and interaction studies
Methods: Sanger sequencing, co-immunoprecipitation, dual luciferase assay

- 11.2018 – 01.2019 Research intern in Biochemistry Department III at Bielefeld University. Project: Influence of the Parkinson-associated A53T mutation of α -synuclein on cell viability
Methods: RNA isolation, reverse transcription, PCR, preparation of primary cultures of embryonic murine hippocampal and cortical neurons, lentivirus production in HEK293-FT cells, lentiviral infection of neurons, rotenone treatment, XTT cell viability assay
- 01.2018 – 08.2018 Research assistant in Biochemistry Department III at Bielefeld University. Project: Effect of a double knockout of the SNARE proteins Vti1a and Vti1b on the development of the central nervous system
Methods: Purification of postsynaptic densities from embryonic murine brains
- 04.2018 – 10.2018 Research assistant in Biochemistry Department III at Bielefeld University to supervise the practical courses of biochemistry I and biochemistry II
- 07.2017 – 09.2017 Bachelor's student in Biochemistry Department III at Bielefeld University. Project: Effect of hypoxia on the intracellular localization of NDRG3: a lactate sensor in tumor tissue
Methods: cell culture with HeLa und COS-7 cells, hypoxia incubation, cloning technics, isolation of plasmid DNA

PUBLICATIONS

Hassani Nia, F., Woike, D., Bento, I., Niebling, S., Tibbe, D., Schulz, K., Hirnet, D., Skiba, M., Hönck, H. H., Veith, K., Günther, C., Scholz, T., Bierhals, T., Driemeyer, J., Bend, R., Failla, A. V., Lohr, C., Alai, M. G., & Kreienkamp, H. J. (2022). Structural deficits in key domains of Shank2 lead to alterations in postsynaptic nanoclusters and to a neurodevelopmental disorder in humans. *Molecular psychiatry*, 10.1038/s41380-022-01882-3.

Tibbe, D., Ferle, P., Krisp, C., Nampoothiri, S., Mirzaa, G., Assaf, M., Parikh, S., Kutsche, K., & Kreienkamp, H. J. (2022). Regulation of Liprin- α phase separation by CASK is disrupted by a mutation in its CaM kinase domain. *Life science alliance*, 5(10), e202201512.

Woike, D., Wang, E., Tibbe, D., Hassani Nia, F., Failla, A. V., Kibæk, M., Overgård, T. M., Larsen, M. J., Fagerberg, C. R., Barsukov, I., & Kreienkamp, H. J. (2022). Mutations affecting the N-terminal domains of SHANK3 point to different pathomechanisms in neurodevelopmental disorders. *Scientific reports*, 12(1), 902.

Tibbe, D., Pan, Y. E., Reißner, C., Harms, F. L., & Kreienkamp, H. J. (2021). Functional analysis of CASK transcript variants expressed in human brain. *PLoS one*, 16(6), e0253223.

Pan, Y. E., Tibbe, D., Harms, F. L., Reißner, C., Becker, K., Dingmann, B., Mirzaa, G., Kattentidt-Mouravieva, A. A., Shoukier, M., Aggarwal, S., Missler, M., Kutsche, K., & Kreienkamp, H. J. (2021). Missense mutations in CASK, coding for the calcium-/calmodulin-dependent serine protein kinase, interfere with neurexin binding and neurexin-induced oligomerization. *Journal of neurochemistry*, 157(4), 1331–1350.

POSTER PRESENTATION

Pan Y. E., Tibbe, D., Harms, F., Kutsche, K., and Kreienkamp, H.-J., (2019). Functional Characterization of CASK Missense Mutations. Poster presented at: 39th Blankenese Conference; May 2019; Hamburg, Germany.

Tibbe, D., Ferle, P., Kutsche, K., and Kreienkamp, H.-J. (2022). Regulation of Liprin- α phase separation by CASK is disrupted by a mutation in its CaM kinase domain. Poster presented at Cell Symposia - The Biology of Neuropsychiatric Disorders, Sitges, Spain.

CONFERENCE ATTENDANCE

Argonauts Conference at the University of Regensburg, Germany (2022). Presentation of data from my PhD project in the presentation of my supervisor Prof. Kreienkamp.

CERTIFICATES

Laboratory Animal Science – Basic Course (formerly CAT. B FELASA)
Main Focus: Mice/Rats

Mouse course fulfilling the EU recommendations of Expert Working Group (EWG). Covers function D – humane killing of animals and function A1 – minimally invasive procedures

Project leader course according to § 15 (4) of the Genetic Engineering Safety Regulations (GenTG)

Advanced Light Microscopy Workshop, UKE Microscopy Imaging Facility

Proof of competence for toxicology and hazardous substances according to §5 of the Chemicals Prohibition Ordinance

COMPUTER SKILLS

Microsoft excel
GraphPad Prism
OriginLab
Programming: R

LANGUAGES

German, native speaker
English, fluent
isiZulu, basic

VOLUNTEER WORK

08.2013 – 08.2014 Voluntary service abroad funded by ELM *weltwärts*. Worked at ELC Art and Craft Centre Rorke's Drift, Republic of South Africa

9. Acknowledgements

First, I would like to express my deepest gratitude to my PhD supervisor Prof. Dr. Hans-Jürgen Kreienkamp. It was always a great pleasure to work in his lab, to exchange ideas about many interesting projects and to be guided on my way to becoming a neuroscientist. I especially thank him for taking me to great conferences, for the experiences we had there, and for the people we got to meet and present our research projects to.

I would like to express my sincere thanks to my second PhD supervisor Prof. Dr. Andrew Torda, who gave me the opportunity to do my PhD at the Chemistry Department of the University of Hamburg.

In addition, I would like to thank Dr. Dr. Jan Broder Engler, who supervised me in terms of RNA precipitation methods and performed essential parts of the bioinformatics. I thank him for his expertise and for his contributions to this work.

I would also like to thank the members of my disputation committee, Prof. Dr. Hans-Jürgen Kreienkamp, Prof. Dr. Andrew Torda, Prof. Dr. Zoya Ignatova, Prof. Dr. Hartmut Schlüter and Prof. Dr. Daniel N. Wilson.

I had the pleasure of collaborating with Dr. Fabio Morellini for behavior studies, who was always very welcoming to let me work in his facility. Additionally, I would like to acknowledge Dr. Hannah Voß for performing and analyzing mass spectrometry and proteomics.

I would like to express my deepest appreciation to all my colleagues at the Institute of Human Genetics. Especially, I thank all former and present members of the Kreienkamp group. I greatly value the friendships we built and all the fun we had. Our motto has always been: success is our only option, failure is not.

Ich bedanke mich ganz herzlich bei Hinne, der guten Seele unseres Labors. Es war schön mit dir das Labor teilen zu dürfen und mit dir Rücken an Rücken zu sitzen. Nicht zuletzt, warst du neben Hans-Jürgen die einzige Konstante in meiner Zeit am UKE. Vielen Dank für deine immense Hilfsbereitschaft beim Klonieren, Bestellen und allen anderen Dingen, die du mir immer wieder gerne abgenommen hast. Außerdem möchte ich mich für deine Witze und ehrliche Art bedanken.

Many thanks to Edward and Jonas for proof reading of the thesis and to Joschka for technical support.

This endeavor would not have been possible without my partner Jakob. Words cannot express my gratitude for the love and friendship we share. I am deeply indebted to him for his immense amount of emotional support, for stepping up when I needed him most, and for always being at my side from the very beginning in Hamburg to becoming PhDiddy.

I sincerely thank Jonas, my best friend and ally science lover. I am extremely grateful for the long phone calls, for always being interested in every detail of my work, as well as my personal life. I shared the whole experience with you, and I would not have made it without your motivational speeches.

Special thanks to my dearest friends, Dunja, Henni and Amber. Every single one has a special place in my heart for always listening, cheering me up and supporting me to become the best I can be.

Last, but not least, I thank my family and Jakob's family for their love and support, especially Papa and Carmen, my sisters Becky and Canan, as well as Harriet, Peter, Hannah, Olli, and Oskar. I know that you never doubted me, and it means the world to me to make you proud.

10. Eidesstattliche Versicherung

Hiermit erkläre ich an Eides statt, die vorliegende Dissertation selbst verfasst und keine anderen als die angegebenen Hilfsmittel benutzt zu haben.

Declaration on oath

I hereby declare, on oath, that I have written this dissertation myself and that I have not used any materials other than those indicated.



Hamburg, 05.07.2023

Debora Tibbe